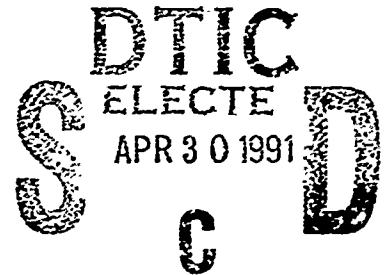# AD-A235 174

AFGL-TR-88-0159

Long Duration Exposure Facility

Peter J. McNulty

Orapin Wipasuramontin

Clarkson University
Division of Research
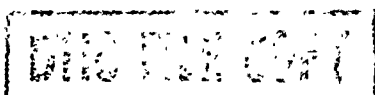Potsdam, New York 13676

Date of Report   June 30, 1988

DTIC
ELECTE
APR 3 0 1991
S
C
D

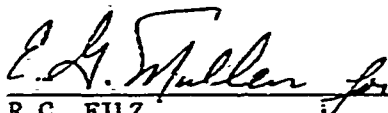Final Report
Period Covered   12/29/1983 - 9/30/1987

APPROVED FOR PUBLIC RELEASE; DISTRIBUTION UNLIMITED

AIR FORCE GEOPHYSICS LABORATORY
AIR FORCE SYSTEMS COMMAND
UNITED STATES AIR FORCE
HANSCOM AIR FORCE BASE, MASSACHUSETTS 01731-5000

91 4 29 015

"This technical report has been reviewed and is approved for publication".

R.C. FILZ
Contract Manager

E.G. MULLEN
Branch Chief

FOR THE COMMANDER

R.C. SAGALYN
Division Director

This report has been reviewed by the ESD Public Affairs Office (PA) and is releasable to the National Technical Information Service (NTIS).

Qualified requestors may obtain additional copies from the Defense Technical Information Center. All others should apply to the National Technical Information Service.

If your address has changed, or if you wish to be removed from the mailing list, or if the addressee is no longer employed by your organization, please notify AFGL/DAA, Hanscom AFB, MA 01731-5000. This will assist us in maintaining a current mailing list.

REPORT DOCUMENTATION PAGE		Form Approved OMB No. 0704-0188

1a. REPORT SECURITY CLASSIFICATION Unclassified	1b. RESTRICTIVE MARKINGS

2a. SECURITY CLASSIFICATION AUTHORITY	3. DISTRIBUTION/AVAILABILITY OF REPORT Approved for public release; distribution unlimited
2b. DECLASSIFICATION/DOWNGRADING SCHEDULE	

4. PERFORMING ORGANIZATION REPORT NUMBER(S)	5. MONITORING ORGANIZATION REPORT NUMBER(S) AFGL – TR – 88 – 0159

6a. NAME OF PERFORMING ORGANIZATION Clarkson University	6b. OFFICE SYMBOL (If applicable)	7a. NAME OF MONITORING ORGANIZATION Air Force Geophysics Laboratory

6c. ADDRESS (City, State, and ZIP Code) Division of Research Director of Grants & Contracts Potsdam, New York 13676	7b. ADDRESS (City, State, and ZIP Code) Hanscom Air Force Base Massachusetts 01731-5000

8a. NAME OF FUNDING/SPONSORING ORGANIZATION	8b. OFFICE SYMBOL (If applicable)	9. PROCUREMENT INSTRUMENT IDENTIFICATION NUMBER F19628 – 84 – K – 0032

8c. ADDRESS (City, State, and ZIP Code)	10. SOURCE OF FUNDING NUMBERS			
	PROGRAM ELEMENT NO.	PROJECT NO.	TASK NO.	WORK UNIT ACCESSION NO.
	62101F	7601	12	BA

11. TITLE (Include Security Classification)

Long Duration Exposure Facility

12. PERSONAL AUTHOR(S)
Peter J. McNulty and Orapin Wipasuramontin

13a. TYPE OF REPORT Final technical	13b. TIME COVERED FROM 12/29/83 TO 9/30/87	14. DATE OF REPORT (Year, Month, Day) 1988 June 30	15. PAGE COUNT 170

16. SUPPLEMENTARY NOTATION

17. COSATI CODES			18. SUBJECT TERMS (Continue on reverse if necessary and identify by block number)
FIELD	GROUP	SUB-GROUP	light scattering fluorescence microstructures Raman scattering

19. ABSTRACT (Continue on reverse if necessary and identify by block number)

The LDEF satellite carried glass and plastic microstructures in the form of spherical particles. Moreover, the radiation-induced tracks in the CR-39 plastic track detectors yield conical microstructures when the plastic foils are etched in NaOH for extended period. The shape and size of the cone depends on the LET of the incident particle and its angle of incidence. The optical properties of these microstructures are analyzed by elastic and inelastic light scattering. The results of these investigations point to new techniques for neutron dosimetry.

20. DISTRIBUTION/AVAILABILITY OF ABSTRACT ☐ UNCLASSIFIED/UNLIMITED ☒ SAME AS RPT. ☐ DTIC USERS	21. ABSTRACT SECURITY CLASSIFICATION Unclassified
22a. NAME OF RESPONSIBLE INDIVIDUAL R. C. Filz	22b. TELEPHONE (Include Area Code) 22c. OFFICE SYMBOL AFGL/PHP

DD Form 1473, JUN 86   Previous editions are obsolete.   SECURITY CLASSIFICATION OF THIS PAGE

TABLE OF CONTENTS

iii

TABLE OF CONTENTS (Continued)

STATEMENT OF WORK

The near-earth environment of space poses a radiation hazard to both human and electronic systems flown in space. Some of the adverse effects of the near-earth radiation environment such as the single-event-upset (SEU) phenomena in microelectronic circuits and the somatic mutations induced in humans cannot be adequately predicted on the basis of measured dose alone. These phenomena are known to depend only on ionizations generated within certain sensitive volume elements that have microscopic dimensions and they are relatively independent of ionizations which occur in parts of the circuit or cell which lie outside the sensitive volumes. This sensitive volume may surround a reverse-biased n-p junction in a memory circuit or surround a gene in the chromosome of a cell. In either case, what determines whether a SEU or a mutation occur in a low does-rate environment is whether more than a threshold number of ionizations are generated within the sensitive volume. In other words, only when more than a threshold dose is absorbed within one of these sensitive microvolumes does the corresponding SEU or mutation occur.

The rate at which events (SEUs or mutations) occur in a given system flown in space depends on the product of the number of sensitive target volumes at risk and the probability of that threshold (or critical charge) will be exceeded in any given target microvolume. In a given biological or microelectronic system, there may, of course, be more than one type of sensitive volume; each with its own dimensions and thresholds.

It is now a well established principal of Health Physics that human subjects or patients not exposed to a new radiation beam or environment until it has been characterized by microdosimetric measurements. In microdosimetry one attempts to determine the pulse-height spectra of the does which would be absorbed by a large number of sensitive microvolumes exposed to the radiation. These data then allow one to predict the number of events or mutation to be expected. It is becoming increasingly obvious that such measurements are necessary to characterize the radiation environments of space for SEU events in microelectronics.

In Radiation Biology, the microdosimeter is typically a gas proportional counter with the gas at a sufficiently low pressure that the number of molecules in the sensitive volume is comparable to that in a sensitive volume in a biological cell. The gas is chosen to have the same mean ionization potential as tissue.

An alternative approach is to fly or expose a sufficiently large number of sensitive volumes to obtain the necessary statistics. This can be done by flying polymer and glass microspheres which can be made quite spherical and monodisperse in diameter. The optical and geometrical properties of each sphere as well as its motion under an applied

electric filed can under the proper conditions provide data on the dose absorbed within the microsphere.

A second alternative approach is to measure the charged particle spectra directly under different layers of shielding using plastic detectors. Use of CR-39 polymer allows measurements of the low-energy portion of the proton spectra. Higher Z particles will be measured on LDEF by the Dublin Institute for Advanced Study in a separate experiment. The proton spectra will be measured from the stacks flown in the Geophysics Lab package on LDEF. By measuring the number of low-energy protons at different depths in the stack of CR-39, the incident proton spectra can be unfolded. The stack of CR-39 will be oriented to preferentially record tracks of protons trapped in the belts.

In preparation for the return of LDEF, the optical properties of the microstructures obtained on CR-39, the material flown on LDEF, were studied for a variety of validations typical of the type to be experienced by the LDEF package. Secondly, modeling will be performed to determine the significance of proton-induced nuclear reactions to the SEU problem in low-earth orbits of the type experienced by Air Force satellites.

An analysis was to be carried out on microspheres to determine whether their optical signal could be clearly separated from that of simple filter holders. If not separable, suitable alternatives techniques for studying the change in optical properties resulting from the irradiation of the microspheres.

SUMMARY OF RESULTS

Nuclear track detectors exposed to cosmic ray particles produce conical pits when etched. The shape of each pit is determined by the speed or, to a good approximation, the LET of the ionizing particle. Optical techniques previously developed to measure the size and cone angle of the pit and to count them involve sequential examination by human operators or computers. This report describes a study of the optical properties of such etched pits with a view of obtaining the information required for developing improvements in techniques for obtaining data from the packages flown on LDEF and from similar dosimeters placed in intense high LET radiation environments. The study is expected to provide valuable new insights into light scanning by simple conical structures.

The angular distributions of light elastically scattered by conical and cylindrical microstructures at the surface of plastic nuclear track detector have been measured. These microstructures were obtained by chemically etching tracks of various nuclei, including protons, neutrons, He-3, alphas, and Fe-56. The base diameters of the structures are in all cases larger than twice the wavelength of the incident light. The results show the dependence of the scattering patterns on shape, size, orientation, and refractive index of the structures as well as the polarization of the incident light. It is also observed that in the single and independent scattering regime, the intensity at the intermediate angular region exhibits linear proportionality to the number of the microstructures per unit area.

Measurements of the angular fluorescent scattering patterns by dye molecules deposited in conical and cylindrical microstructures in plastic plane surfaces reveal the effects of the shape and orientation of the microstructures. Consideration of the polarization of the scattered fluorescence indicates that the excited molecules are free to rotate during the period between the absorption and emission. Application of these techniques developed in this study to dosimetry problems including measuring fission neutron fluences is discussed. Techniques were developed for causing fluorescent dye to adhere to the sides of wide, angle conical pits. These procedures may provide new techniques for dying polymer surfaces.

1. INTRODUCTION

When heavily ionizing nuclear particles traverse a solid state nuclear track detector (SSNTD), narrow regions of the atomic-scale damage are created along their paths. It has been well established in solid state nuclear track technology that, by a simple chemical etching method, these damage tracks can be stabilized, amplified, and rendered visible under an optical microscope. Figure 1.1 shows a photograph from a scanning electron microscope (SEM), showing conical pits from the top. The fiducial line to the right is 1 μm long. The simplicity of the techniques involved, combined with its unique capability of generating the etched structures in SSNTD surfaces or foils from as small as 10 nm upward with controllable size, shape, orientation, and areal density (fluence), has led to applications in diverse scientific and technological areas.

Among different insulating solids that record nuclear tracks, polymers are the most sensitive, and make the detection of nuclei as light as protons feasible. Specifically, the recently found CR-39 plastic has been recognized as the most versatile track detector, not only for its ideal sensitivity and resolution in particle detection, but also for its superior homogeneity, isotropy and optical clarity. The refractive index of CR-39 plastic is slightly lower than that of crown glass.

Studies of elastic scattering of light by small particles show scattered light to be dependent upon the orientation, their geometrical and optical properties, of the conical pits, and upon the wavelength and polarization of the incident light. In addition, recently published research on inelastic light scattering (Raman and fluorescence scattering) from molecules either embedded in or comprising small particles indicates the strong effect on the angular scattering patterns of orientation, size, boundary, and refractive index of the particle, apart from the number and distribution of molecules within it. A wide variety of the applications of elastic and inelastic light scattering studies have been described elsewhere.

For nonspherical dielectric particles, exact analytical results are obtainable only for infinite cylinders and spheroids. Accordingly, it is well acknowledged that the analytical approach alone is insufficient for solving the inverse scattering problems. The organized accumulation experimental information of the scattering by various shapes and sizes is therefore necessary.

In this research, a systematic experimental study of both elastic and inelastic light scattering from randomly distributed conical pits and cylindrical pores of micron size in the CR-39 plastic track detectors' plane surfaces has been carried out. The microstructures are etched tracks of protons, neutrons, He-3 ions, alphas, and Fe-56. The angular distribution patterns of the scattered light from each microstructure, at normal and 45 incidences, were examined for various sizes and fluences of the structures as well as for horizontally and vertically polarized incident light.

1

2. MATERIALS AND METHODS

2.1 Sample Irradiation

Preparation of the CR-39 plastics for each radiation differed in detail from one to the other according to the configuration of the irradiation and the total number of sample pieces needed for a set of irradiation parameters. Generally, a large foil of CR-39 was cut into appropriate smaller foils which were then exposed to the radiation with a particular set of controlled physical parameters. Each exposed foil was then cut into a set of twenty 1.5 cm × 2 cm sample pieces, all with the same corresponding parameters. An alphanumeric label was assigned to each sample, the letter indicating the sample set, (i.e., the associated irradiation parameters) and a number identifying each foil in the set. The irradiated samples were then kept among lead and paper sheets to be shielded from background radiation.

The different irradiations can be summarized as follows:

1. Protons. Pershore CR-39 plastics, of thickness about 0.5 mm., were exposed normally to monoenergetic proton beams from the Van de Graaff generator of RARAF (Radiological Research Accelerator Facility) at Brookhaven National Laboratory. A set of 3 plastic sheets (A, B, C) was exposed to protons of nominal energy 3.5 MeV at fluences of 1.0×10^5, 1.0×10^6 and 1.0×10^7 protons/ cm^2 , respectively. The same fluences were kept for the other set of samples (D, E, F) with protons of nominal energy 2.0 MeV. Dosimetry was carried out using a solid state detector and a LET (Linear Energy Transfer) chamber before and after the irradiations. The spread of energy ranged from a maximum of ±5.0 % for the 2.0 MeV beam, to the minimum of ±1.0 % for the 3.5 MeV beam. The drift of the beam flux was ± 1.0 % between the before and after dosimetry measurements.

2. Helium-3 Ions. Irradiation to monoenergetic He-3 beams was also performed at RARAF. Three sets of Homalite plastic sheets were exposed at normal incidence to He-3 beams with three different nominal energies. The first set of 4 sheets (H, I, J, K) was exposed to the 8.12 MeV beam at fluences 0.95×10^5, 2.0×10^5, 5.0×10^5 and $1.0 \times 10^6 / cm^2$, respectively. The second set of one sheet (G), was exposed to the beam of nominal energy 8.2 MeV at the fluences of 5.0×10^4 $/cm^2$. The last set of 3 sheets (L, M, N), was exposed to the beam with nominal energy 5.6 MeV at fluences: 2.0×10^5, 5.0×10^5, and 1.0×10^6 / cm^2, respectively. Fluctuations of fluences ranged from ±3 % for both first and third sets to ±10 % - 20 % for the G set. Less than 1 % low energy proton contamination was estimated in these runs.

3. Alphas. The American Acrylics and the (pre-etched) Orma Optical CR-39 plastic sheets of thickness 0.3 mm. and 1.8 mm., respectively, were used for the irradiations. The radioactive source employed was a 0.05 μCi Am-241 source from which alpha particles with nominal energy of 5.486 MeV were emitted. The irradiations were carried out in an

evacuated decicator. The plastics were exposed perpendicularly at a distance of 12 cm from the source. Only one sample (TAL2) was irradiated close to the source. Several sets of samples (AALs and TALs) were irradiated with exposure durations varied from 16 hours to 6 days.

4. Neutrons. The Pershore CR-39 plastic sheets of thickness 0.5 mm. were chosen for this case. The irradiations were done in a NH-3 Neutron Howitzer in which a 1 Ci Pu-Be neutron source was available. The neutron energies ranged from 0 up to a maximum of 10.5 MeV with an average of 4.2 MeV. The samples were placed in a side-port drawers, against a 1.3 cm thick lucite window of the port. The geometries of the Howitzer and a side port drawer are shown in Fig. 2.1. The durations of irradiation varied from 1 day to 12 days.

5. Iron-56. These sets of samples were acquired with courtesy of G.F. Siegmon, Institute for Rein Und Angewandte Kernphysik, W. Germany. They were prepared originally for the study of nuclear track filters made from the CR-39 plastic foils. The foil thickness was approximately 80 - 100 μm. Three sets (S, P, and B) of the foils were exposed to the monoenergetic Fe beams of nominal energy 16.3 MeV/AMU with various fluences. For the set S, the fluence was kept at 1.0×10^6/ cm^2 Set P consisted of samples with fluences 1.0×10^4, 1.0×10^5, and 1.0×10^6 per cm^2 For set B, the controlled fluences covered from 1.0×10^3/cm^2 up to 1.0×10^6/ cm^2.

2.2 Chemical Etching

Microstructures in the plane surfaces of the irradiated sample were developed by the chemical etching techniques. An etch condition involved, primarily, the etchant (with certain concentration), the fixed temperature, and the etching duration. The general conditions incorporated in this study were selected, following recipes in the literature and our preliminary experiments, to render etched tracks of desired geometry with the least harm done to the optical property of the plastics. The conditions and procedures associated with the production of the micropits for this study are stated below.

2.2A Etching Recipes

Two etching recipes were used for the samples in this study. The first recipe was applied to the proton, neutron and He-3 irradiated samples. The etch was carried out in 6N NaOH at 50 degrees centigrade. The alpha irradiated samples were etched in 6.25 N NaOH at either 50 or 70 degrees centigrade. The etch period was varied from batch to batch, to yield a wide size range of the developed pits.

The Orma Optical CR-39 were pre-etched in 40 % 6.25 N NaOH 60 % methanol, at 70 degrees centigrade for 2 hours before irradiation.

2.2B Procedures

The samples selected for a given set of light scattering measurements were etched simultaneously. For instance, to produce a set of samples with microstructures with the same distribution in geometries but different densities of samples, the sample plates irradiated by beams of the same particles and energy but two different fluences were etched simultaneously under identical etching conditions and parameters. Control blanks (unirradiated), cut from the same corresponding plastic sheets, were included in the batch, whenever available. A constant temperature water bath served as an etching reservoir. In one processing procedure, the samples were placed (with the irradiated surfaces up) individually in flasks filled with etchant that had been warmed to the set temperature of the water bath. Evaporation of etchants was diminished by sealing the beaker top with rubber corks. The etchant was gently agitated by setting the bath to shake at about 70 strokes/min. In this configuration, as schematically shown in Fig. 2.2A, the back (unirradiated) surfaces of the samples were also being etched.

Chemical etching inevitably introduces additional and undesirable inhomogeneity to the plastic surfaces. This was partly due to manufacturing defects and partly due to the background tracks. To eliminate this etch-induced irregularity on the back of a sample surface, a one-sided etch configuration was devised and utilized in a few sample productions. A sketch of the configuration is given in Fig. 2.2B. A glass bottle 5.5 cm. long and 2 cm. in diameter was used as an etchant container. The bottle (A) was held between two thick flat plexiglass plates (B) connected by two parallel rods (C), a 2x3 cm. rubber sheet (D) with 1 cm. hole at the middle was centered on top of the bottle. A sample was then placed between the rubber and the top plate and was kept intact by tightening the screws (E) on top of the plate properly. In etching, the unit was laid lengthwise and immersed in the water of the shaking bath. This arrangement allowed the area of the sample exposed through the rubber hole to be etched only. After the etching process had been completed, the samples were rinsed thoroughly in distilled water, wrapped separately in lens papers and dried in a vacuum oven at (40 ± 2) degrees centigrade for at least a day, before undergoing any light scattering measurements. Any etched samples whose surfaces, when viewed under a microscope, appeared rough or with overwhelming defects not introduced by irradiations were discarded.

2.3 Dye Treatments

Two types of laser dyes that are compatible with the incident laser wavelength were considered for the study of fluorescence scattering, namely, Nile Blue A perchlorate and Oxazine-170 perchlorate. The absorption and emission wavelengths, as specified by the Polysciences Ltd., are listed in Table 2.1.

Several techniques were attempted in order to deposit an amount of dye in the pits in

the plastic samples. The dye powder was dissolved in an ethanol solvent. In an early trial, a few drops of the dissolved dye were added into the etchant during a sample etching. However, no fluorescence was detected from that sample. Rubbing the sample surface repeatedly with the dissolved dye still did not yield sufficient signals above noise level. It was discovered that satisfactory fluorescence could be detected if the sample soaked in a mixture of dye dissolved in distilled water while exposed to sound waves in an ultrasonic bath for several hours. Accordingly, preparation of an etched sample for fluorescence measurements consisted in drops of a dye solution being applied on and steadily rubbed along the sample surface (with the openings of the pits) followed by the surface being treated with the dye solution mixed with distilled water in the ultra-sonic bath. The treatment was carried out by employing the one-sided etch device in which the distilled dye solutions replaced the etchant and the unit was held upside down in the ultrasonic bath.

2.4 Deposition of Microspheres

Glass microspheres of larger and comparable sizes as compared with the microstructures under investigation were selected for this purpose. A dilute solution of spheres was prepared by dispersing a small number of the spheres in a weak detergent solution (SDS) in the ultra-sonic bath. The solution was then promptly spread onto the sample surface of interest and let dry.

For this preliminary study, glass microspheres of average size 2 μm with 65 % std. dev., and 11.3 μm with 15 % std. dev., purchased from Duke Science, were chosen. The SDS solution concentration was 0.00257 gm/cc.

The production and treatment of the samples for this study are summarized in Table 2.2.

It should be noted that care had to be taken in handling the samples in all steps to avoid fingerprints and scratches on the surfaces in order to retain the optical quality of the samples for further light scattering measurements.

3. LIGHT SCATTERING MEASUREMENTS

3.1 Elastic Light Scattering

3.1A Experimental Setup

A photograph depicting an overall view of the light scattering experimental setup used in this study is shown in Fig. 3.1. A schematic representation of the setup is illustrated in Fig. 3.2. Brief descriptions of the components in the set up and the instrumentation follows:

a. Goniometer Unit. As shown in Fig. 3.2 the unit consists of a 50 cm diameter tiltable horizontal rail (A) to which a vernier (B) for angular readings has been attached. A vertical quadrant (C) is rotatable along the goniometer. The quadrant serves as a base for mounting a light detector unit. The whole instrument is installed on a solid platform (D), which in turn is fixed on the top of a 1.5 m long optical bench.

b. Sample Holder Unit. This unit consists of a holder housing (E) and a holder mounting bracket (F), as shown in Fig. 3.2. The housing is located near the center of the goniometer and is installed on the same platform. An extended shaft (G) is built with a groove in which the end of the mounting bracket is fitted and kept in place. The housing is designed and constructed to permit rotations of the bracket shaft horizontally around the column (H) and vertically about the base (I). In addition, the rotation of the sample bracket shaft around its own axis can be done by turning a knob (J) around the shaft G. The amount of this rotation is indicated by an angular scale graduated on a disk (K). These degrees of freedom of the unit facilitated sample adjustment and alignment with respect to the light beam.

c. A Light Source. In this investigation, a Model 120 He-Ne laser purchased from Spectra-Physics, Inc. was used as a light source. With output power ¿ 5mW, it provides TEM linearly polarized light of wavelength 0.6328 nm. The Model 120 body is 478.0 cm long and was situated at the bottom end of the optical bench.

d. Light Detection Unit (LD). A GE L14G3 photo transistor and a GE L14F1 photo-darlington amplifier were employed as light detectors in measurements of scattered light signals throughout the study. They are identical in shape and dimension. Fig. 3.3A provides a sketch with the dimensions of the detector. The lens cap which serves as an aperture of the detector is 0.5 cm across. The relative intensity of scattered light was monitored by a Keithley 181 Nanovoltmeter as a voltage drop across a resistor (R), which was connected in series with a detector and a DC power supply. A diagram of the light detection circuit is shown in Fig. 3.3B. The typical electrical characteristics of both detectors are given in Appendix A. Accordingly, a standard resistor of 10K, and operating voltages of 5 V and 10 V for L14G3 and L14F1, respectively, were chosen in operating the photodetector circuit.

A few sets of measurements were taken using the photo detector with the collimator and lens cap removed. In these cases the detector was mounted in a small plexiglass housing whose geometry is illustrated in Fig. 5.4. A groove (A) at the back is designed to allow positioning and sliding of the detector along the goniometer rail.

Most of the measurements were taken by using the photo detector with collimator 1. The design of this tubular collimator is depicted in Fig. 3.5. The base (A) of the unit is attached to the vertical quadrant of the goniometer. The detector is mounted at the back, just behind a slot for a polarizer. The slot allows a 90 degree rotation of the polarizer around the collimator axis. The removable middle body part (B) is built with slots for circular filters. The removable front part (C) with slots is constructed with a smooth curved surface with an aperture 0.5 cm in diameter. The polarizer employed is fixed in a typical cylindrical holder with a polarization axis indicator projecting out of the colliimator.

The analog output from the voltmeter was digitized using an Omega WB-31 Analog/Digital converter and a Z-100 microcomputer, with several readings taken and stored in a floppy disk via a Z-basic program.

3.1B Procedures

The experiment was carried out in a dust-free clean room. Figure 3.6 depicts the geometry of a typical light scattering measurement. In this study, the scattering plane or the observation plane was set to be coincident with the yz (horizontal) plane. In each measurement, the relative intensity of the scattered light in both forward and backward directions was measured. The scattering angle, O, considered was confined to 5 - 175 degrees due to blockage of the incident beam by the edges of the photodetector unit at the narrow forward and backward directions. The laser was set at a position such that the polarization of the emitting line was either parallel (horizontal) or perpendicular to the scattering plane. This was done by mounting a polarizer at cross polarization in the beam and adjusting the laser position until the minimum intensity of the beam exiting the polarizer was observed. Once this had been achieved, the polarizer was removed from the incident beam.

A few preliminary measurements were taken for a number of selected samples, in order to establish stability and reproducibility of the experimental system. Data acquisition was computerized with the angular position of the photodetector assembly being monitored and changed by computer signals to the stepping motor. Care was taken in aligning a sample surface relative to the incident beam. For normal alignment, the reflected beam spot was aligned along the incident direction. To avoid misinterpretation of the obtained results, only the 'clean' sample areas, i.e., the ones that gave smooth, streak-free intensity distribution in the observation plane as observed on a temporary screen by unaided eyes,

7

have been investigated.

In each measurement, the relative scattered intensity from a sample was recorded for every degree in the angular range 10 - 170 degrees.

For both conical and cylindrical microstructures, measurements were made for sample surfaces aligned normal to the laser beam. A few preliminary results for 45 degree alignment have also been studied.

For a given polarization of the incident laser light, the parallel and cross polarizations of the scattered light from a few selected samples over the angular range have been examined.

Studies of the effects of moisture and changes of refractive index of microstructures on the scattering pattern proceeded as follows: A dry sample was treated in an ultrasonic bath with distilled water with no dye for 2-3 hours, measurements were taken, and the patterns compared with those obtained from the sample before the bath treatment. The parallel procedure was applied to selected samples that underwent dye treatments as well as water baths.

Effects of deposition of small particles on the microstructures on scattering patterns have been studied as follows: A layer of glass-microspheres was spread on the sample surfaces with pits and the resulting angular distribution patterns were compared with the corresponding ones without spheres.

3.2 Flourescence Measurements

3.2A Experimental Setup

The setup used in elastic light scattering studies (Figs. 3.1 - 3.5) was employed with minor modifications to the detector unit in fluorescent scattering measurements. Fluorescence signals are much weaker than elastic signals. As a result, the collimator 1 was used without the front part (D) for these studies.

A GE L14F1 photo-darlington was used as a fluorescence detector. The spectral response curve of the detector is given in Appendix A.

A long pass cut-on filter was placed in a slot in front of the photodetector to filter out the incident wavelengths. In an ORIEL Model 5133 filter which has 50 % transmission for 0.670 nm wavelengths, and higher transmission for longer wavelengths up to the near infrared was used to measure the fluorescence associated with Nile Blue. In case of Oxazine, an ORIEL Model 5134 filter with 50 % transmission point at 0.705 nm. was used. The transmission curves and specifications of these filters are included in Appendix B.

3.2B Measurements and Methods

The geometry of fluorescence measurements carried out in this research was the same as that of elastic scattering (Fig. 3.6). For each sample mounting, the scattered flu-

orescence signals at scattering angles, θ, between 10 and 170 degrees were monitored. Investigations of the dependence of the angular distribution of the scattered fluorescence by the dye molecules deposited in microstructures on various parameters of interest proceeded as follows: Dye treatments were carried out for various plastic samples with conical as well as cylindrical microstructures of different fluences and sizes selected for the study. For cone shape, angular scattering patterns were measured for each sample at tip-on and base-on incidences in the plane parallel to the cone axis. Measurements for the cases in which the microstructures oriented 45 degrees with respect to the scattering plane were also obtained.

For some samples measurements were made after each repetition of the dye treatments to observe changes in fluorescence signals with numbers of the dye molecules.

Polarizations of the fluorescence were considered for samples that gave sufficiently high scattered signals.

4. ELASTIC LIGHT SCATTERING RESULTS

4.1 Angular Distribution of Scattered Intensity From Conical Microstructures

4.1A General Features of the Angular Scattering Patterns

The dimensions and a sketch of the representative geometry of the microstructures in each sample as determined from the scanning electron microscope (SEM) measurements are listed in Table 4.1. In this study, the etched tracks produced by the three different nuclei, viz., He-3, He-4 (alpha particles) and protons assume three distinct conical shapes, respectively: sharp, round (corresponding to the spherical phase in etch track formation), and shallow. Various angular distribution patterns of the scattered intensity from sample sets with structures corresponding to these shapes normally aligned in the sample surface for horizontally polarized incident light are shown in Figs. 4.1 through 4.10. The error associated with a measured intensity is $\pm$ (4.17% 0.010 mV). The first term indicates the uncertainty in the reproducibility of the reading, and the second term is the systematic noise level at low scattered intensity range. For most measurements the forward angular region from 0 to 10 degrees and the backward region from 170 to 180 degrees around the incident beam are excluded from the measurements because the detection system used is unable to separate the incident light from the forward and backward scattered light.

The asymmetry about 90 degrees observed for all the measured patterns clearly indicates that the scattering structures are far larger than that of Rayleigh scatterers. The condition for Rayleigh scattering is that the scatterer is much smaller than the wavelength of the lights. The scattering patterns from identical sharp cones, as depicted in Figs. 4.1 through 4.4 for both tip-on and based-on incidences, generally consist of a forward narrow bright peak up to around 15, a deep minimum, a broad peak or a 'hump' with one or two shallow minima superimposed on it, followed by a dim region up to 90 degrees. The intensity over the hump region at base-on incidence is higher than that of the corresponding region at tip-on incidence. The backward scattering patterns have similar features with about two orders of magnitude less intensity.

In the patterns from round cones of the size range under consideration (Figs. 4.5 and 4.6), the scattered signal drops off sharply within a narrow forward lobe and no clear maxima are present. The signal scattered into the backward plane is almost zero. The scattered intensity at base-on incidence is approximately two times greater than that of tip-on incidence at larger angles in the lobe.

The forward patterns from shallow small cones shown in Figs. 4.7 through 4.10 resemble those from round cones but the backward patterns are noticeably different both in intensity (with respect to the corresponding forward value) and angular dependence. They are similar, instead, to the larger angle patterns typical of sharp cones.

It has been observed from all sets of samples that the detailed features of the backward

scattering patterns, especially at large angles from the backward direction, vary in random fashion and are not consistent with the corresponding forward patterns. This implies that they are more sensitive to the change in the morphology (including that which results from plastic inhomogeneity) of the scattering structures than are the forward patterns. This assertion agrees with the result of the theoretical study of light scattering by layered spheres.

The etched tracks of the recoil nuclei in the neutron irradiated samples represent a planar distribution of conical pits of random size, shapes and orientations. This is similar to the pattern to be expected on the LDEF samples. The measured forward scattering patterns displayed in Fig. 4.11 for samples with different irradiation durations show a fairly uniform decrease of the intensity with increasing scattered angle. The same measurements were carried out for etched recoil tracks on the back surfaces (down stream from the neutron source) of these samples. The angular distributions, as shown in Fig. 4.12, are essentially identical for the back surface to that from the corresponding front surface. This should be expected since the tracks registered on the front and the back of the irradiated samples are generated by the recoil nuclei resulting from the interactions of the neutrons with the plastics upon entering and leaving, respectively. Both sides of the samples were etched simultaneously under the same conditions. The recoil nuclei are mainly protons with a small fraction being fragments from other heavy nuclei that are also constituents of the plastic. This angular distribution can be interpreted as due to the averaging out of the intensities contributed from all random orientations. It has been noted that the results from the longest irradiated sample, the 12 days irradiated, have been found to be very close to those of 6 days, irradiated sample (not included in the figures). However, examination of the sample under a microscope showed that the number of etched tracks per unit area were also about the same.

4.1B Dependence of the Angular Distribution Pattern on the Polarization of the Incident Light

The angular scattering patterns from sample K3 for both horizontally and vertically polarized incident light are illustrated in Figs. 4.13 through 4.16 . All three scattered intensity elements, total (without analyzer), same polarized (H_h and V_v) and cross polarized (H_h and V_h) components are considered at tip-on incidence as well as at base-on incidence. Introducing the polarizer into the detection unit has been found to reduce the intensity of the original signals by an average factor of 3.7. This arises from a combination of the optical properties of the polarizer material and nonlinearity in the incident polarization. This factor has been taken into account in the following analyses.

Comparison of the H_h and V_v of the forward patterns show that the scattered intensity in the narrow forward lobe around 5 to 15 degrees is less sensitive to the incident

polarization than the lateral angular region. This agrees with the theory that the major contribution to the scattering in the forward lobe is from diffraction which is independent of the incident polarization, whereas at larger angles the geometric optics, which depends on the incident polarization (as well as the morphology of the scatterers) is dominant.

Backward scattering patterns manifest strong dependence on polarization, particularly in the peripheral region, in forms of the 'hump' and peak structures which are more pronounced for one incident polarization than the other. For instance, the hump between V_v 152-168 degree is more pronounced in H_h pattern than that in V_v, but the reverse is true for the hump between 102-116 degrees. The polarization dependence is associated with reflection and refraction, which in turn relates to the morphology of the scattering particles. This again shows that backward patterns are very sensitive to the geometry and refractive index of the scattering media. Accordingly, the backward scattering patterns can be used to obtain information on the geometric uniformity of the microstructures and the homogeneity of the scattering media.

It follows from symmetry considerations that scattering from a collection of identical structures (in size, shape, and orientation) should result in cancellation in the cross polarization intensity component. The sample K3 is assumed to contain $1.0 \times 10^6/cm^2$ conical pits of diameter 5.0 μm and a cone half angle of 45. The deviations from zero of H_h and V_h components for this sample, in the forward hump region at base-on incidence and in the backward shoulder region at tip-on incidence, may indicate the degree of nonuniformity in size, shape, and orientation of the scattering conical structures. A slight shift in the conical tip alignment off the measurement plane can destroy the symmetry property of the problem. Since the structures are rigidly suspended in the plastic plane surface, misalignment of the whole collection with respect to the incident direction can be easily introduced by inaccuracy in aligning the sample surface perpendicular to the incident beam. This argument leads to the deduction that the forward hump region at base-on incidence and the backward shoulder region at tip-on incidence contain useful information on scattering from cone edges and tips.

The degree of linear polarization, which is defined by $(V_v - H_h)$ $(V_v + H_h)$, of the scattered light for unpolarized incident light obtained from the measurements at tip-on incidence from the conical pits in sample K3 is plotted as a function of scattering in Fig. 5.17. Comparison is made with the results calculated by Mie theory for spheres of equal surface area. The degree of polarization varies drastically with angle. This variation follows a trend that is roughly similar to that of spheres in the forward direction although the sign is opposite in certain regions.

4.1C Dependence of the Angular Scattered Intensity on Fluence

The word "fluence" used in this study for irradiation to monoenergetic ion beams,

fluence means the number of ions incident on the detector surface per unit area. The areal density of micropits should be proportional to the fluence particles incident on the nuclear track detector foil. The dependence of the scattered intensity on the areal density of the micropits with fixed orientations can be inferred from the plots of intensity versus nominal fluence, in Figs. 4.18-4.25, for several sample batches whose angular scattering patterns have been presented previously. The diameter of the cones considered ranges from 1.46 μm (A1) to 2.53 μm (I18) and the nominal fluence from 0.95×10^6 per cm^2 to 3.0×10^5 per cm^2 The geometry of cones in the same batch is assumed identical because their exposure and etch conditions were identical. The optimal angles are selected to provide high scattering intensity with smooth variation.

The contributions from each particle to the light scattering measured at any angle should be additive under the assumption of incoherent scattering by individual structures. Then the total scattered intensity at any angle is directly proportional to the number of scatterers in the scattering volume. In this study the plots show a linear dependence of scattered intensity with nominal fluence for most sample sets in agreement with this assumption. However, this assumption must break down above some critical fluence due to the onset of multiple scattering or to the merging of individual micropits into larger structures with a different shape. Either would lead to a deviation from a linear dependence on fluence. A superlinear relationship is evident in two sample sets as shown in Figs. 4.20 through 4.23. The deviation from linearity becomes noticeable at the intensity corresponding to the highest fluence in each set. In addition, observations using an optical microscope and a scanning electron microscope (SEM) show clustering and merging of structures in these samples. It is, therefore, not possible to separate the effect of the multiple from the independent scattering. Accordingly this superlinear dependence may suggest the breakdown of the single scattering or the independent scattering assumption. It should be remarked that the results of SEM observations reveal that the size and volume of the structures vary slightly among the samples in a batch irradiated and etched under identical conditions. This may also contribute, to some extent, to the denation from linearity the plots.

For neutron irradiated samples, the fluence was at first presumed to be directly proportional to the duration of irradiation. In a study of the relation between scattered intensity and fluence, the forward angular distribution for these samples was measured. It was found to decrease fairly uniformly from 7 to 17 degrees. A straight line was fit to the data in this region for each sample. The intensity at 12 degrees from this curve is taken to represent the intensity variation for the region. The plots of the intensity at 12 degrees against the irradiation duration corresponding to both front and back surfaces are shown in Fig. 4.26 . The results shows linear correlation between intensity and durations of irradiation for all but the 12 days irradiated sample. The fluences of individual samples

were estimated by counting the number of the pits observed by an optical microscope per unit area. The results for the front surface are given in Table 4.2. The counted fluences for 6 days and 12 days irradiated samples are comparable as can be seen in the plot of fluences versus durations of irradiation (Fig. 4.27). In Fig. 4.28, the scattered intensity is plotted versus fluence counted manually for these foils. Here all the data points including the 12 day sample are fit by a linear relationship. This implies that there was an interruption in the neutron irradiations due to unknown causes. In any event the light scattering results of manual counting are in agreement.

4.1D Dependence of the Scattered Intensity on Volume of the Scattering Particles

Five randomly selected pieces of samples that have been irradiated by 8.2 MeV He-3 ions with the same nominal fluence of $5.0 \times 10^4 / cm^2$ (Gs samples). They were etched under the same condition for different durations, in order to produce a set of samples with cones of different sizes but the same number per unit area. The sequence of geometries resulting from 8 to 24 hour-etches as obtained by the SEM observations, are given in Table 4.1. The SEM photographs also occasionally reveals the presence of long sharp cones with oblique orientation in samples etched for 16 hours or more. Notice that the changes of diameter and cone length with etching time are nonuniform and the resulting conical wall profile evolves from slightly to sharply convex and straight line in the last sample. The angular distribution patterns for these samples are depicted in Figs. 4.29 and 4.30 at tip-on and base-on incidence, respectively. The scattered intensity increases with the etch period. The hump structure that emerges after 8 hour etching in the forward patterns at base-on incidence suggests the association of this structure with size and shape of the scattering particle. Quantitatively, the average intensity at the peak of the hump increases linearly with the volume of the cone as shown in the plot in Fig. 4.31. This linear dependence is also evident at other optimal angles, for example at 10 degrees, as presented in the same figure for both tip-on and base-on illuminations.

It was shown earlier that the broad peaks are consistently observed in the scattering patterns for both tip-on and base-on incidence in samples N17, K18, and K3 all with the same fluence of $1.0 \times 10^6 / cm^2$ Figure 4.32 shows the average scattered intensity at the peak plotted against the volume of the corresponding conical pits for both forward and backward incidence. Note that the values of the peak intensity are higher at base-on incidence than the corresponding values at tip-on incidence. The results for base-on incidence again reflect the linear dependence upon volume, but for tip-on incidence the linearity is not obvious. It should be remarked that the volumes were calculated assuming right circular conical shape for all samples, this assumption is not strictly true for many of the samples considered.

4.1E Peak Position vs Cone Half Angle for Base-on Incidence

14

Peak structures are observed in the intermediate angular regions of the light scattering patterns. In general, contributions to light scattering in this region are from both diffraction and geometrical optics, i.e., reflection and refraction. In the large structure limit, diffraction is confined within the narrow forward lobe. The refraction contribution predicted by geometrical optics can be obtained by using simple ray tracing and applying Snell's law of refraction, as demonstrated in Fig. 4.33A. Rays incident base-on on a straight wall of a cone suspended in a plastic film will be refracted one at the air-plastic interface and then at the plastic-air interface. The refraction angle at emergence from the plastic is given by

$$\theta_r = \arcsin[(\frac{n_p}{n_{air}}) \sin(90^o - \theta_t)]$$

where $\theta_t = \arcsin[(\frac{n_{air}}{n_p}) \sin(90^o - \theta_c)]$, θ_c is the cone half angle, and n_p is the refractive index of the plastic. For CR-39 plastic, $n_p = 1.4503$.

Accordingly, this double refraction will contribute significantly to the scattering angle pattern at the scattering angle $\theta = \theta_r$ and a peak should be observed at this position. Apparently, the observed base-on incidence hump structure can be interpreted as associated with this double refraction peak. Hence θ_r can be deduced from the light scattering measurement for this configuration. Consequently, the hump angular position will contain information on the conical shape, i.e., θ_c, as calculated from equation 4.1 once θ_r is known. To justify this, the cone half angles of the pits in samples K3, K18, L15, M6, N17, G(12 Hr.), G(16 Hr.), G(20 Hr.) and G(24 Hr.) were calculated from the SEM measurements of cone diameter and length, based on the assumption that they are right circular cones, i.e., with uniform wall slopes. The corresponding values of θ_r predicted by Eq. 4.1 were determined and compared with the observed average angular position (the middle) of the base-on incidence hump. Good agreements are found only for three samples: K3, G(12 Hr.) and G(24 Hr.). These turn out to be those whose shapes are seen to be circular cones in SEM photographs. For other samples with convex conical walls the observed positions are shifted from the estimated positions toward the incident direction. This can be explained qualitatively by investigating the tracing of rays incident on the convex conical wall in comparison with that on straight wall as illustrated in Fig. 4.33 B. The convex wall, apparently, converges the rays closer to the incident direction at the back surfaces of the plastic film. Consequently, smaller values of 0 result, which is consistent with the light scattering observation. In addition, the broadening of the jump can be attributed, in part, to the nonuniformity of the slope along the conical wall.

4.1F Effect of Multiple Scattering

A common feature evident in the scattering pattern obtained from high-fluence sam-

ples at tip-on incidence is a rise of backward scattered intensity at the intermediate angular region between 120 and 160 degrees. As a result, the symmetry between the forward and backward patterns (about 90) is destroyed. For these samples, the ratio of the scattered intensity in the cones ponding forward region (i.e., 20 - 60 degrees) to that of the backward region becomes unusually low. This can be seen from the plots of the ratio of the intensity at 30 degrees and 150 degrees versus fluence for various sets of samples (Fig. 4.34). The SEM observations also reveal that the size and/or density of the conical pits in these high-fluence samples cause the pits to lie very close to each other and clustering and merging of pits are common. Accordingly, this characteristic may indicate the breakdown of the single and/or independent scattering assumptions. It is, therefore, asserted that the intermediate angular region at tip-on incidence is sensitive to the effects of multiple scattering.

4.1G Comparison with MIE Calculations

The diameters of the conical pits under this study range from 1.46 μm to 6.00 μm. The lengths range from 0.28 μm to 4.32 μm. The volume ranges from 0.204 to 40.7 cubic μm. Spheres having the same surface area would have size parameter $a=2\eta a/\gamma$ (a=radius) ranging from 4.18 to 14.75. Using the computer code developed originally by IBM, MIE calculations for spheres having the same cross sectional area were carried out for a few selected samples and compared with the measured angular scattering patterns at tip-on incidence. The results for H_h of K18 (a= 7.817) and V_v of K3 (a eq = 14.75) are given in Fig. 4.35 and 4.36, respectively. The patterns from spheres and cones are drastically different, especially in the backward patterns. For K3 whose size parameter is larger than the resonance region, however, the first minimum coincides. This reflects the dominance of diffraction in the narrow forward lobe for this size range. The comparison is a clear demonstration of how strongly the angular scattering pattern depends on the shape of the scatterers. For equivalent surface area, spheres scatter more light in the lateral angular region than cones. Furthermore, the scattering from these intermediate size particles is a result of complicated contributions from both diffraction and geometric optics throughout the entire angular region.

4.2 Angular Distribution of Scattered Intensity from Cylindrical Pores

4.2A General Features of the Angular Scattering Patterns

The length of cylindrical pores, assuming uniform and normal alignment of the CR-39 foils, is specified by the thickness of the foils which can be measured by a micrometer. The average diameter of the pores in each sample measured from the SEM photographs of the sample directly or from the replicas is given in Table 4.1. The diameters range from 1.9 μm to 5.5 μm and the lengths range from 90 to 100 μm. For samples with low

fluence (1.0×10^3 up to $1.0\times10^5/cm^2$), the general features of forward angular scattering patterns at head-on incidence, measured in the plane parallel to the cylindrical axis, as shown in Figs. 4.37 through 4.39, consist of a series of unequally spaced maxima and minima whose intensity decrease with increasing angle. The scattered intensities are confined within a narrow forward lobe. The backward pattern is similarly characterized but with the scattered intensity approximately an order of magnitude lower. The scattering patterns are not symmetric about 90 for these samples. For samples with high fluence, light scattered into the lateral region in both forward and backward patterns increases considerably. Consequently, the scattering pattern becomes more symmetric, as depicted in Fig. 4.40.

The patterns obtained from both surfaces of a sample are comparable except at the lateral regions. The discrepancy may be attributed to the slight difference in pore opening at both ends, or to a slight tapering of the cylinder, assuming accurate alignment of the sample. Evidence of the geometric peaks at large angles close to 90 degrees in both the forward and backward pattern is also an indication of tapering in the cylinder shape. It can be shown by ray tracing that a taper in the cylinder wall of 5 degrees will give rise to geometric peaks (due to reflection and refraction) at scattering angles 74.4 and 105.6 degrees.

Notice that the notable minima occur approximately at the same angular position among all samples (B3 through B6), indicating the relative uniform pore size among the samples which agrees with the SEM observation.

It should be noted that the available theoretical algorithm numerical simulations of light scattering by finite dielectric cylinders is applicable for cylinders whose axial ratios are comparable to that of spheroids. Accordingly, the solution is not suitable for the size range of cylinders considered in this investigation. Calculations of the angular scattering pattern based on the diffraction theory approximation, which is valid for a large opaque cylinder, show striking differences from the measured pattern corresponding to the same cylinder dimensions, and therefore will not be presented.

4.2B Dependence of Scattered Intensity on Pore Density

Variation of the scattered signal with pore density was examined in the optimal angular region, i.e., in the region free from maxima and minima, at about 25 to 40 degrees. In this region, the signals from sample B3 are small and may not be reliable. Consequently, only data from B4, B5, and B6 with pore density 1.0×10^4, 1.0×10^5, and 1.0×10^6 per cm^2, respectively, have been considered. Fig. 4.41 illustrates the linear increase of scattered intensity with pore density at different scattering angles, for densities up to $1.0\times10^5/cm^2$ For the density $1.0\times10^6/cm^2$, the intensity is consistently higher than the corresponding linear trend by an average factor of 3.5. As in the case of scattering from conical pits, this

17

superlinear dependence at high fluence may indicate the violation of single or independent scattering approximations.

4.2C Dependence of the Scattering Intensity on Polarization of the Incident Light

The dependence of the scattering pattern from cylindrical pores on polarization of the incident light were deduced from the complete measurements made on sample B3. Figures 4.42 and 4.43 show characteristics consistent with that from cones. The results confirm that the narrow forward and backward lobes are less sensitive to the polarization of the incident light then the light scattered through intermediate angles. Fine structures (humps and peaks) in backward patterns strongly depend on the incident polarization. This assertion is positively supported by the later results obtained with the cylinder aligned 45 degrees to the incident beam, which will be discussed in the next section.

4.2D Light Scattering from Cylinders versus Cones

A study of the difference between scattering patterns from cylindrical pores and cones of comparable diameters was carried out by comparison of the patterns obtained from B5 (V_v Component) with those from K3 normalized to correspond to the same fluence. It was observed that the general features of patterns from cylinders resemble those from cones at tip-on incidence. However the diffraction-like peaks are more pronounced in pattern from cylinders and the intensity drops off faster toward the larger forward angles.

Comparison of the patterns from cylinders with those from cones at base-on incidence shows that in spite of smaller volume, cones scatter more light in the angular regions: 18 through 35 degrees and 155 through 165 degrees. In the region around forward and backward directions, however, cylinders yield more scattered signals over cones, especially at the diffraction-like peaks.

The above comparison implies that conical walls play an important role in scattering into certain regions. Cones do not exhibit the deep diffraction-like minima in the regions around the forward and backward directions.

4.3 Dependence of Angular Scattering Pattern on the Alignment of Scattering Microstructures with Respect to the Incident Beam

4.3A Cones Aligned 45 degrees with the Scattering Plane

For this alignment, the cone tips were shifted off the scattering plane resulting in an asymmetry of the cones in this plane with respect to the beam. For cones with cone half angles less than 45 degrees (K18), the backward scattered signals are greatly reduced. This can be seen in Figs. 4.44 and 4.45. For cones with half angle of 45 degrees (K3, Figs. 4.46 and 4.47), the backward scattering, is markedly altered while the forward patterns still

retain their general characteristics except for a few modifications. The forward pattern broadens out toward 90 degrees and the scattered intensity around the forward direction remains comparable while it decreases significantly over the intermediate angular region. The fine structures become slightly more pronounced for the K18 sample. For the K3 sample, a new shallow minimum is introduced in place of the former deep minimum at 15 degrees which becomes less pronounced and shifts toward a larger angle, as do the other corresponding fine structures that follow. Decomposition of the total scattered intensity into the parallel polarized and cross polarized components shows that the cross polarized components contribute significantly to the scattered intensity over the angular region 40 to 75 degrees and 100 to 130 degrees for the tip-on incidence. The same effect is noticed in the hump region for this alignment corresponding to the base-on incidence.

The above analysis illustrates the sensitivity of angular scattering patterns to the shape of the scatterers, the role of the cross polarized component as a measure of the symmetry property of the scatterers, and in the case of the cone, the angular regions that strongly depend on the conical geometry.

4.3B Cylinders Aligned 45 with the Scattering Plane

For this alignment, the cylindrical axes are inclined 45 degrees with the scattering plane. Fig. 4.48 and 4.49 show the resulting angular scattering patterns from samples B4 $1.0 \times 10^4/cm^2$, and B6 $1.0 \times 10^6/cm^2$, respectively, in comparison with the measurements made in the plane parallel to the axes. Apparently, the diffraction-like peaks in the forward and backward lobes disappear from the scattering plane, and the overall scattered intensity increases appreciably when measured off this plane. This agrees qualitatively with the deduction drawn by Bohren and Huffman in considering light scattering from an infinite right circular cylinder at arbitrary incidence, using the diffraction approximation. The authors have derived the general expression for the fraction of the total scattered light at a given direction and from this inferred that, for long cylinders (R = 1 /a ¿ 10), where l =length and a=radius of the cylinder), the scattered light is concentrated in the plane perpendicular to the cylinder axis. As R is increased more light is confined in this plane. In other words, there will be comparatively less light scatter in the planes deviating further from the plane perpendicular to the cylinder axis. It has been established from the asymptotic solution of light scattering from an infinite cylinder that the light scattered by a long cylinder takes the form of a conical wave, and the pattern formed on a plane perpendicular to the incident beam will be a conic section. When the incident beam is normal to the axis, the pattern is a straight line. As the angle of incidence decreases the pattern turns into a succession of hyperbola, parabola and finally a circle, for zero degree incidence. In this investigation, for samples with fluence lower than $1.0 \times 10^6/cm^2$, two bright conic sections have been observed tangent to the beam in the perpendicular plane.

Part of these sections intercept the measurement plane (which contains the incident beam). Consequently, they are evident as peaks superimposed in the measured patterns as shown in the figures. The appearance of two sections instead of one indicates the nonuniform alignment of the cylindrical pores in the foil surface. For samples with a high density of cylinders, only broad diffuse regions appear instead of the sharp conic sections, hence no sharp peaks are detected in the scattering plane. This may be attributed to the averaging out of the scattered intensity as a result of multiple scattering as the space between cylinders decreases.

Polarized and cross polarized components of the scattered light from cylinders aligned 45 degrees to the scattering plane (Fig. 4.50 and 4.51) follow essentially the same characteristics as those from cones. Contributions of the polarizations to the scattered intensity over the entire angular range are large, particularly in the backward patterns. A comparable or even higher fraction of cross polarized scattered light (V_h) was detected in the backward angular range for vertically polarized incident light. A relatively high fraction of the V_h component was also measured in the forward pattern. These results again verify: (1) the sensitivity of the angular scattering pattern on polarization and the alignment or the orientation of the scatterer, and (2) the association of the cross polarized scattered intensity components with the symmetry of the scatterer. For a cylinder of the dimensions considered (5.5 μm in diameter, 100 μm in length), suspended in plastic with its axis tilted 45 degrees off the scattering plane, a fraction of the light scattered into the plane reverses polarization upon scattering. This process is more favorable for the incident light polarized perpendicularly to the plane of scattering.

4.4 Dependence of Angular Scattering Pattern on Changes in Relative Refractive Index

Comparison of the scattering patterns before and after introduction of moisture (water) into the cylindrical pores (Fig. 4.53) shows insignificant changes in the patterns except for a slight 'washing out' of the minima around the forward and backward directions. This may be due to the opening being less well defined (coated with water), relative to air. This implies that the scattering pattern from microstructures is not sensitive to accumulation of natural moisture inside the microstructures. However, remeasurement of the scattering patterns from a few samples that underwent dye treatment (originally for the purpose of introducing dye molecules into the microstructures) illustrates a noticeable decrease in the elastically scattered light over the whole angular range (Figs. 4.53 and 4.54). The change is more drastic in the peripheral backward pattern. This preliminary result demonstrates the dependence of the scattering pattern on the changes in the optical as well as the geometrical property of the scatterers. It also suggests that the dye treatment performed may cause relative changes in both optical and geometrical properties of the scattering

microstructures.

4.5 Angular Scattering Pattern From Combinations of Microstructures

The general effects on the angular scattering pattern from a filter foil due to a deposition of small filtered particles on the foil have been studied by arbitrarily spreading a layer of glass microspheres (about 2 μm in diameter) on a surface of a filter foil and comparing the measured scattering patterns in contrast with the previous pattern (without any deposition). In Fig. 4.55, the scattering patterns for a filter with pore density $1.0 \times 10^4 / cm^2$ and 1.6 μm in diameter, resulting from illuminating the surface with spheres (side 1) and from the opposite surface (side 2) to the incident beam are shown in comparison with that from the filter itself (side 1). In this case, the density of the deposited spheres is higher than the pore density and the size and distribution of spheres is not uniform (clusters and chains of spheres also evidenced). The scattered intensity from the filter itself is confined within the narrow forward and backward lobes (0 - 30 degrees, 160 - 180 degrees) with a few diffraction-like peaks around the forward and backward directions. Deposition of glass spheres diminishes these fine structures and increases the scattering considerably over all directions, particularly in the peripheral region (up to about 2 orders of magnitude higher). When the surface with spheres was exposed directly to the incident beam a few prominent scattered interference fringes, caused by the roughness introduced by spheres on this surface, were observed in the backward pattern around 70 degrees. The resulting pattern obtained when the spheres were downstream from the incident beam exhibits noticeable deviation from the former at large angles around 90 degrees. For the case in which the filter pore density is higher than the density of deposited spheres, and the spheres are sparsely distributed so that no chains of spheres present, as shown in Fig. 4.56, the same general effects were observed. However, in this case, the increase of the scattered intensity is more uniform over the angular range.

Deposition of large spheres (11.3 microns diameter) on CR-39 foil surface with cone openings also results in significantly higher scattered intensity as shown in Fig. 4.57 and 4.58. The change in intensity is more pronounced in the peripheral region in the forward patterns. A broad shoulder structure is introduced at larger angles in the forward pattern when the spheres are down stream from the incident beam (Fig. 4.57).

This preliminary study indicates that the measurement of angular scattering is an effective nondestructive tool to gain information on changes in size, and composition of small particles. It also suggests a means for counting particles in a given size range trapped by a filter.

5 FLUORESCENT SCATTERING RESULTS

5.1 Angular Distribution

The angular scattering pattern of the fluorescence (H_t) from Oxazine dye molecules embedded in conical pits in Figs. 5.1 through 5.8 for both (cone) tip-on and base-on incidences of the exciting light. The pits chosen were produced by a beam of accelerator protons (F9), He-3 (K10), and distant alpha source (AAL10 and TAL1) and are thus relatively parallel. The patterns from Nile Blue dye molecules deposited in conical pits which have little or no common orientation because they were formed from irradiation by a close alpha source are presented in Figs. 5.9 and 5.10 (TAL2). In each figure the average signal (V_d) associated with the dark current in that measurement is also indicated. The number of conical pits per unit area (V_d) (fluence) in these samples is on the order of $1.0 \times 10^6 / cm^2$. Dimensions of the pits in each sample are estimated from SEM photographs and are summarized in Table 4.1 along with descriptive remarks where applicable.

The general form of the measured angular scattering patterns qualitatively resembles that of the simple dipole or that from fluorescing molecules in bulk matter. However, there are a few features to the fluorescence data that are quite different from the dipole pattern. First, there is the asymmetry of the forward and backward patterns about 90 degrees for both tip-on and base-on incidences. The broad diffuse peak or shoulder structure over the lateral angular region is constantly present only in the half pattern which is facing the cone base, i.e., in the backward pattern at base-on incidence and in the forward pattern at tip-on incidence. These features are absent from the fluorescent scattering patterns from the dye molecules deposited on a blank (controlled) plastic surface (Fig. 5.6, 5.11 and 5.12). In Fig. 4.6, a comparison is made between the radiation patterns of a blank sample (AQ2) etched and treated with dye in the same manner as the sample with cones (AAL10). Both were wiped after the treatment to remove dye from the surface. No evidence of fluorescence by dye is seen in the blank sample. Accordingly, the angular pattern obtained with the cones represent effects on the angular scattering pattern from dye molecules which are embedded in the conical microstructures.

The asymmetry characteristic has been predicted theoretically by numerical calculation of angular scattering patterns for molecules uniformly distributed on a spherical surface and for molecules distributed within dielectric spheres. It has been shown that, for certain values of the relative refractive index, the asymmetric characteristic, or the deviation from dipolar patterns, becomes more pronounced as the size parameter of the spheres increases.

It is also observed that although the over-all scattered signals are consistently higher for the tip-on incidence than those for base-on incidence, the forms of the scattering patterns for these two configurations are qualitatively at least, the reverse of the other. This

22

indicates that the fluorescent pattern depends on the orientation of the cone rather than the direction of the incident beam.

The enhancement of the scattered signals corresponding to tip-on incidence over those from base-on incidence may be ascribed in part to the differences in intensity of the local internal electric fields exciting the dye molecules and differences in the number of molecules available to be excited. One should note that at tip-on incidence, the cone presents a larger front surface to the incident beam than at base-on incidence. For cones with half angles between 22 and 46 at tip-on incidence, total internal reflection occurs along the conical plastic-air interface. The generation of an evanescent waves may result in an enhancement of the internal exciting field at the surface of the cone and thus increases the measured fluorescent signals. Moreover, it has been shown by theoretical numerical calculation dealing with inelastic scattering from molecules embedded in spherical particles, the power associated with the internal exciting field can vary drastically with the position of the molecule. The intensity of the internal fields may therefore be different at different locations inside the cone depending on the direction of incidence.

5.2 Fluorescence From Dye Molecules Deposited in Cylindrical Pores

General Features of the Fluorescent Angular Scattering Pattern Measured in the Plane With the Cylinder Axis Parallel to the Beam Direction.

The fluorescent scattering patterns from three different filter foils (P5, S1, and S2) treated with Nile Blue dye are shown in Fig. 5.13 - 5.18, for both foil surfaces exposed normally to the incident beam. All general features observed in the patterns resulting from molecules in conical pits again appear. There are, of course, differences with different pore sizes. The cylindrical pores are suspended in a thin (90 - 100 μ m) plastic foil. The asymmetry of the pattern about 90 degrees is less prominent in the cylinder case. Broad peaks or shoulders at large angles are generally evident in both forward and backward patterns but less pronounced. The angular distribution of the fluorescence resulting when either end of the cylinders are illuminated by the incident light parallel to their axes are of comparable magnitude for samples P5 and S1. For sample S2, the fluorescence signals over all scattering angles were measured for when side 1 is illuminated are moderately higher than these for side 2 illumination. This may reflect a tapering toward one end (side 1) of the cylinders in this foil. The electronmicrograph suggests a small taper. The above results affirm the sensitivity of the fluorescent scattering to the particle geometry and orientation (or alignment).

5.3 Pattern From Molecules in Microstructures Aligned 45 Degrees off the Scattering Plane

Figs. 5.19 and 5.20 illustrate the fluorescent scattering (V_t) from dye molecules residing in conical pits (sample K11) aligned 45 degrees out of the scattering plane in comparison with that obtained when the cone axes were paralleled to the plane, for tip and base illuminated upstream to the incident beam, respectively. Evidently, the broad peak or shoulder at large angles vanishes when the tips and openings of the cones are tilted off the plane and the symmetry of the cones in this plane is no longer present. The resulting patterns become less asymmetric for this orientation. The difference between the fluorescence associated with tip and base upstream diminishes. Presumably at 45 degrees orientation the differences in the variation of the internal exciting fields at different locations are not great for both configurations.

The corresponding fluorescent scattering patterns obtained from dye molecules deposited in cylindrical pores (P5(1), P5(2), Figs. 5.21 and 5.22, respectively) conform with those from cones at base upstream configuration. This consistency supports the reliability of the measurement as well as the validity of the above interpretation. Accordingly, the effects of particle geometry and alignment on the scattering pattern by active molecules confined within the particles have been demonstrated.

5.4 Polarization of Fluorescence From Molecules Deposited in Microstructures

The polarization employed in this investigation has been found to reduce the initial intensity by a factor of 3.6. Hence, the decomposition of the scattered signals into polarized components were carried out for those samples that yield sufficiently high total signal so that the magnitudes of the polarized components are still reliable. The total, parallel, and cross polarized incident light in various fluorescence measurements in the plane parallel to the cone axis are given in Figs. 5.9 and 5.10 (TAL2), and Fig. 5.23 and 5.24 (K11) for tip-on and base-on incidences, respectively. The results of the scattering in the plane parallel to the cylinder axis are depicted in Fig. 4.13 (P5(1)) and Fig. 4.18 (S2).

The same measurements were made for the vertically polarized incident light and the results are presented in Figs. 5.25 and 5.26 for tip-on (K11(T)) and base-on (K11(B)) incidences, respectively.

A common feature inferred from these results is that regardless of the polarization of the incident radiation, the total scattered fluorescence either from the molecules deposited in cones or cylinder consists of comparable contributions from the parallel and cross polarized components.

The V_v and V_h components of the fluorescent scattering patterns of the sample K11(B) with conical pits aligned 45 degrees off the scattering plane (Fig. 4.27) exhibit characteristics consistent with the above results. This implies that the direction of the polarization of the dipoles associated with the fluorescing molecules is independent of the direction of the polarization of the exciting field. Furthermore, the dipoles (associated with the excited

24

molecules) are free to rotate randomly upon absorption and emission. As a result, there is not preferential polarization observed or the scattered radiation becomes unpolarized. The lack of polarization has been observed for both shapes, with the axis of symmetry aligned in as well as off the scattering plane. Therefore, it is not specific to the geometry and orientation of the microstructures.

5.5 Dependence of Fluorescent Scattering on the number of Dye Molecules and Dye Species

The previous analyses and interpretations were based on the conformal features of the independently measured scattering patterns, including the characteristics of the polarized components, by two different dye species: Oxazine and Nile blue, deposited in conical pits (in samples K11 and TAL2, for examples). Accordingly, they appear to be independent of the dye species. This result complies with the assumption that the physical molecular processes by what the molecules are excited and fluoresce fact that the molecules are embedded in a small particle.

The qualitative indication of the proportionality of the fluorescent scattering signals to the number of dye molecules deposited in the conical pits can be realized by the appreciable increase of the scattered signals over all angular positions after a longer duration of dye treatment in the ultrasonic bath as illustrated in Fig. 5.28.

5.6 Edge Refraction in Dye Treated Thick Samples

A series of prominent peaks has been consistently observed superimposed on the fluorescent scattering patterns from the thick (2 mm. thick) plastic samples: TAL1, TAL2, and TAL3 when the (side) edges of these samples were not painted or taped black as illustrated, for example, in Figs. 5.28 - 5.31. It has also been noted (Figs. 5.32 and 5.35) that the blank (unirradiated, etch or unetched) samples (TQ2, for instance) that had been treated with dye exhibit the same structures, the untreated blank (TQ0) do not. These peak structures seem to be reversed when the opposite surface of the sample is illuminated. The peak positions obtained for a sample associated with a certain configuration shifted slightly upon remounting the sample but the general features remain the same.

These edge phenomena can be described as a result of the total internal reflection of the dye treated plastic plane surfaces and the reflections and refractions at the two surfaces of the side edge (facing the 90 scattering direction). It is widely known that plastic exhibits a light guide or total internal reflection property over a certain propagation distance. The dye treated surface may behave as a layer of intermediate refractive index between the plastic and air. When the sample is exposed to the incident light, the fluorescent emissions from the dye molecules are trapped between the plastic surfaces, and propagate along to

the edge (about 1 cm distance). Although absorption and refraction out of the plastic probably occurs along the path, a considerable amount of the light will reach the edge and will undergo reflection and refraction at both surfaces. Consequently, the series of peaks correspond to the primary refraction and secondary refraction (reflected to the opposite surface and then refracted) of fluorescent radiation that arrives at the edge at some proper angles. The peak around 90 degrees may also contain contributions from other refraction processes as indicated by the presence of a small peak around 90 degrees in the angular scattering pattern from an untreated blank sample.

6. SUMMARY AND DISCUSSION

6.1 Elastic Scattering

This systematic experimental study of light scattering by finite dielectric conical and cylindrical microstructures in plastic nuclear track detector plane surfaces has resulted in complicated angular distributions of the scattered light in the plane parallel to the structures' axes as well as off the plane. The measured angular scattering patterns depend on shape, size, orientation and refractive index of the structures as well as on the polarization of the incident light. They cannot be described rigorously by diffraction theory nor by geometrical optics. To date, no exact compatible theoretical solution is available for the problem of light scattering by a finite dielectric cone. The theoretical numerical calculation that is available for the scattering by a finite cylinder, is applicable only for smaller cylinders than studied here. However, the analyses of the measured angular scattering patterns in this investigation plausibly indicates that certain angular regions are more sensitive to specific parameters of the structures than the rest of the region. Accordingly, various types of information regarding the microstructures can be drawn from the different angular regions. The qualitative information on cone shape and volume should be sought in the intermediate angular region in forward scattering patterns at base on incidence. The orientation or alignment and homogeneity of the structures can be deduced from the lateral region in the backward patterns. The multiple and dependent scattering effects may be inferred from the lateral region at tip-on incidence. In the single and independent scattering regime, the quantitative information on volume and fluence of the microstructures can be estimated from the scattered intensities at the intermediate optimal angular regions. Elastic scattering signals were found to proportional to volume and fluence over wide ranges.

Light scattering from nonspherical microstructures at arbitrary incident angles, in general, are not symmetric about the incident direction.

6.2 Fluorescence

The resulting angular fluorescent scattering patterns by dye molecules deposited in conical and cylindrical microstructures in plastic plane surfaces exhibit several prominent characteristics that differ from the bipolar scattering patterns produced by the molecules in bulk material. The observed asymmetry of the scattering patterns about 90 degrees has been predicted theoretically for spheres and infinite cylinders (at normal incidence). Investigations of the polarizations states of the scattered fluorescence implies that the dye molecules are free to rotate upon absorption and emission. Dependence of the angular patterns on the geometrical properties of the microstructures has been affirmed by the

27

presence of the features that associate solely with a particular configuration and orientation of the microstructures. An increase of scattered signals in every scattering direction has been detected after a longer time period of the dye treatment. To obtain quantitative information on microstructures and dye molecules, further investigations that cover a wider range of controlled parameters such as the fluence of the microstructures, and the amount of dye deposition, are suggested.

7 BIBLIOGRAPHY

1. P.J. McNulty, 'Radiation Effects on Electronic System' in proceedings of the Air Force Geophysics Laboratory Workshop on Earth's Radiation Belts; January 26-27, 1981; R.C. Sagalyn, W.M. Spjeldvik and W.J. Burke Eds. (Air Force Geophysics Laboratory, Report # AFGL-TR-81-0311, Hanscom AFB, MA 01731, 1981). pp. 99-123. ADA113959

2. P.J. McNulty, 'Charged Particles Cause Microlectronics Malfunction in Space', Physics Today 36, 9 (1983).

3. R.L. Fleischer, P.B. Price, and R.M. Walker Nuclear Tracks in Solids (university of California Press, Berkely, 1975).

4. H.C. Van de Hulst, Light Scattering by Small Particles, Wiley Sons, New York (1975).

5. P. Barber and C. Yeh, Appl. Opt., 14, 2864 (1975).

6. D. Cooke, Thesis: Light Scattering from Long Thin Glass Cylinder at Oblique Incidence, Dept. of Chem., Clarkson College of Technology (1969).

7. Craig F. Bohren and Donald R. Huffman, Absorption and Scattering of Light by Small Particles, John Wiley Sons, New York (1983).

8. P.J. McNulty, H.W. Chew and M. Kerker, Topics in Current Physics, W.H. Marlow Ed., Springer-Verlag Berlin Herdelberg, Germany, 91 (1980).

9. S.D. Druger and P.J. McNulty, Appl. Opt., 2, 75 (1983).

10. S.D. Druger and P.J. McNulty, Phys. Rev. A, 29, 1545 (1984).

11. H. Chew, Phys. Rev. A, 19, 2137 (1979).

8 PAPERS PUBLISHED AND SUBMITTED UNDER THIS CONTRACT

A. Papers Published

1. P.J. McNulty, W.D. Shirky, S.R. Palmer, O. Wipasuramontin and R.C. Filz, 'Low Energy Proton Measurements Using CR-39', Nuclear Tracks and Radiation Measurement, 8, 139-142 (1984).

B. Papers in Preparation

2. P.J. McNulty and Orapin Wipasuramontin, 'Elastic and Inelastic Light Scattering by Nuclear Tracks in CR-39'.

3. P.J. McNulty and S.D. Druger, ' Fluorescence by Active Molecules in Liquid Proplets'.

4. P.J. McNulty and Orapin Wipasuramontin, 'Proposed Use of Light Scattering Techniques in Neutron Dosimetry'.

9. THESIS COMPLETED

'Light Scattering by Microstructures in Plastic Nuclear Track Detector Plane Surfaces'. Submitted by Orapin Wipasuramontin for completion of Ph.D thesis in Physics to Clarkson University.

Figure 2.1. Sketche of a NH-3 Neutron Howitzer unit and a side-port drawer.

Hinged Cover

Source Raising Rod

Side Port

Lucite Window

1.3 cm
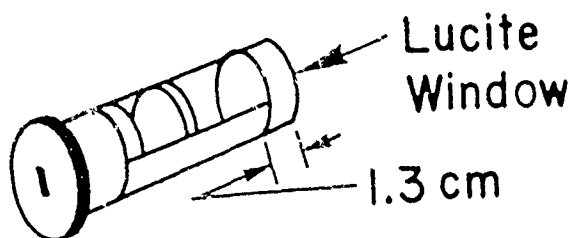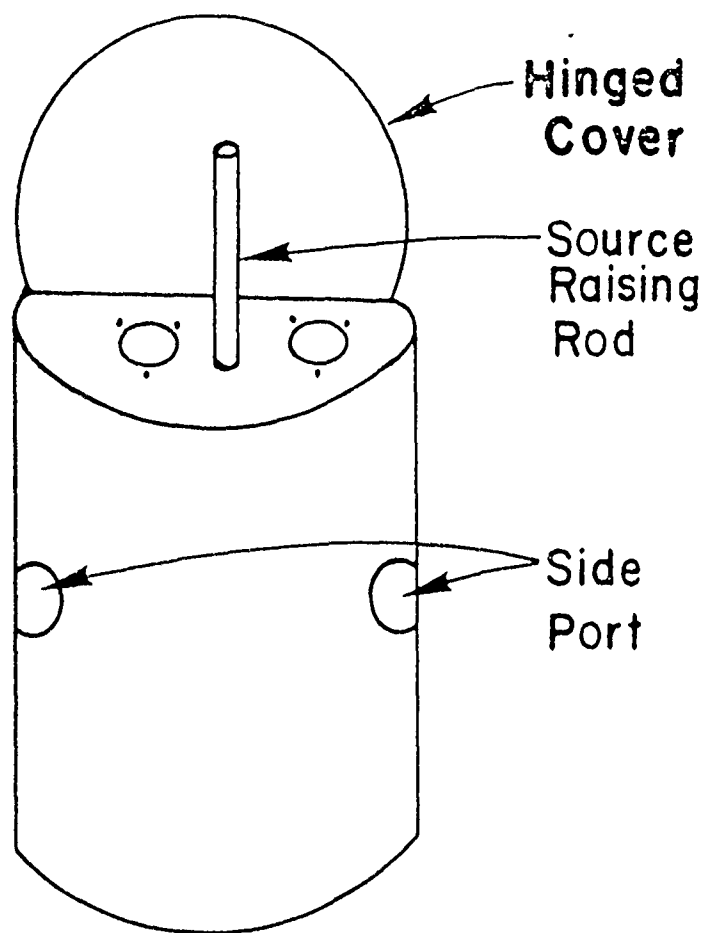
Side-Port Drawer

Table 2.1.   Absorption and Lasing Wavelengths of Nile Blue and Oxazine Dyes.

Name	Absorption Maximum nm. (solvent)	Lasing Wavelengths nm. (solvent)
Nile Blue A, perchlorate	635 (ethanol)	690 (ethanol)
Oxazine 170 perchlorate	627 (ethanol)	710 (ethanol)

Table 2.2. Summary of Sample Characteristic and Production.

1. Sample with conical pits (0.3-0.5 mm. thick)

Sample	Irradiation	Fluence(/cm^2) (Irradiation Duration)	Etching Condition
K3	8.12 Mev He-3 (normal incidence)	1×10^6	6 N NaOH 50 $^\circ$C, 15 hr.
H1	8.12 MeV He-3	0.95×10^5	3 hr. 55 $^\circ$C,
I18	(normal)	2×10^5	7 hr. 50 $^\circ$C,
K18		1×10^6	6 N NaOH
L15	5.6 MeV He-3	2×10^5	6 N NaOH
M6	(normal	5×10^5	50 $^\circ$C, 10 hr.
N17	incidence)	1×10^6	(1 sided)
G15	8.2 MeV He-3	5×10^4	8 hr.
G6	(normal		12 hr.
G17	incidence)		16 hr.
G8			20 hr.
G7			24 hr.
			6 N NaOH, 50 $^\circ$C (1 sided)
AAL0		0 hr.	6.25 N NaOH
AAL1	0.05 µCi	16 hr.	50 $^\circ$C, 10.5 hr.
AAL2	Am-241	22 hr.	(1sided)
AAL3	He-4 source	40.5 hr.	

Sample	Irradiation	Fluence(/cm^2)	Etching
A1	3.5 MeV	5×10^5	6 N NaOH
B18	Protons	1×10^6	50°C, 15 hr.
C9	(normal incidence)	3×10^6	(2 sided)
Q1	(unirradiated)		
D15	2.0 MeV	5×10^5	6 N NaOH
E7	Protons	1×10^6	50°C, 10 hr.
F20	(normal) incidence)	3×10^6	(2 sided)
Q2	(unirradiated)		
PNH1	1 Ci Pu-Be	3 day	6 N NaOH
PNH2	Neutron	6 day	50°C, 6 hr.
PNH3	Source	9 day	
PNH4		12 day	
PNHQ	(unirradiated)		

2. Filter foils (90-100 μm thick)

Sample	Irradiation	fluence (/cm^2)	Etching Condition
S1	16.3 MeV/u	1×10^6	not specified.
S2	Fe-65		
	(normal		
	incidence)		
P4	16.3 MeV/u	1×10^4	6 N NaOH
P5	Fe-65	1×10^5	40 min.
P6	(normal	1×10^6	
	incidence)		
F40	unirradiated		
B3	(not specified,	1×10^3	Not specified
B4	likely as above)	1×10^4	
B5		1×10^5	
B6		1×10^6	

36

3. Dye treated sample (with conical pits, 0.3 mm. and 1.8 mm. thick)

Sample	Irradiation	Fluence (/cm2) (Irradiation duration)	Etching Condition
F9	2.0 MeV Protons (normal incidence)	3×10^6	6 N NaOH 50 C, 15 hr. (1 sided)
K10	8.12 MeV He-3	1×10^6	6 N NaOH 50 C, 10 hr., + 6 hr. (drops of Oxazine added)
K11	8.12 MeV He-3	1×10^6	6 N NaOH 60 C, (5+3) hr., + 5 hr. (drops of oxazine added)
AAL10	0.05 uCi Am-241	3 day	6 N NaOH 50 C, 18 hr.
AQ2	Alpha source unirradiated		
TAL1 (thick)	0.05 uCi Am-241 Alpha source	6 day	6.25 N NaOH (1 sided)
TAL2 (thick)	0.05 uCi Am-421 Alpha source (contact irradiation)	1 day	6.25 N NaOH 70 C, 10 hr.
TAL3 (thick)	0.05 μCi Am-241 Alpha source	1 day	6.25 N NaOH 70 C, 7 hr.
TQ1 (thick)	unirradiated treated with Nile Blue		

Sample	Irradiation	Fluence (/cm2)	Etching
TQ2 (thick)	unirradiated treated with Nile Blue		
TQ0 (thick)	unirradiated No dye treated.		

Figure 2.2A. Two-sided sample etching arrangement showing the individual sample
flasks arranged in a constant temperature bath during etching.
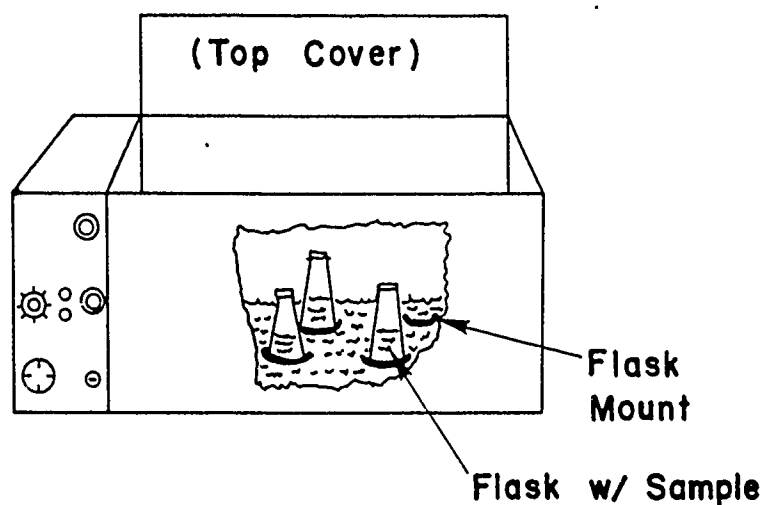
Figure 2.2B. A sketch of an individual sample unit of the one-sided etch. A: etchant
container, B: plexiglass plate, C: parallel rod, D: rubber sheet, and E:
screw.
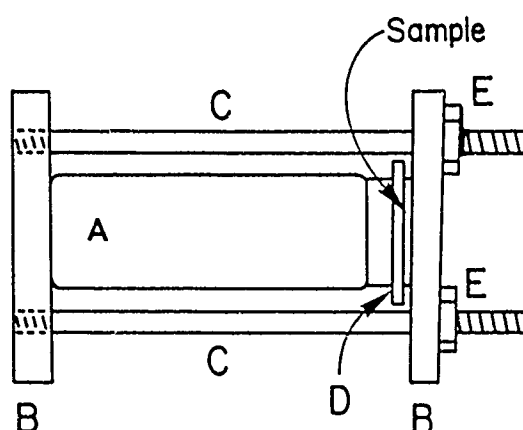
Figure 3.1. Photograph of a general view of the light scattering experimental setup.
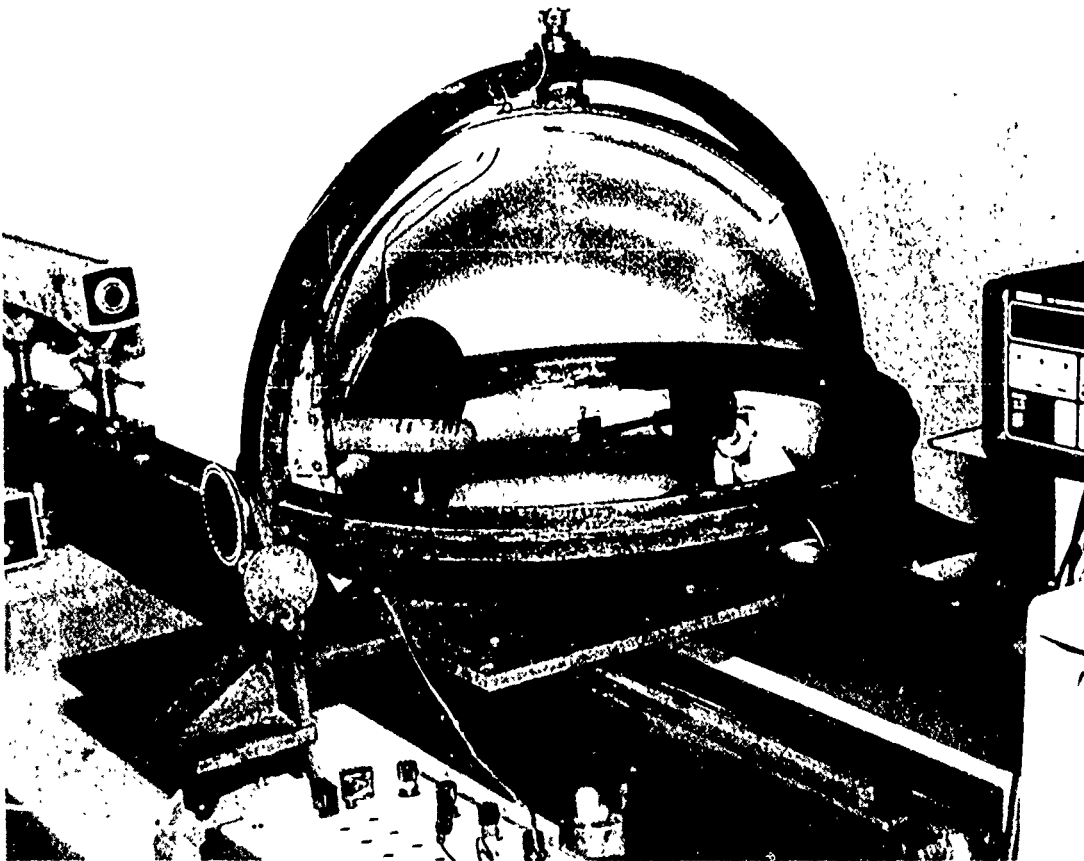
Figure 3.2. Schematic representation of the light scattering experimental setup, showing parts of the goniometer:

A: horizontal rail

B: vernier for angular reading

C: vertical quadrant

D: platform   E: holder housing

F: holder mounting bracket

G: shaft   H: vertical column

I: base   J: knob

K: disk with angular scale

LD: light detection unit.
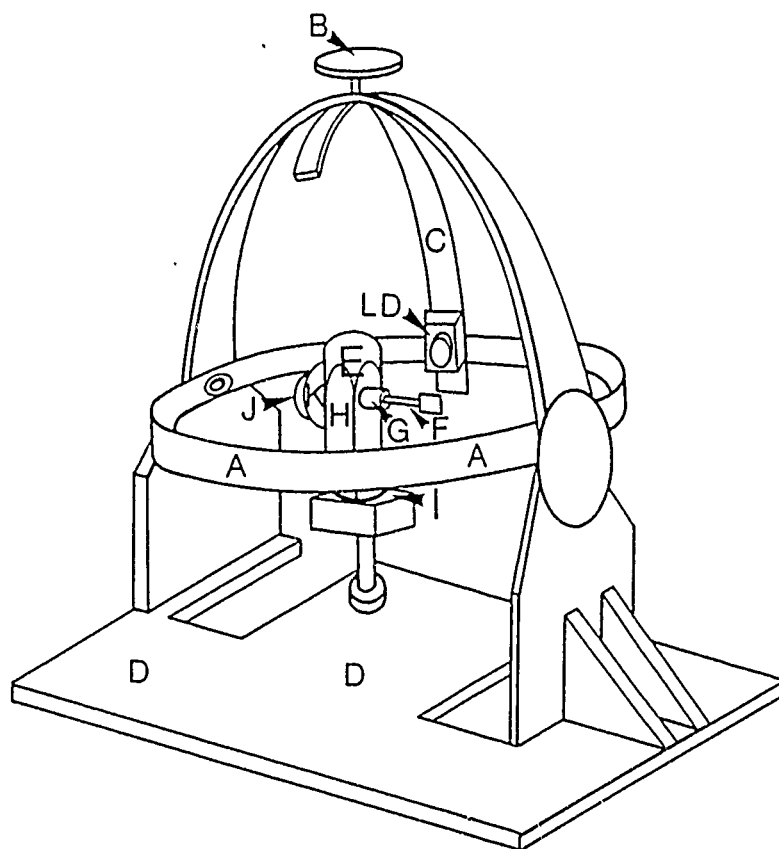
Figure 3.3A.   Drawing of a L14F1 photo-darligton detector.
Figure 3.3B.   Light detection circuit.

0.5 cm dia.

GE LI4FI

(A)

Scattered
signals

B   C

R
10 kΩ

E

$V_{CC} = 10v$

To
Voltmeter
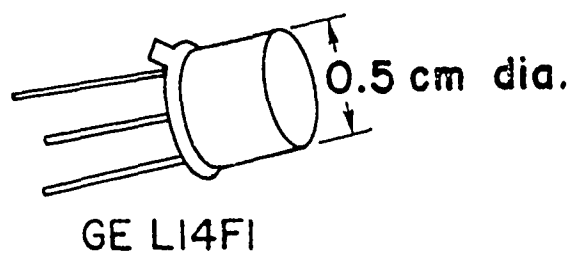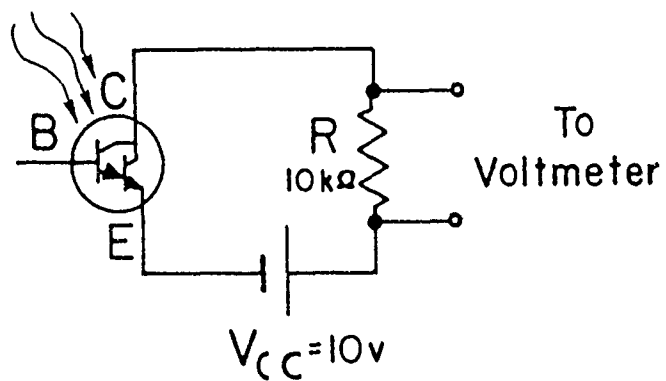
(B)

Figure 3.4. Photodetector housing when used without any collimator.
    A: groove
    B: plastic screw
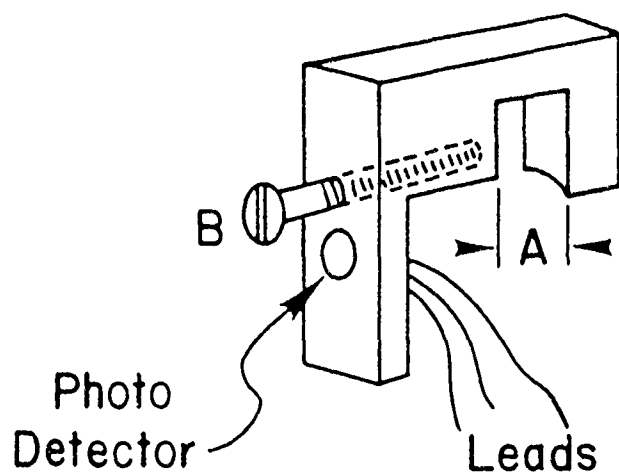
Figure 3.5. Sketch of the collimator unit showing removable parts and slots for polarizer and filters.

a: base
B: removable middle part
C: removable front part
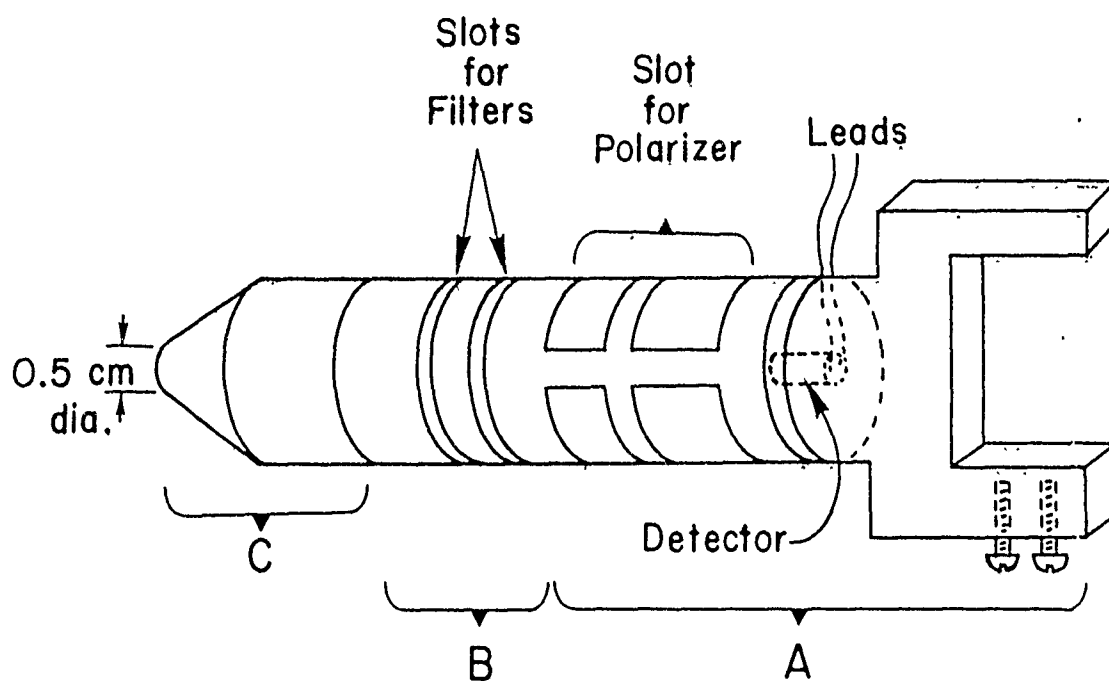
Figure 3.6. Geometry of light scattering measurement.
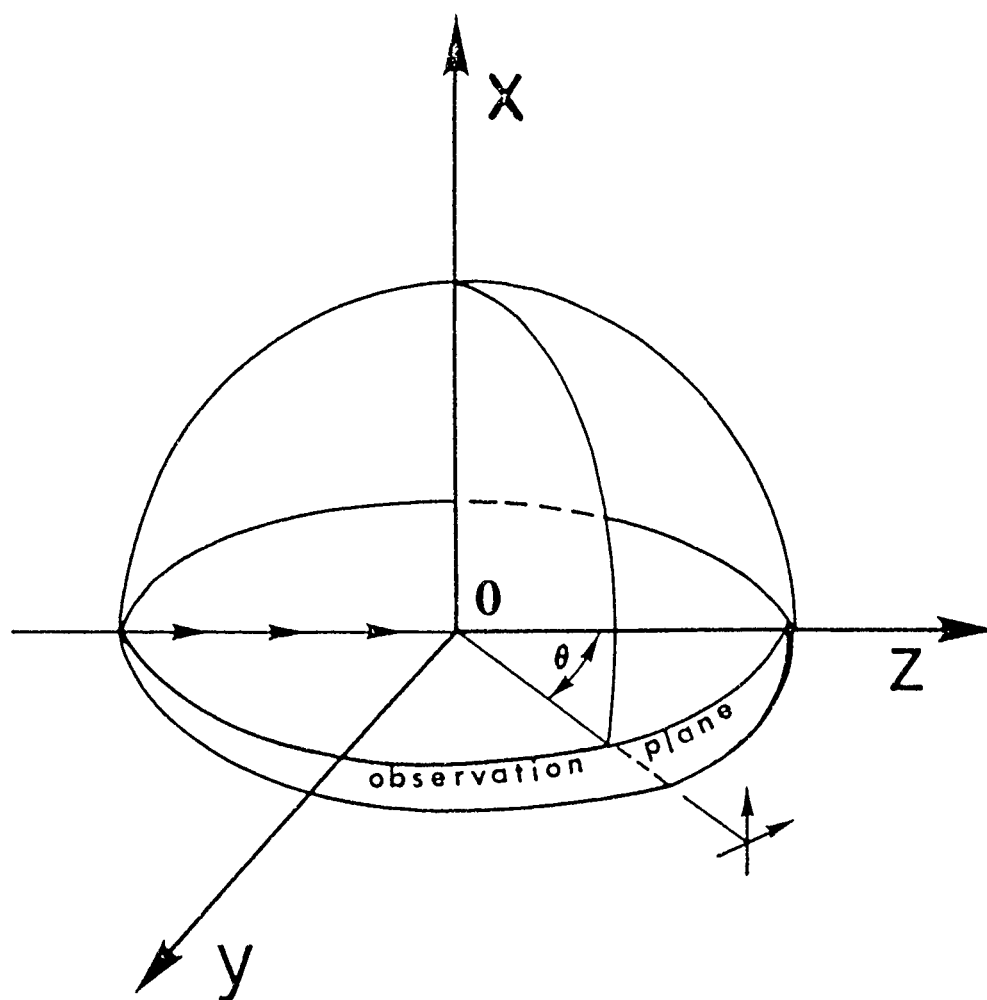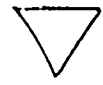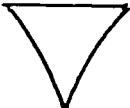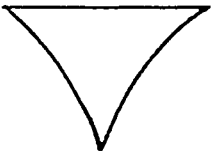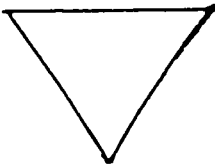
Table 4.1. Microstructure Geometry Estimated from SEM Observations.

1. Samples with conical pits employod in the elastic light scattering

Sample	Diameter (μm)	Length (μm)	Cone Half Angle(deg) **	Volume 3 (μm) **	Structure Sketch
K3 *	5.00	2.5	45	16.36	
H6	2.07	1.25	39.6	1.402	
I18	2.53	1.68	36.9	2.81	
K18	2.24	1.91	30.3	2.508	
L15	2.46	2.10	30.3	3.327	
M6	2.33	2.00	30.2	2.842	
N17 *	2.41	2.20	28.7	3.345	

Sample	Diameter (µm)	Length (µm)	Cone Half Angle(deg) [**]	Volume [**] 3 (µm)	Structure Sketch
G15	1.50	1.00	36.8	0.589	▽
G6	2.30	1.36	40.2	1.883	▽
G17[+]	3.75	3.00	32.0	11.0	▽
G8[+]	5.00	4.00	32.0	26.17	▽
G7[+]	6.00	4.32	34.7	40.7	▽
AAL1	3.20	1.85			⌣
AAL2	3.83	2.70			⌣
AAL3	5.00	2.33			⌣

Sample	Diameter (μm)	Length (μm)	Cone Half Angle(deg) **	Volume ** 3 (μm)	Structure Sketch
A1	1.46	0.28	69.0	0.156	
B18	1.68	0.28	71.4	0.204	
C9	1.96	0.28	74.1	0.304	
D15	3.20	0.80	63.4	2.144	
E7	3.20	0.80	63.4	_.144	
F20	3.3	0.85	62.7	2.42	
PNH1 PNH2 PNH3 PNH4	Conical pits of various sizes, shapes and orientations				
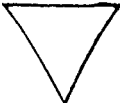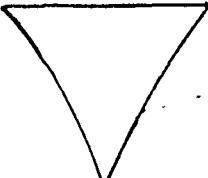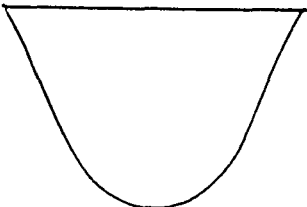
2. Filter foils

Sample	Diameter (μm)	Length (μm)	Remark
S1	2.4	90	
S2	4.66	90	
P4	1.6	100	Number of deposited particles per unit area is larger than the pore density. Deposited particle size ranges from smaller to larger than the pore size. Deposited particles are mixture of spheres of various sizes and other irregular shape particles.
P5	5.0	100	
P6	1.6	100	

Sample	Diameter (μm)	Length (μm)	Remark
B3	5.0	100	
B4	4.37	100	
B5	5.5	100	
B6	5.55	100	

3. Dye treated sample

Sample	Diameter (μm)	Length (μm)	Cone Half Angle(deg)[**]	Volume[**] (μm^3)	Structure Sketch
F9	2.0	0.95	46.4	0.994	
K10	3.65	3.0	31.3	10.46	
K11	6.16	5.0	31.6	49.67	
AAL10	13.5	10			
TAL1	Round conical pits with the diameter ranges from 4 μm t0 10.6 μm and the length ranges from 2 μm to 8 μm. The majority is of 10.6 μm in diameter and 8 μm in length The areal density of the structures is estimated as 1.42×10^6 /cm^2. A few of mergings and clusterings of pits are observed.				
TAL2	Conical pits of various sizes and orientations.				

	Diameter ranges from 0.3 μm to 10 μm. The estimated fluence is 1.06×10^6 /cm^2.
TAL3	Round conical pits. The diameter and the length of the majority tracks is 10 μm. and 8.5 μm., respectively. The estimated fluence is 2.4×10^5 /cm^2.

** : assumed right circular cones

* : clusterings and mergings observed

+ : evidence of a few sharp cones due to heavy charged particles

Table 4.2 List of Netron Irradiated Sample and the
Photocounted Fluence

Sample	Irradiation (days)	Fluence(/cm^2)
PNHQ	0	$(0.407 \pm 0.040) \times 10^5$
PNH1	3	$(2.27 \pm 0.22) \times 10^5$
PNH2	6	$(3.47 \pm 0.53) \times 10^5$
PNH3	9	$(4.78 \pm 0.53) \times 10^5$
PNH4	12	$(3.94 \pm 0.45) \times 10^5$

Figure 4.1. Angular distribution of scattered intensity from conical pits in samples H6, I18, and K18, for horizontally polarized incident light, at tip-on incidence. [The conical pits in these samples are etched tracks of 8.12 MeV He-3 ions, incident normally on the plastic sample surfaces, with fluences of 0.95×10^5, 2×10^5, and 1×10^6 / cm^2, respectively].

53
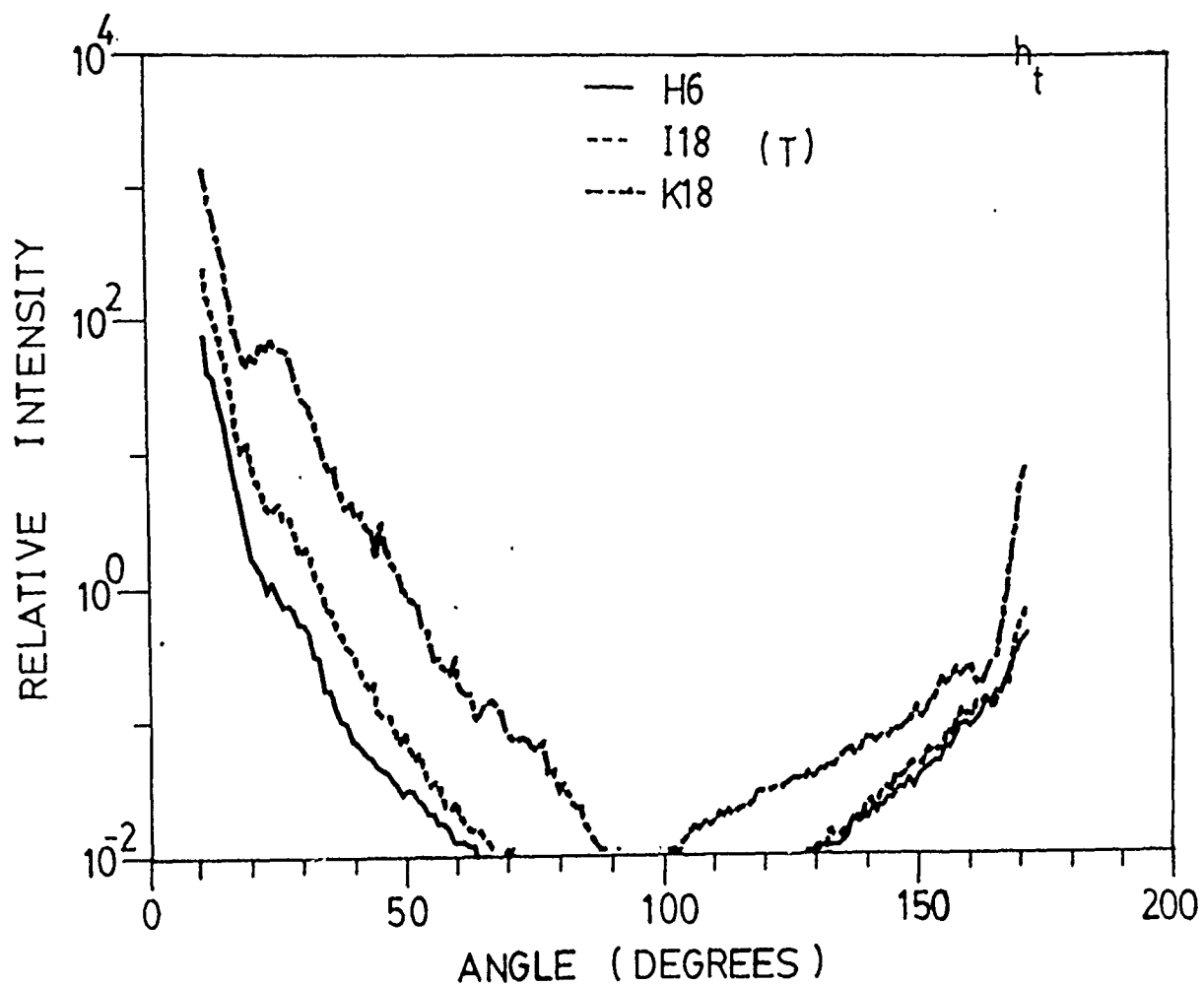
Figure 4.2. Same as Figure 4.1 except for base-on incidence. Below are typical electronmicrographs of replicas of the samples.

H 6
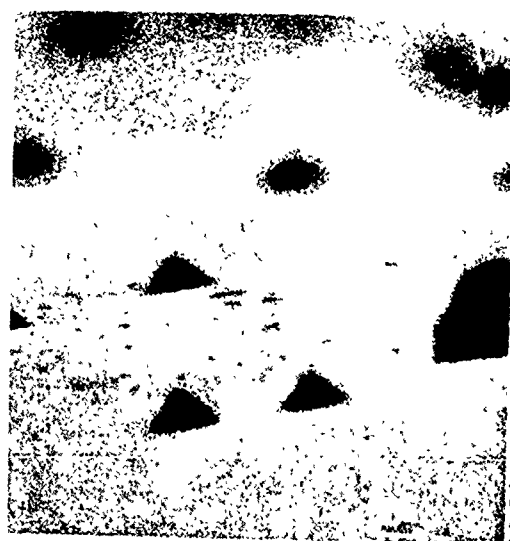
I 1 8
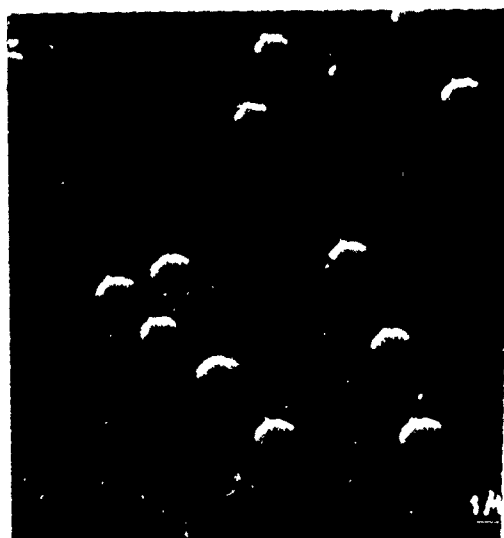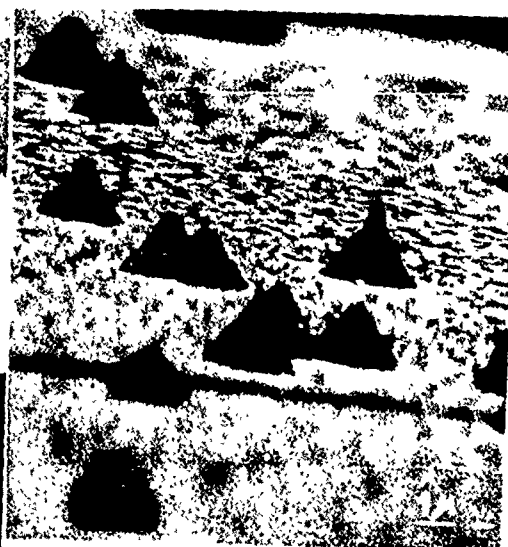
K 1 8
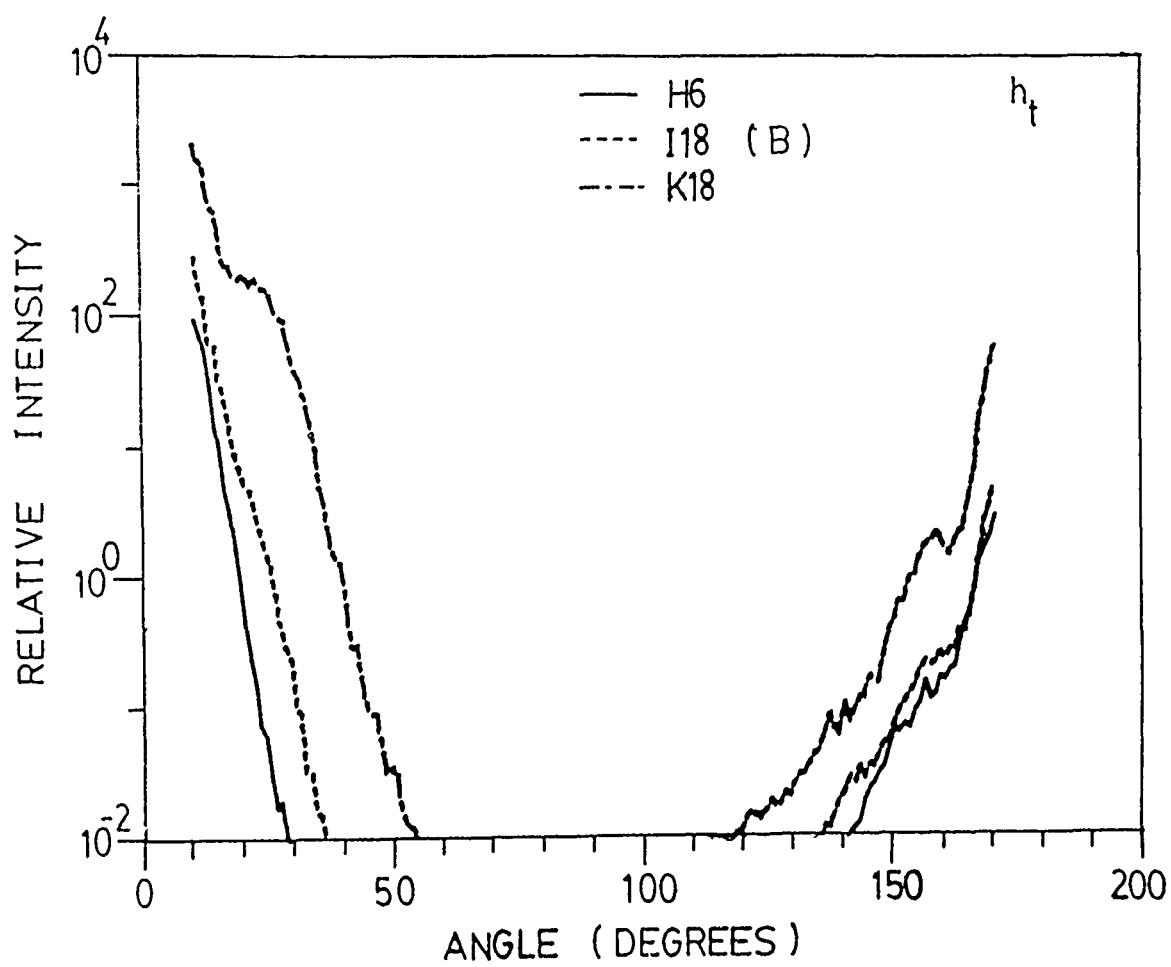
Figure 4.3. Angular distribution of scattered intensity from conical pits in samples L16, M6, and N17, for horizontally polarized incident light, tip-on incidence.

[The conical pits in these samples are etched tracks of 5.6 MeV He-3 ions, incident normally on the plastic sample surfaces, with fluences of 2×10^5, 5×10^5, and 1×10^6, respectively].
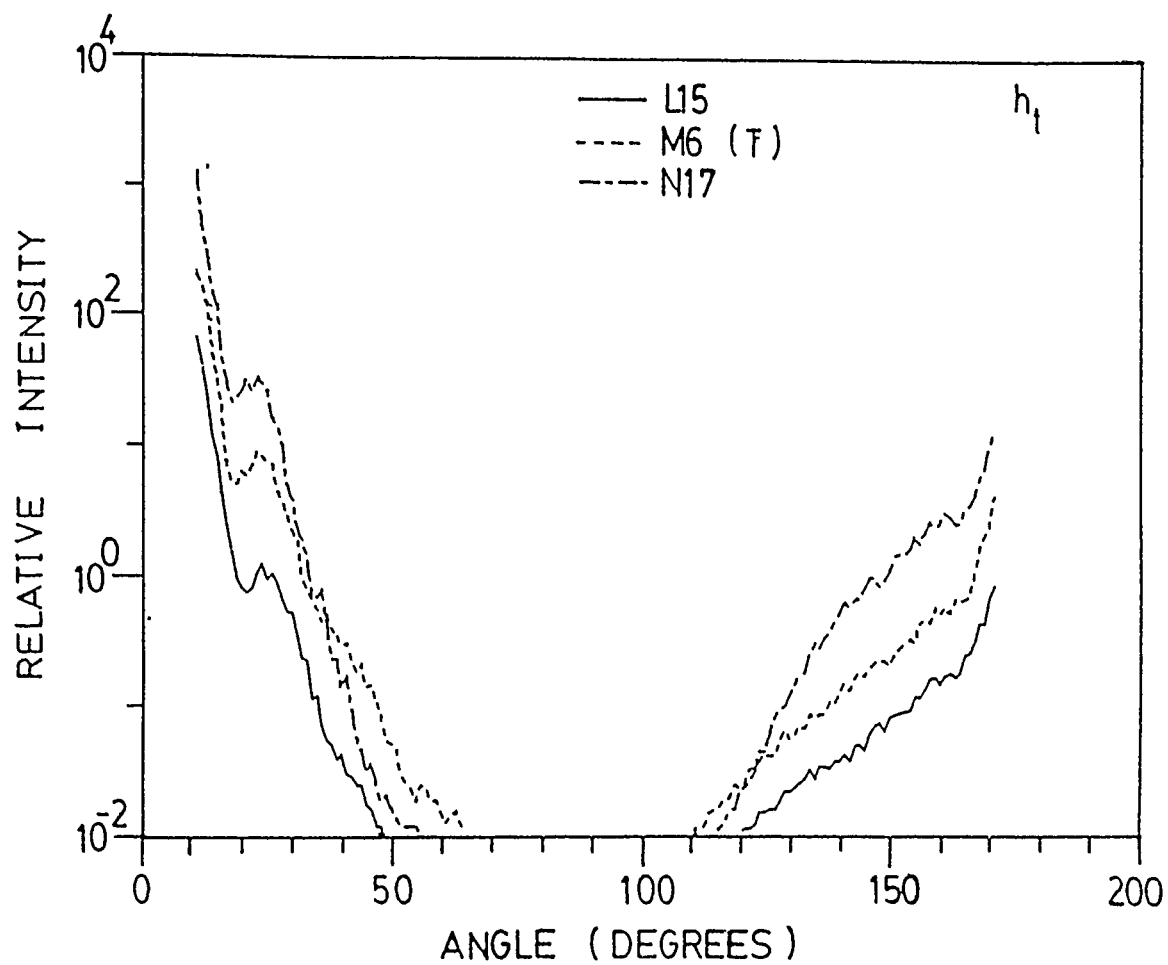
Figure 4.4. Same as Figure 4.3 except for base-on incidence. Below are typical electronmicrographs of replices of the samples.

Figure 4.5. Angular distribution of scattered from conical pits in samples AAL0 (blank), AAL1, AAL2, and AAL3, for horizontally polarized incident light, at tip-on incidence.
[The conical pits in these samples are etched tracks of alpha particles from 0.05 μCi Am^{2}41 source, with irradiation durations: 0,16,22, and 40.5 Hr., respectively.

59
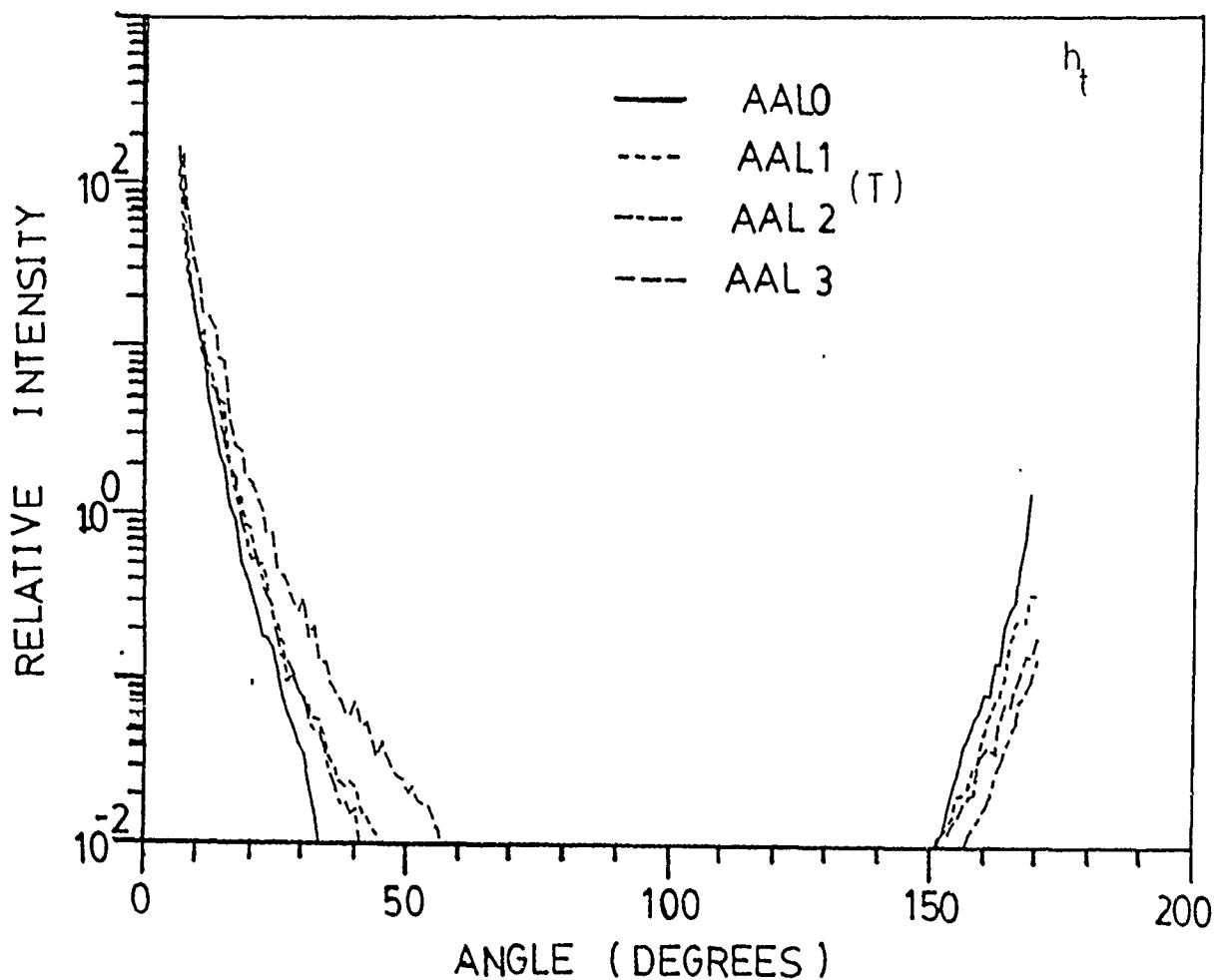
Figure 4.6. Same as Figure 4.5 except for base-on incidence. Below are typical electronmicrographs of replices of the samples.

AALO

AAL1
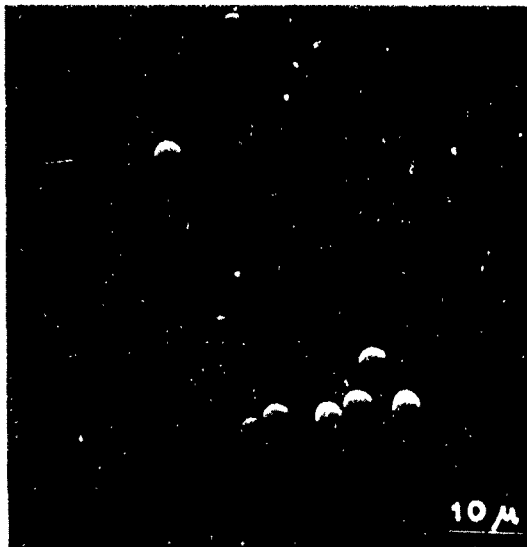
AAL2

AAL3
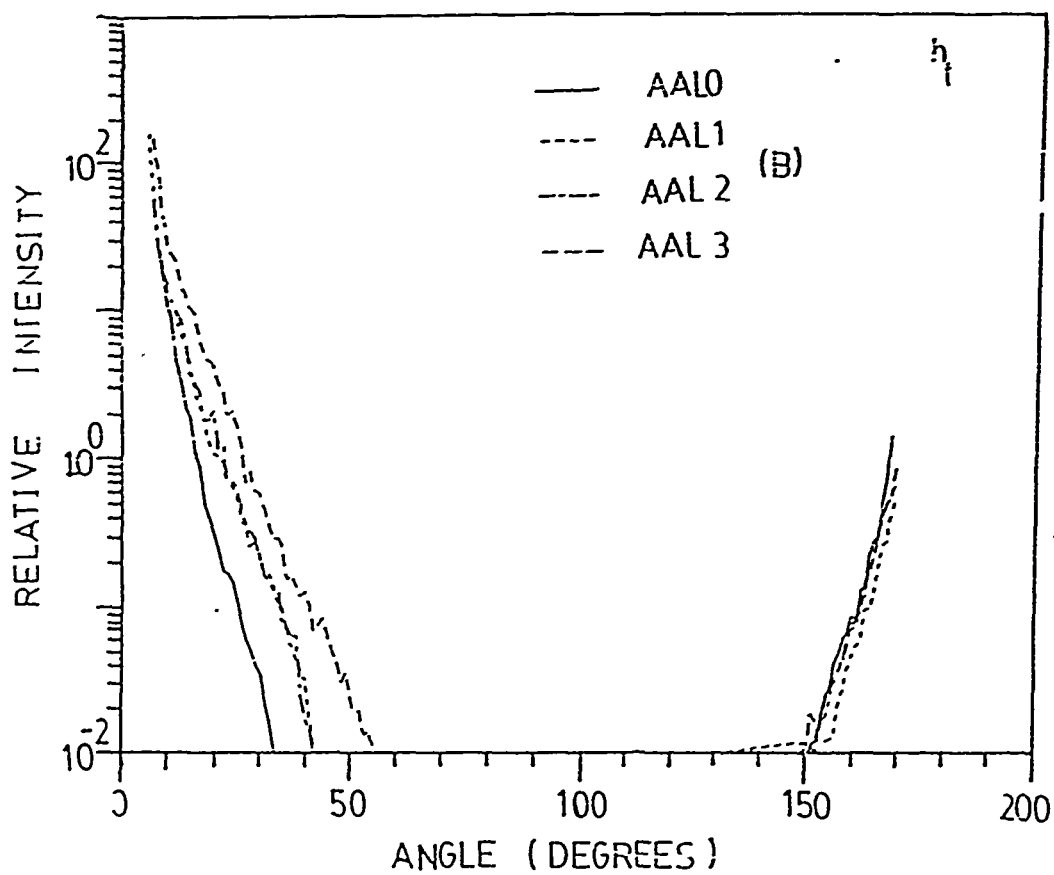
Figure 4.7. Angular distribution of scattered intensity from conical pits in samples Q1 (blank), A1, A18, and C9, for horizontally polarized incident light, at tip-on incidence.

[The conical pits in these samples are etched tracks of 3.5 MeV proton beam, incident normally on the plastic sample surfaces, with fluences: 0. 5×10^5, 1×10^6, and 3×10^6, respectively].
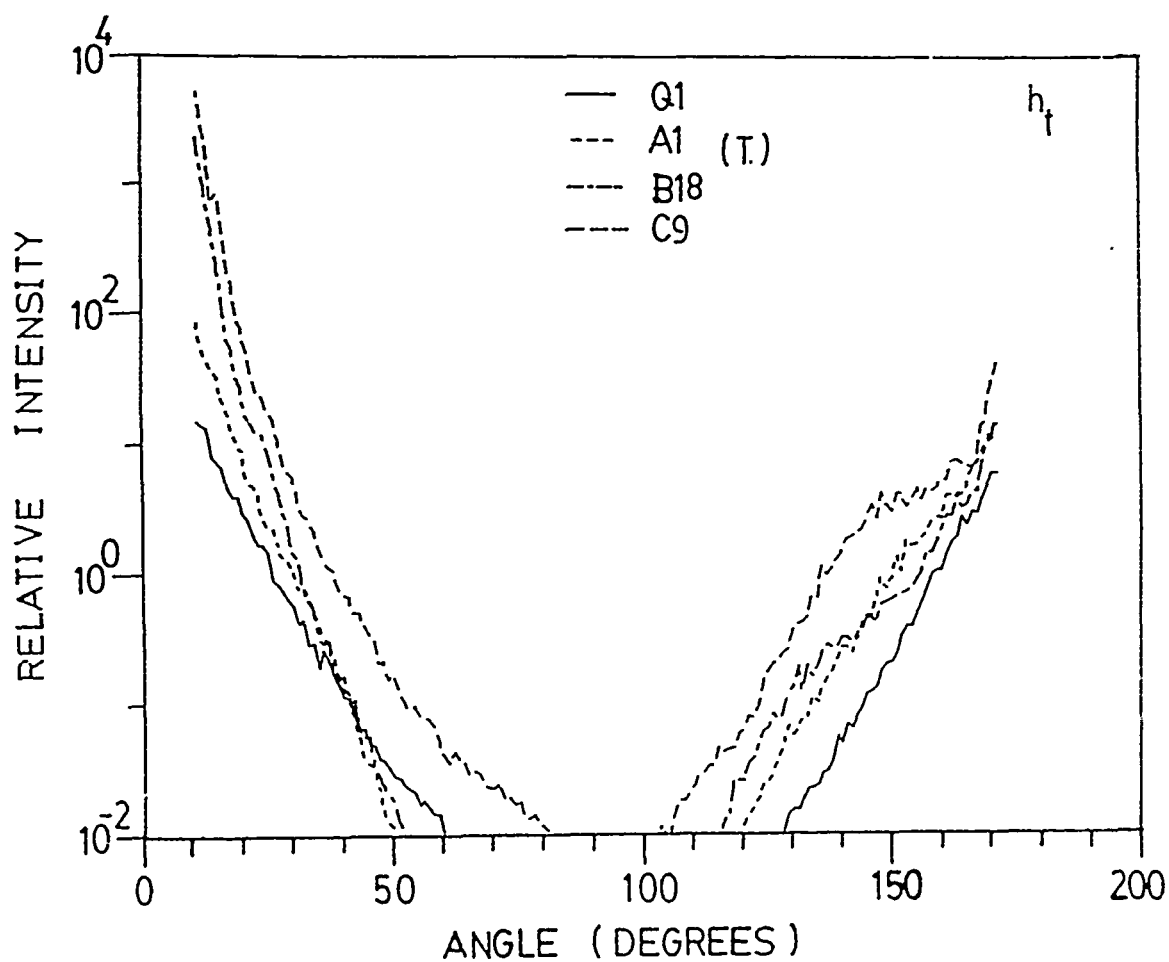
Figure 4.8. Same as Figure 4.7 except for base-on incidence. Below are typical electronmicrographs of replices of the samples.

Q 1

A 1

B 18

C 9

Figure 4.9. Angular distribution of scattered intensity from conical pits in samples
Q2 (blank), D15, E7, and F20, for horizontally polarized incident light, at
tip-on incidence.
[The conical pits in these samples are etched tracks of 2.0 MeV proton
beam, incident normally on the plastic sample surfaces, with fluences: 0,
5×10^5, 1×10^6, and 3×10^6, respectively].
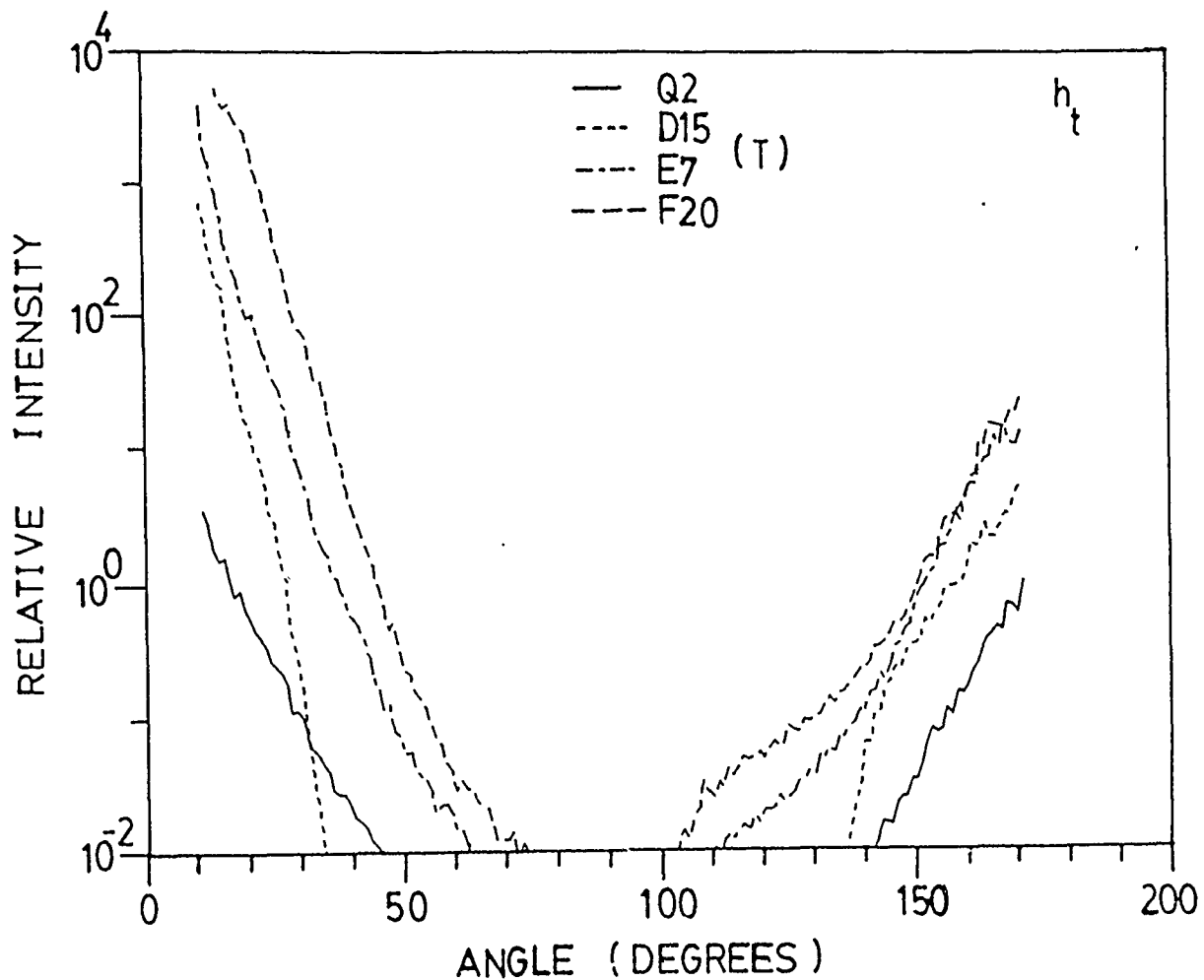
Figure 4.10. Same as Figure 4.9 except for base-on incidence. Below are typical electronmicrographs of replices of the samples.

D 15

E 7

1μ
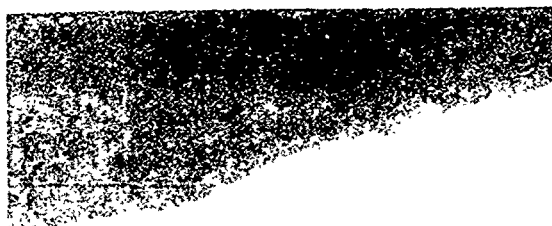
F 20
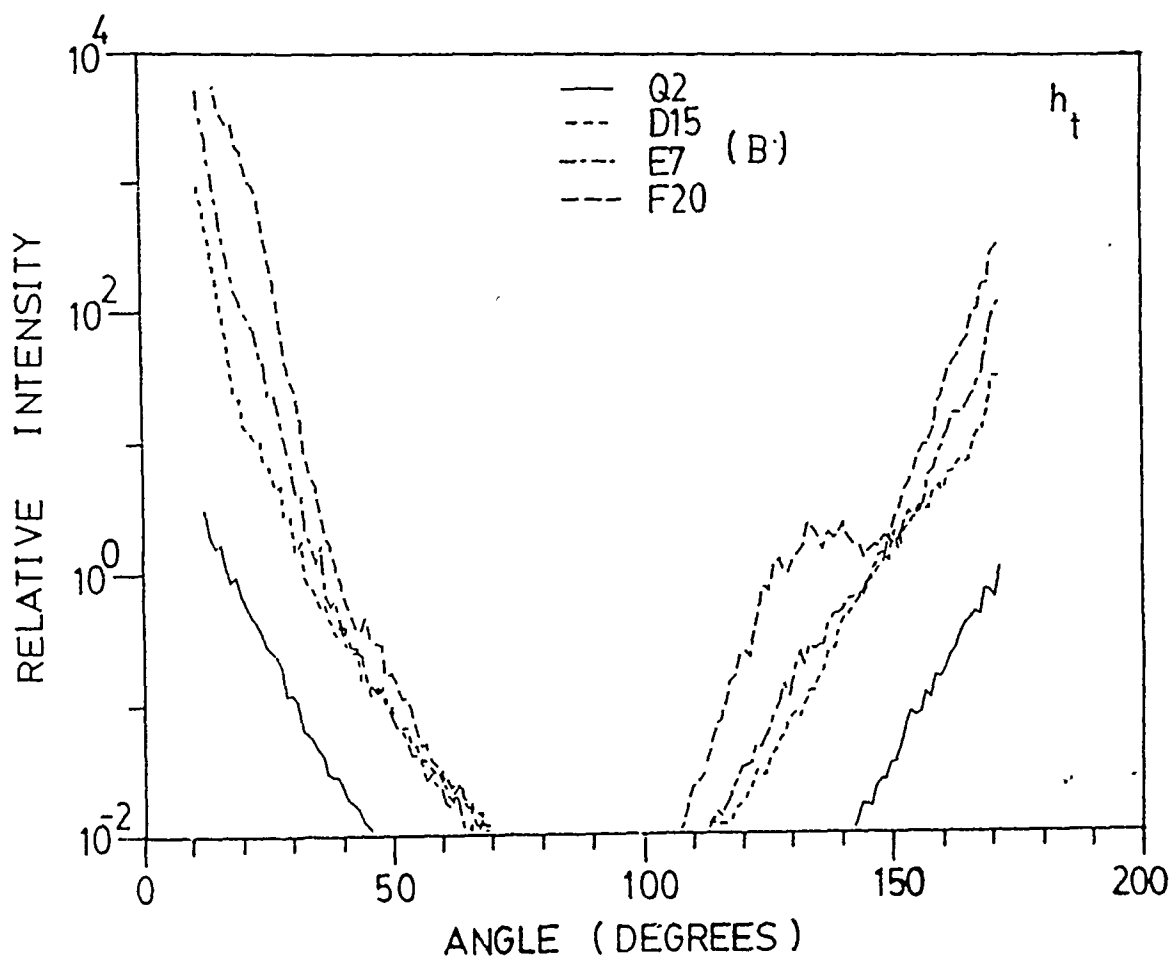
Figure 4.11. Angular distribution of scattered intensity from conical pits in samples
PNHQ(blank), PNH1, PNH2, and PNH3, for vertically polarized incident
light.

[The conical pits in these samples are etched tracks of the recoil particles
resulting from irradiation of the plastic samples by neutrons from 1Ci Pu-
Be source for 0, 3, 6 and 9 days, respectively].

The patterns measured when exposed the front (up stream from neutron
source) surfaces of samples normally to the incident light.
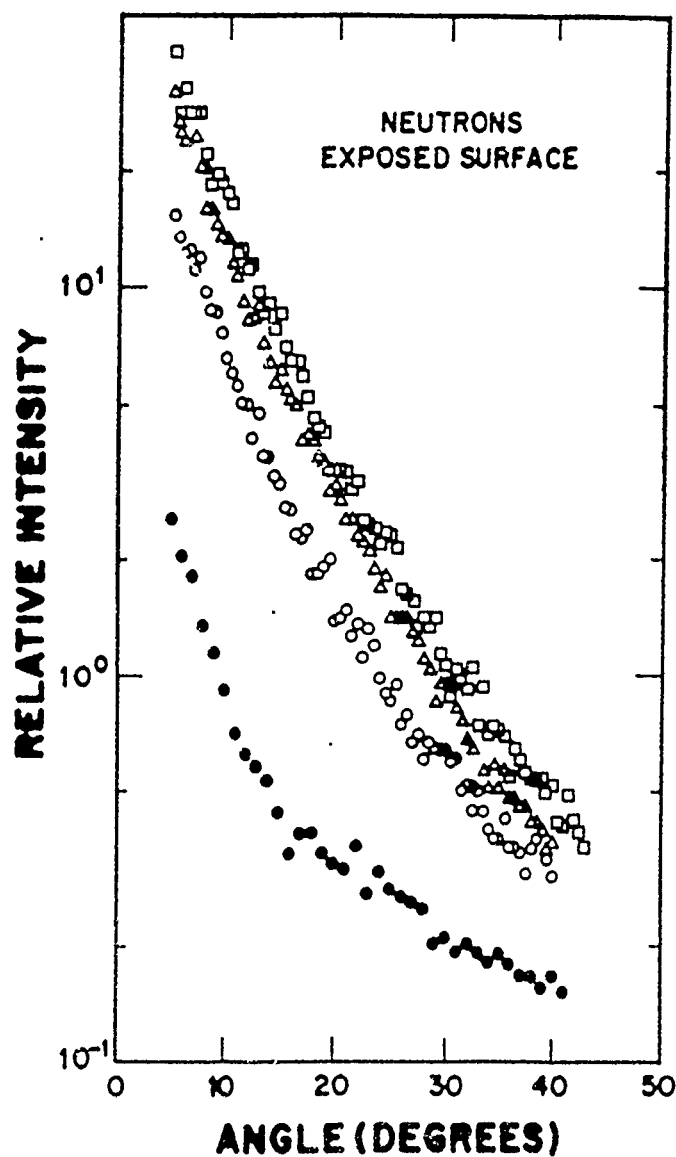
Figure 4.12. Same as Figure 4.10 except for the back surfaces were exposed normally to the incident beam.

Below are typical electronmicrographs of replices of the samples.

PNH 1

PNH 2

PNH 3

PNH 4

NEUTRONS
BACK SURFACE
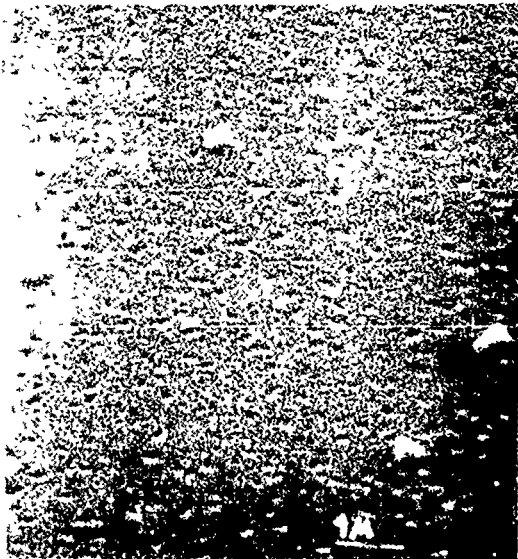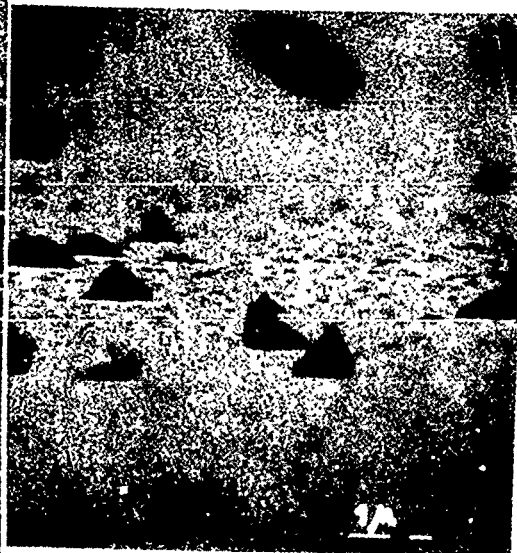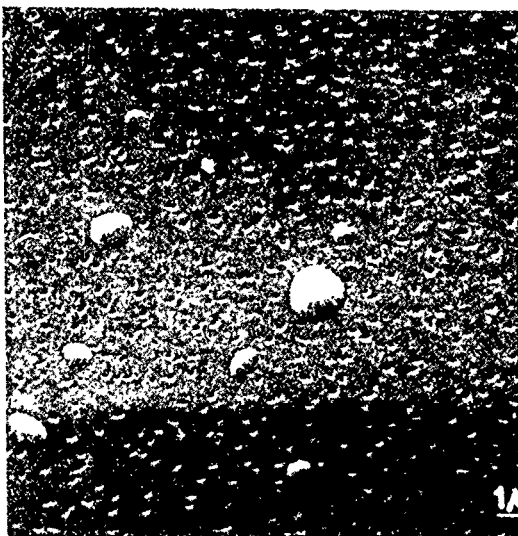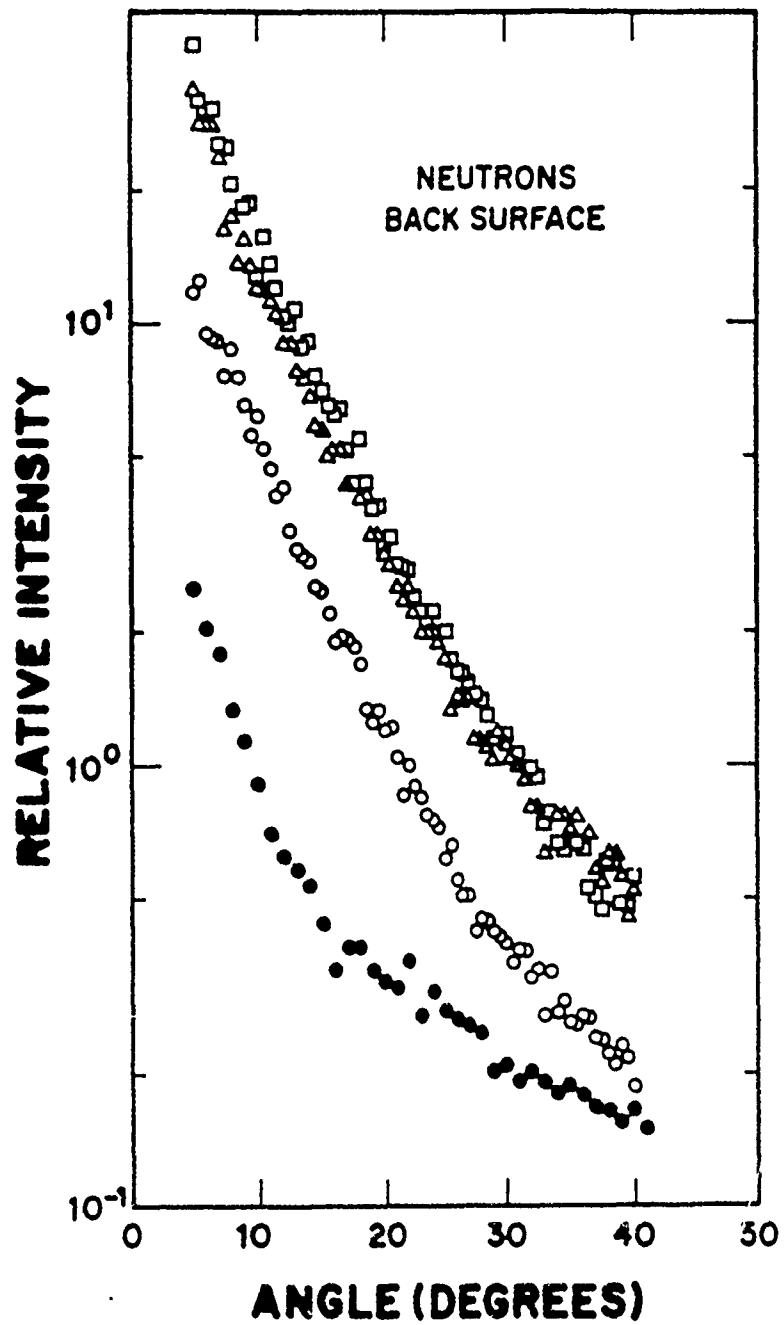
Figure 4.13. Angular distribution of scattered intensity from conical pits in sample
K3, for horizontally polarized incident light, at tip-on incidence, showing
parallel (H_h), cross (H_v) and total (without polarizer) polarization com-
ponents of the scattered light.

[The conical pits in these samples are etched tracks of 8.12 MeV He-3 ions
normally incident on the plastic sample surface with fluence 10^6 /cm^2].
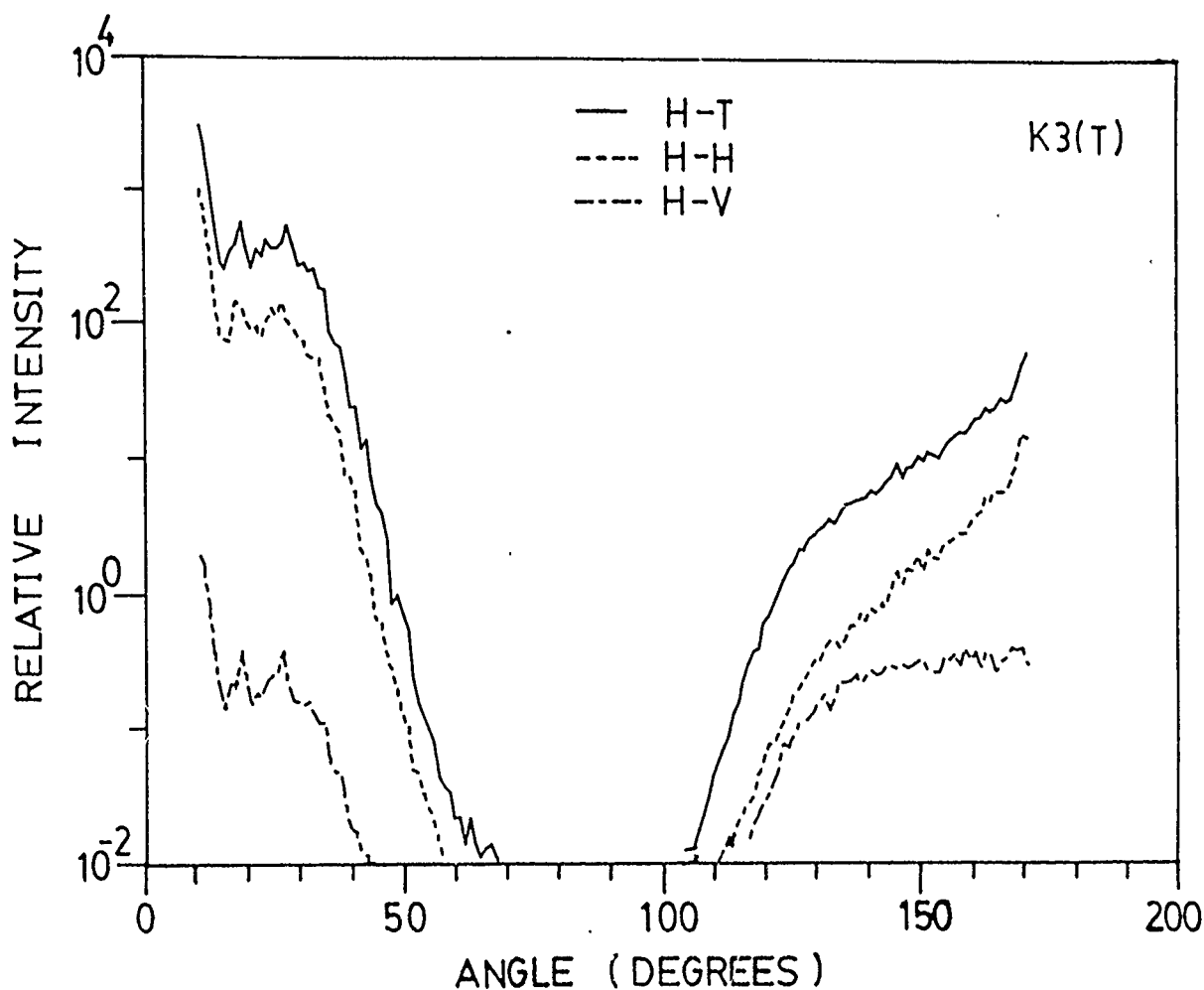
Figure 4.14. Same as Figure 4.13 except for base-on incidence. Below is an electron-micrograph of a replica of the sample.
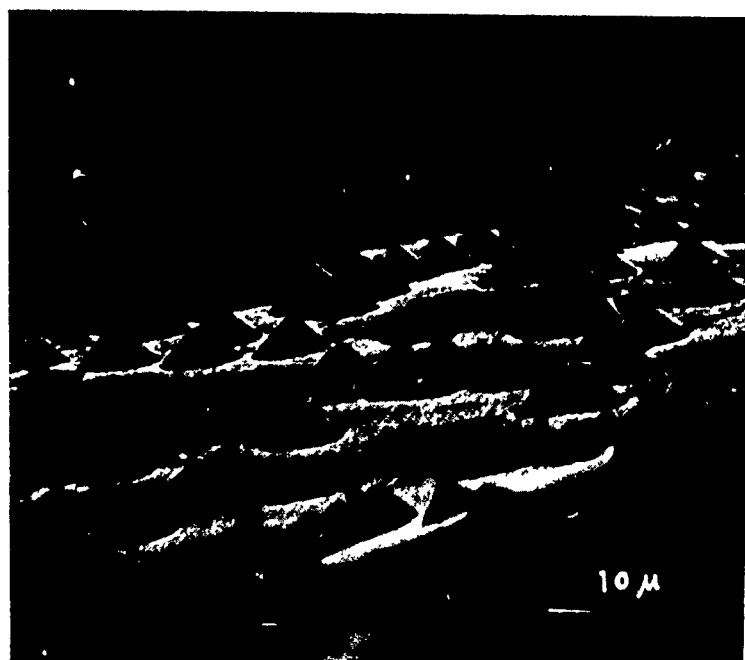
K 3

Figure 4.15. Angular distribution of scattered intensity from sample K3, for vertically polarized incident light, at tip-on incidence, showing parallel (V_v), cross (V_h) and total (without polarizer) polarization components of the scattered light.
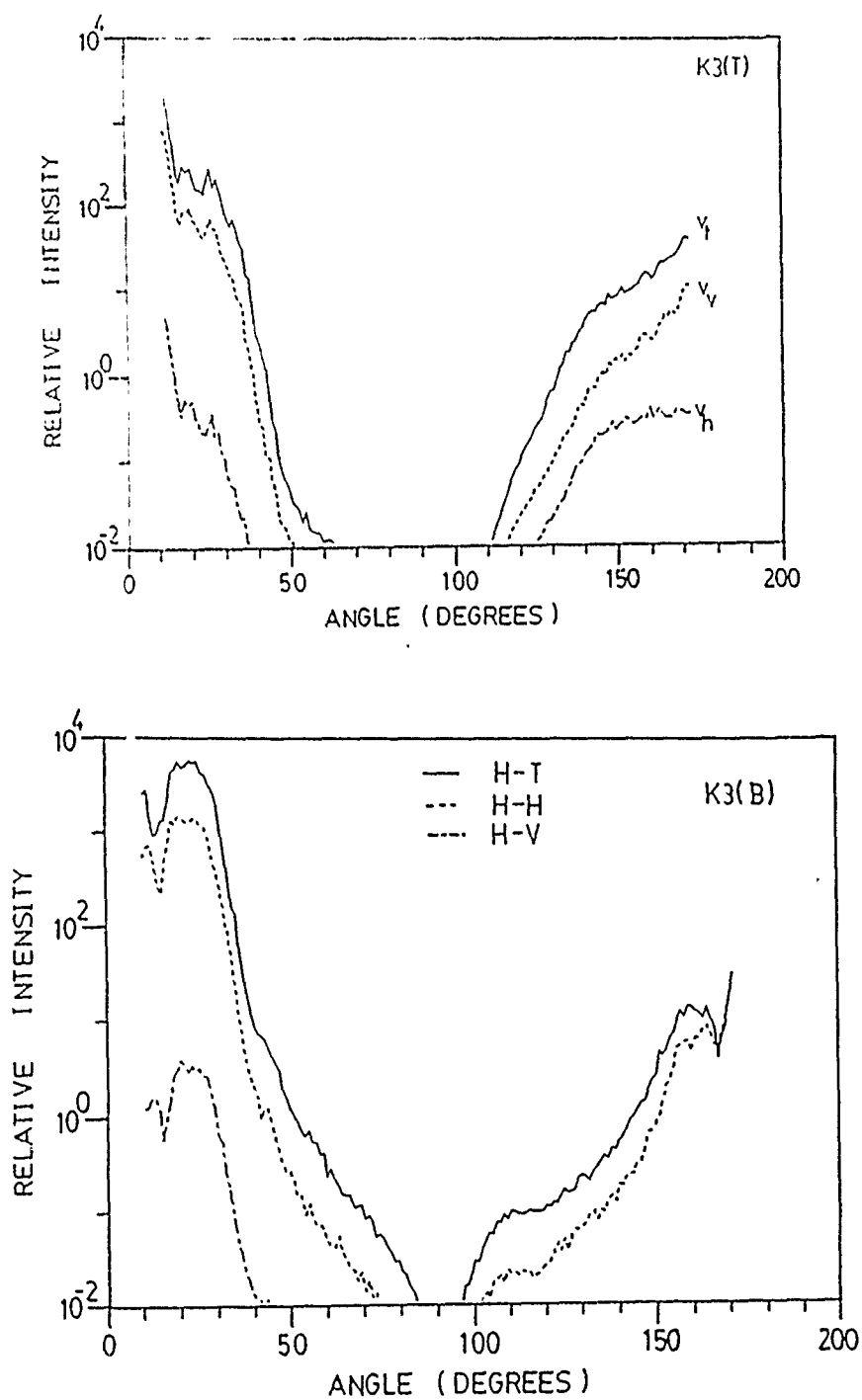
Figure 4.16. Same as Figure 4.15 except at base-on incidence.
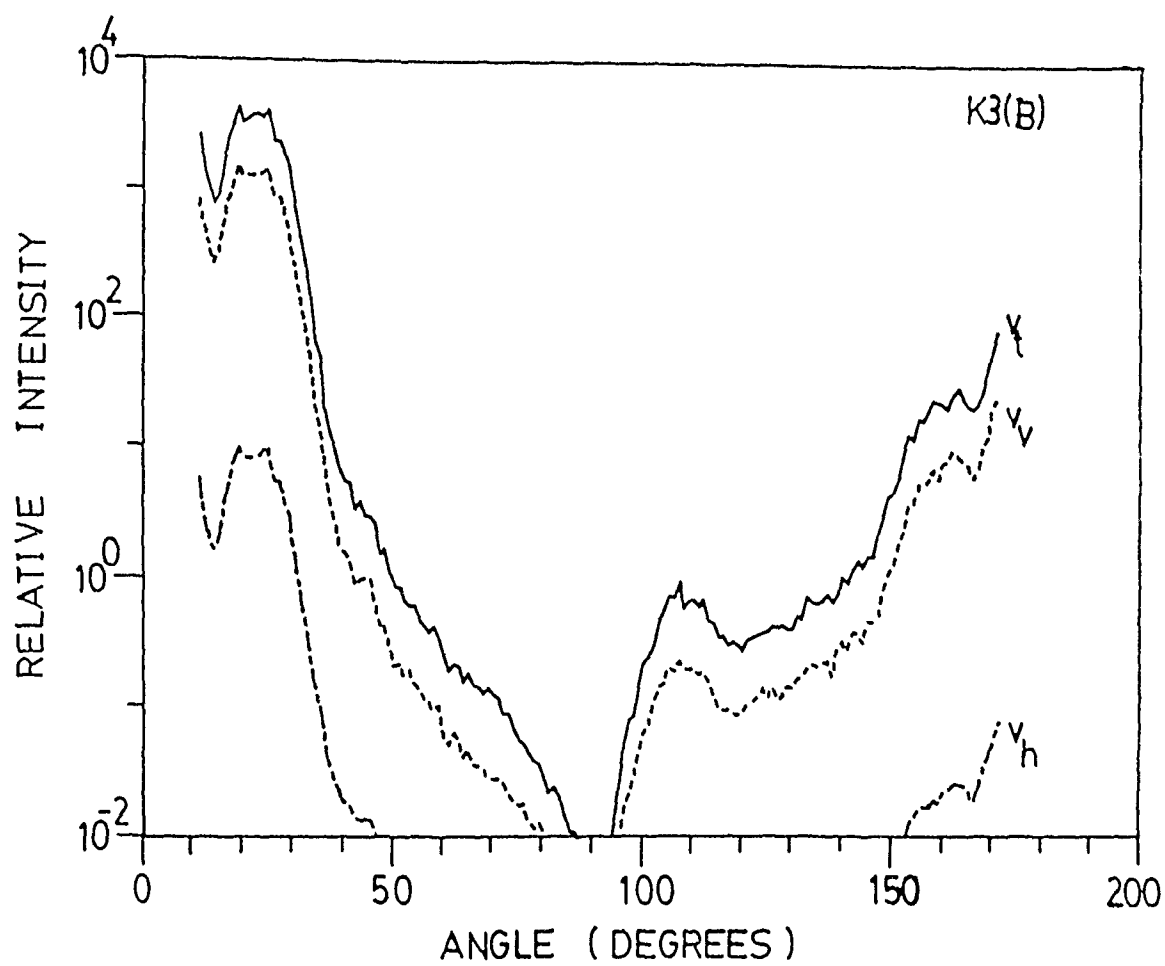
Figure 4.17. Degree of linear polarization versus scattering angles obtained from the measured light scattering from pits in sample K3 (dotted curve), as compared with that from MIE calculations from equal spheres (solid curve).
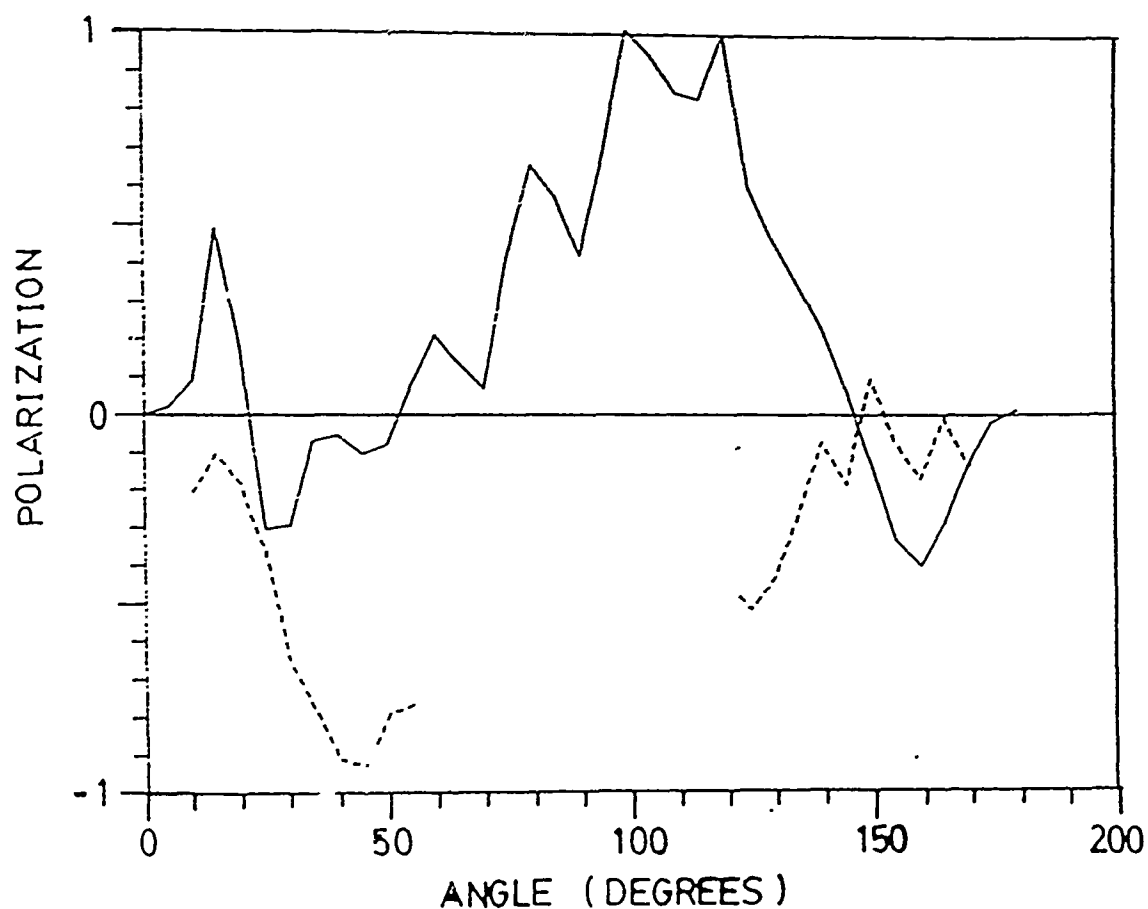
Figure 4.18. Relative scattered intensity at selected angles versus nominal fluences. for micropits in samples H5, I18 and K18 at tip-on incidence (shown in Figure 4.1). At 30° : solid circle (intensity scale as shown) At 12° : cross (intensity scale × 25).
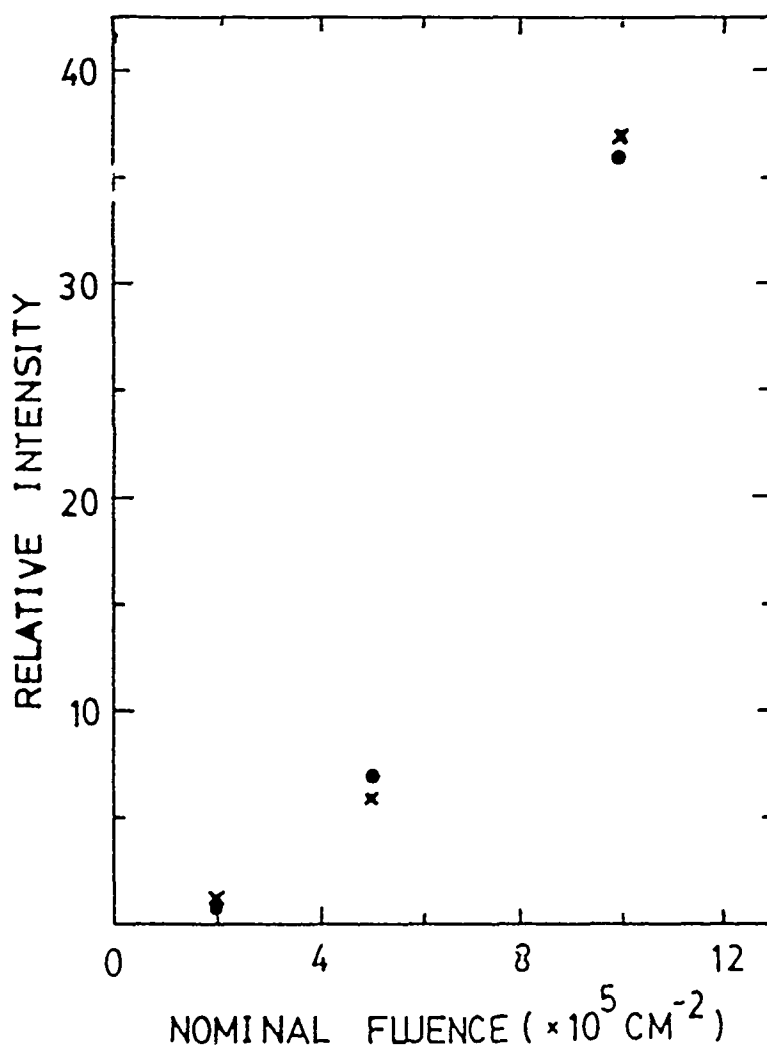
Figure 4.19. Relative scattered intensity at selected angles versus nominal fluences, for micropits in samples H6, I18 and K18 at base-on incidence (shown in Figure 4.2).

At 15° : closed circle

At 12° : cross.
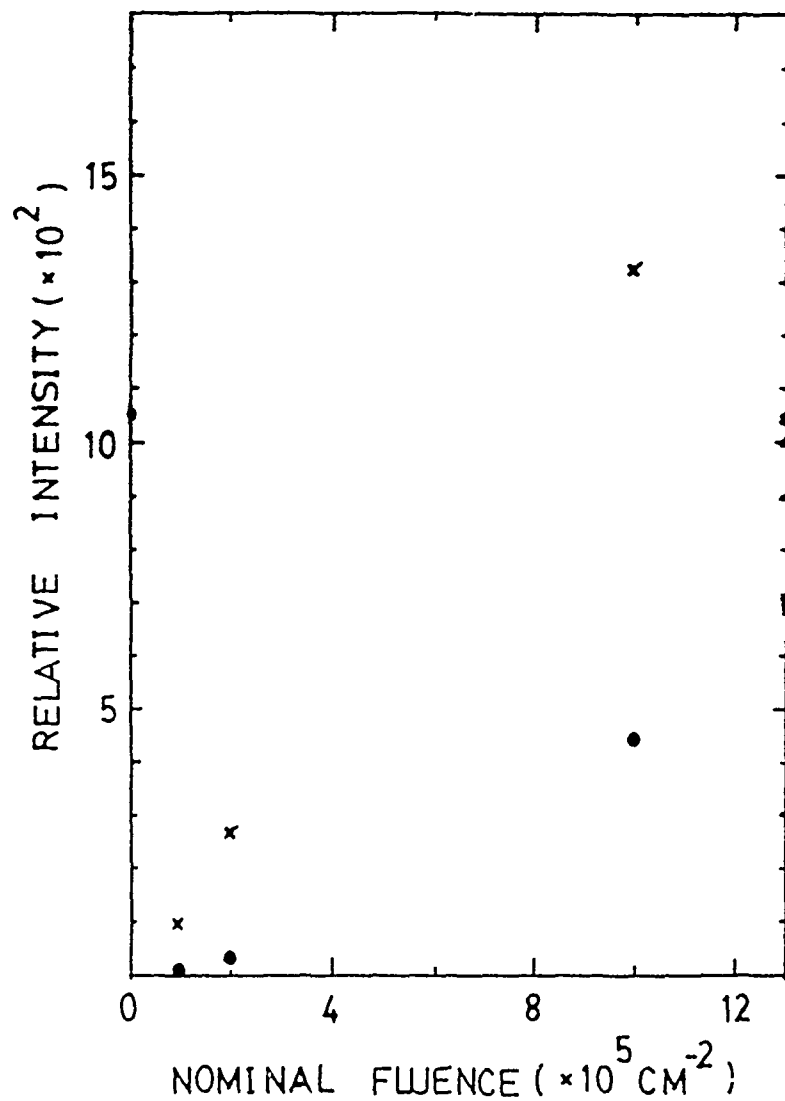
Figure 4.20. Relative scattered intensity at selected angles versus nominal fluences, for micropits in samples L15, M6 and N17, at tip-on incidence (shown in Figure 4.3).

At 30° : solid circle (intensity scale as shown)

At 12° : cross (intensity scale × 20).
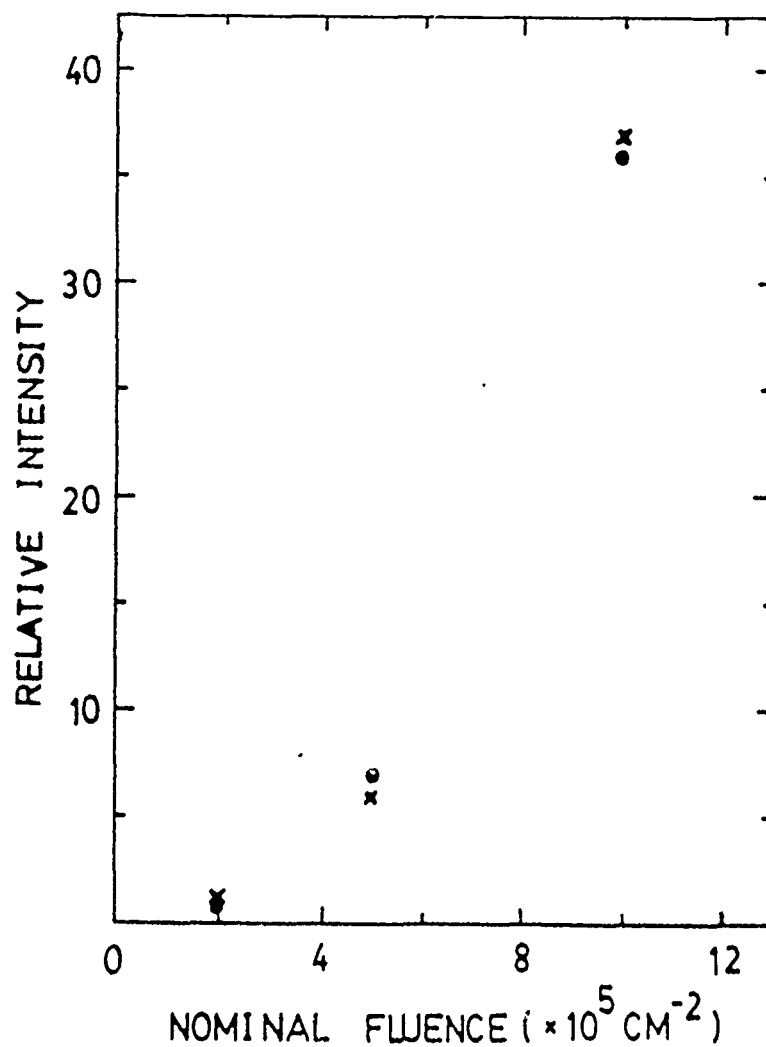
Figure 4.21. Relative scattered intensity at selected angles versus nominal fluences, for micropits in samples L15, M6 and N17 at base-on incidence (shown in Figure 4.4).

At refraction peaks: cross (intensity scale as shown)

At 30 ° : solid circle (intensity scale × 0.5)

At 12 ° : circle (intensity scale × 2.5).
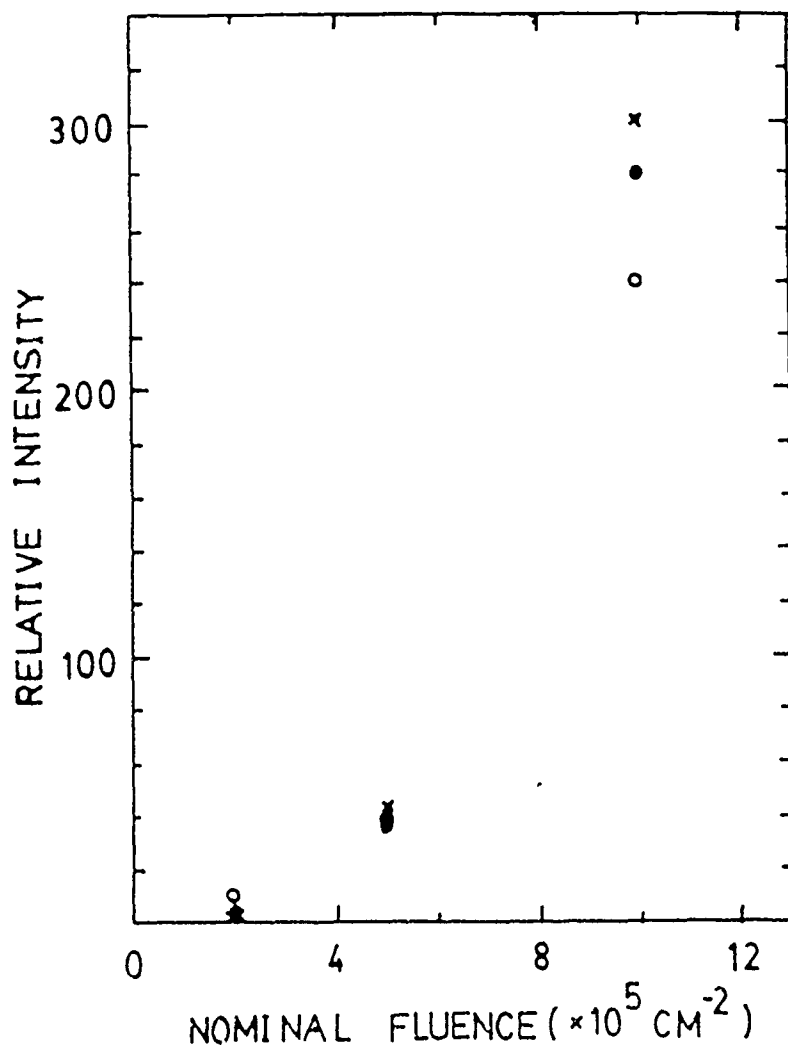
Figure 4.22. Relative scattered intensity at selected angles versus nominal fluences, for micropits in samples Q1, A1, B18 and C9 at tip-on incidence (shown in Figure 4.7).

At 17°: cross (intensity scale as shown)

At 20° : solid circle (intensity scale as shown)

At 26° : triangle (intensity scale × 0.1)

At 28° : circle (intensity scale × 2.5).
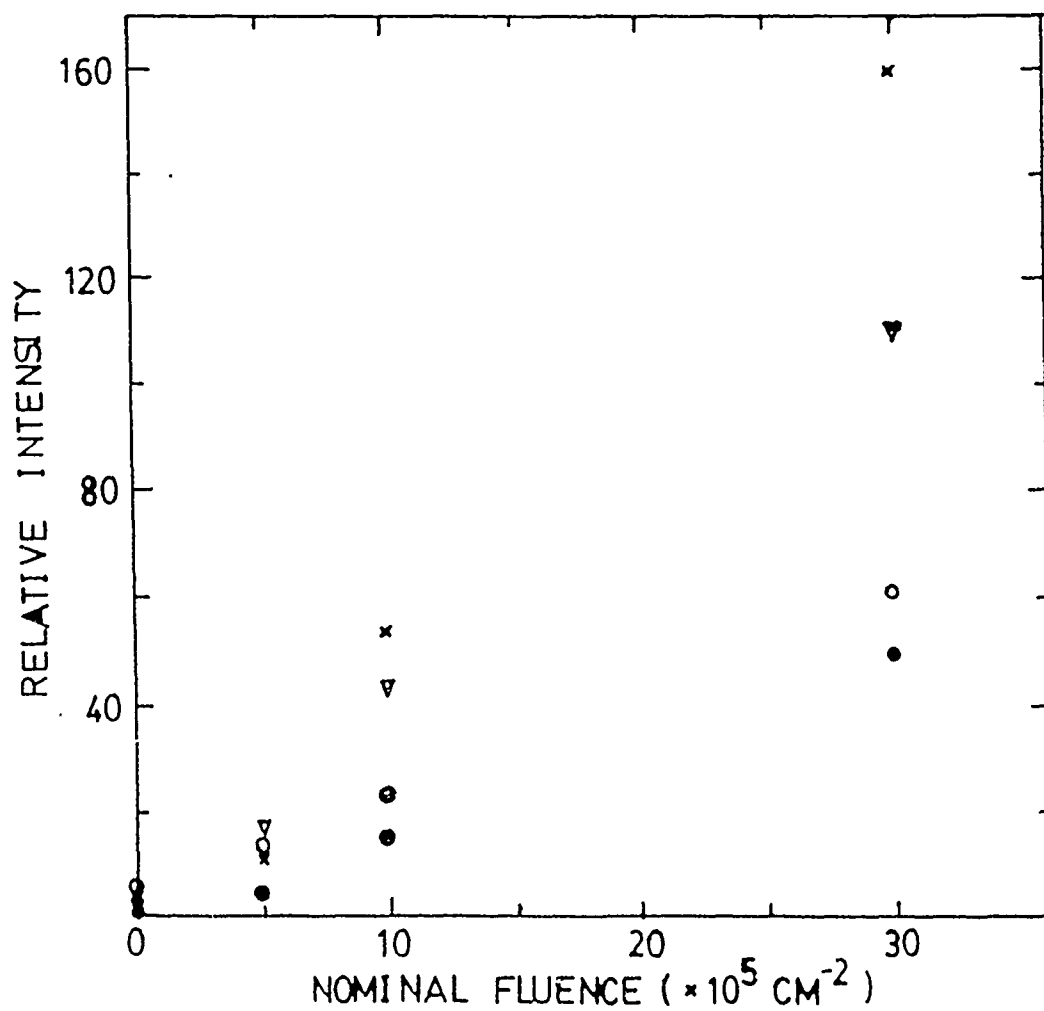
Figure 4.23. Relative scattered intensity at selected angles versus nominal fluences, for micropits in samples Q1, A1, B18 and C9 at base-on incidence (shown in Figure 4.8).

At 17°: circle

At 20° : solid circle.
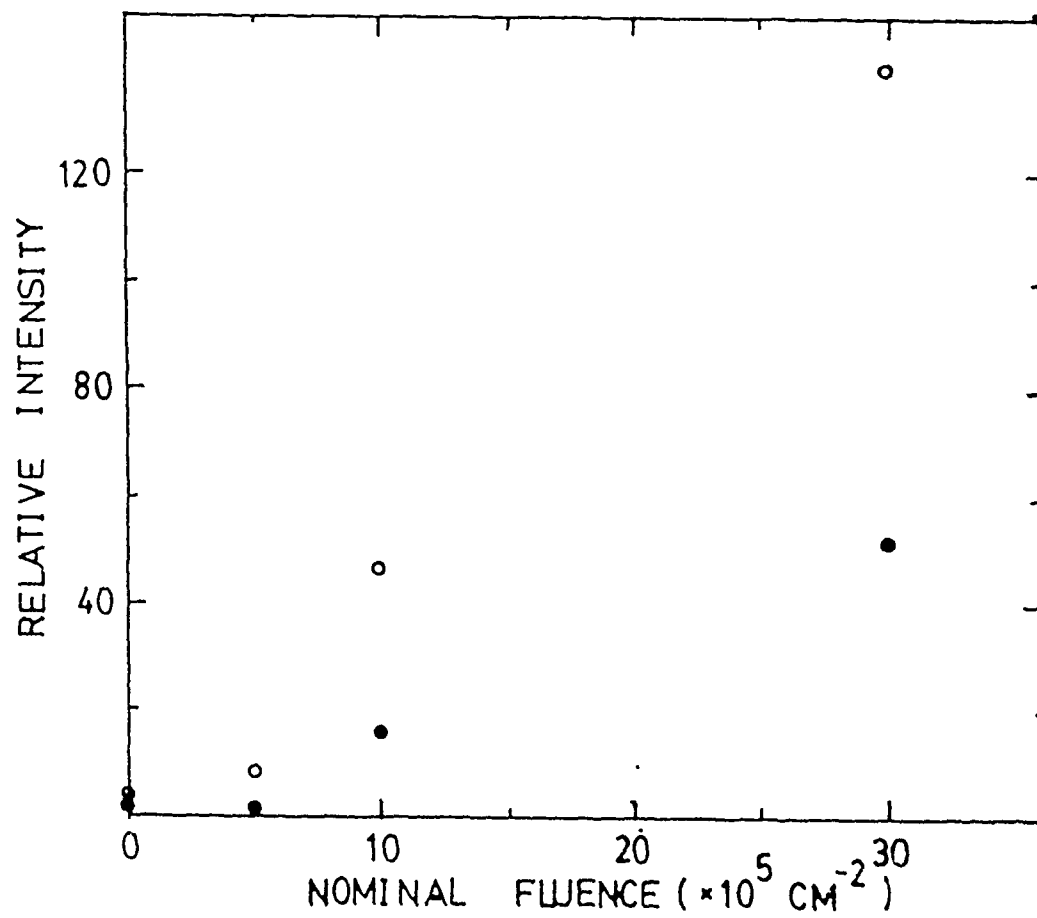
Figure 4.24. Relative scattered intensity at selected angles versus nominal fluences, for micropits in samples D15, E7 and F20, at tip-on incidence (shown in Figure 4.9).

At 26°: solid circle (intensity scale as shown)

At 15° : circle (intensity scale × 20).
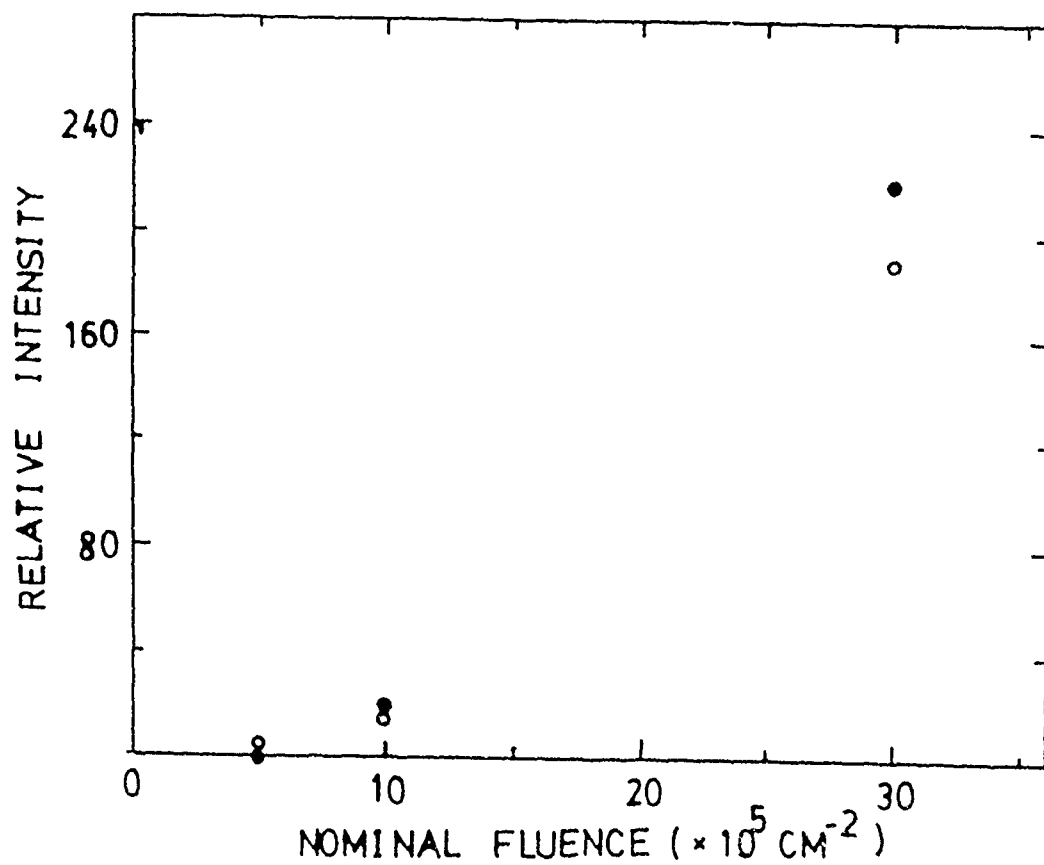
Figure 4.25. Relative scattered intensity at selected angles versus nominal fluences, for micropits in samples D15, E7 and F20, at base-on incidence (shown in Figure 4.10).

At 26°: solid circle (intensity scale as shown)

At 22° : circle (intensity scale × 10)

At 15°: cross (intensity scale × 20).
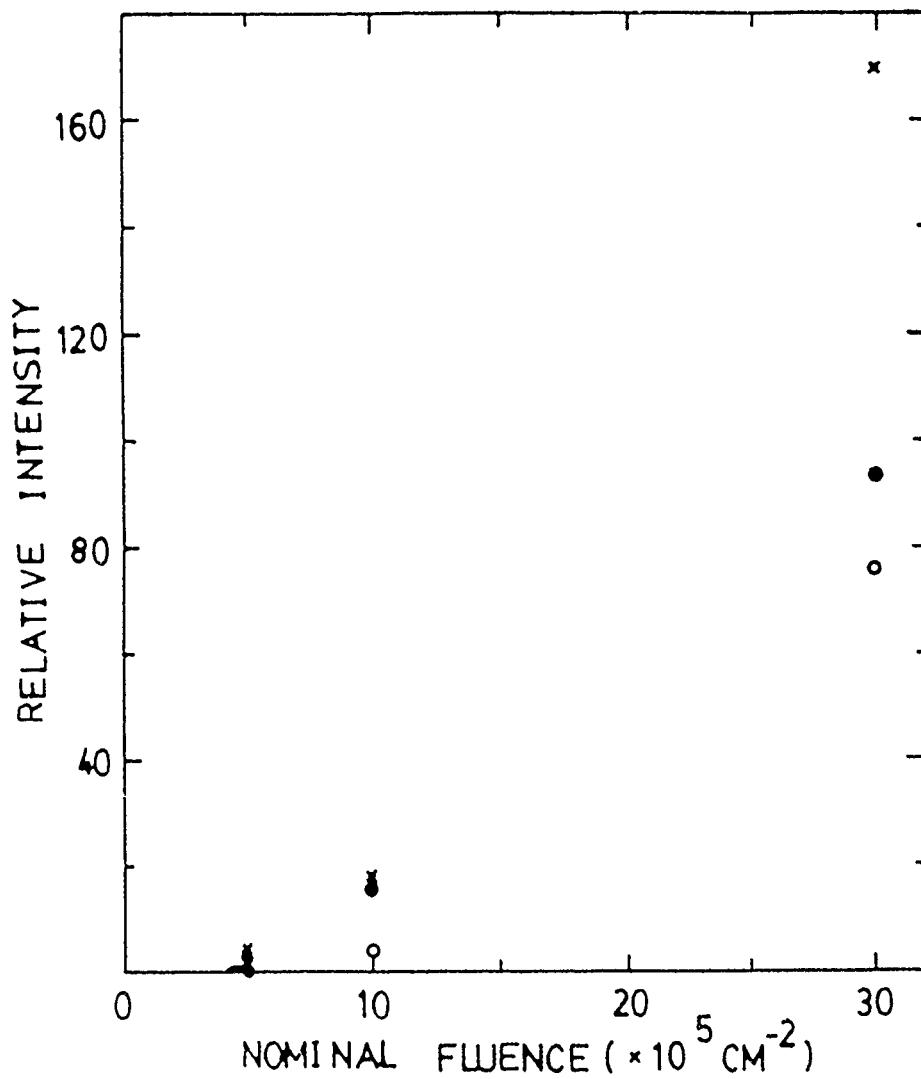
Figure 4.26. Scattered Intensity at a selected optimal angle (12°) versus duration of
irradiation of neutron irradiation samples (shown in Fig. 4.11 and 4.12).
front surface: circle
back surface: solid circle.
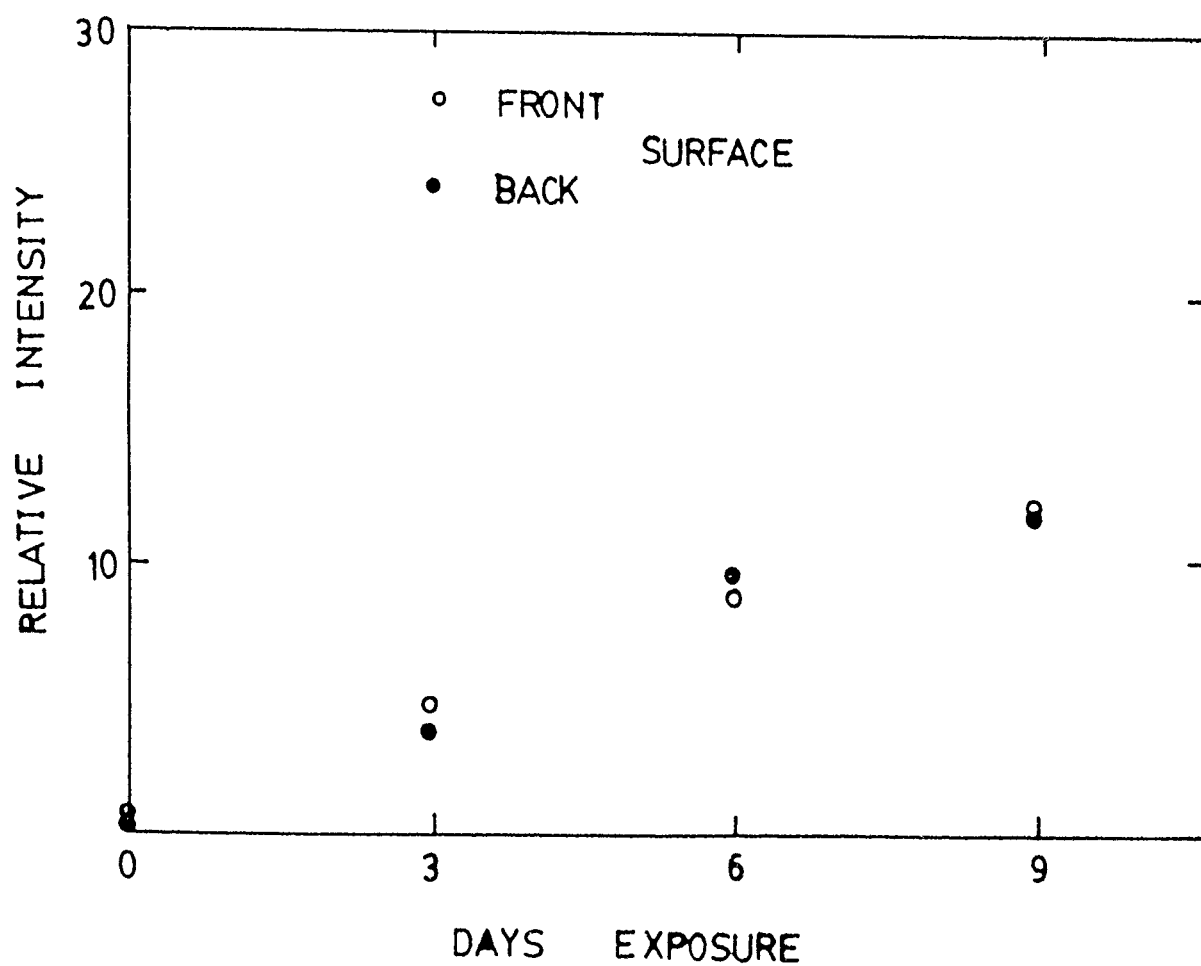
Figure 4.27. Photocounted fluence versus duration of irradiation to neutrons.
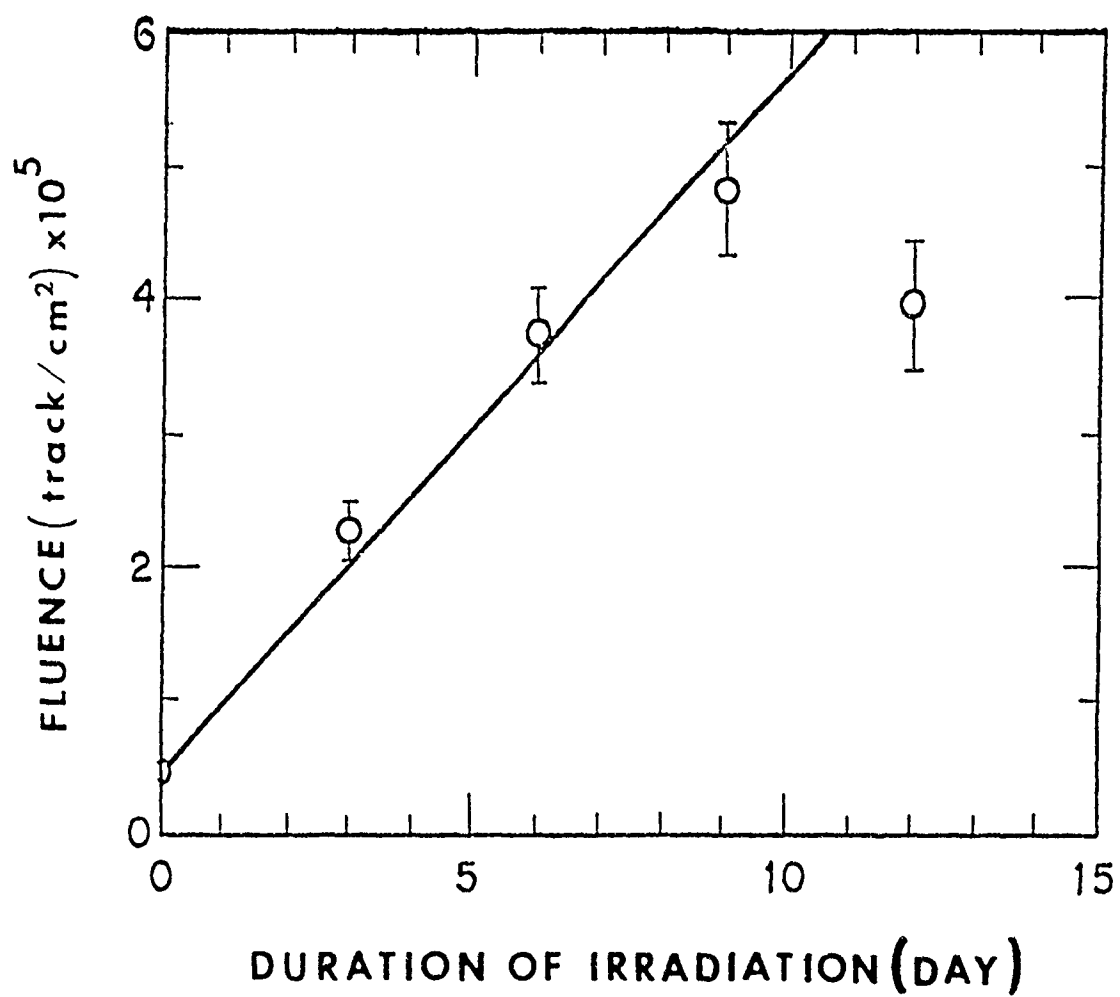
Figure 4.28. Scattered intensity at a selected optimal angle (12°) versus photocounted fluences of neutron irradiated samples.
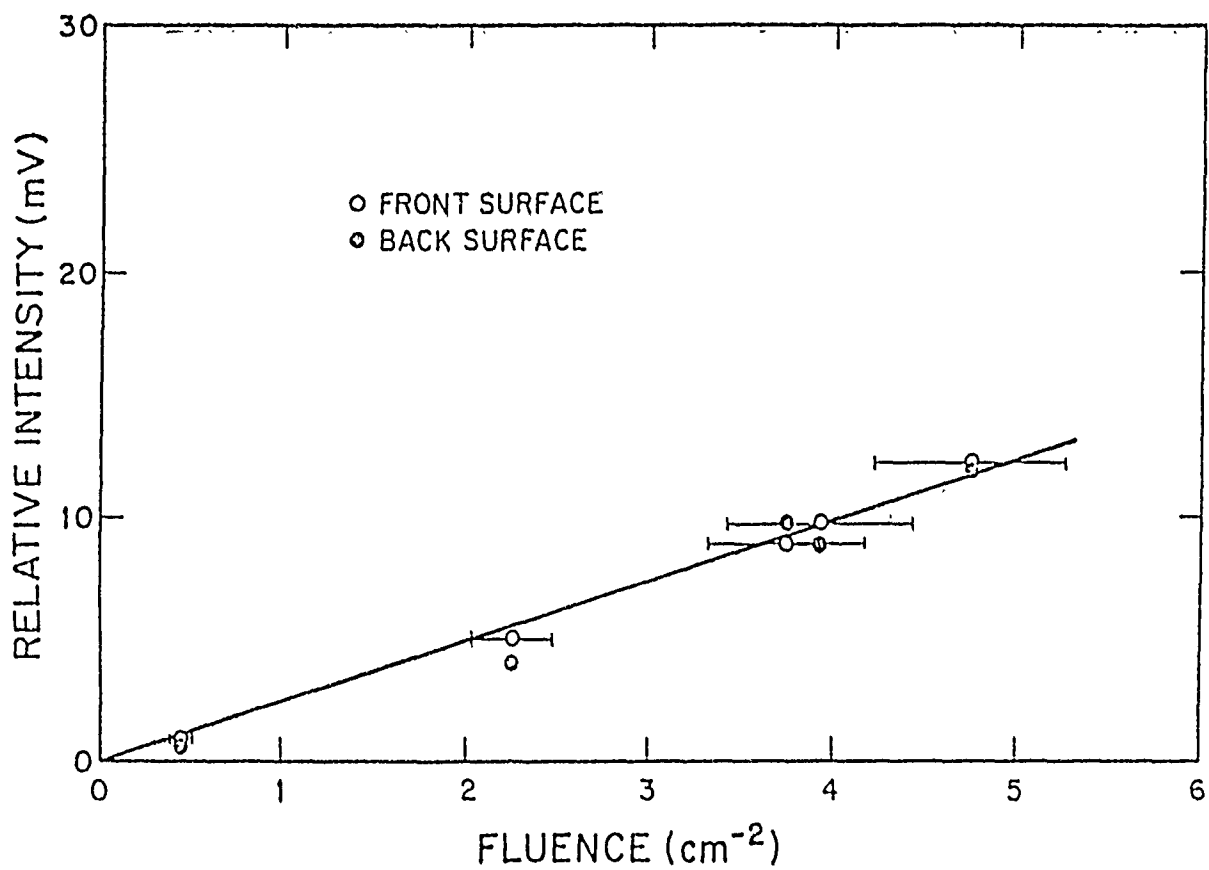
Figure 4.29. Angular distribution of scattered intensity from conical pits in samples G15, G6, G17, G8 and G7, for horizontally polarized incident light, at tip-on incidence.
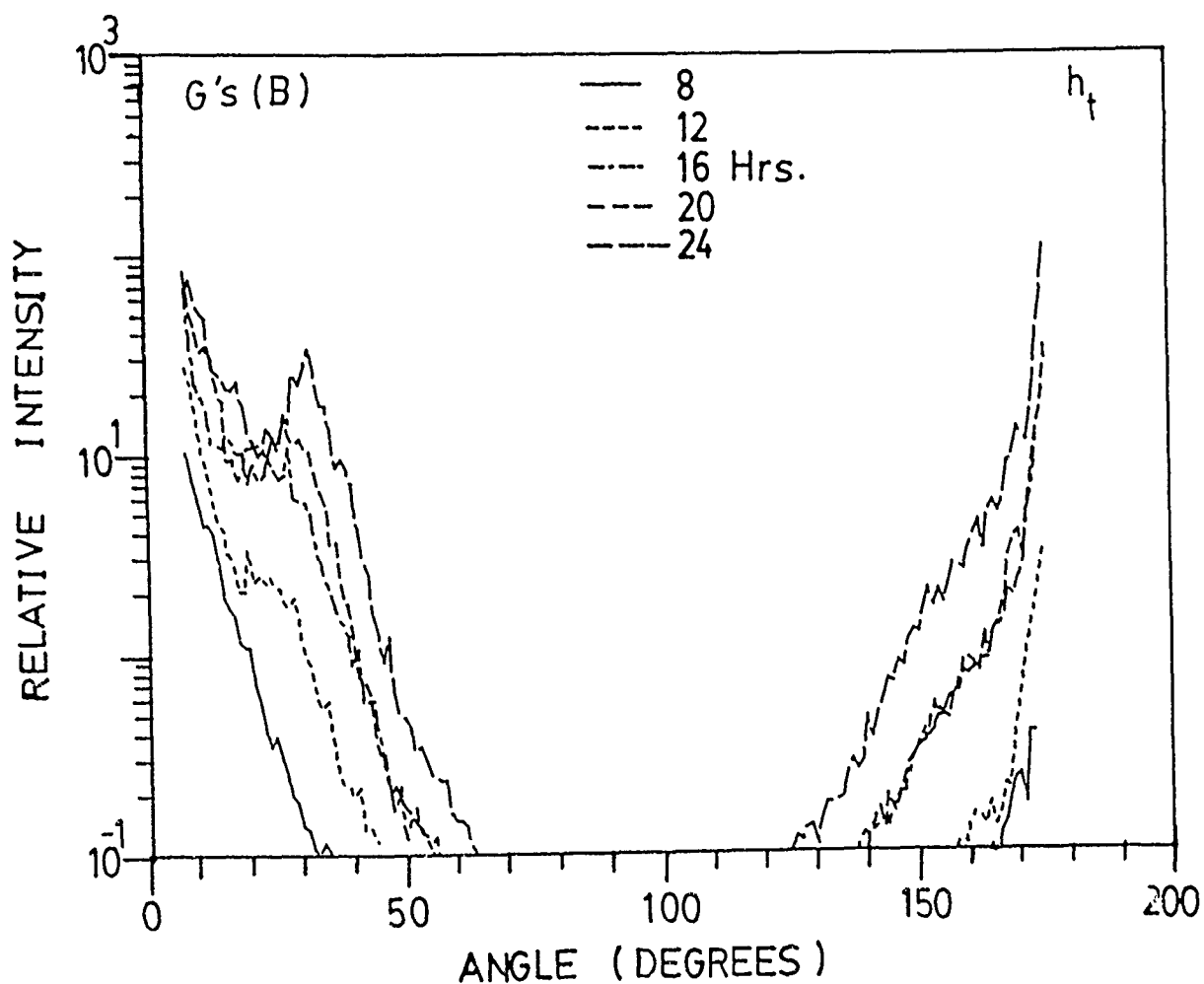
[The conical pits in these samples are etched tracks of 8.2 MeV He^3 ions, normally incident on plastic sample surfaces, prepared with different etching periods].

Figure 4.29. Angular distribution of scattered intensity from conical pits in samples G15, G6, G17, G8 and G7, for horizontally polarized incident light, at tip-on incidence.

[The conical pits in these samples are etched tracks of 8.2 MeV He³ ions, normally incident on plastic sample surfaces, prepared with different etching periods].

G 15

G 6

G 17
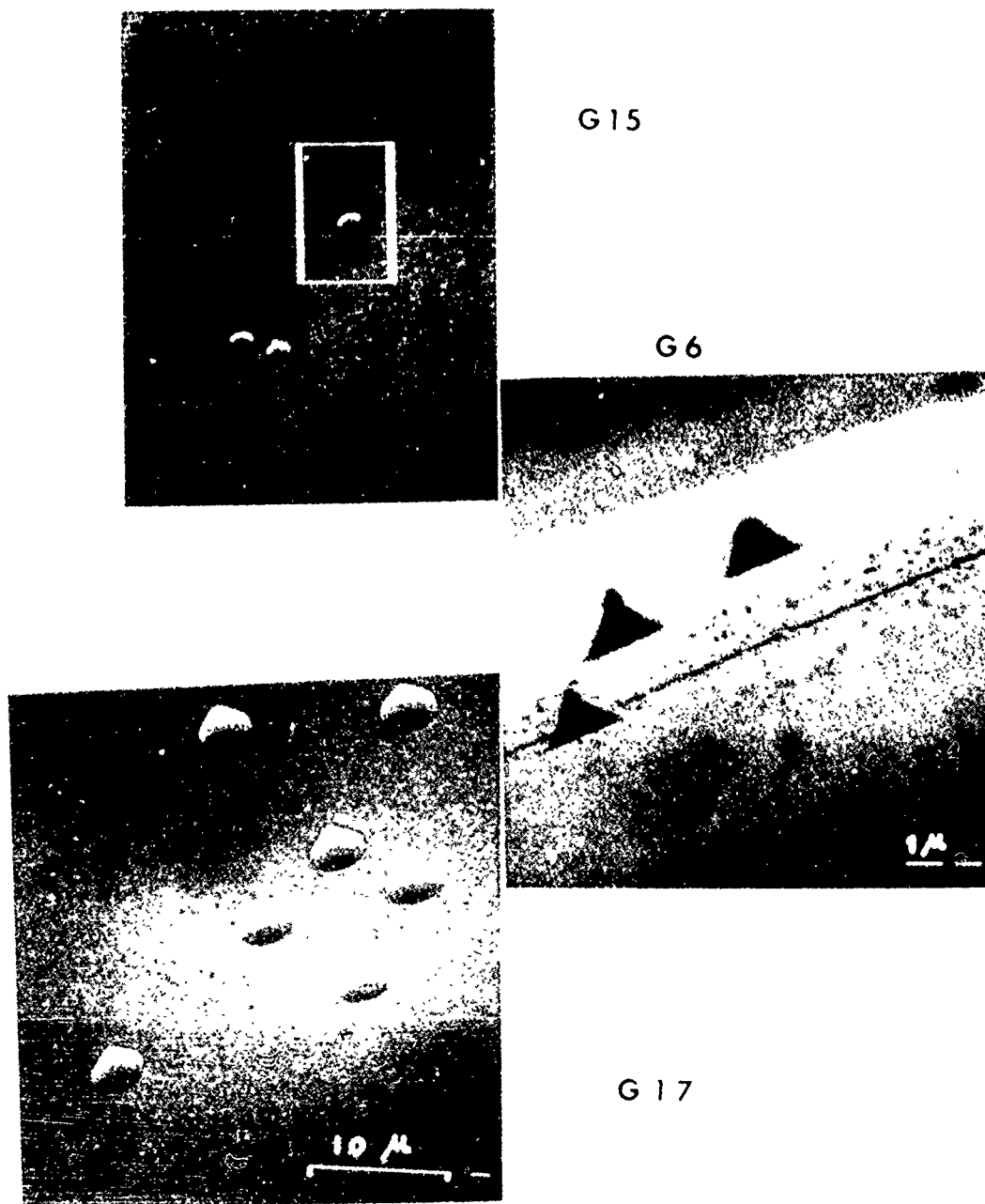
Figure 4.30. Same as Fig. 4.29 except at base-on incident. Below are typical electron-micrographs of replicas of samples.

G 8
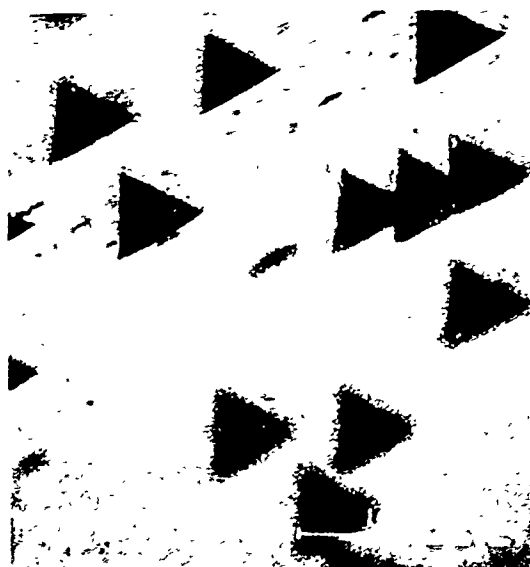
G 7
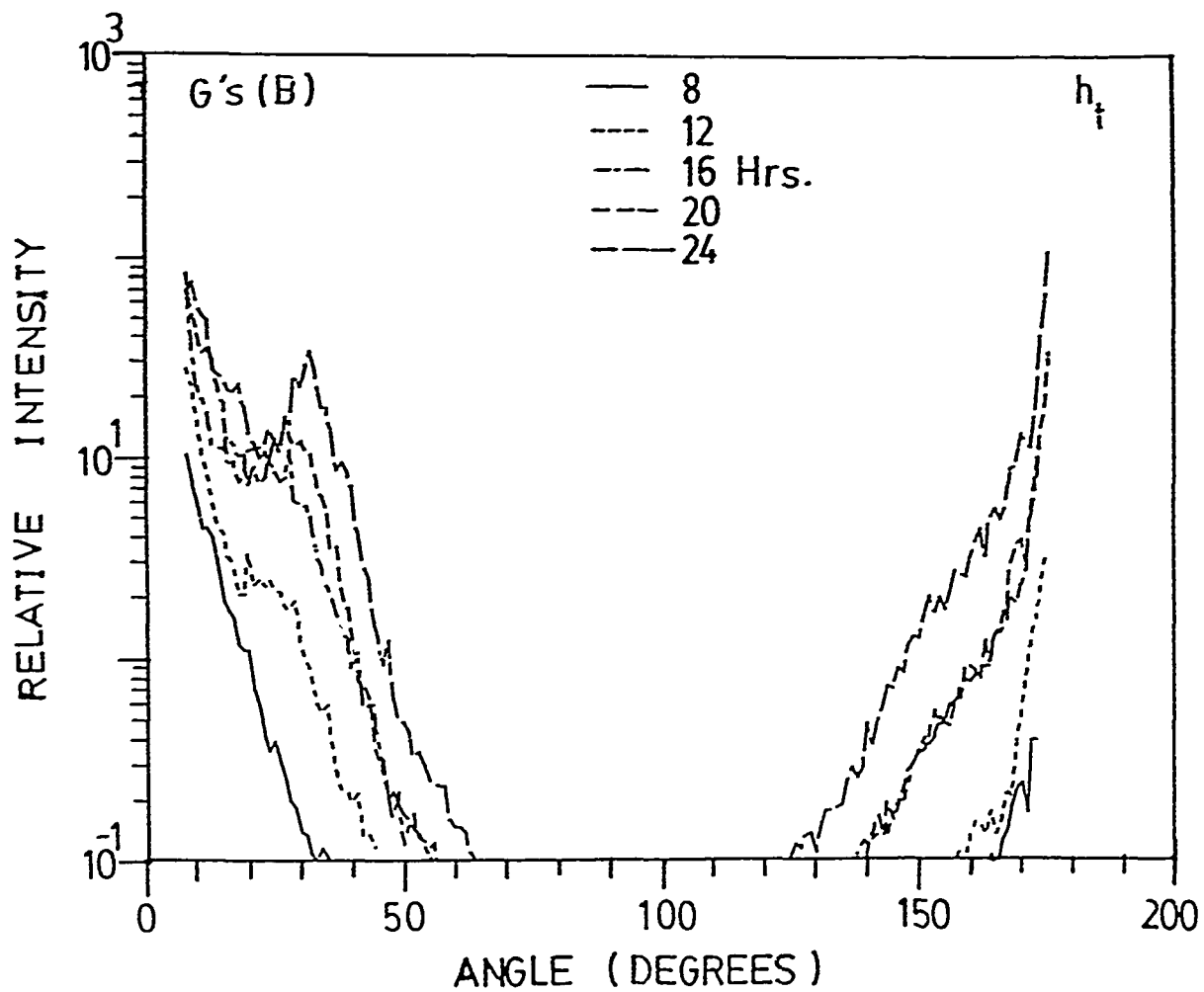
Figure 4.31. Relative scattered intensity at selected angles versus pit volumes, of Gs samples (shown in Fig. 4.29 and 4.30).

At refraction peak: solid circle (base-on incidence)

At 10° (base-on): Triangle (intensity scale × 2.5)

At 10° (tip-on): circle (intensity scale × 2.5).
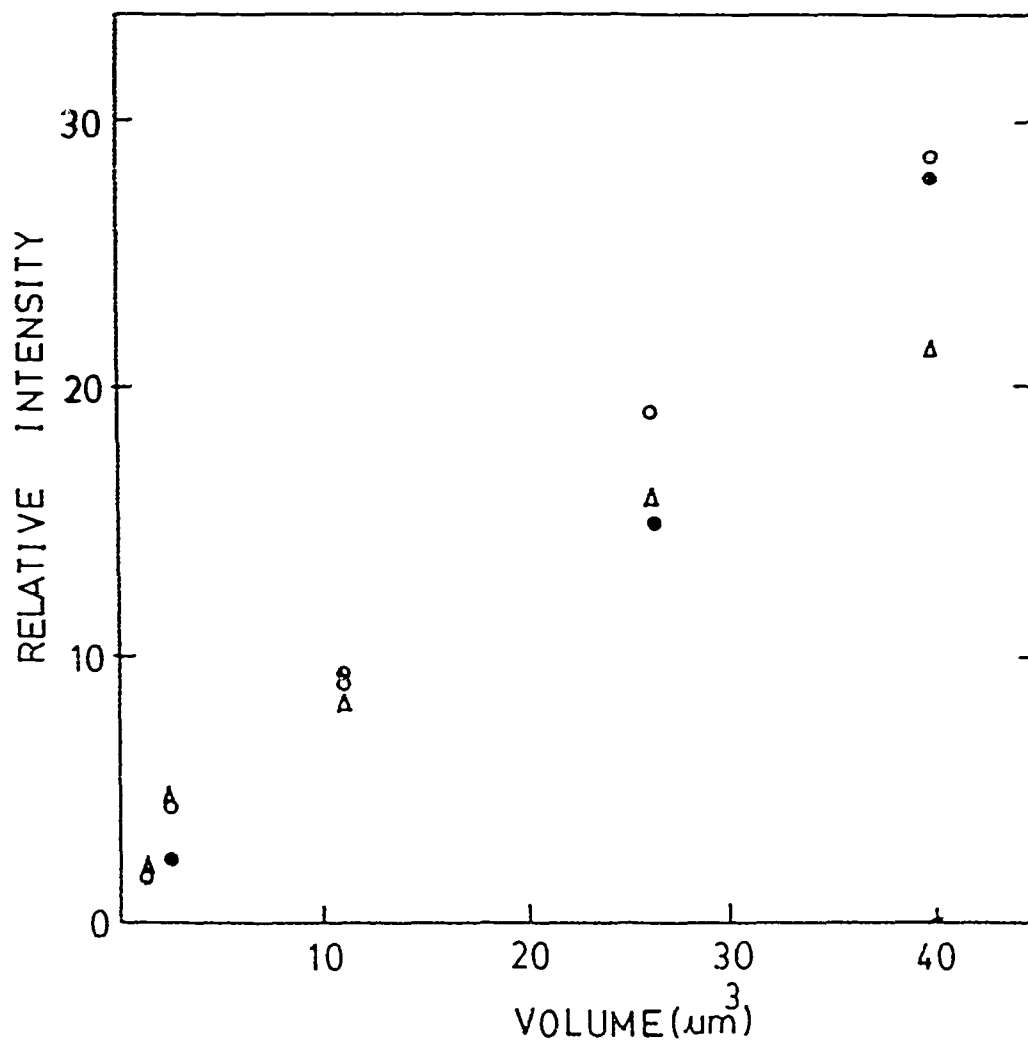
Figure 4.32. Relative scattered intensity at the 'humps' versus pit volumes, of samples N17, K18, and K3, for tip-on incidence hump (circle), for base-on incidence hump (or refraction peak: solid circle).
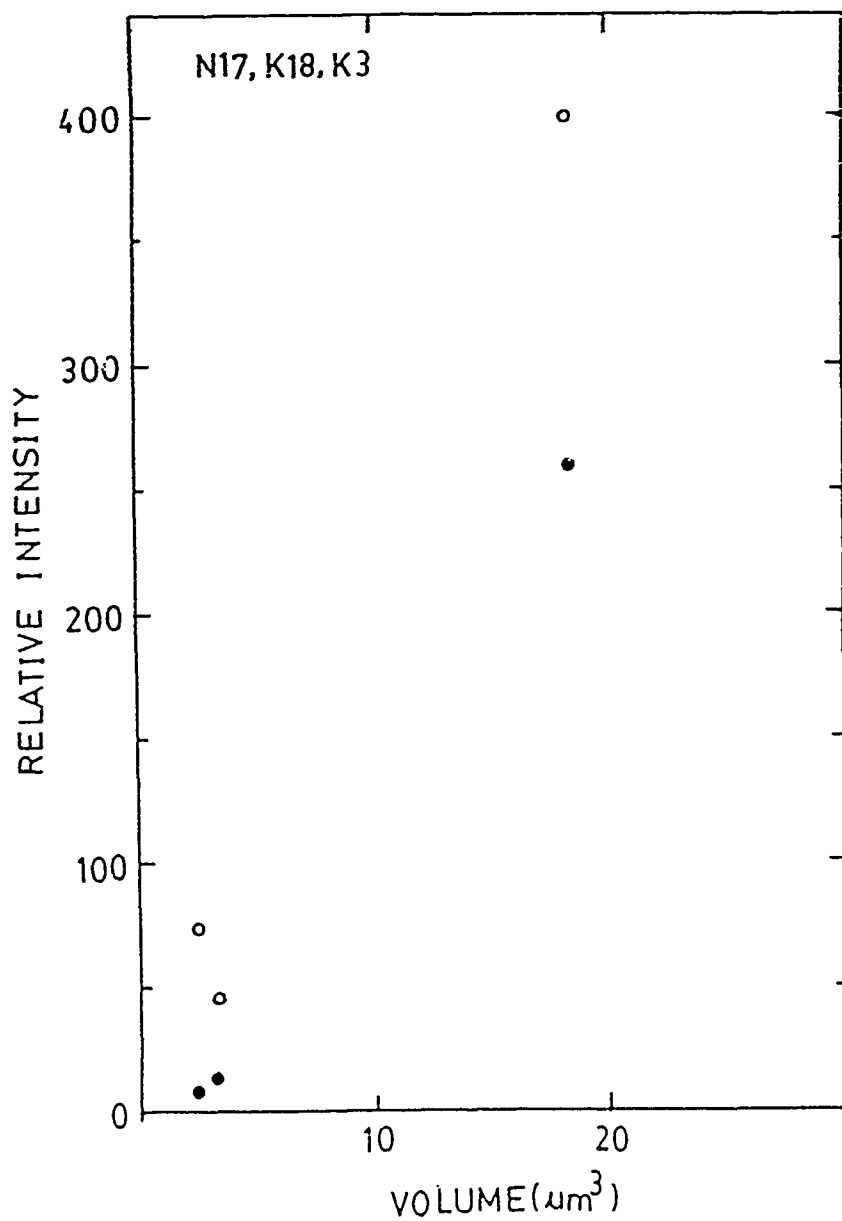
Figure 4.33A. Ray tracing of a cone through plastic plane surface.

Figure 4.33B. Ray tracing in case of a cone wit convex wall (dotted line) as compared with that of right circular cone (solid line).
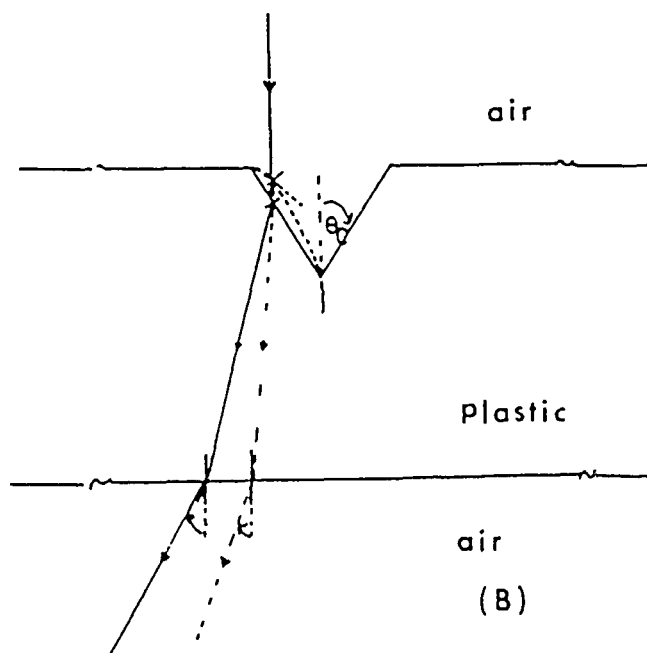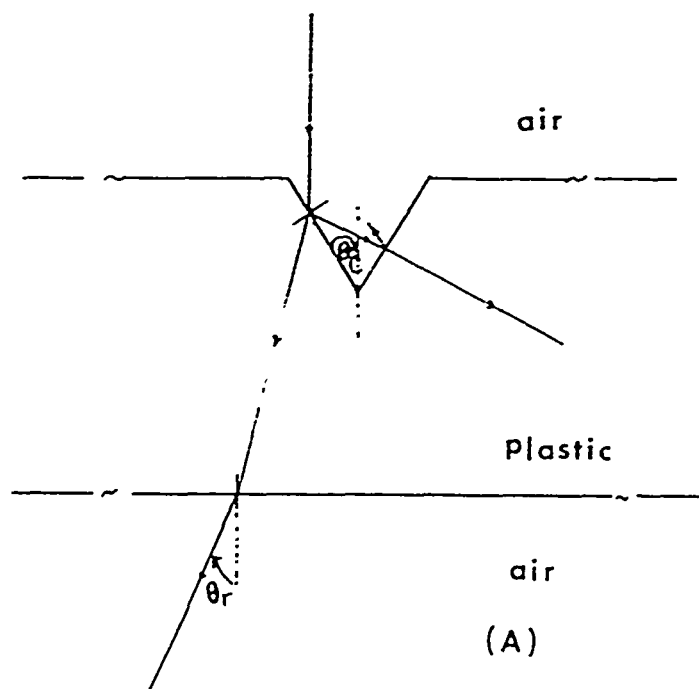
Figure 4.34. Ratio of the scattered intensities at 30° and 150° , at tip-on incidence, plotted against fluences, for various sets of samples: A1, B18 and C9 (circle), y-axis/100, x-axis × 2), D15, E7, and K18 (triangle), and L6, M15, and N17 (solid circle, y-axis/10).
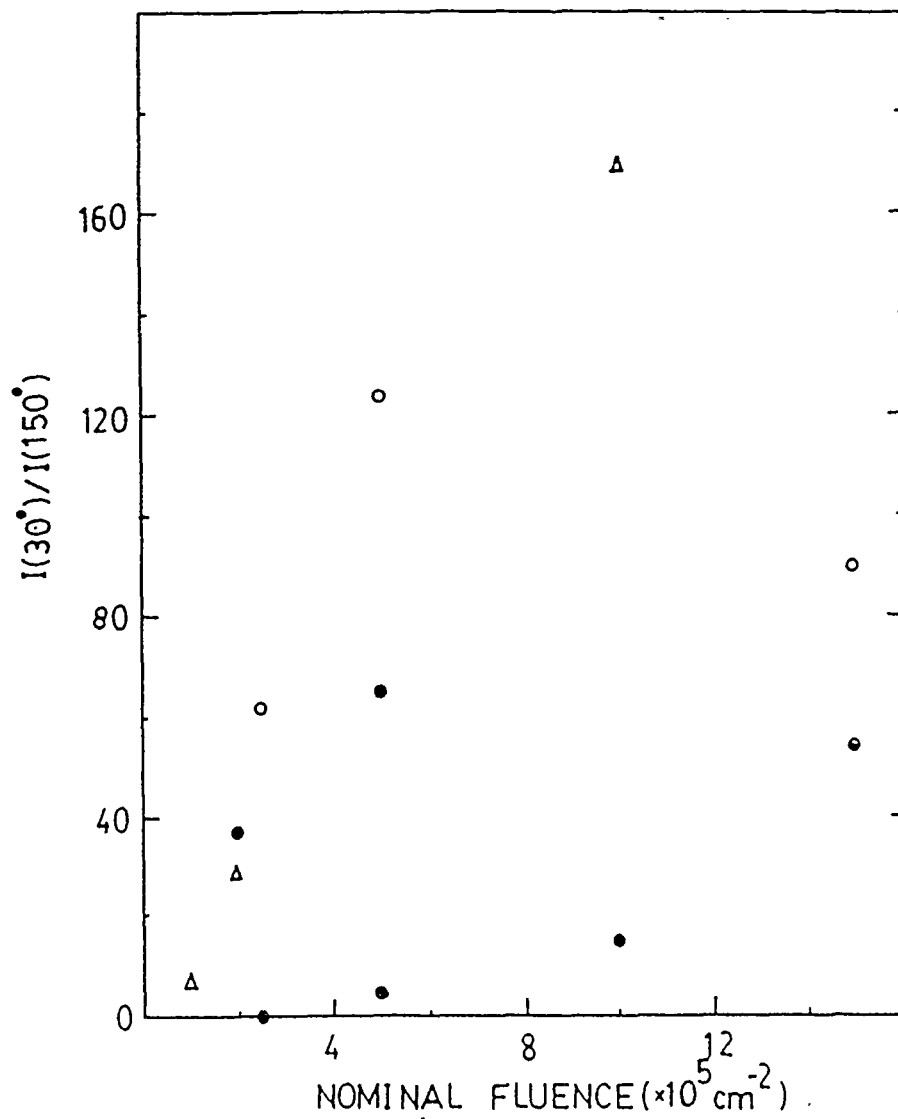
Figure 4.35. Angular scattering pattern (H_h) from conical pits in sample K18, at tip-on incidence (solid curve) versus the corresponding result based on MIE theory for the equal spheres (dotted curve).
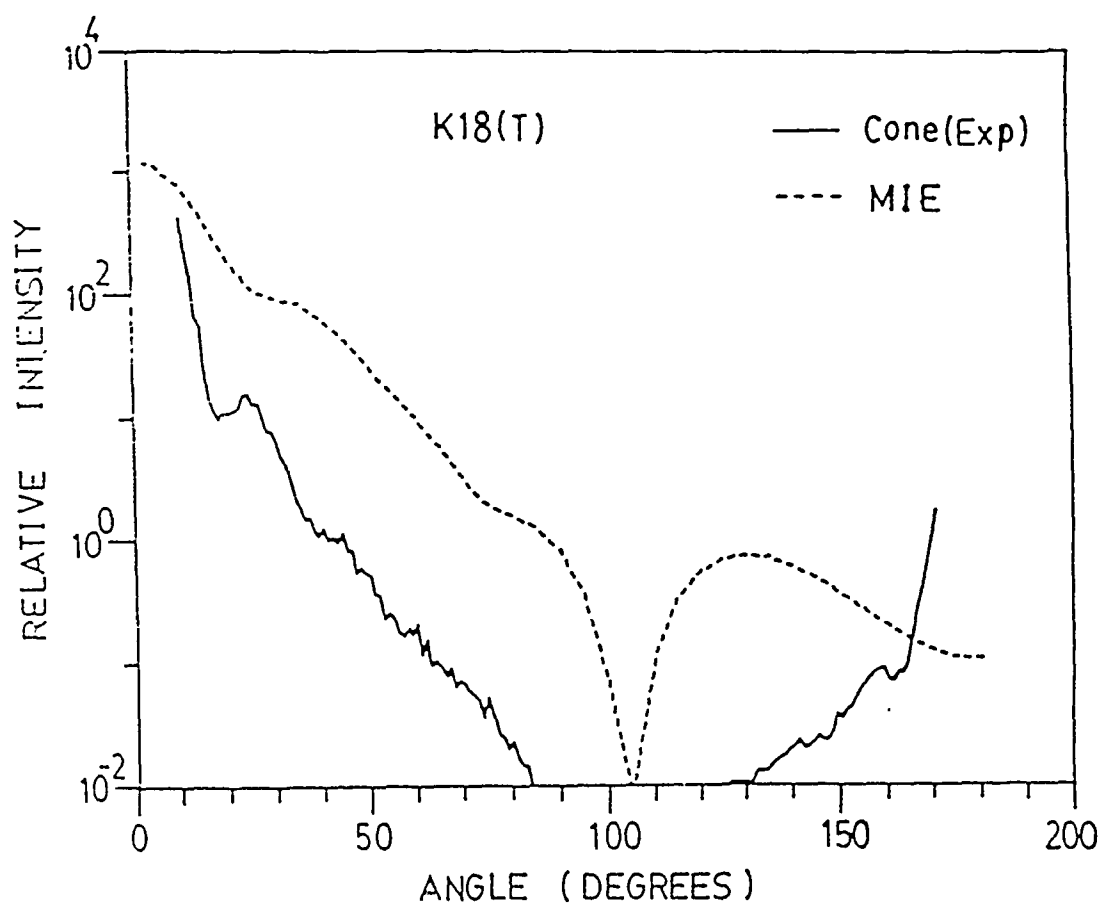
Figure 4.36. Angular scattering pattern (V_v) from conical pits in sample K3, at tip-on incidence (solid curve) versus the corresponding result based on MIE theory for the equal spheres (dotted curve).
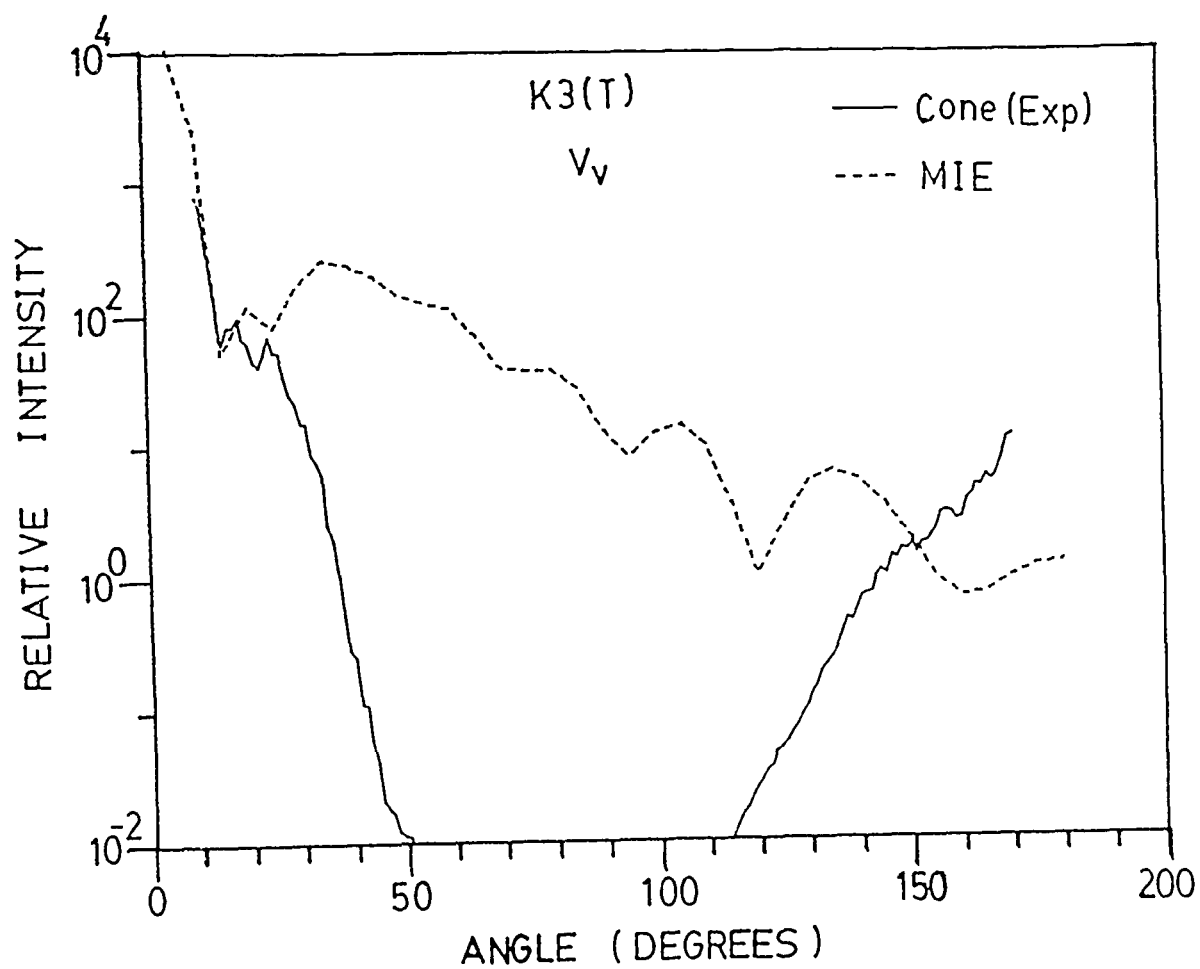
Figure 4.37. Angular distribution of scattered intensity from micropores in filter foil B3 (solid line) and from 'blank' foil F40 (dotted line), at base-on incidence, for horizontally polarized incident light.

[The micropores are etched tracks of 16.3 MeV/amu Fe-56 incident normally on the plastic foil surface with fluence of $10^3/cm^2$].

Below is an electronmicrograph of a replica of the sample.
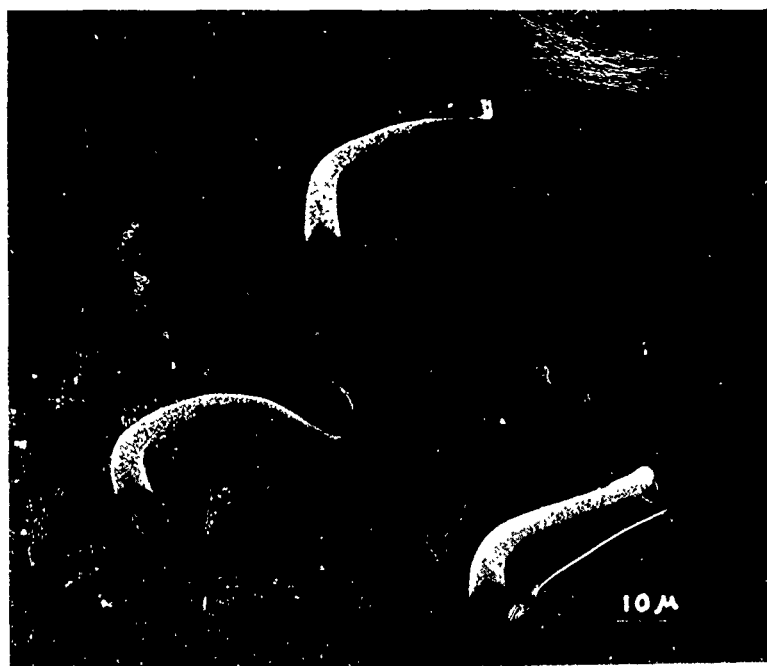
B 3
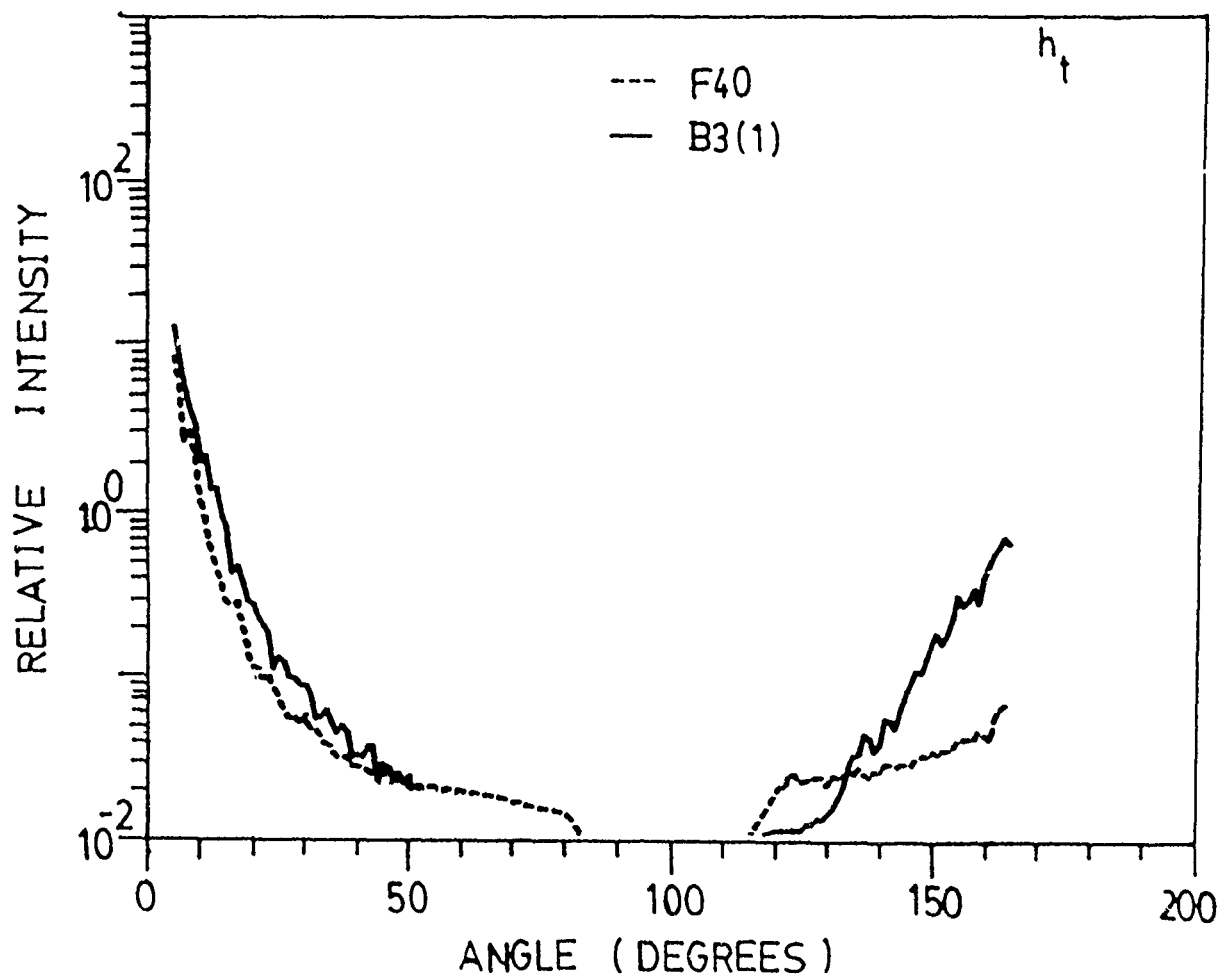
Figure 4.38. Angular distribution of scattered intensity from micropores in filter foil B4 surface 1 (solid line) and from surface 2 (dotted line), at base-on incidence, for horizontally polarized incident light.

[The micropores are etched tracks of 16.3 MeV/amu Fe-56 incident normally on the plastic foil surface with fluence of $10^4/cm^2$].

Below is an electronmicrograph of a replica of the sample.
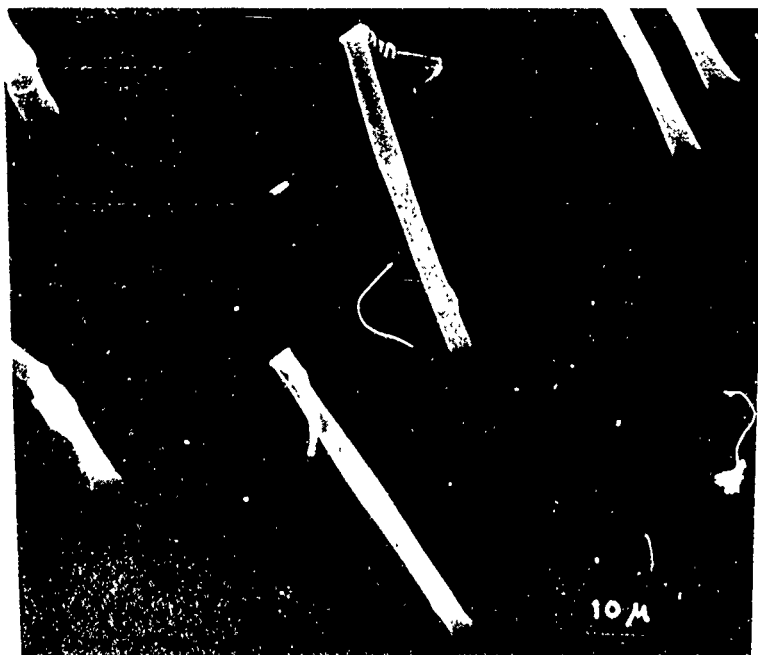
B 4
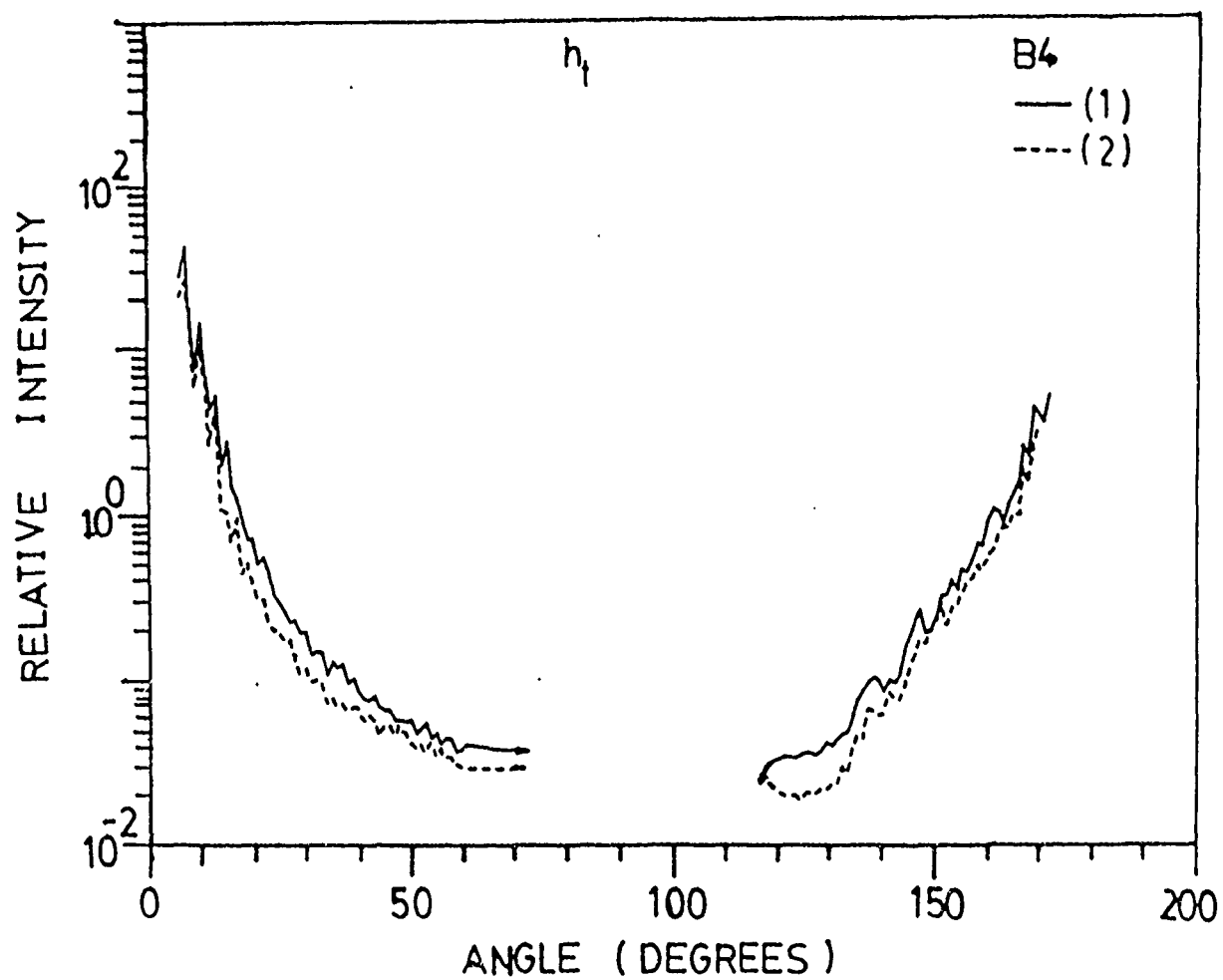
Figure 4.39. Angular distribution of scattered intensity from microspheres in filter foil B5 surface 1 (solid line) and from surface 2 (dotted line), at base-on incidence, for horizontally polarized incident light.

[The micropores are etched tracks of 16.3 MeV/amu Fe-56 incident normally on the plastic foil surface with fluence of $10^5/cm^2$].

Below is an electronmicrograph of a replica of the sample.
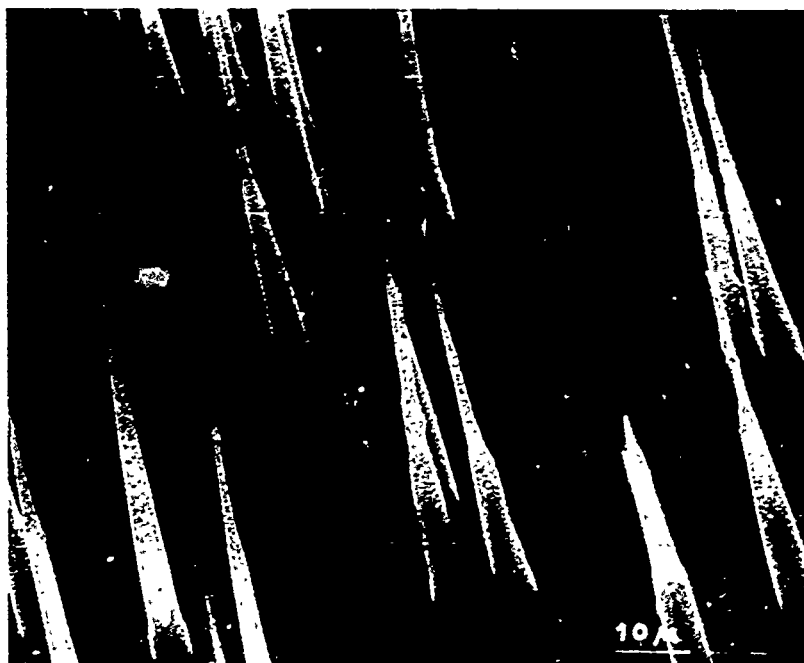
B 5
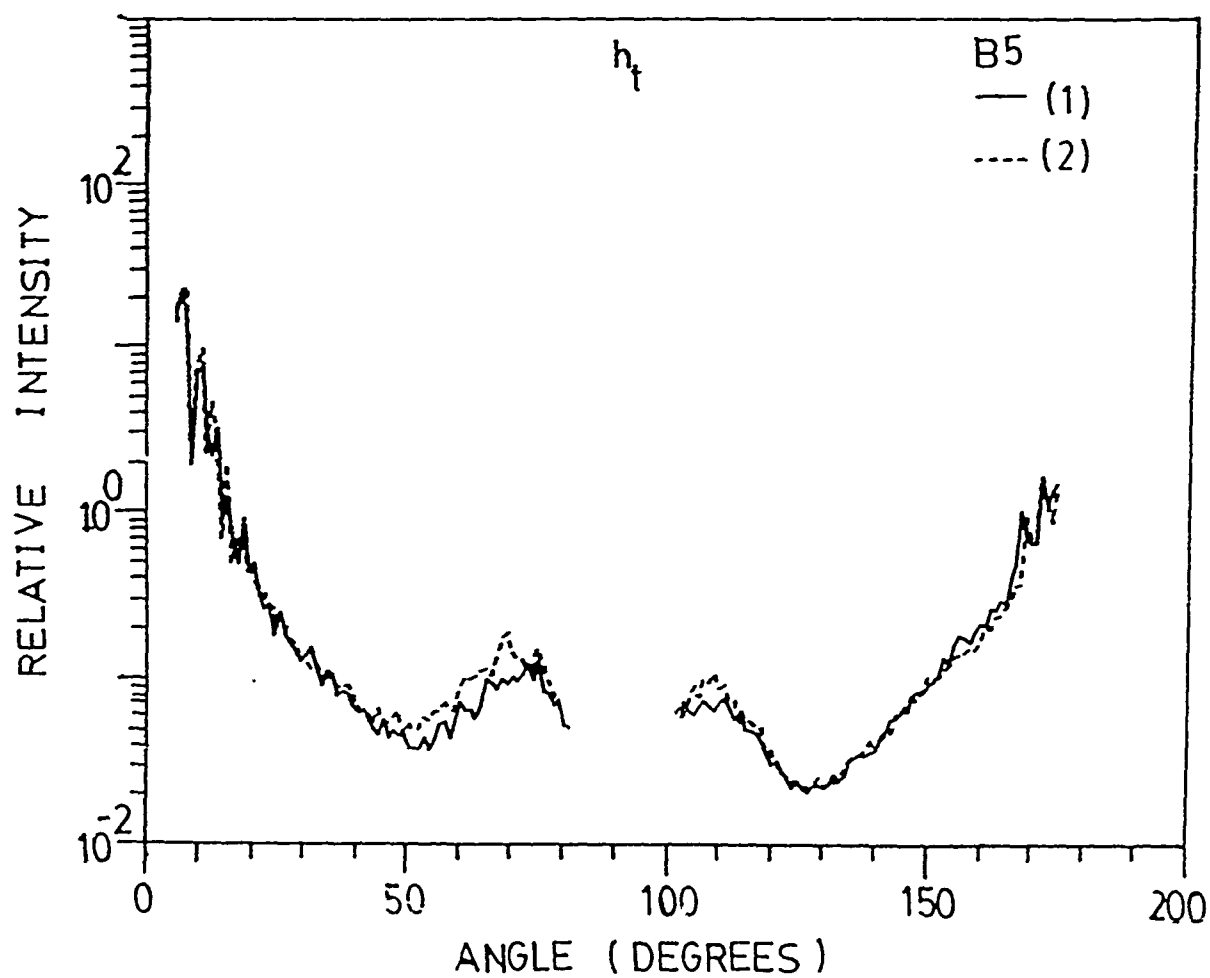
Figure 4.40. Angular distribution of scattered intensity from micropores in filter foil B6 for horizontally polarized incident light.

[The micropores are etched tracks of 16.3 MeV/amu Fe-56 incident normally on the plastic foil surface with fluence of $10^6/cm^2$].

Below is an electronmicrograph of a replica of the sample.
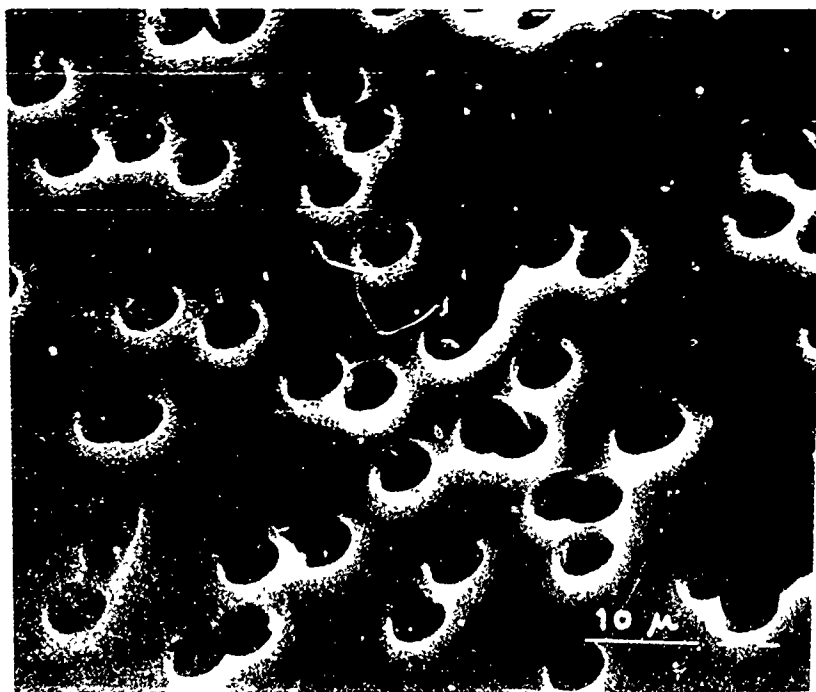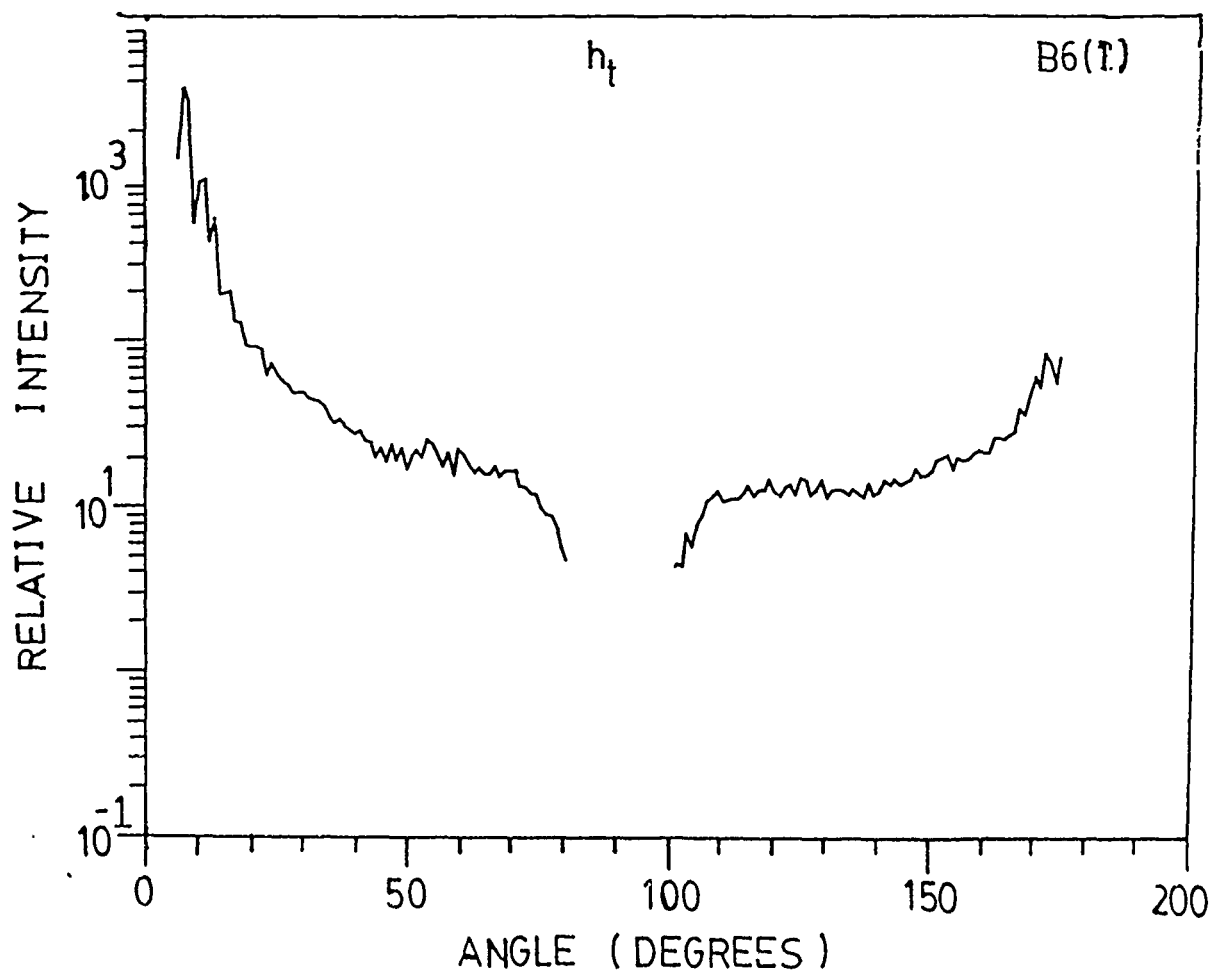
Figure 4.41. Relative scattered intensity at selected angles versus nominal fluences, for micropores in samples B4, B5, and B6 (shown in Fig. 3.38 - 3.40).

At 25°: solid circle

At 30°: circle

At 35°: triangle.
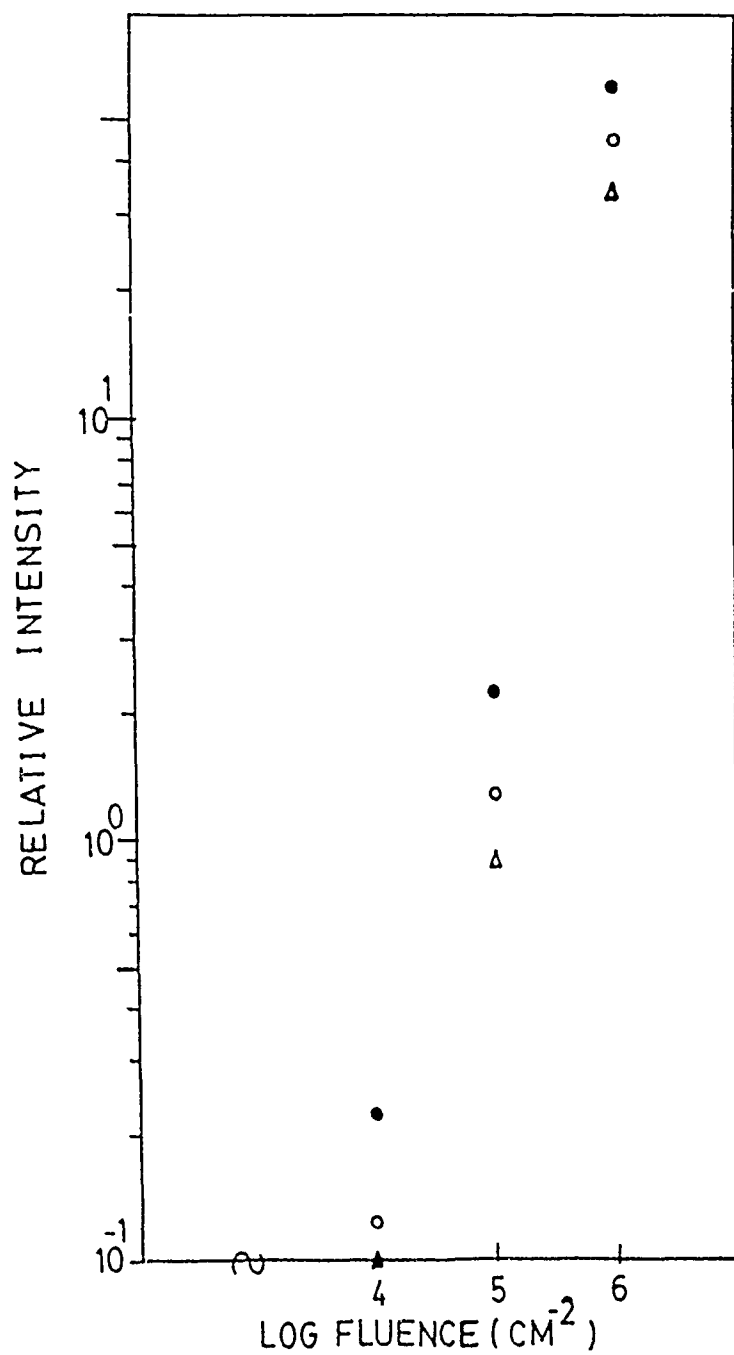
Figure 4.42. Angular distribution of scattered intensity from micropores in sample B5, for horizontally polarized incident light, showing parallel (H_h), cross (H_v) and total (H_t : without polarizer) polarization components of scattered light.
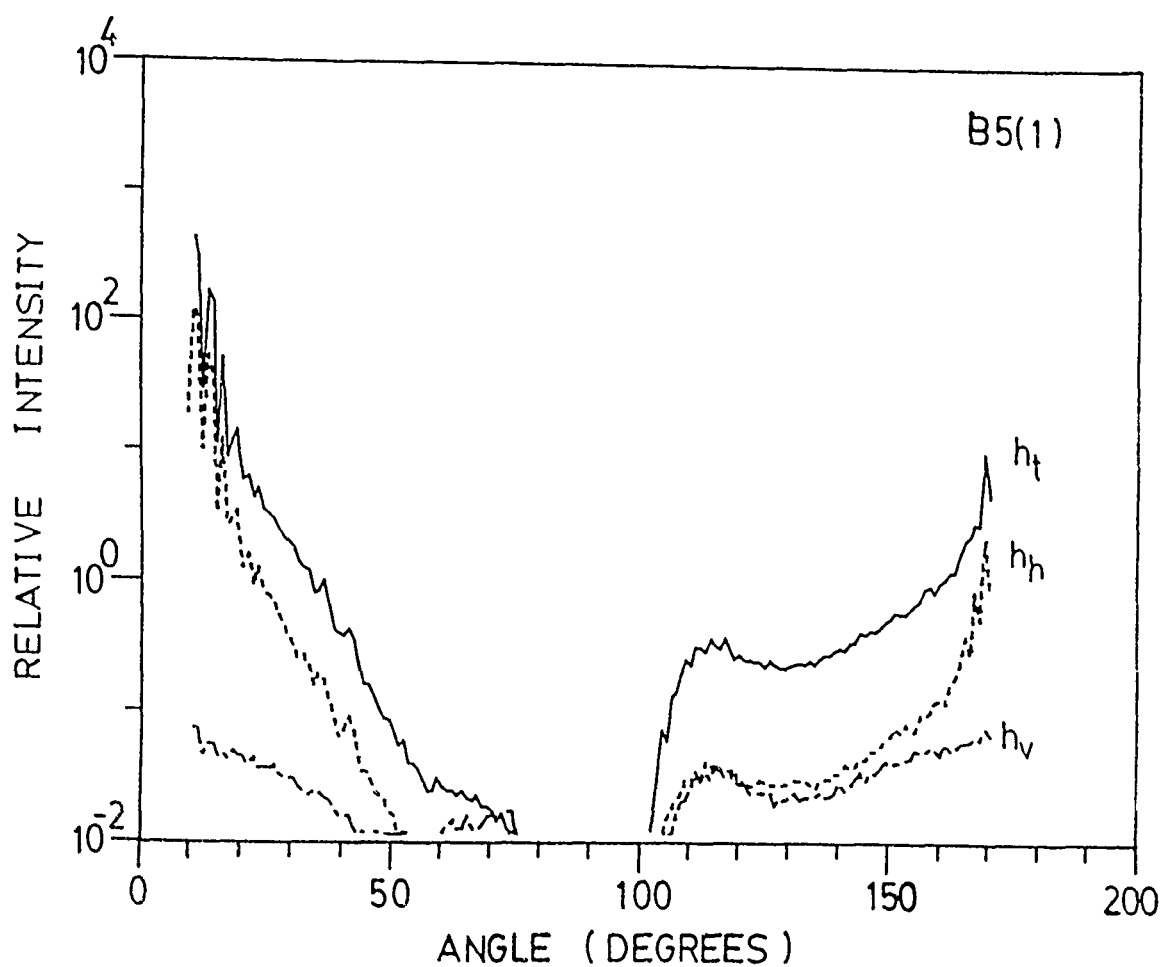
Figure 4.43. Same as Fig. 4.42 except for vertically polarized incident light.
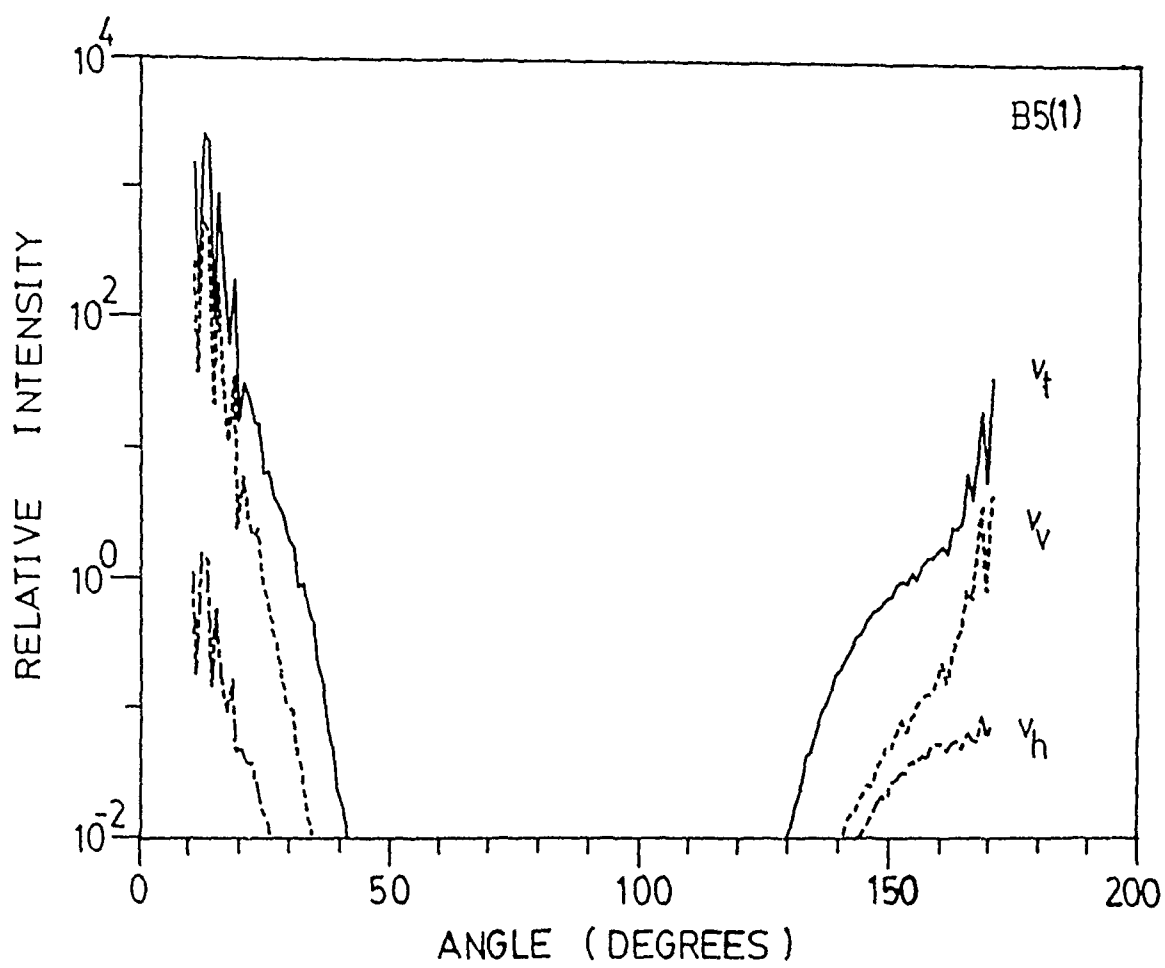
Figure 4.44. Angular distribution of scattered intensity from micropits in sample K18 aligned 45° (to the incident beam), for horizontally polarized incident light, at tip-on stream incidence, showing (H_t) (without polarizer) component of the scattered light.
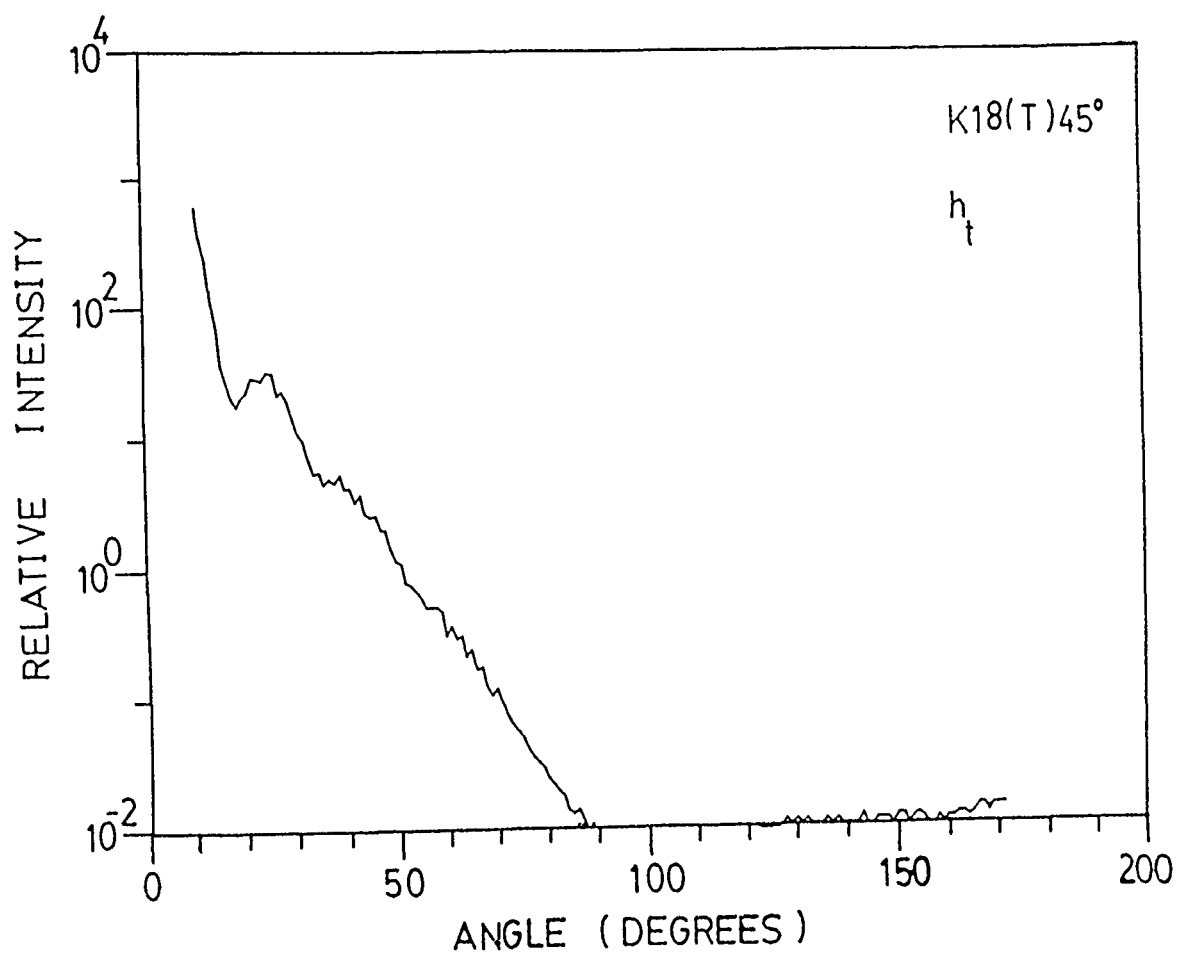
Figure 4.45   Same as Fig. 4.44 except at base-on stream incidence.
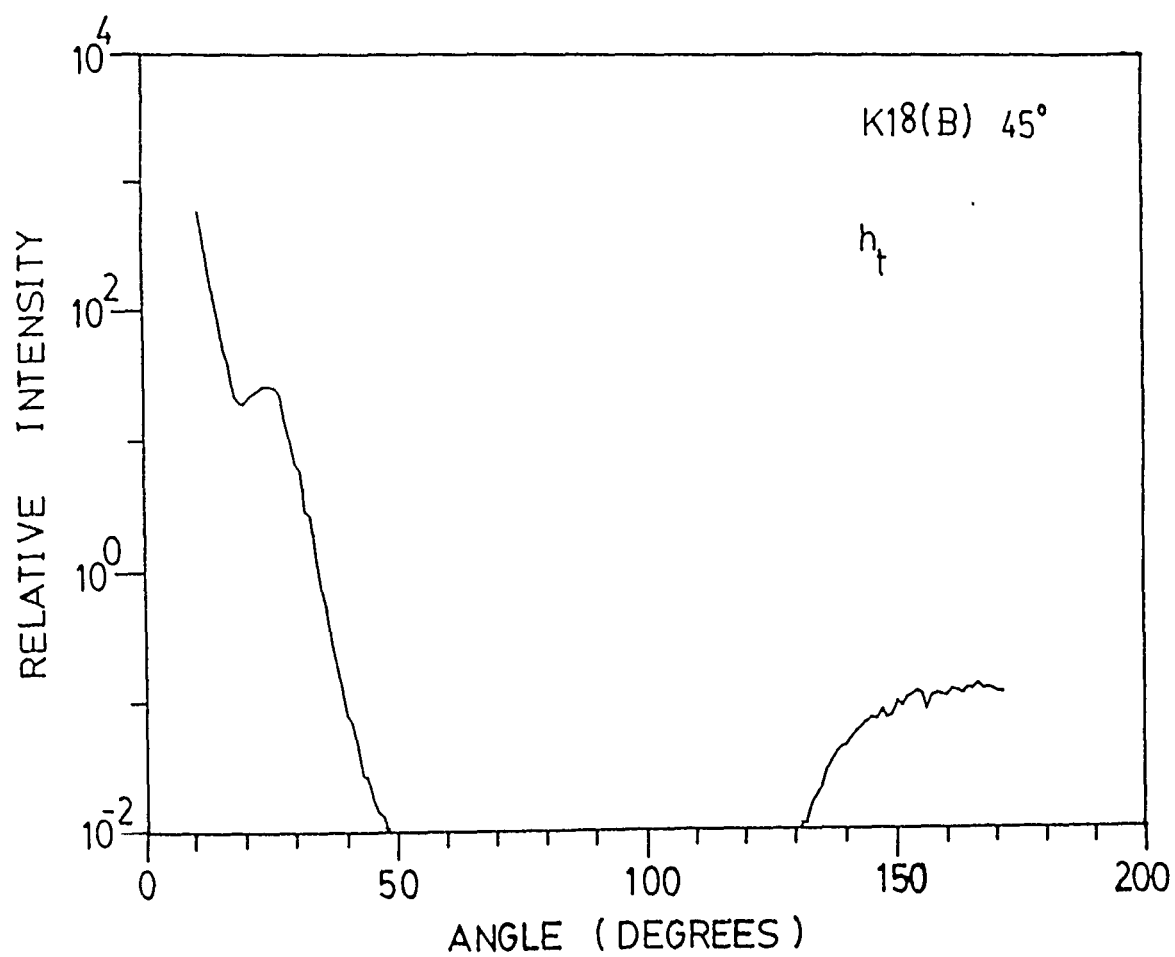
Figure 4.46. Angular distribution of scattered intensity from micropits in sample K3 aligned 45° (to the incident beam), for vertically polarized incident light, at tip-on stream incidence, showing parallel (V_v), cross (V_v) and total (V_t: without polarizer) polarization components of the scattered light.
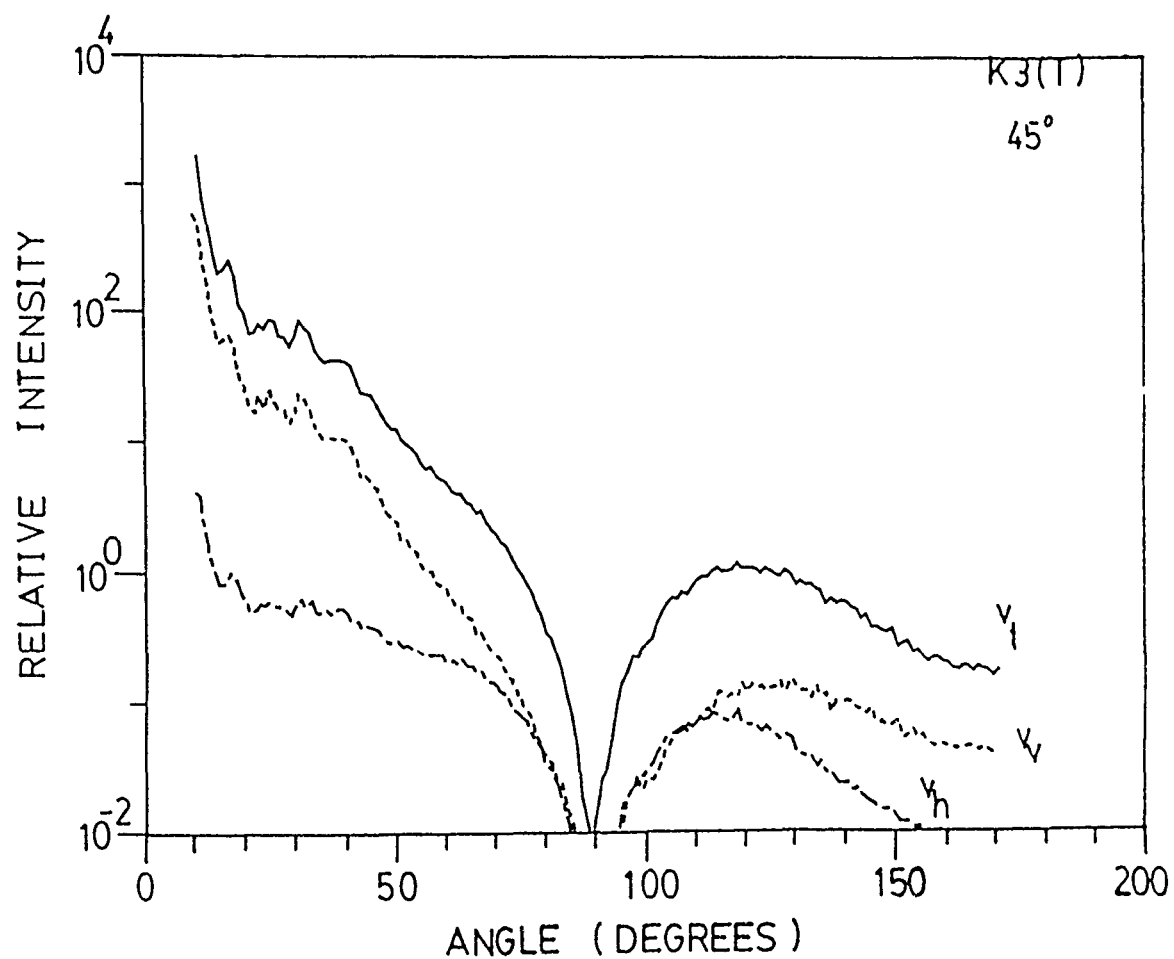
Figure 4.47 Same as Fig. 4.46 except the cone bases are up stream.
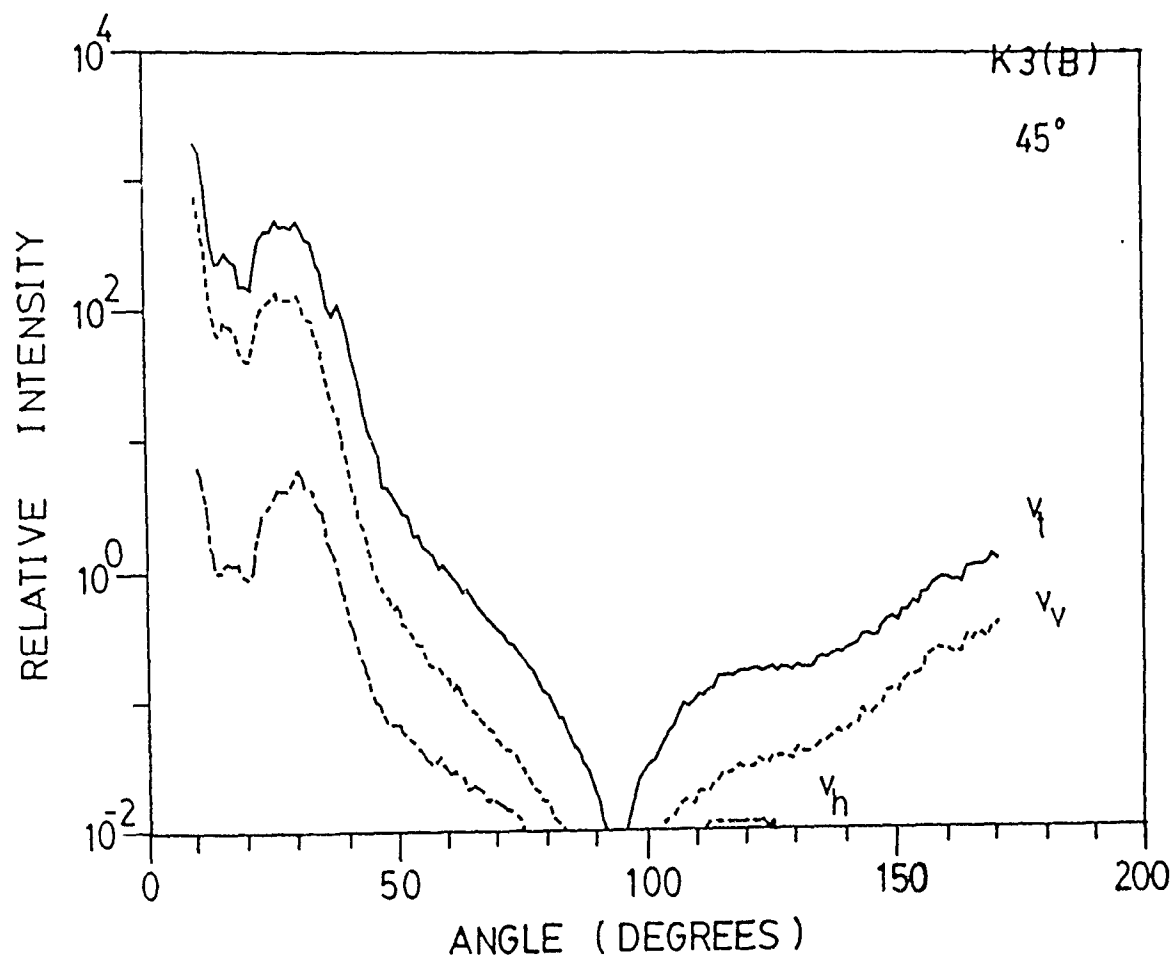
Figure 4.48. Angular distribution of scattered intensity from micropores in sample B3 aligned 45° (dotted line) and 90° (or base-on, solid line), to the incident light, for horizontally polarized incident light, showing H_t (without polarizer) polarization component of the scattered light.
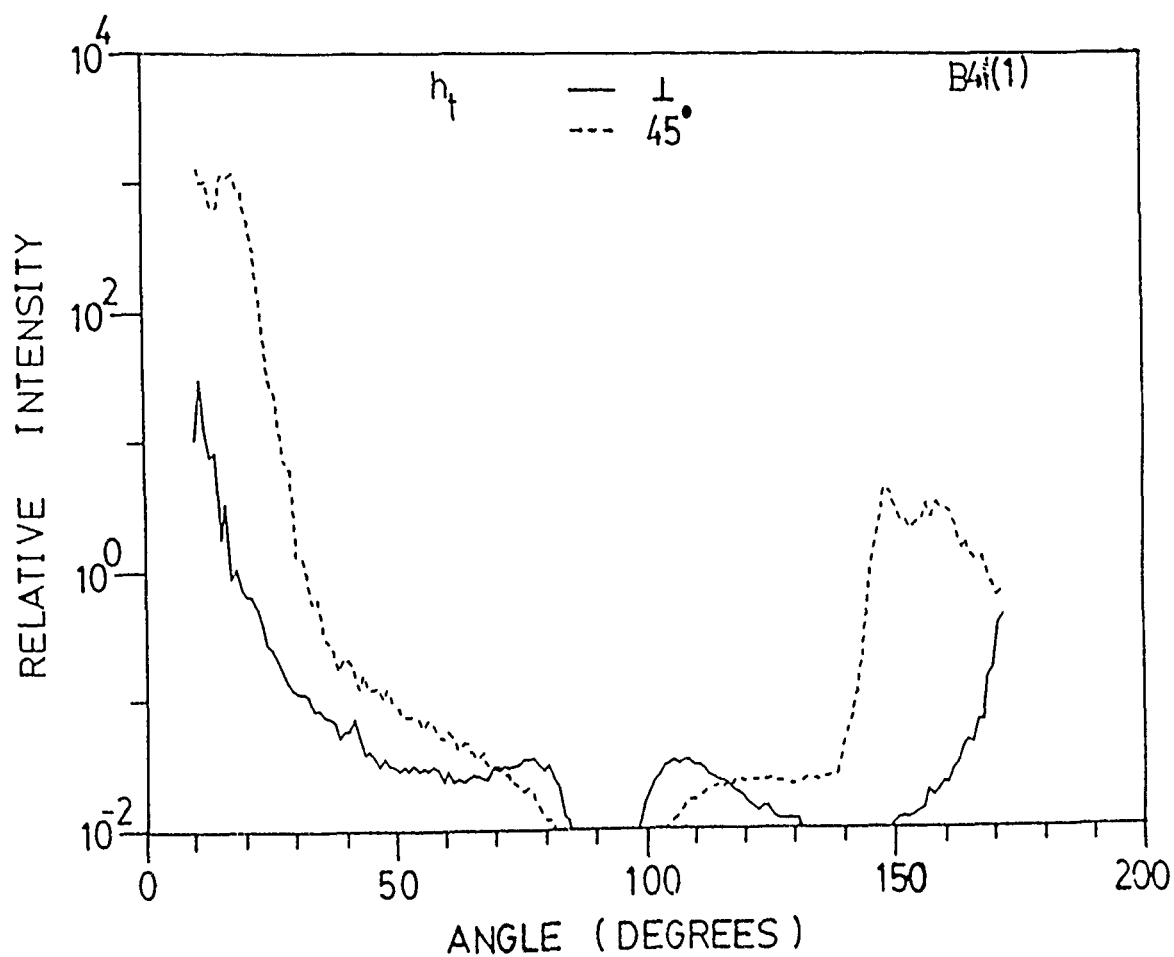
Figure 4.49. Angular distribution of scattered intensity from micropores in sample B6 aligned 45° (dotted line) and 90° (solid line), to the incident light, for horizontally polarized incident light, showing H_t (without polarizer) polarization component of the scattered light.
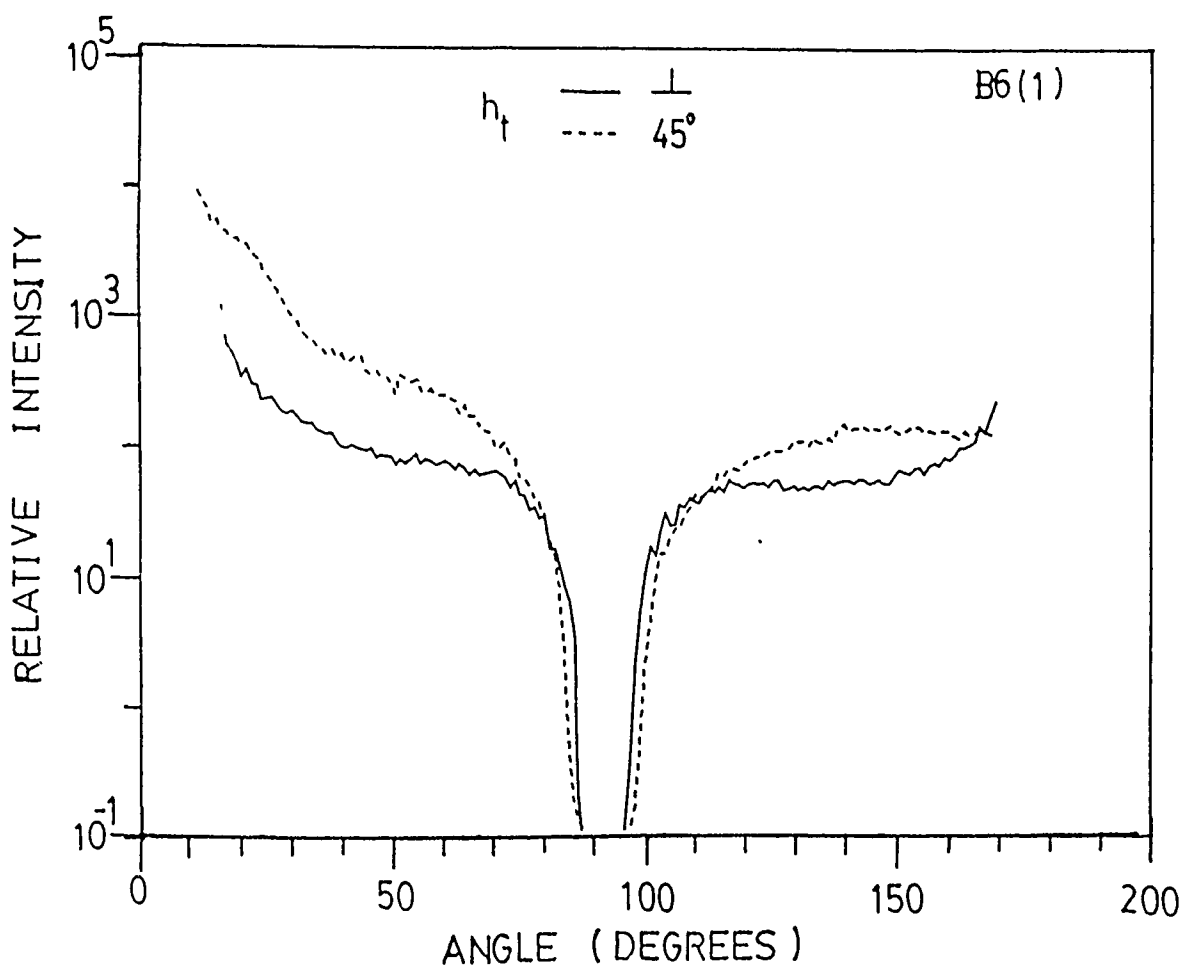
Figure 4.50. Angular distribution of scattered intensity from micropores in sample B5 aligned 45° (to the incident beam), for horizontally polarized incident light, showing parallel (H_h), cross (H_v) and total (H_t: without polarizer) polarization components of the scattered light.
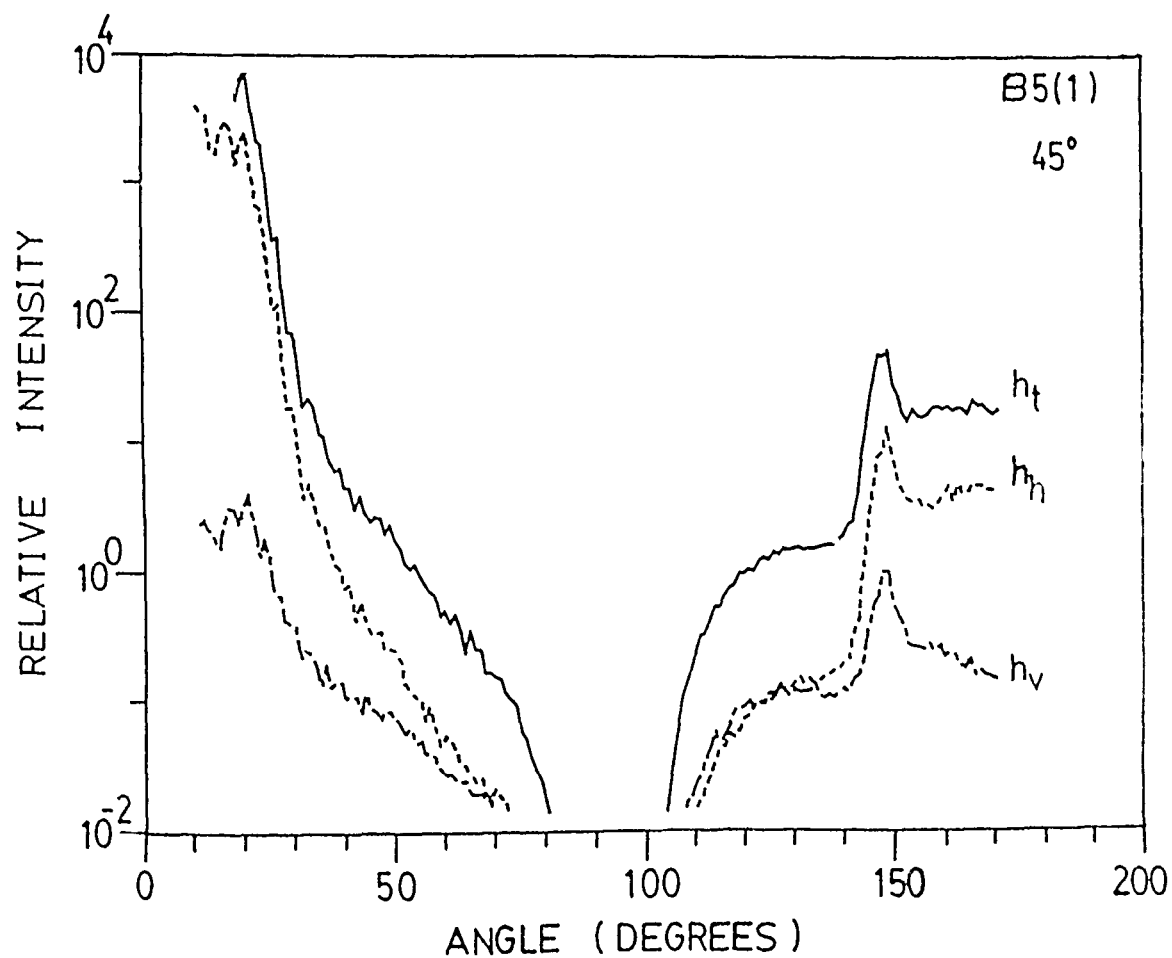
Figure 4.51   Same as Fig. 4.50 except for vertically polarized incident light.
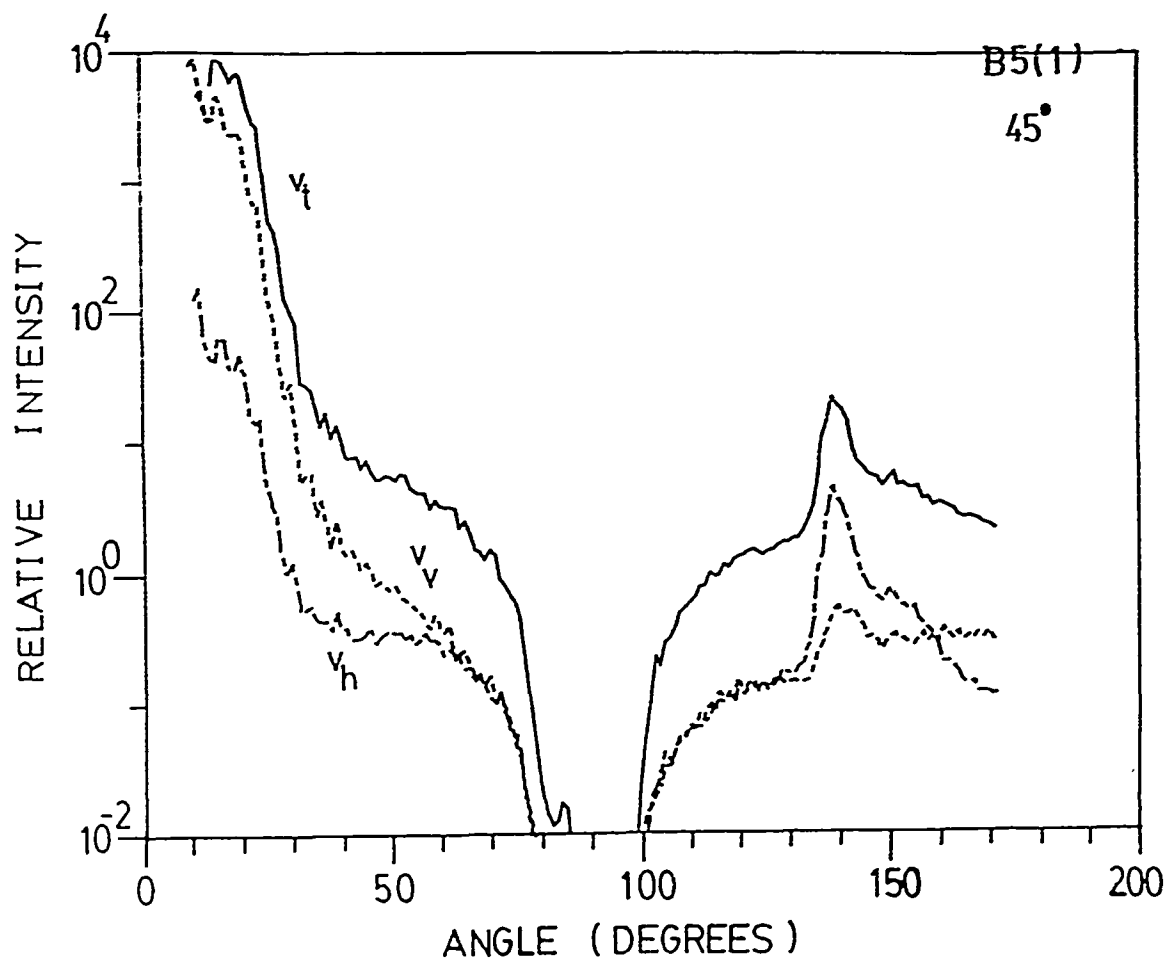
Figure 4.52. Angular distribution of scattered intensity from micropores in filter foil B5 before (solid line) and after (dashed line) water treatment, for horizontally polarized incident light.
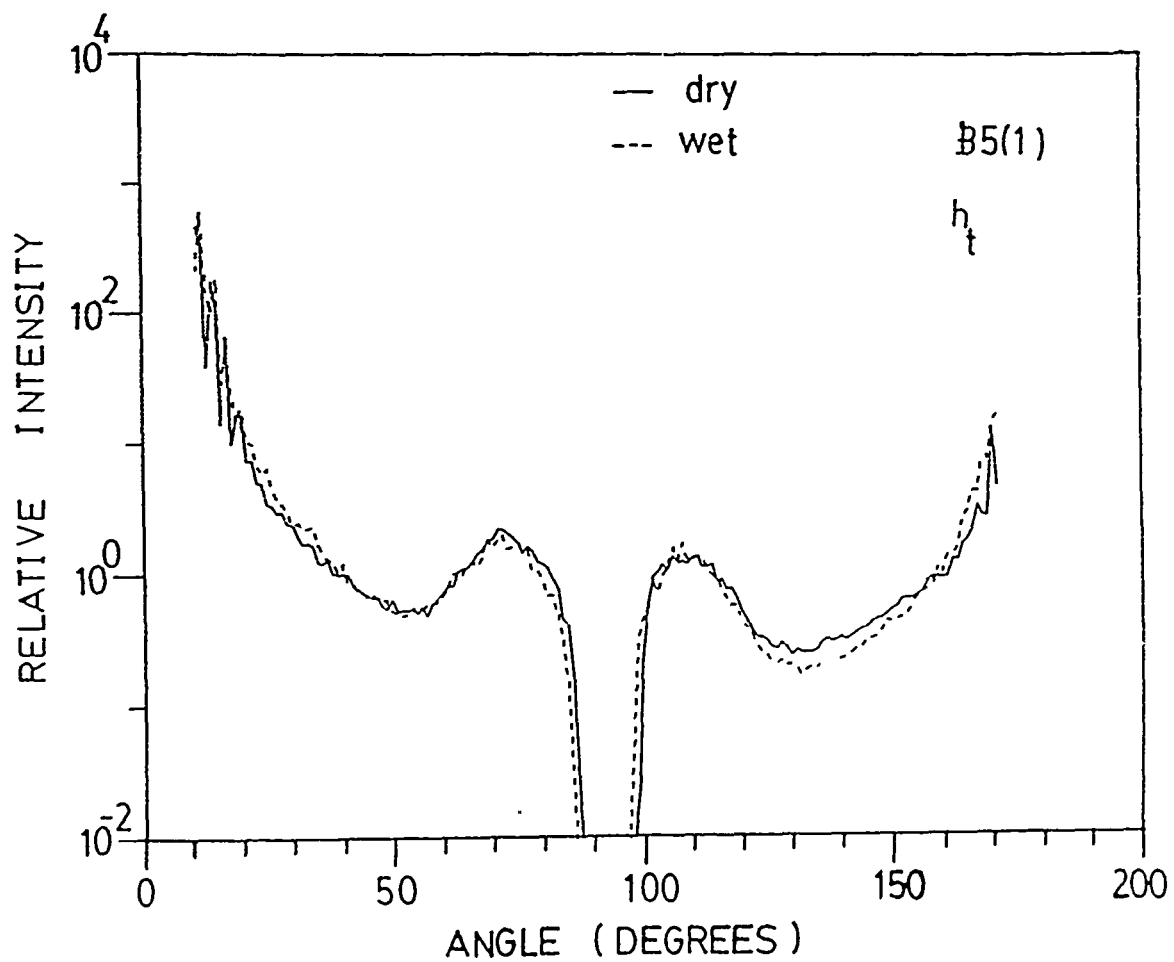
Figure 4.53. Angular distribution of scattered intensity from micropores in filter foil S1 before (solid line) and after (dashed line) dye treatment.
An electronmicrograph of this sample is shown accompanying Fig. 4.15.
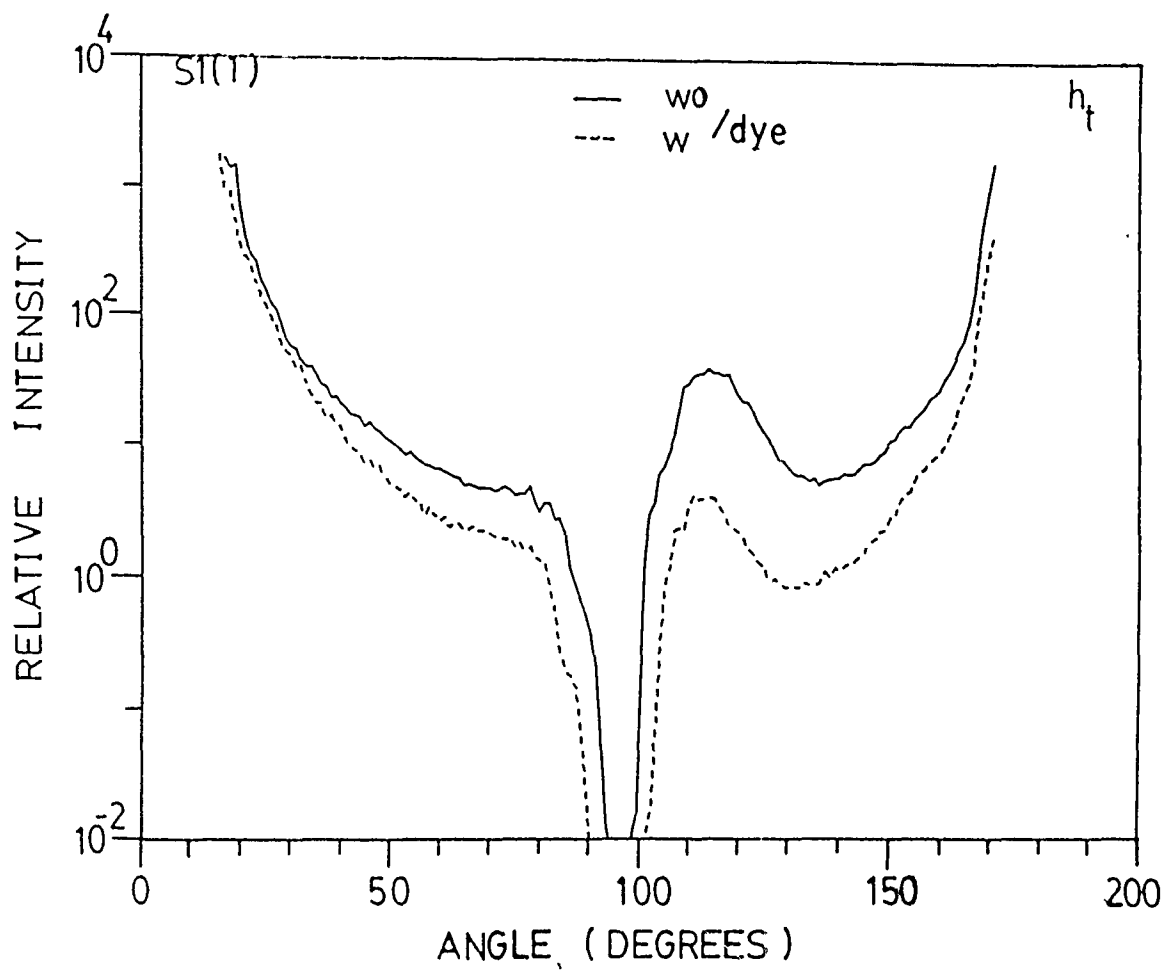
Figure 4.54. Angular distribution of scattered intensity from micropores in filter foil S2 before (solid line) and after (dashed line) dye treatment.
An electronmicrograph of this sample is shown accompanying Fig. 4.17.
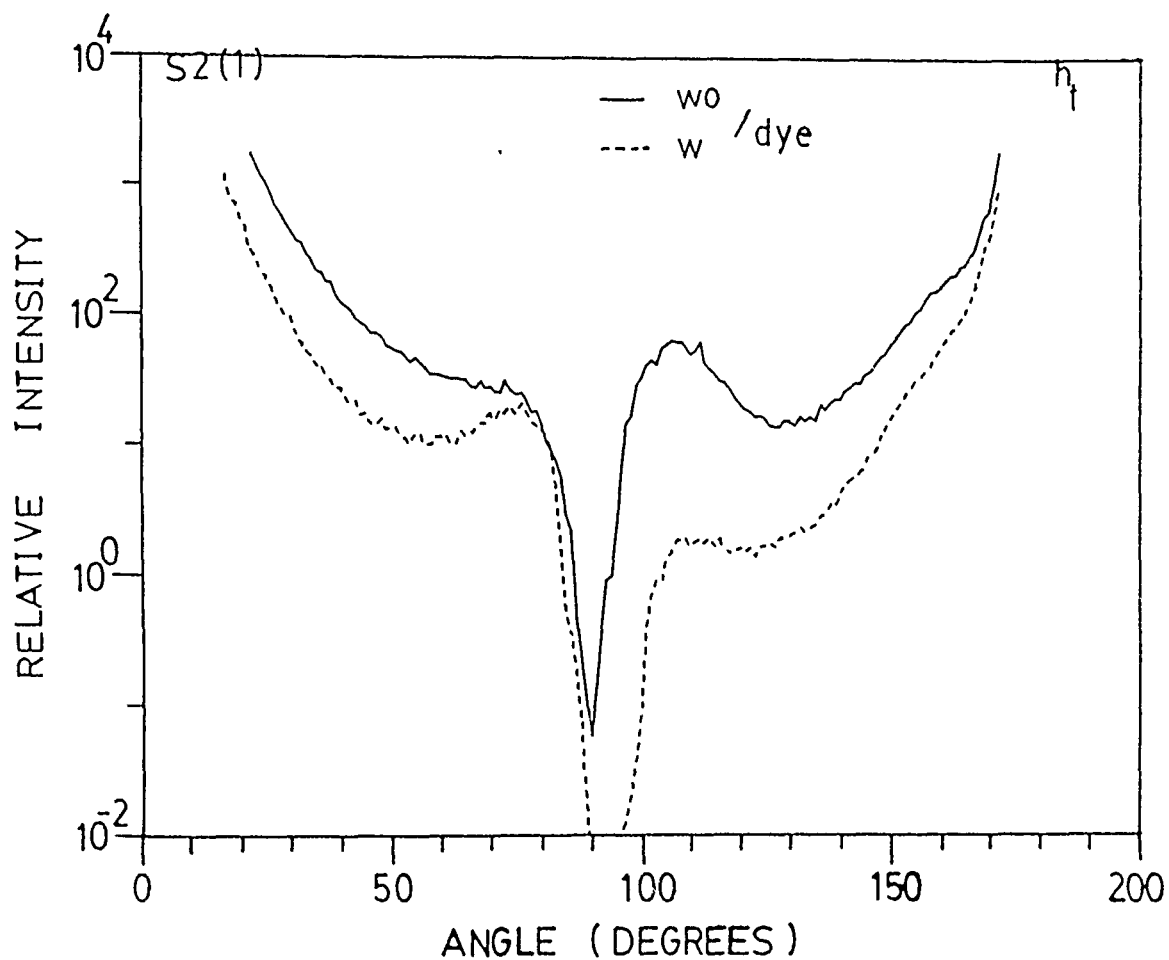
Figure 4.55. Angular distribution of scattered intensity from micropores in filter foil P4 (fluence 10^4 /cm^2) with a deposition of 2 μm glass spheres on surface 1, when surface 1 (square) and the opposite surface (triangle) were illuminated normally to incident laser beam, compared with the result obtained (surface 1, circle) when taken without spheres. Below is an electonmicrograph of that sample.

P4 W Spheres

Figure showing Relative Intensity vs Angle (Degree) for Cylindrical Pores, $1\times10^4/cm^2$, H-T.

Legend:
○ Side 1
□ Side 1, with $2\,\mu m$ glass spheres
▲ Side 2
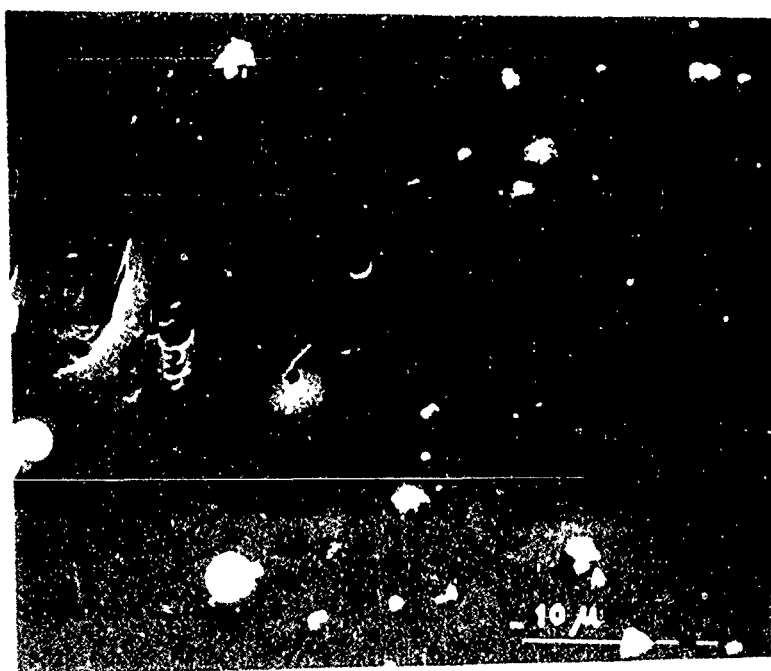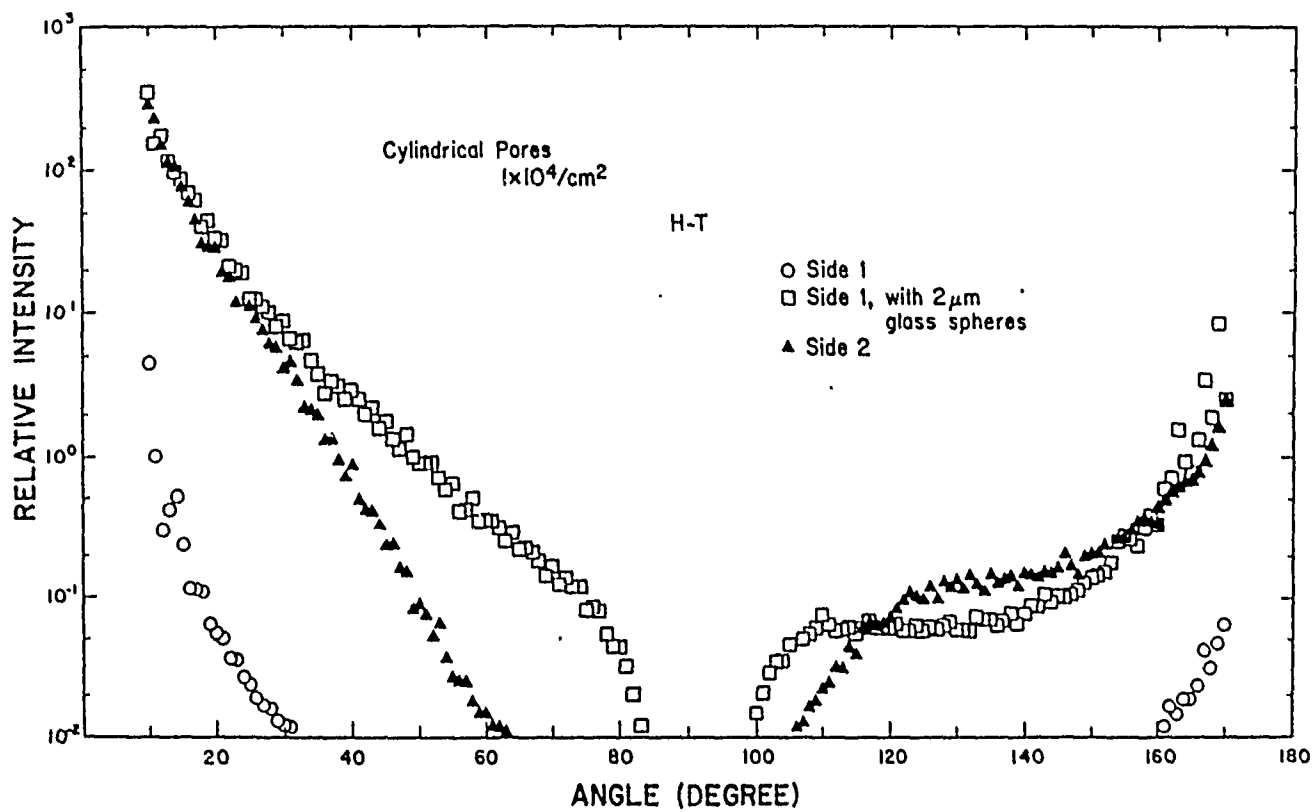
Figure 4.56. Angular distribution of scattered intensity from micropores in filter foil P6 (fluence 10^6 /cm^2) with a deposition of 2 μm glass spheres on surface 1, when surface 1 (square) and the opposite surface (triangle) were illuminated normally to incident laser beam, compared with the result obtained (surface 1, circle) when taken without spheres. Below is an electonmicrograph of that sample.

P6 W Spheres

Cylindrical Pores
1×10⁶/cm²

H-T

o Side 1
□ Side 1, with 2 μm glass spheres
▲ Side 2
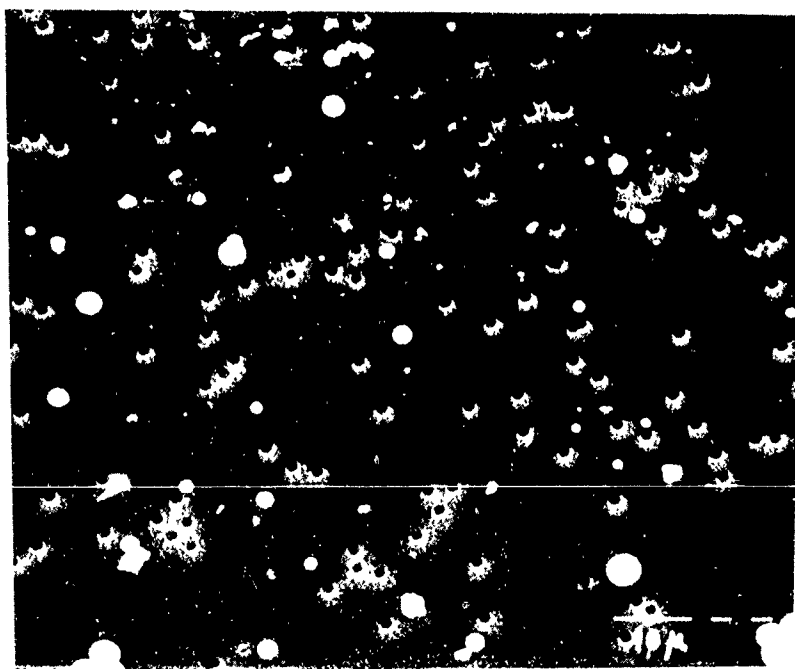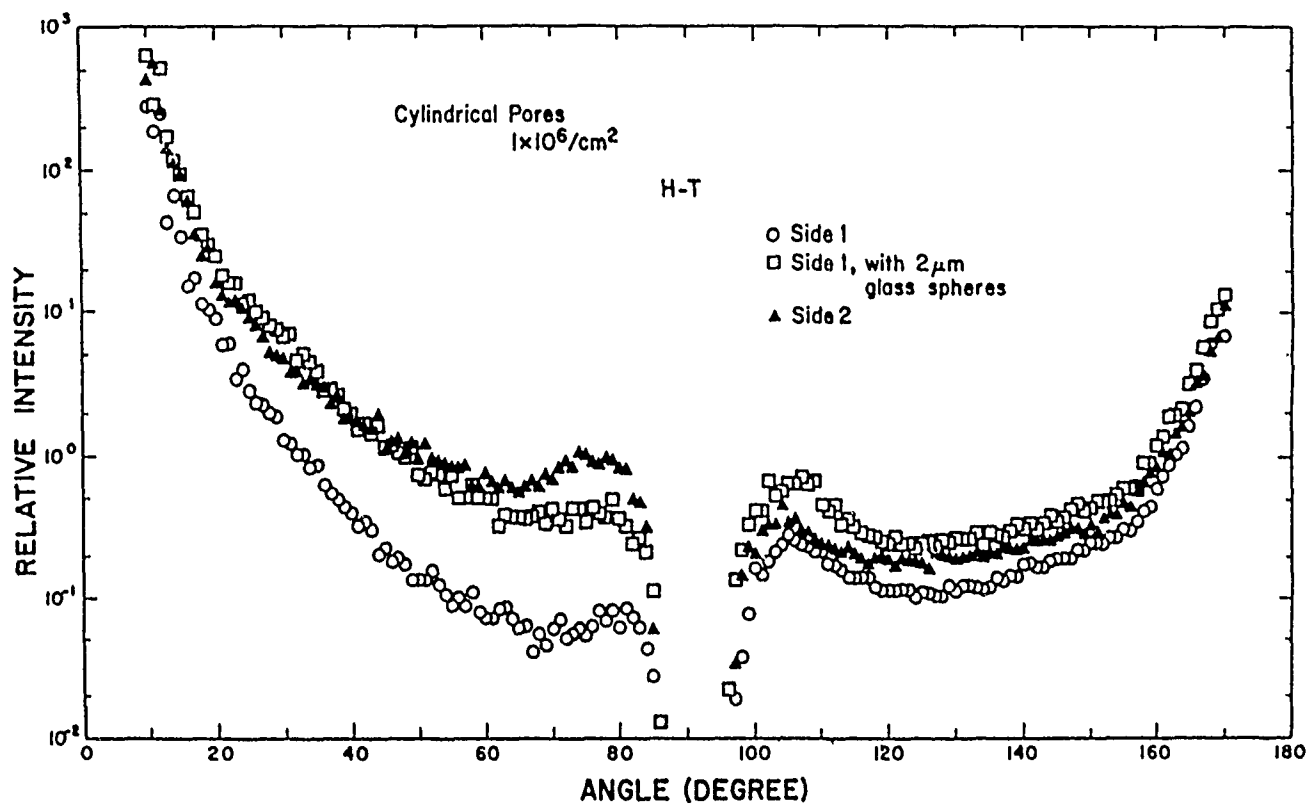
Figure 4.57. Angular distribution of scattered intensity from micropits in sample AAL3 with a deposition of 11.3 μm glass spheres on the surface with cone base, the surface with spheres was illuminated down stream normally to the incident beam (dashed line) compared with the result without sphere.
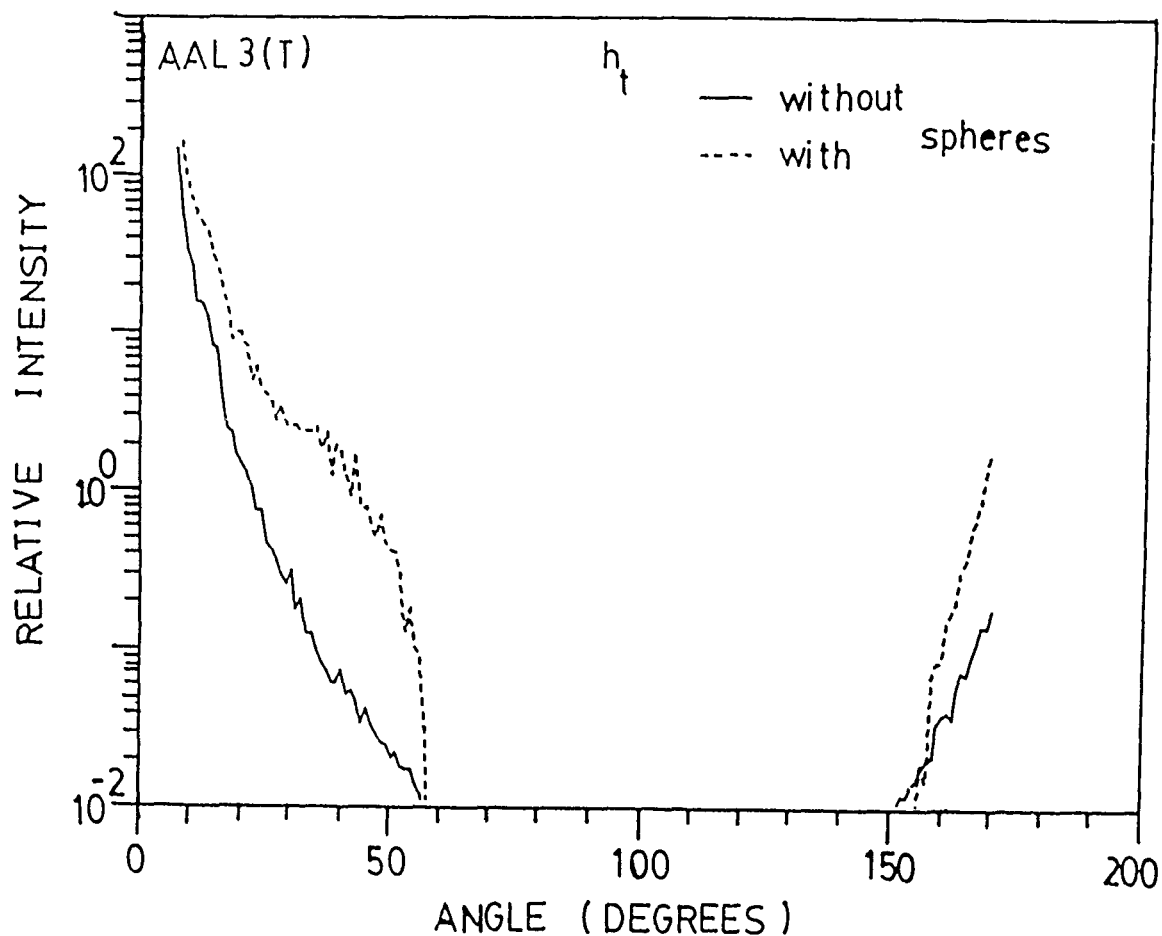
Figure 4.58 Same as Fig. 4.57 except the surface with spheres was illuminated up stream normally to laser beam.
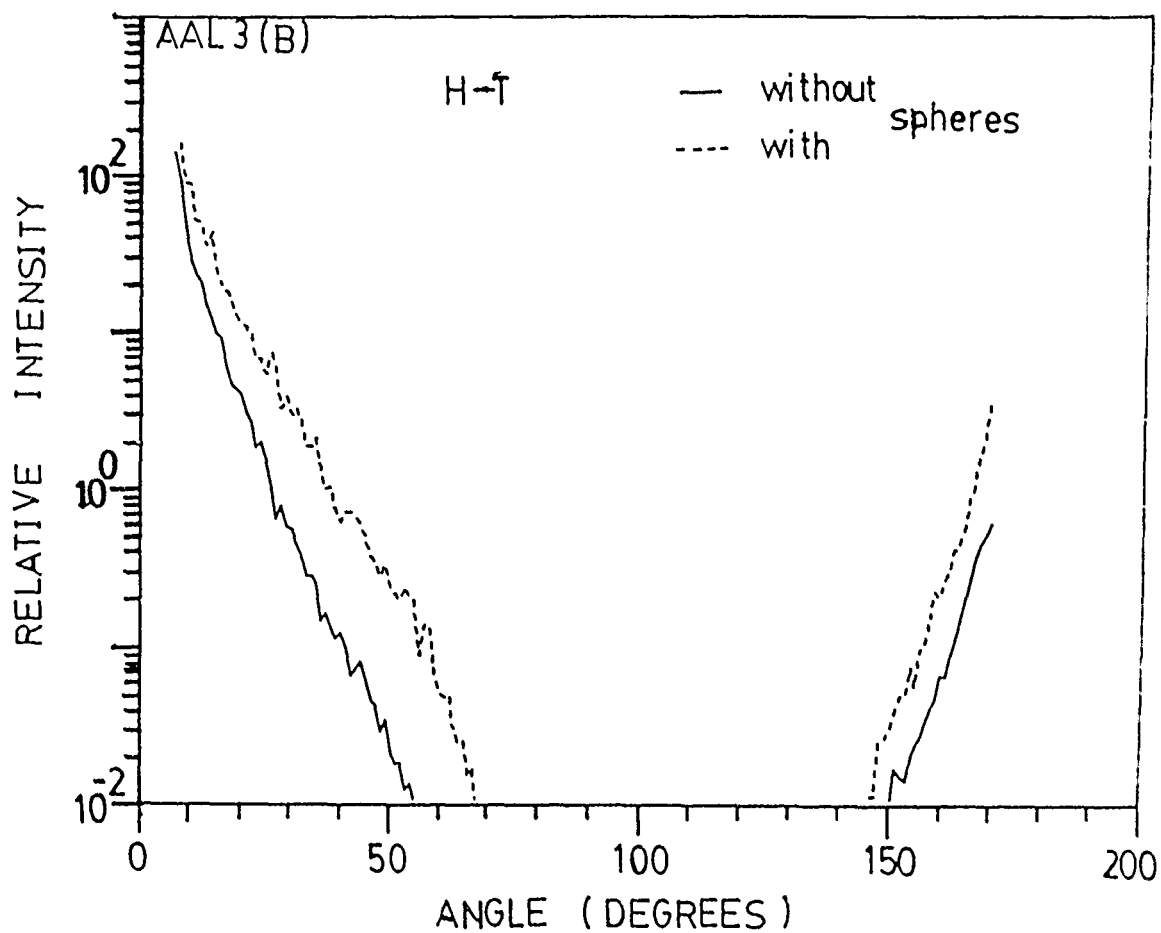
Figure 5.1. Angular distribution of fluorescent scattering from sample f9 treated Oxazine, at tip-on incidence.

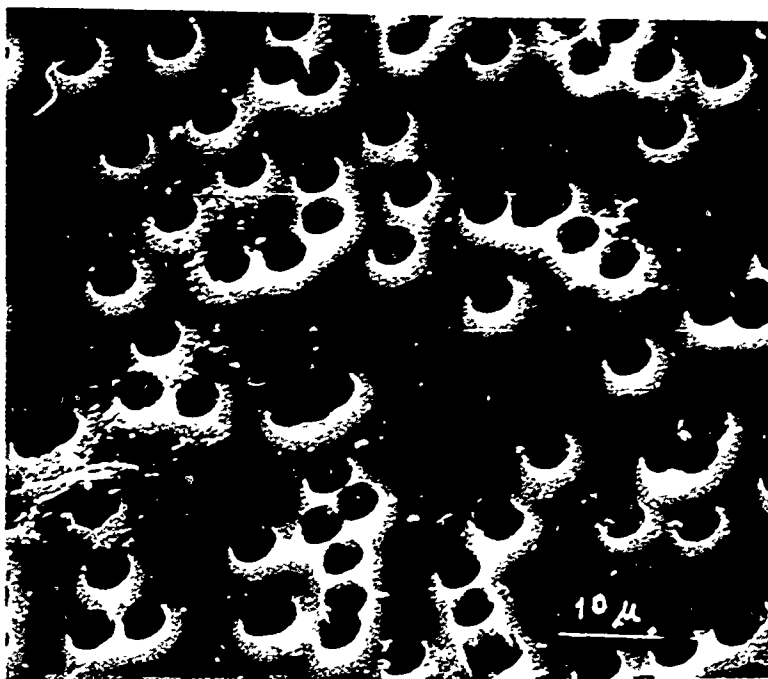Below is a typical electronmicrograph of a replica of the sample.

F 9

Figure 5.2. Angular distribution of fluorescent scattering from sample F9 treated Ox-
azine, for horizontally polarized incident light, at base-on incidence.
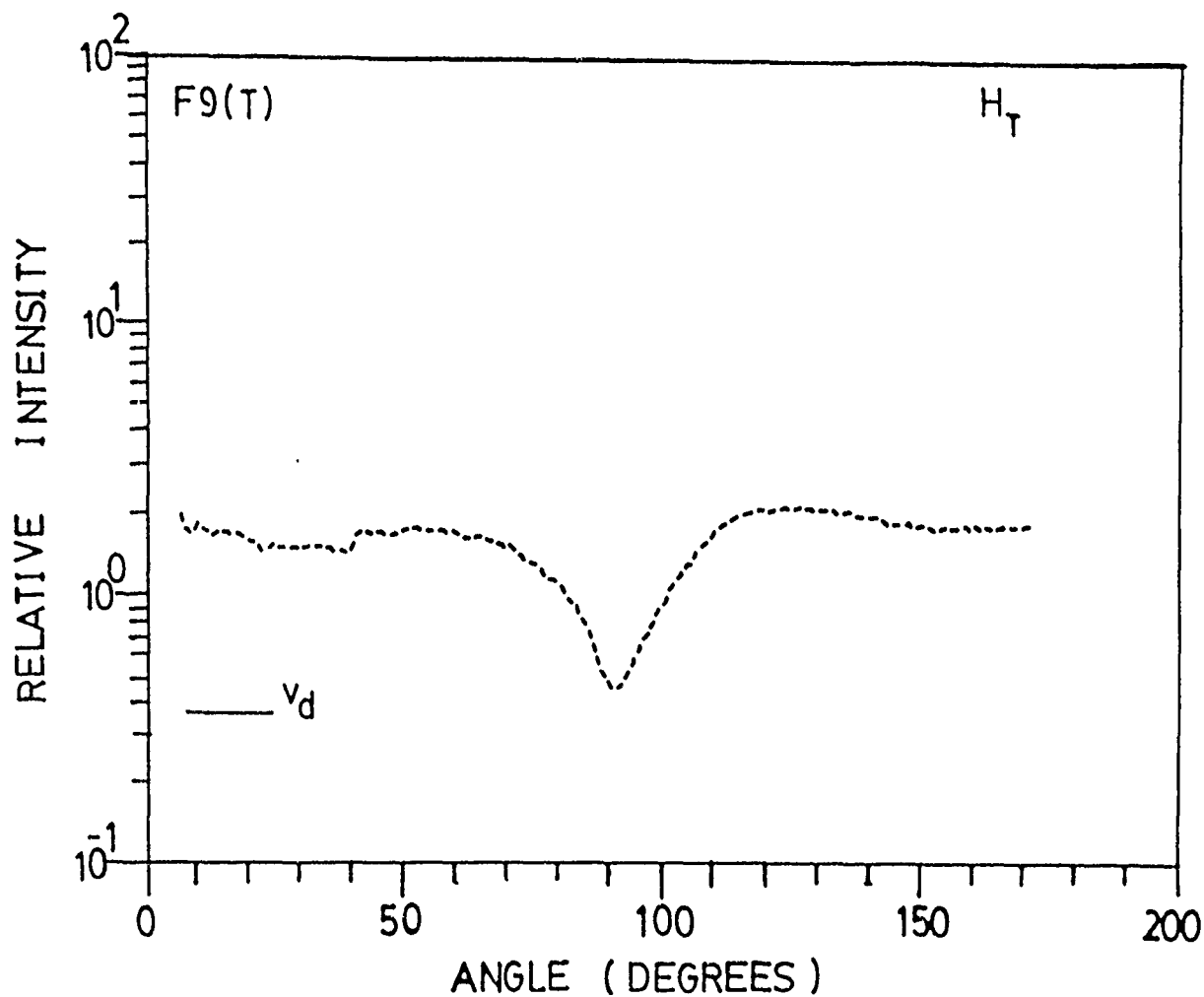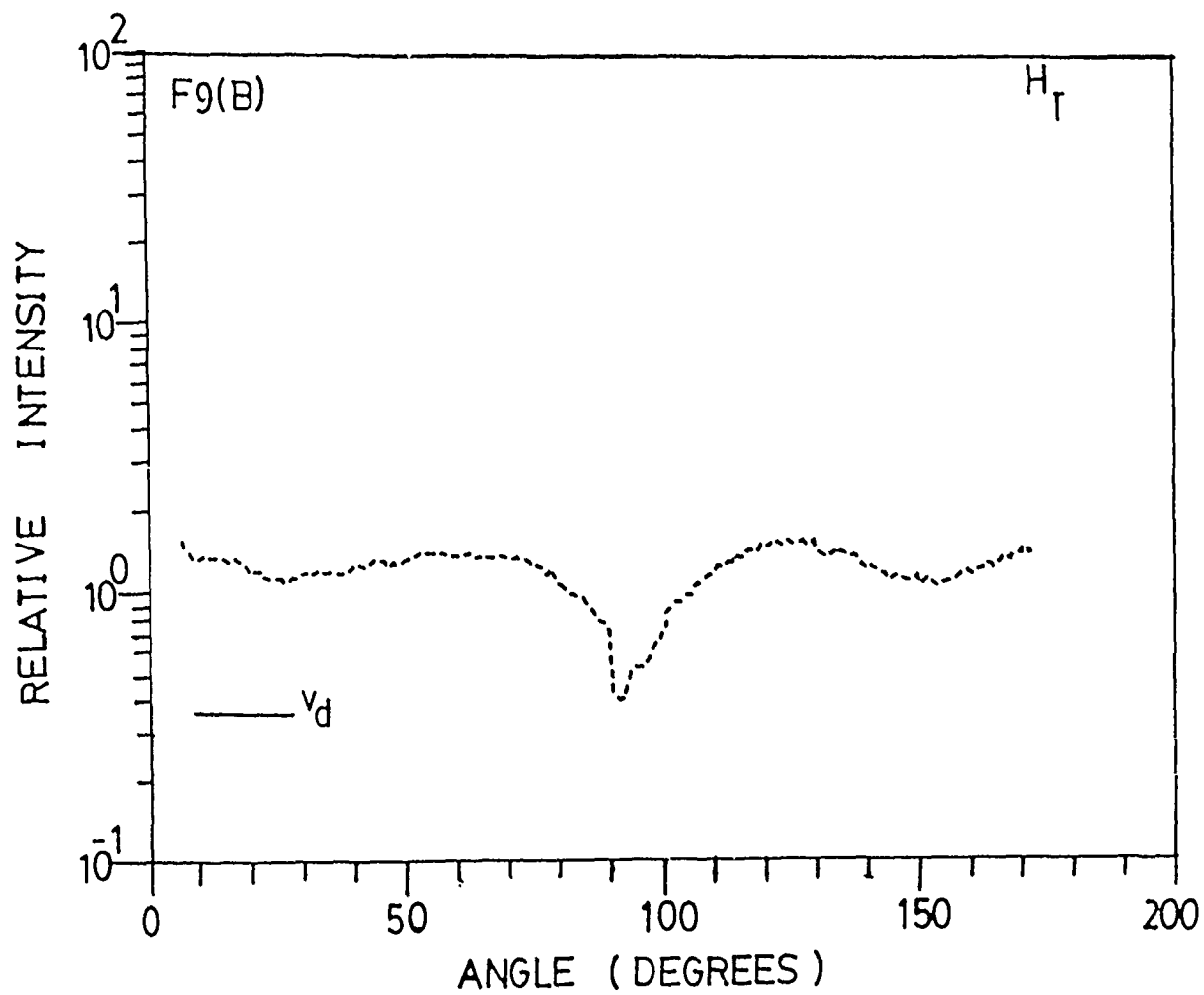
Figure 5.3. Angular distribution of fluorescent scattering from sample K10 treated Oxazine, for horizontally polarized incident light, at tip-on incidence. Below is a typical electronmicrograph of a replica of the sample.

K I 0
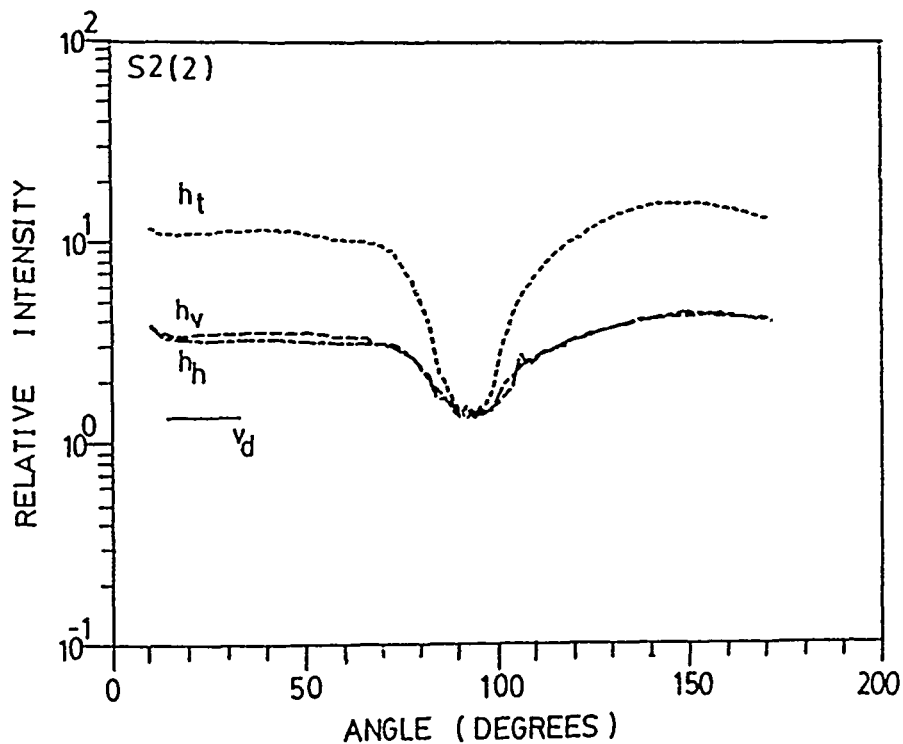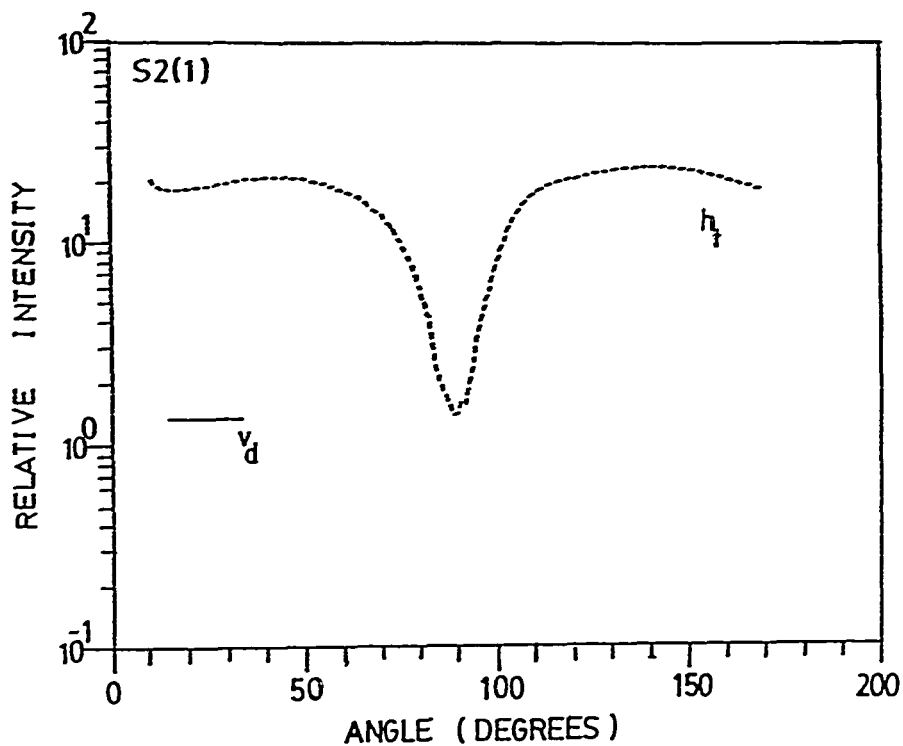
Figure 5.4. Angular distribution of fluorescent scattering from sample K10 treated Oxazine, for horizontally polarized incident light, at base-on incidence.
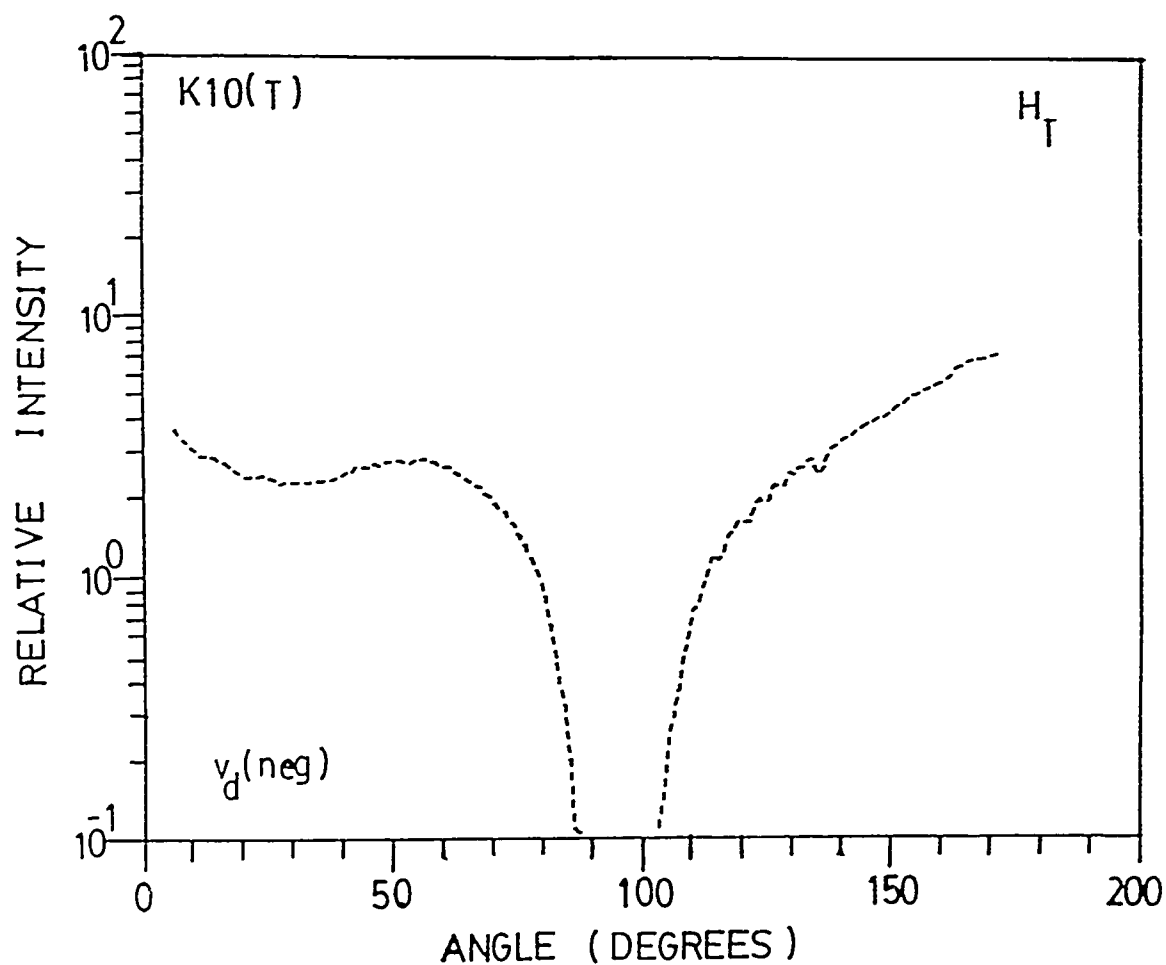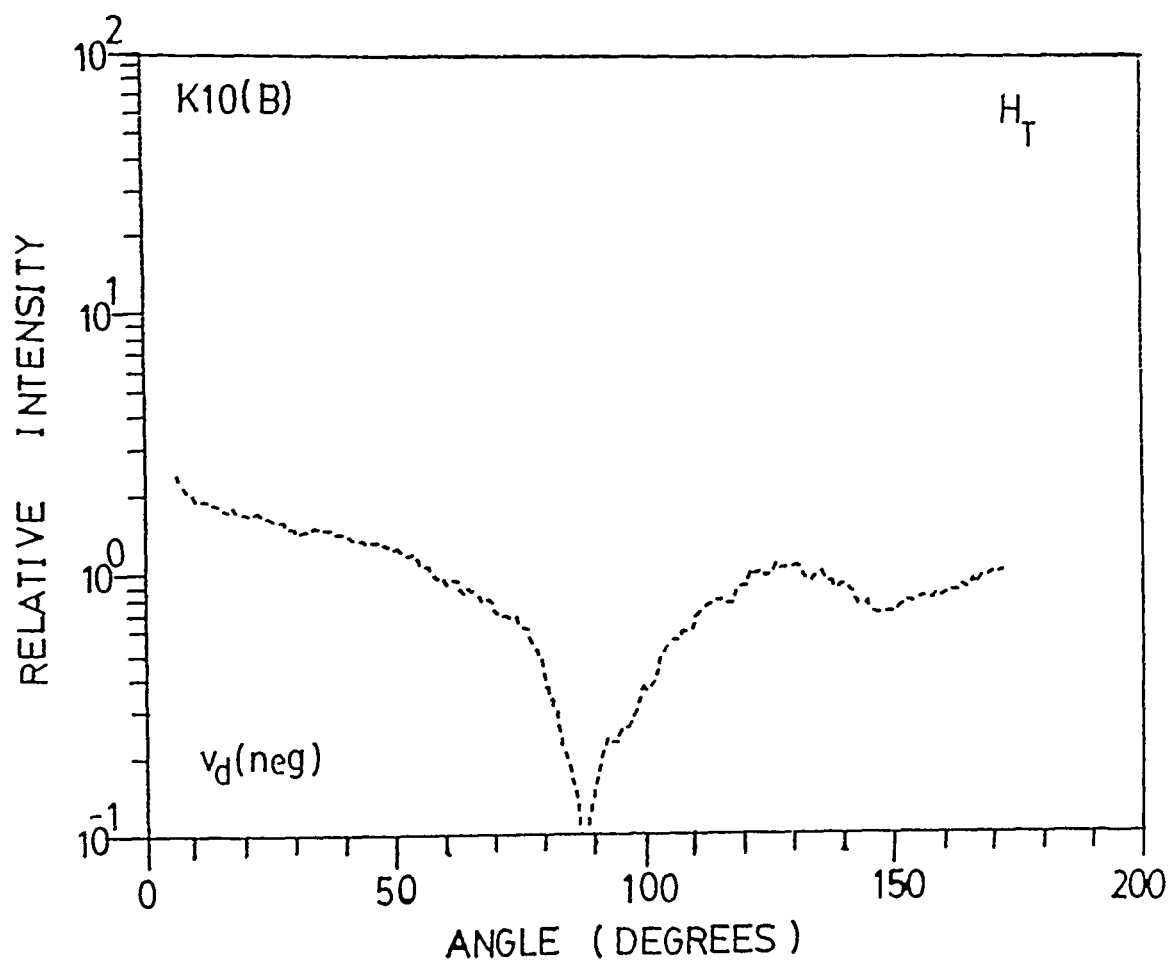
Figure 5.5.   Angular distribution of fluorescent scattering from sample AAL10 treated
Oxazine, for horizontally polarized incident light, at tip-on incidence.
Below is a typical electronmicrograph of a replica of the sample.

A A L I O
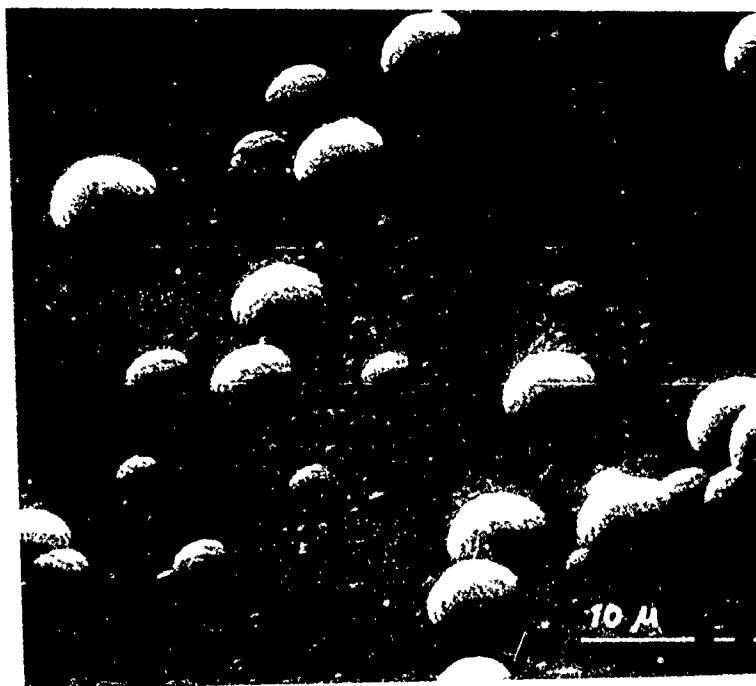
Figure 5.6.   Angular distribution of fluorescent scattering from sample AAL10 treated
Oxazine, for horizontally polarized incident light, at base-on incidence.
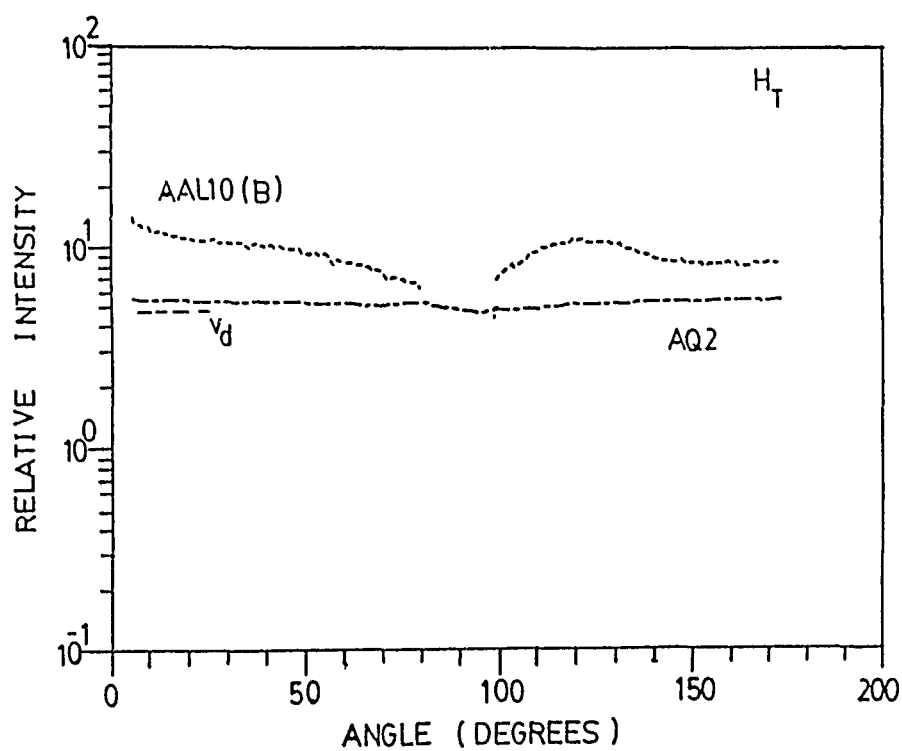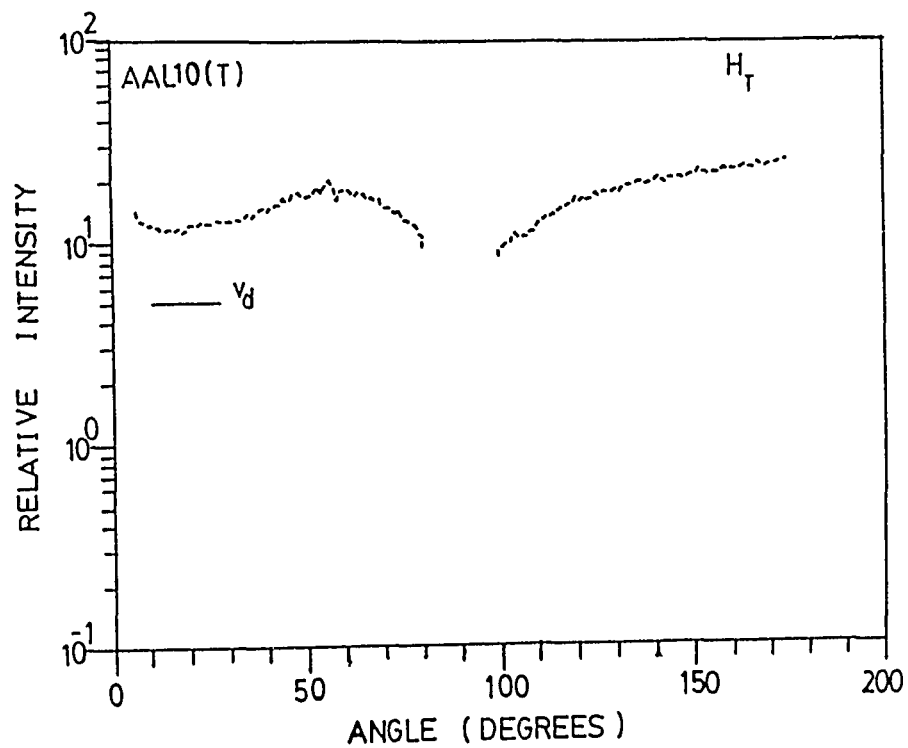
Figure 5.7. Angular distribution of fluorescent scattering from sample TAL1 treated Oxazine, for horizontally polarized incident light, at tip-on incidence. Below is a typical electronmicrograph of a replica of the sample.

T A L 1

Figure 5.8.   Angular distribution of fluorescent scattering from sample TAL1 treated
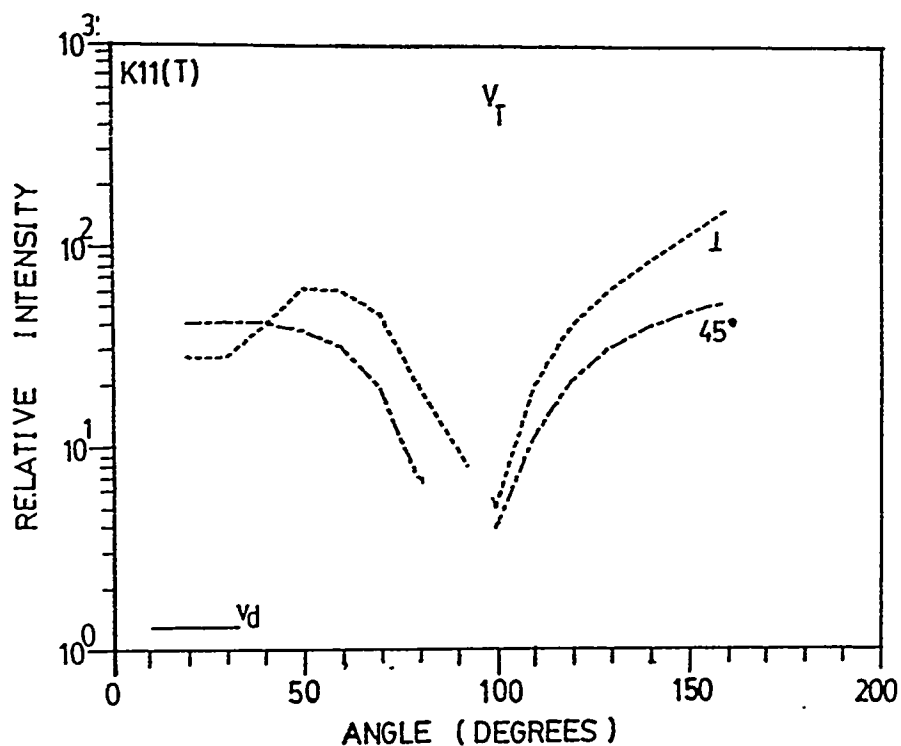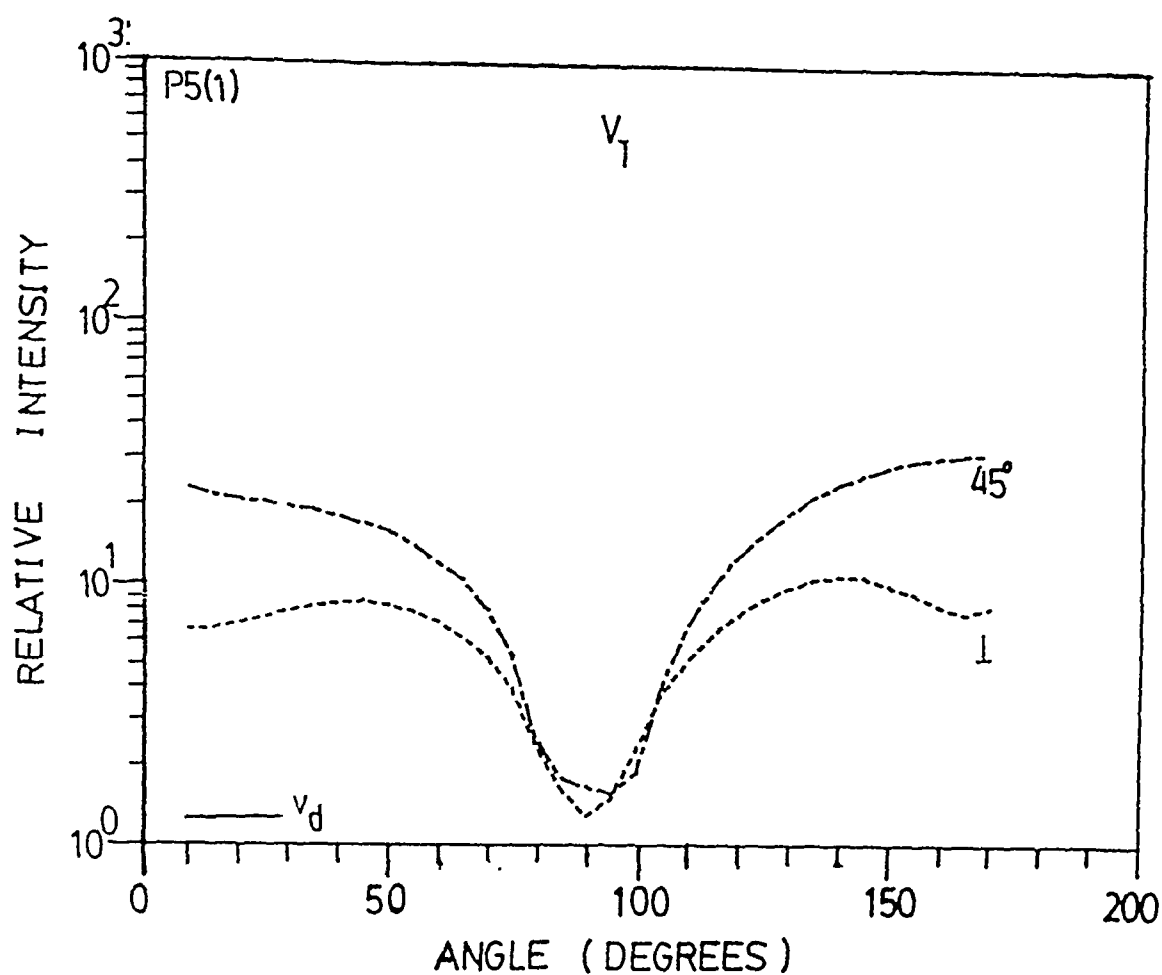Oxazine, for horizontally polarized incident light, at base-on incidence.
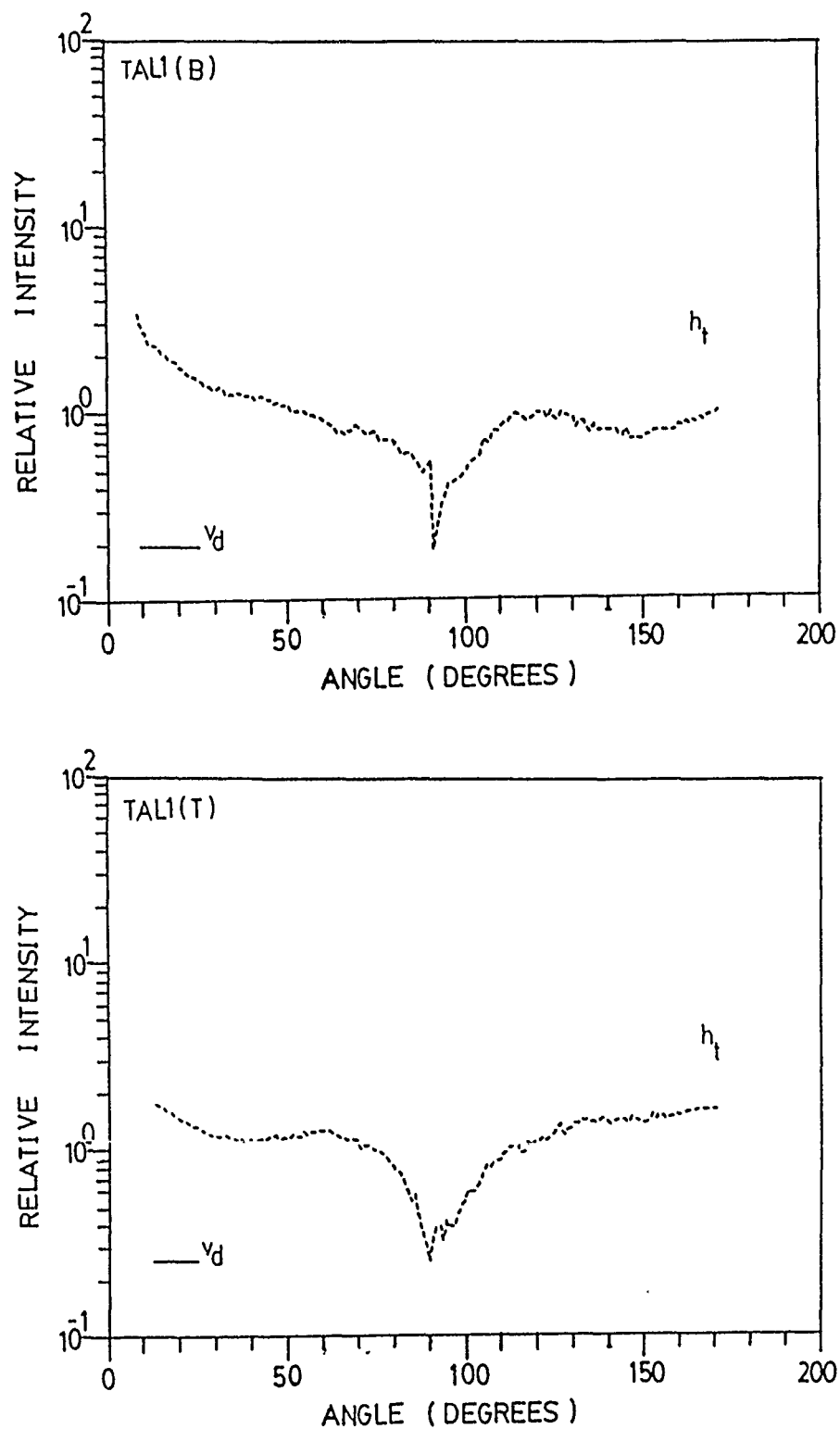
Figure 5.9. Angular distribution of fluorescent scattering from sample TAL2 treated with Nile Blue, for horizontally polarized incident light, at tip-on incidence.

Below is a typical electronmicrograph of a replica of the sample.
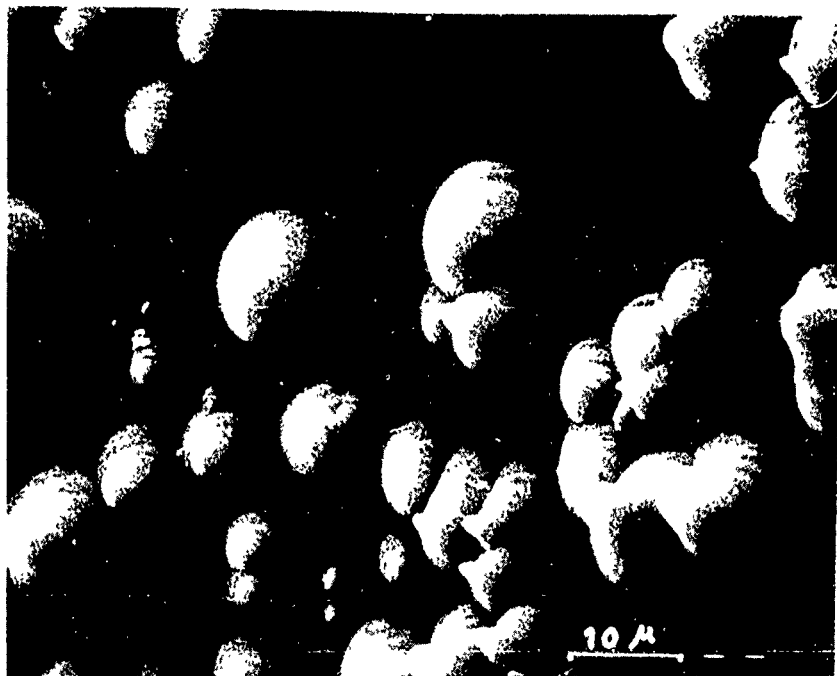
TAL 2

Figure 5.10. Angular distribution of fluorescent scattering from sample TAL treated Nile Blue, for horizontally polarized incident light, at base-on incidence.
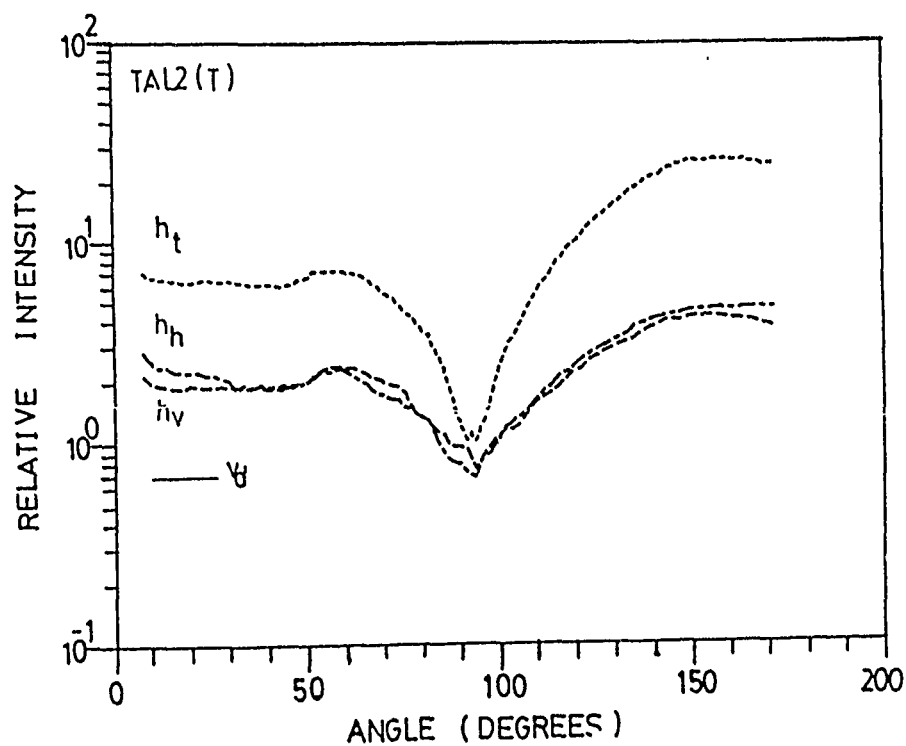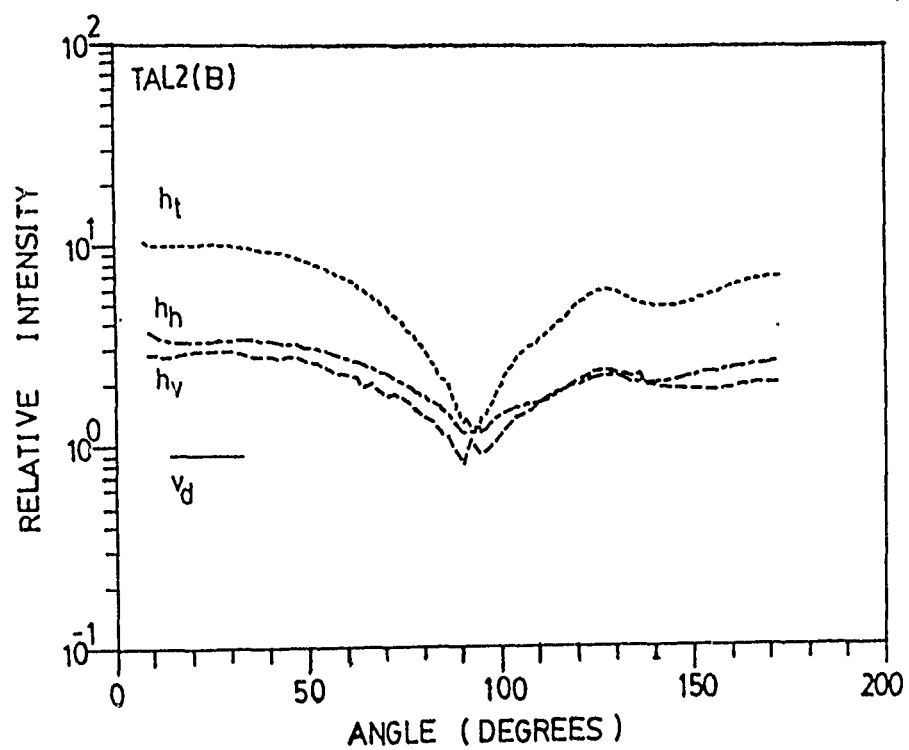
Figure 5.11. Angular distribution of fluorescent scattering from sample TQ1 (blank) treated Nile Blue, for horizontally polarized incident light, when the treated surface is down stream from the incident beam.
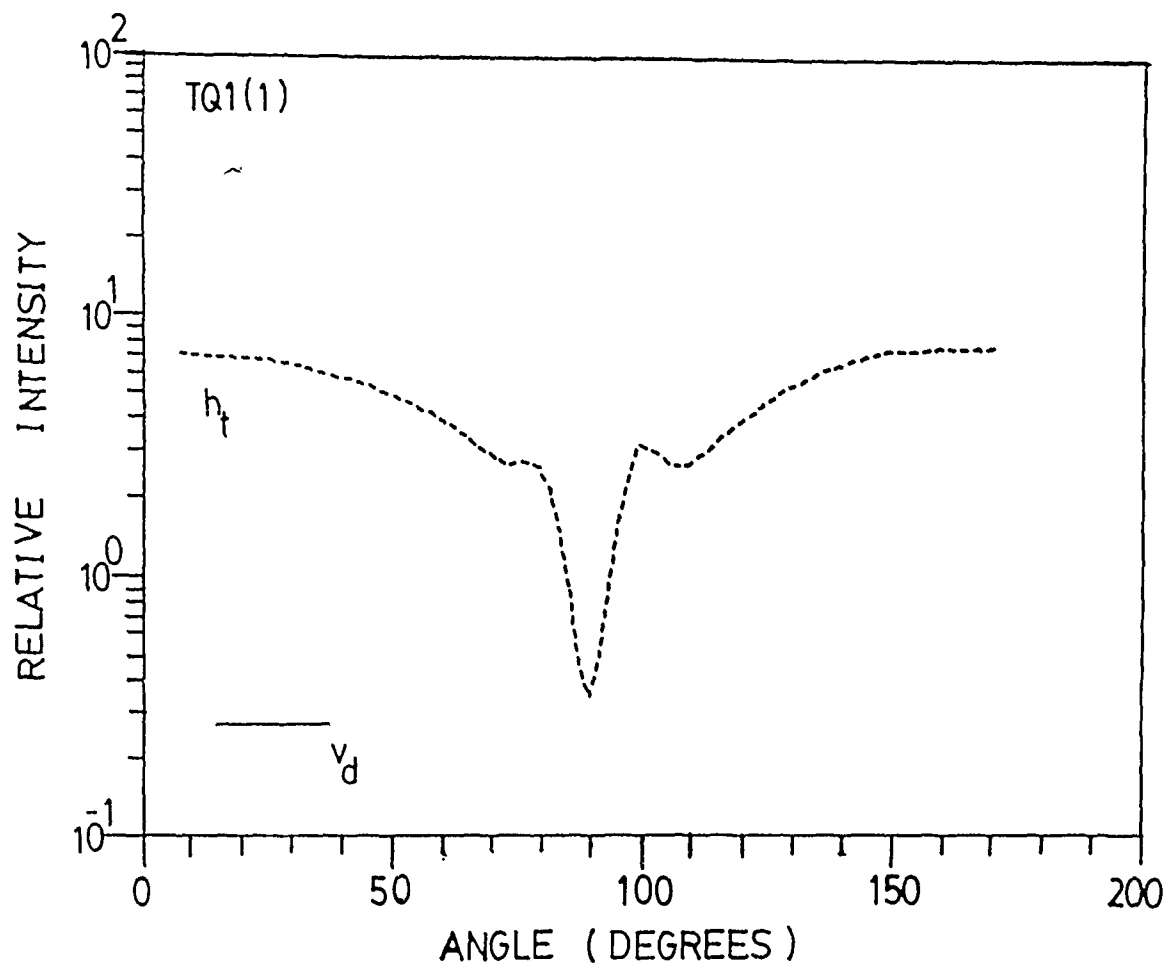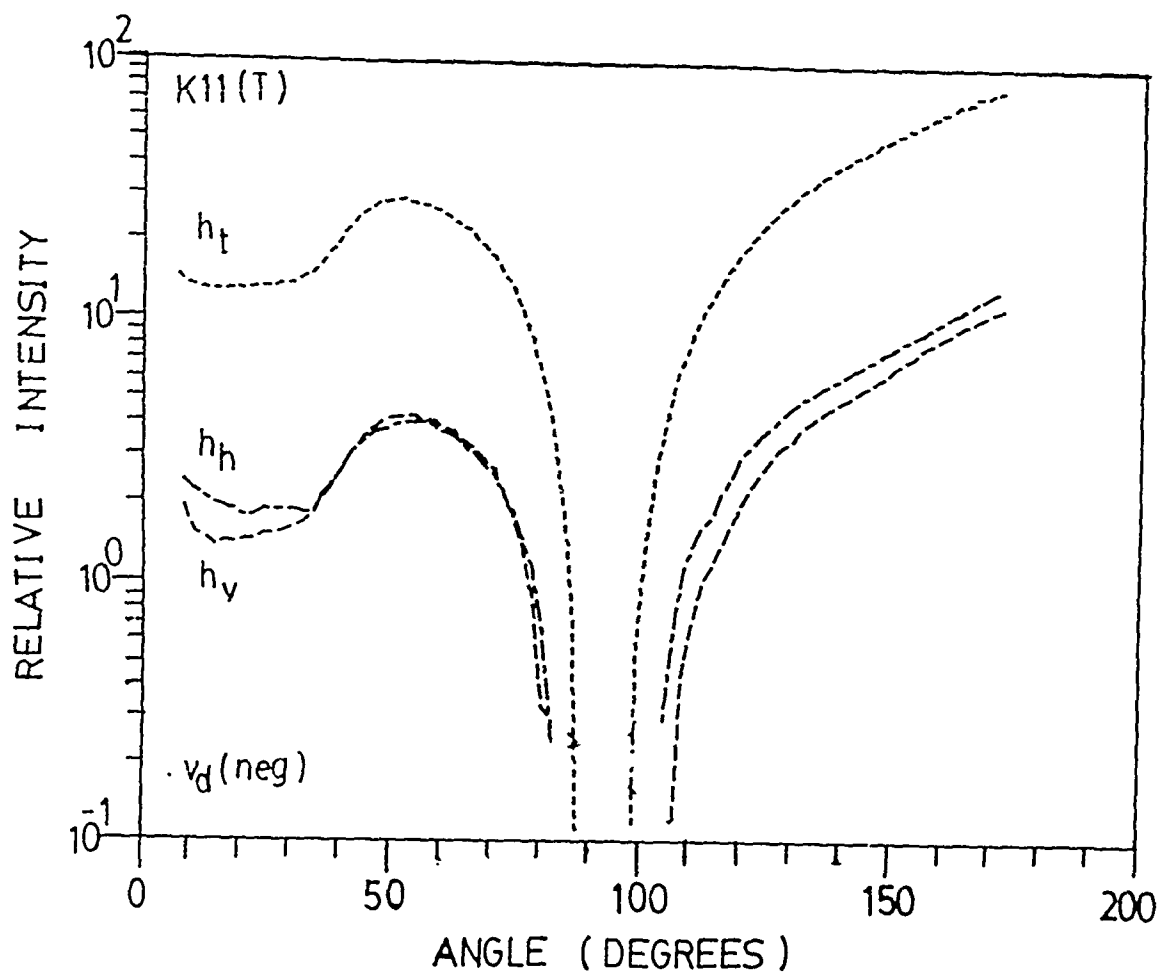
Figure 5.12. Angular distribution of fluorescent scattering from sample TQ1 treated Nile Blue, for horizontally polarized incident light, when the treated surface is up stream from the incident beam.
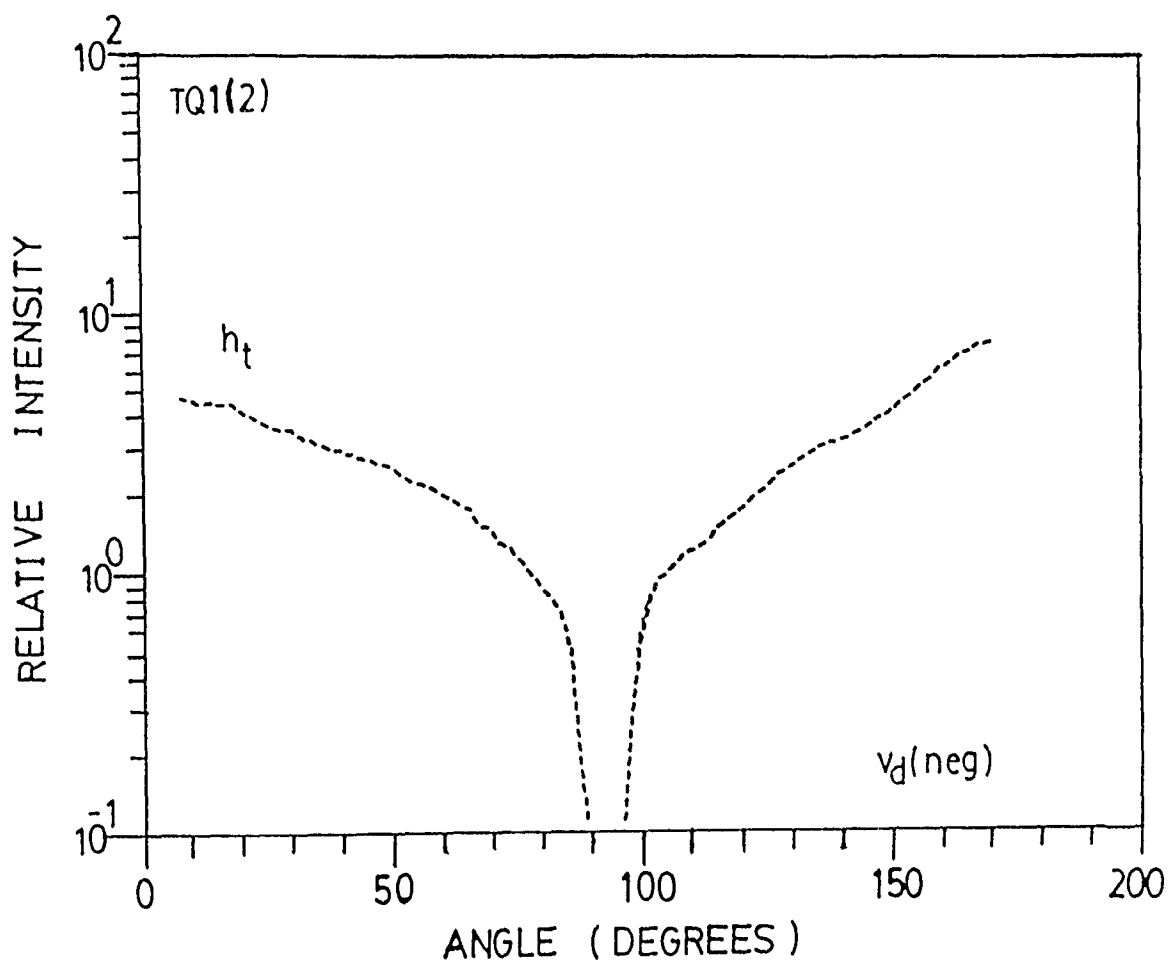
Figure 5.13. Angular distribution of fluorescent scattering from filter foil P5 treated with Nile Blue, for horizontally polarized incident light, when expose surface 1 normally to the incident beam.

Below is a typical electronmicrograph of a replica of the sample.
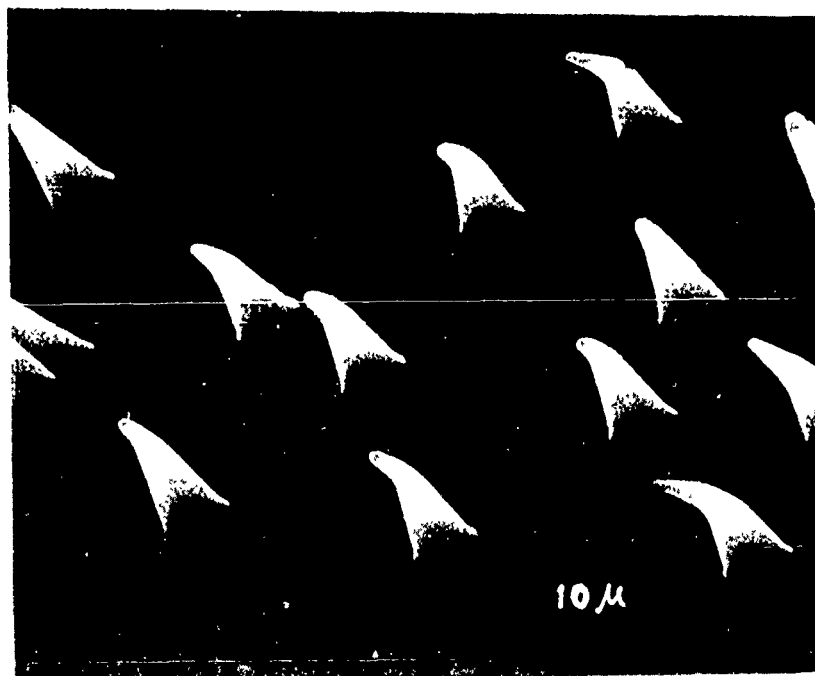
P 5

Figure 5.14. Angular distribution of fluorescent scattering from filter foil P5 treated with Nile Blue, for horizontally polarized incident light, when expose surface 2 normally to the incident beam.
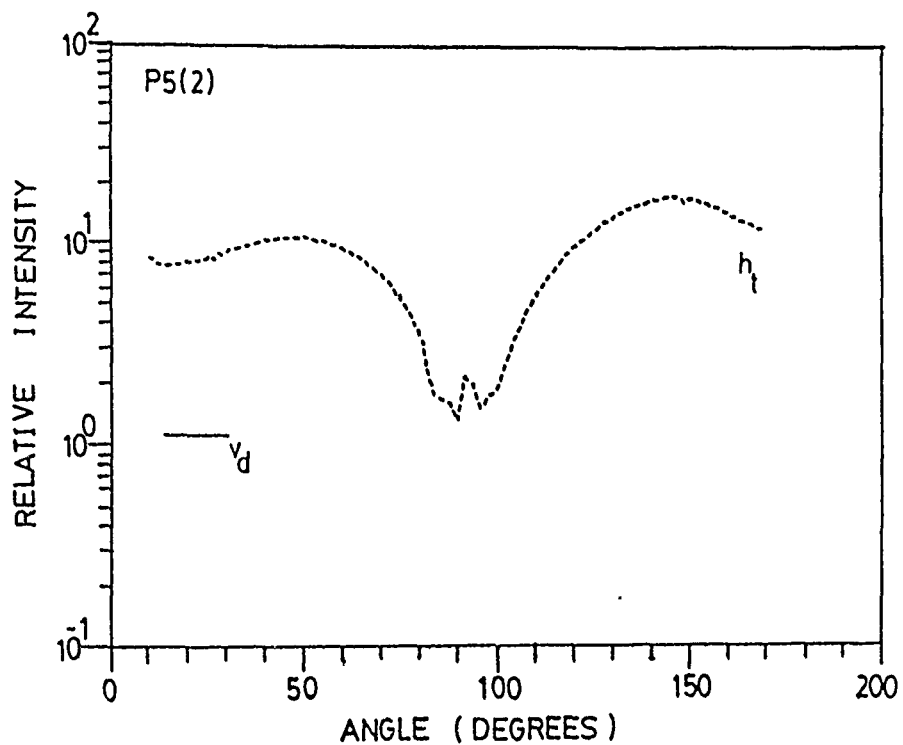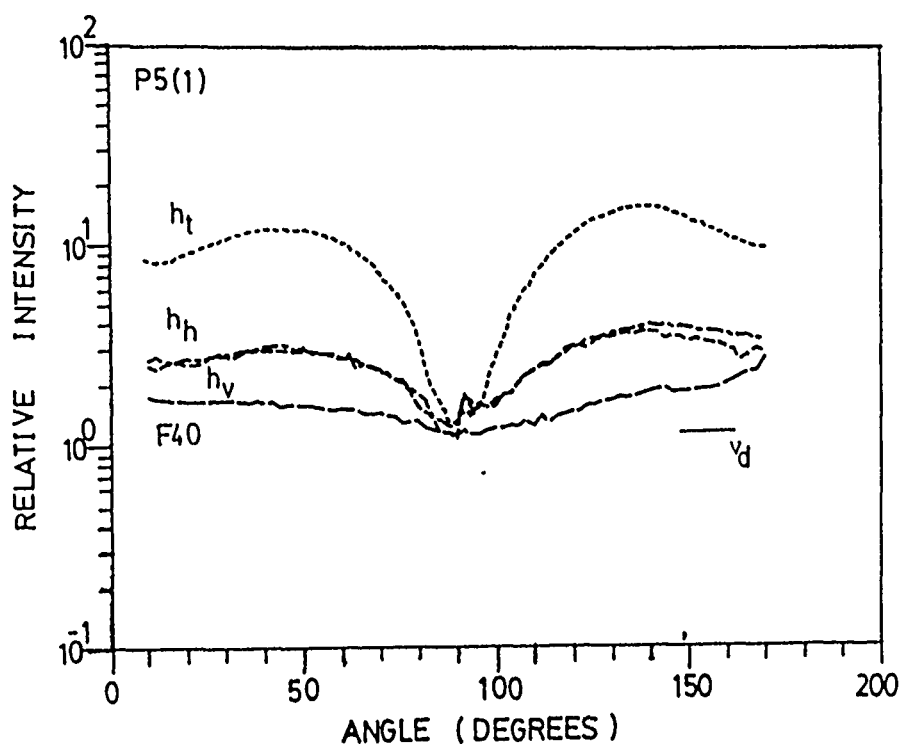
Figure 5.15. Angular distribution of fluorescent scattering from filter foil S1 treated with Nile Blue, for horizontally polarized incident light, when expose surface 1 normally to the incident beam.

Below is a typical electronmicrograph of a replica of the sample.

S 1

Figure 5.16.   Angular distribution of fluorescent scattering from filter foil S1 treated with Nile Blue, for horizontally polarized incident light, when expose surface 2 normally to the incident beam.
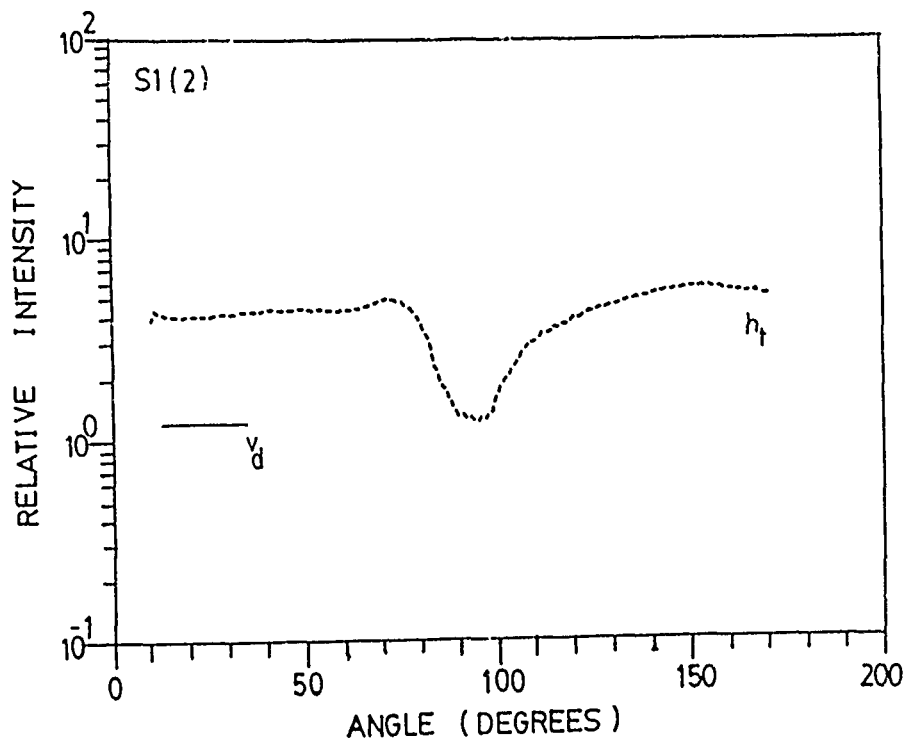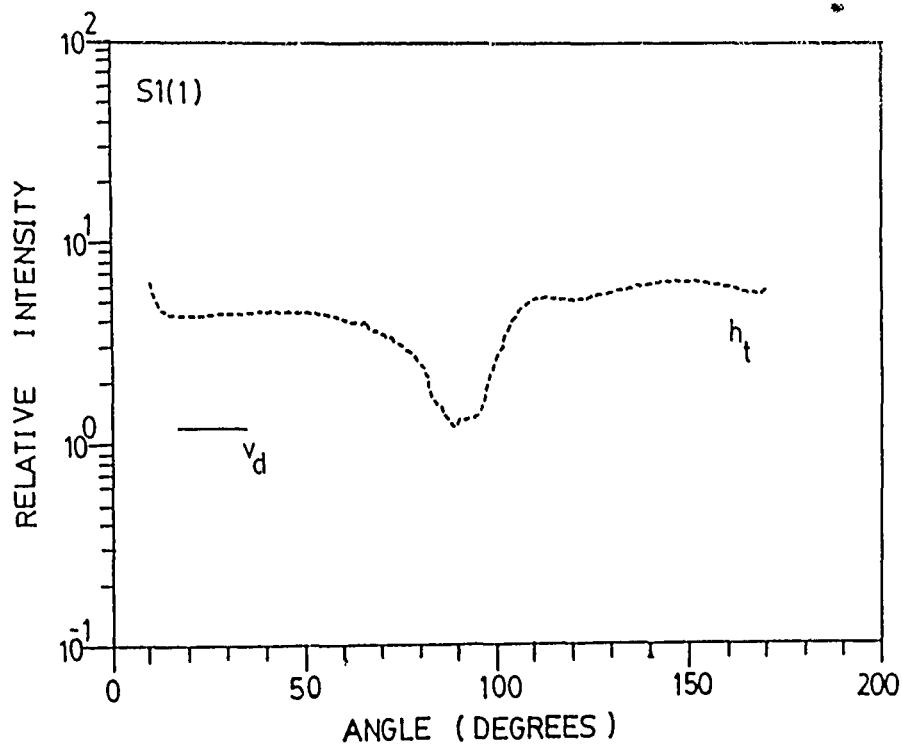
Figure 5.17. Angular distribution of fluorescent scattering from filter foil S2 treated with Nile Blue, for horizontally polarized incident light, when expose surface 1 normally to the incident beam.

Below is a typical electronmicrograph of a replica of the sample.

S 2

Figure 5.18.   Angular distribution of fluorescent scattering from filter foil S2 treated with Nile Blue, for horizontally polarized incident light, when expose surface 2 normally to the incident beam.
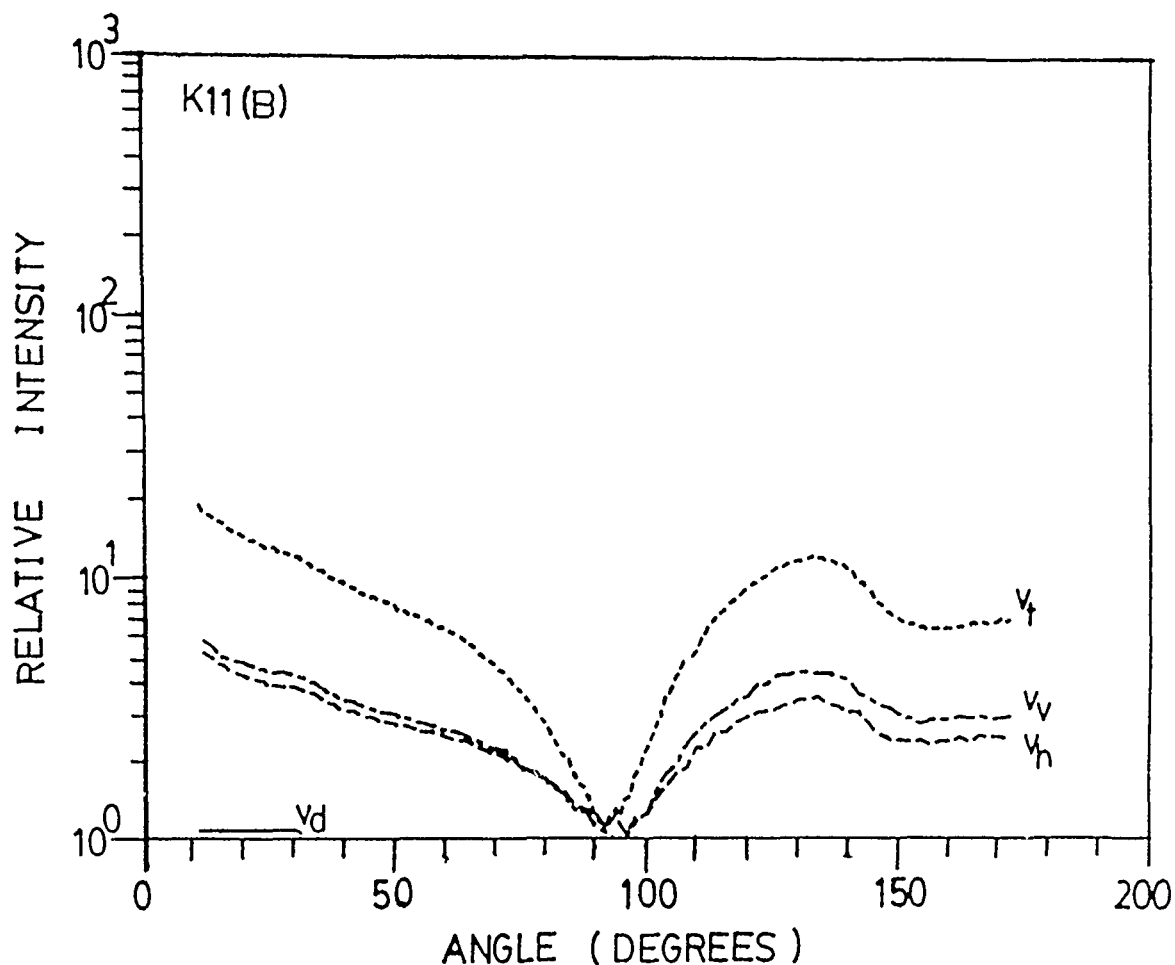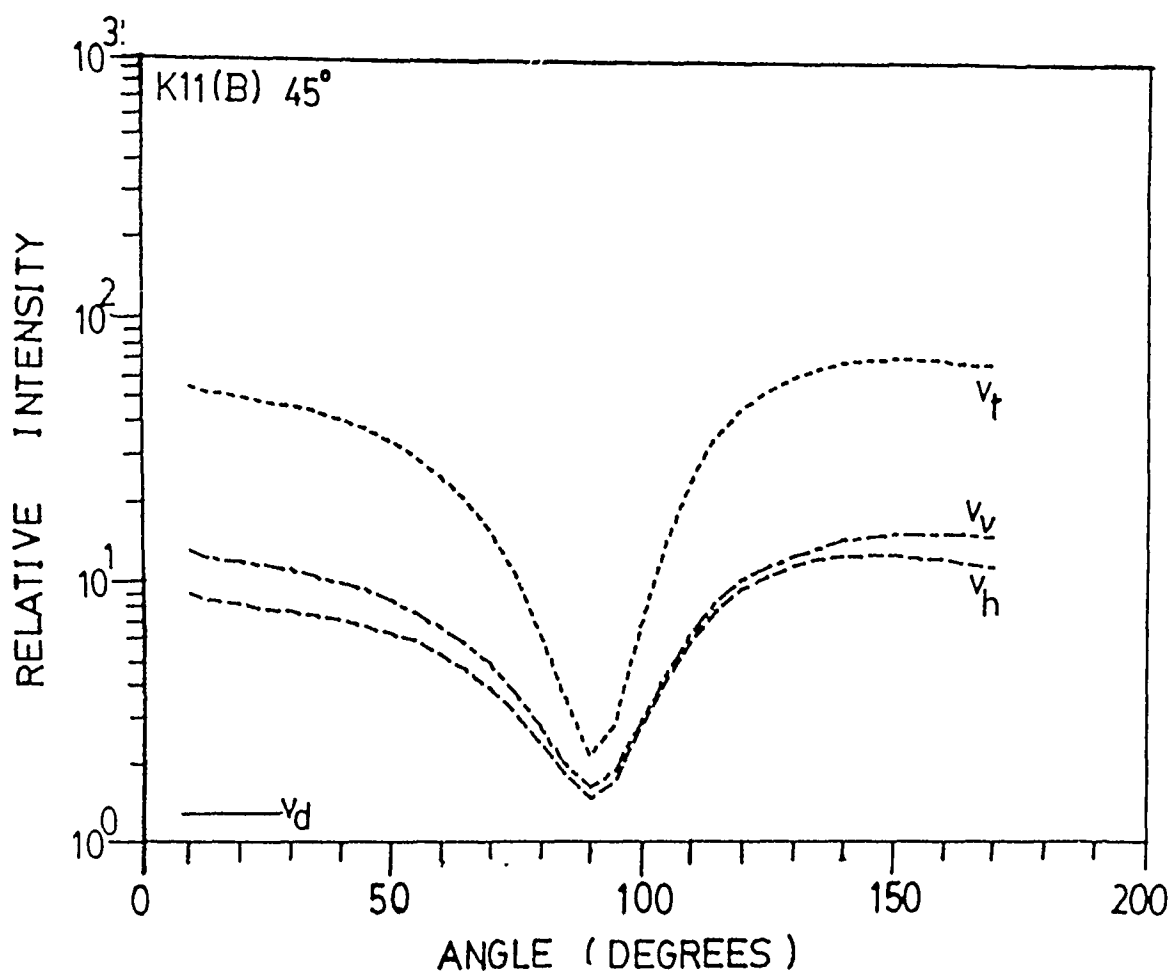
Figure 5.19. Angular distribution of fluorescent scattering from sample K11 treated Oxazine, for vertically polarized incident light, when aligned the sample surface normal and 45° to the incident beam. The cone tips are up stream.

Below is a typical electronmicrograph of a replica of the sample.

K11

Figure 5.20. Angular distribution of fluorescent scattering from sample K11 treated Oxazine, for vertically polarized incident light. The sample was aligned at 45° and 90° to the incident beam. The cone bases are up stream.
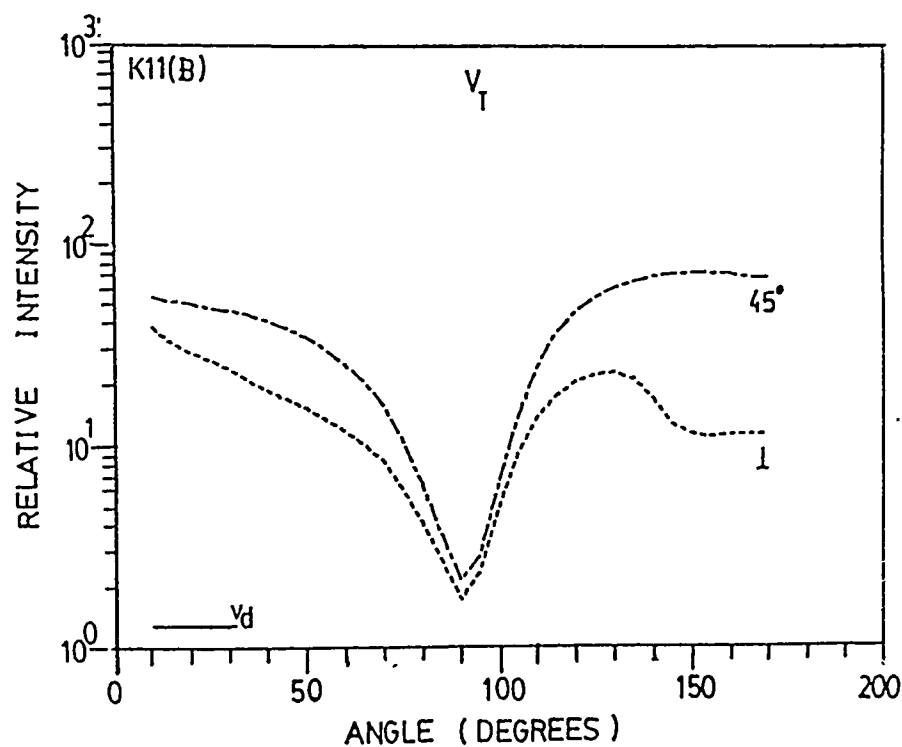
Figure 5.21. Angular distribution of fluorescent scattering from sample P5 treated with Nile Blue, for vertically polarized incident light. The sample was aligned at 45° and 90° to the incident beam. Surface 1 is up stream.

Figure 5.22. Angular distribution of fluorescent scattering from sample P5 treated with Nile Blue, for vertically polarized incident light, when aligned the sample surface 2 normal and 45° to the incident beam.
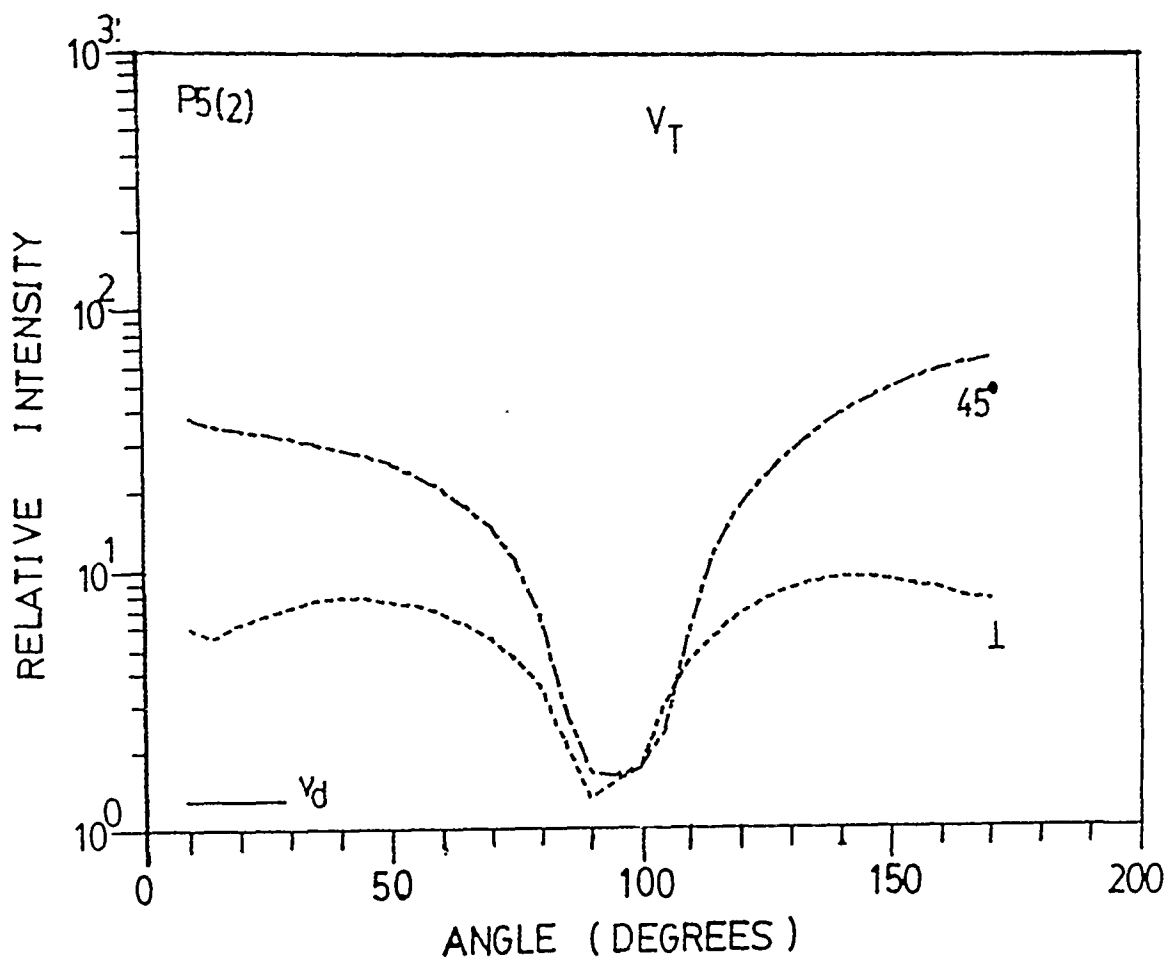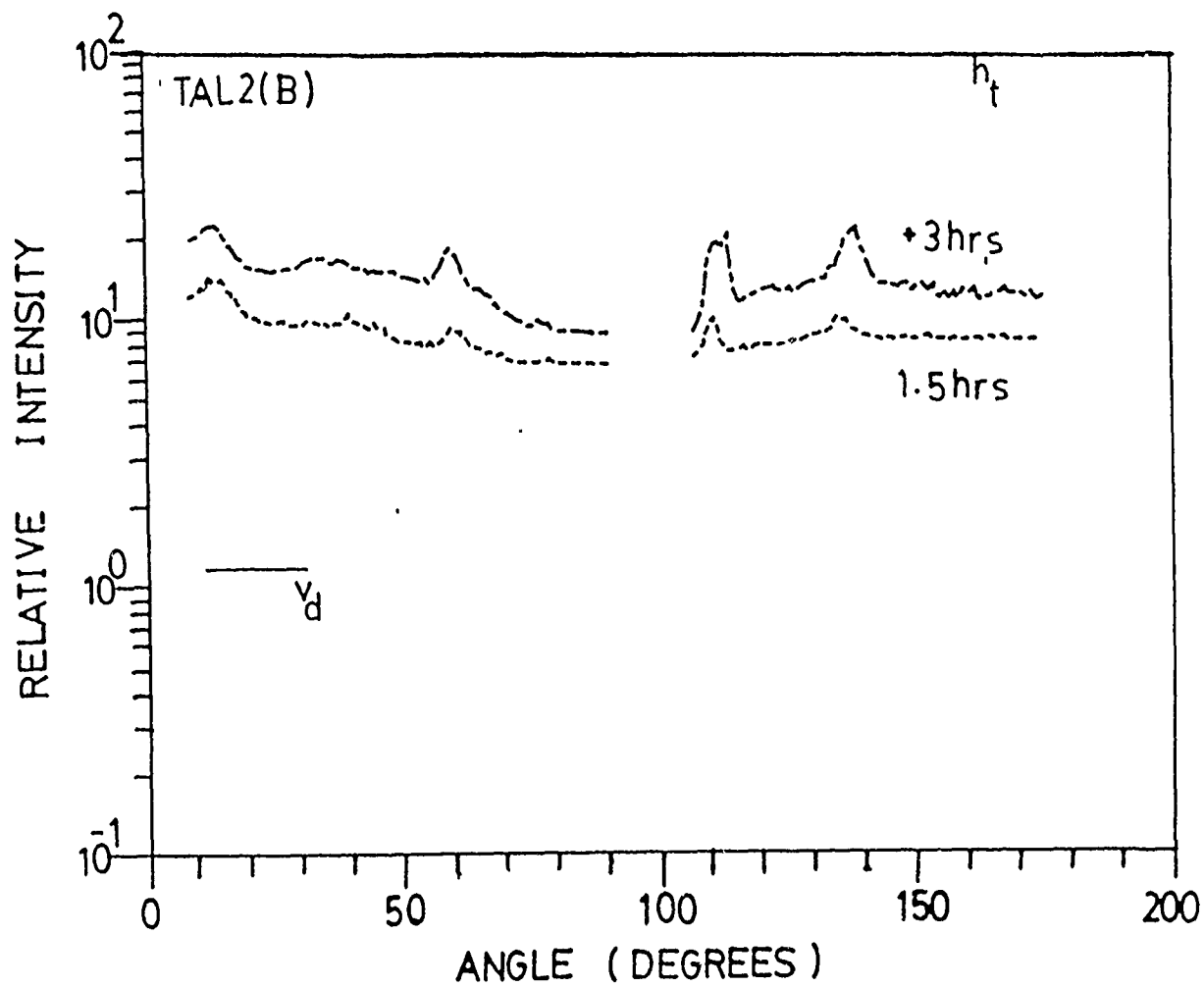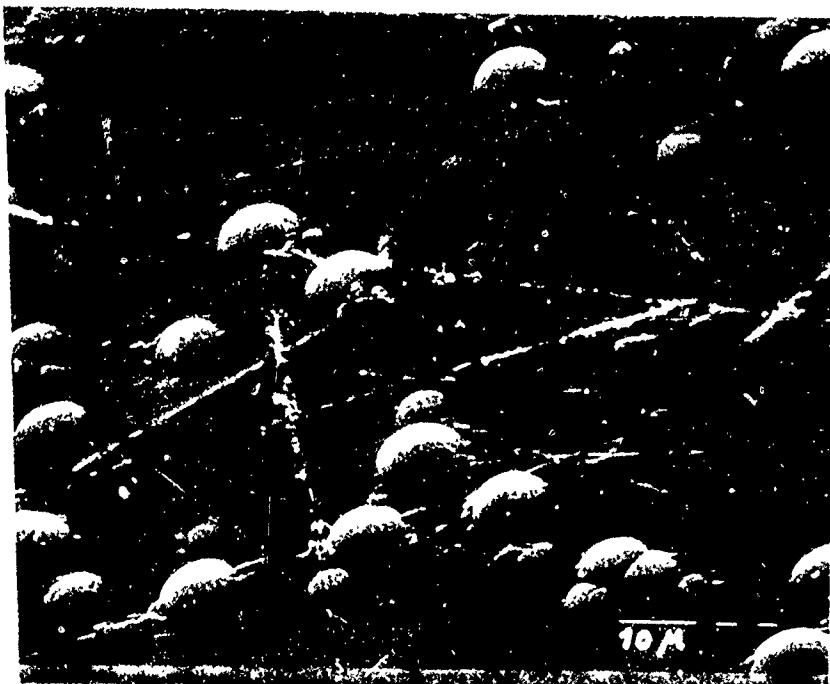
Figure 5.23. Angular distribution of fluorescent scattering from sample K11 treated with Oxazine, for horizontally polarized incident light at tip-on incidence. Total (T: detected without polarizer), horizontal (H) and vertical (V) polarization components of the scattered signals are shown.
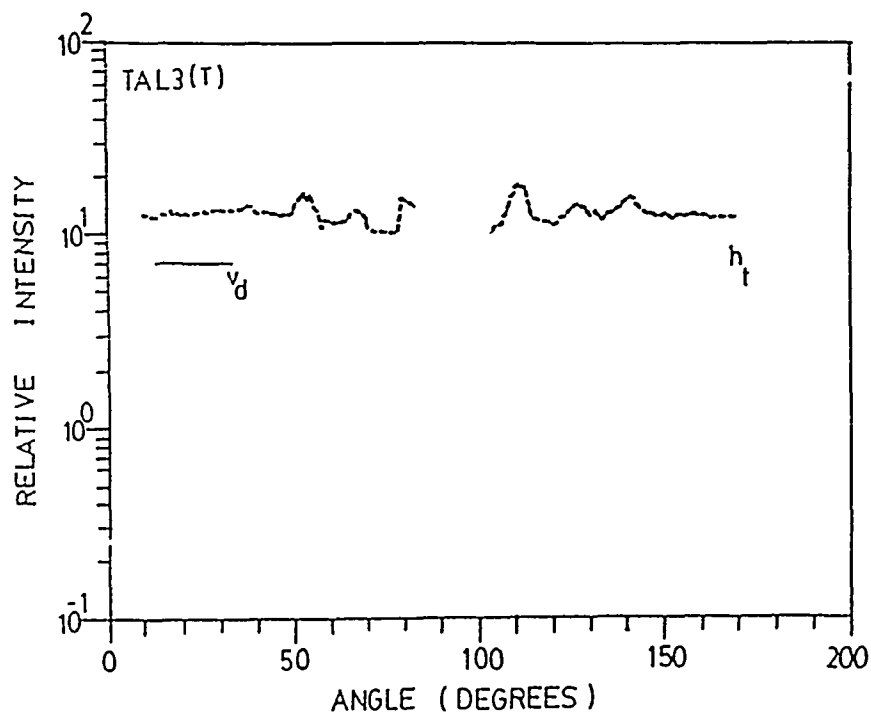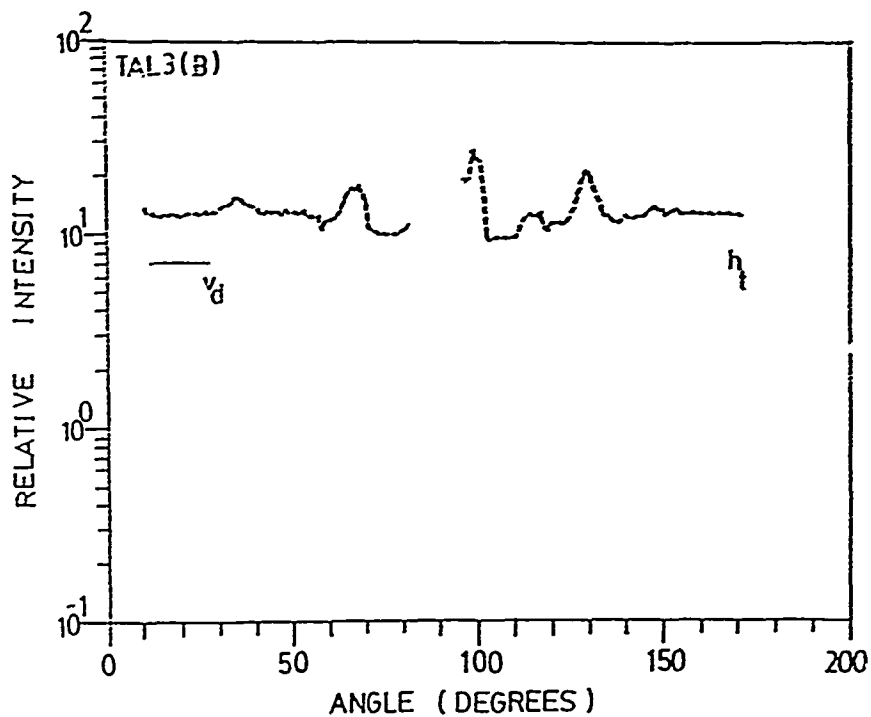
Figure 5.24. Angular distribution of fluorescent scattering from sample K11 treated with Oxazine, for horizontally polarized incident light at base-on incidence. Total (T: detected without polarizer), horizontal (H) and vertical (V) polarization components of the scattered signals are shown.
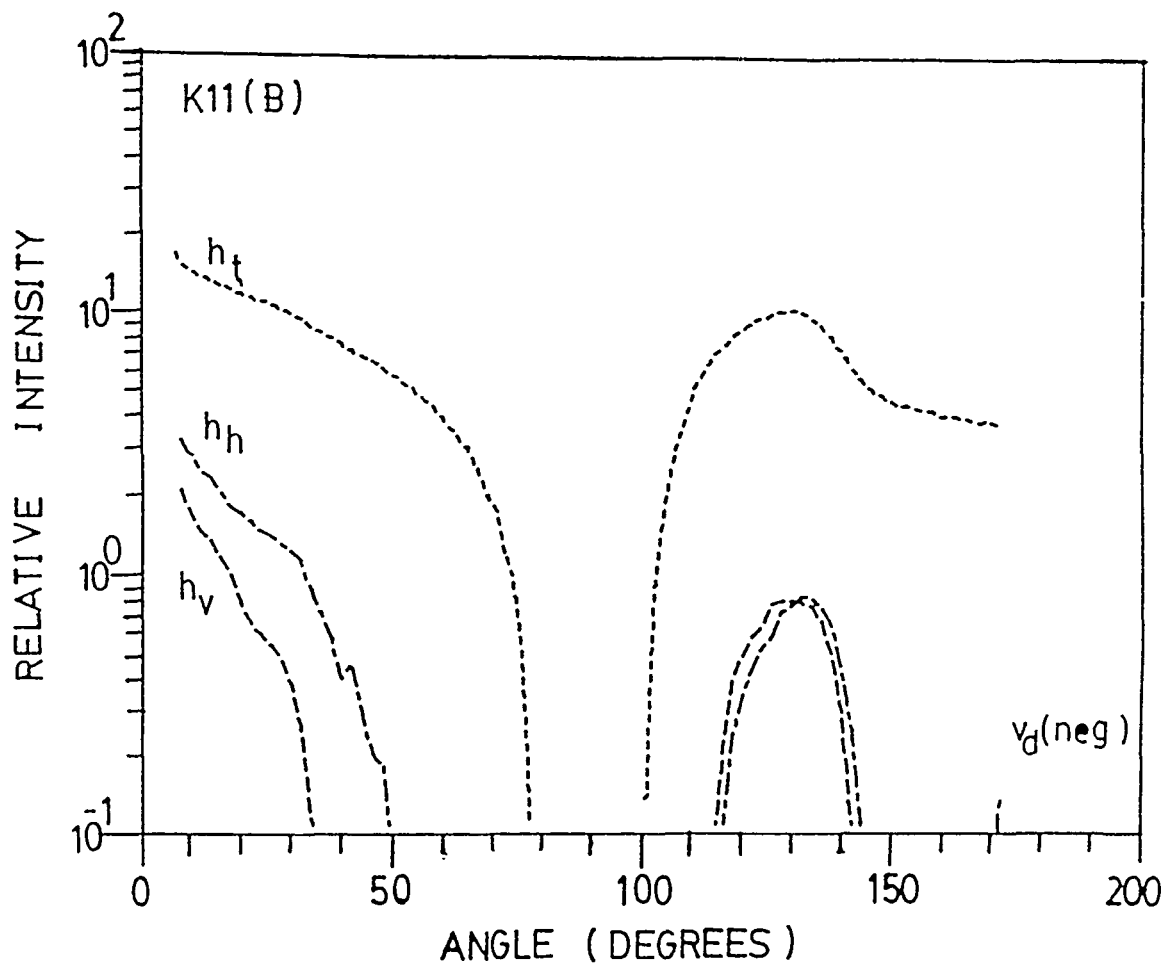
Figure 5.25. Angular distribution of fluorescent scattering from sample K11 treated with Oxazine, for vertically polarized incident light at tip-on incidence. Total (T: detected without polarizer), horizontal (H) and vertical (V) polarization components of the scattered signals are shown.
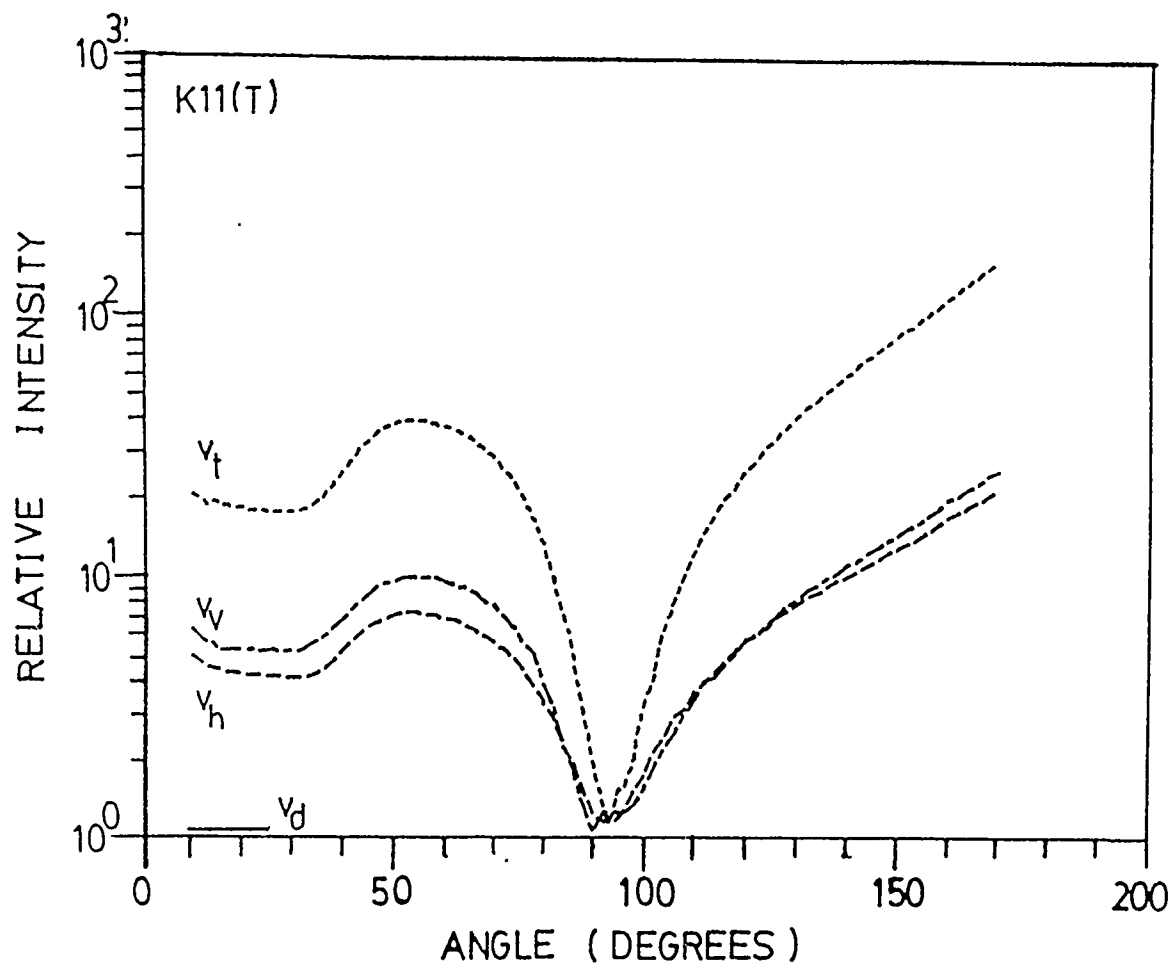
Figure 5.26. Angular distribution of fluorescent scattering from sample K11 treated with Oxazine, for vertically polarized incident light at base-on incidence. Total (T: detected without polarizer), horizontal (H) and vertical (V) polarization components of the scattered signals are shown.

Figure 5.27. Angular distribution of fluorescent scattering from sample K11 treated
with Oxazine, for vertically polarized incident light when aligned the
sample surface 45° to the incident beam. The cone bases are up stream.
Total (T: detected without polarizer), horizontal (H) and vertical (V)
polarization components of the scattered signals are depicted.

Figure 5.28. Angular distribution of fluorescent scattering from sample TAL2 treated with Nile Blue, for horizontally polarized incident light at tip-on incidence, when the sample edge (toward 90° scattering angle) is left open. After 1/2 hr. dye treatment, and after 3 hr. additional treatment.
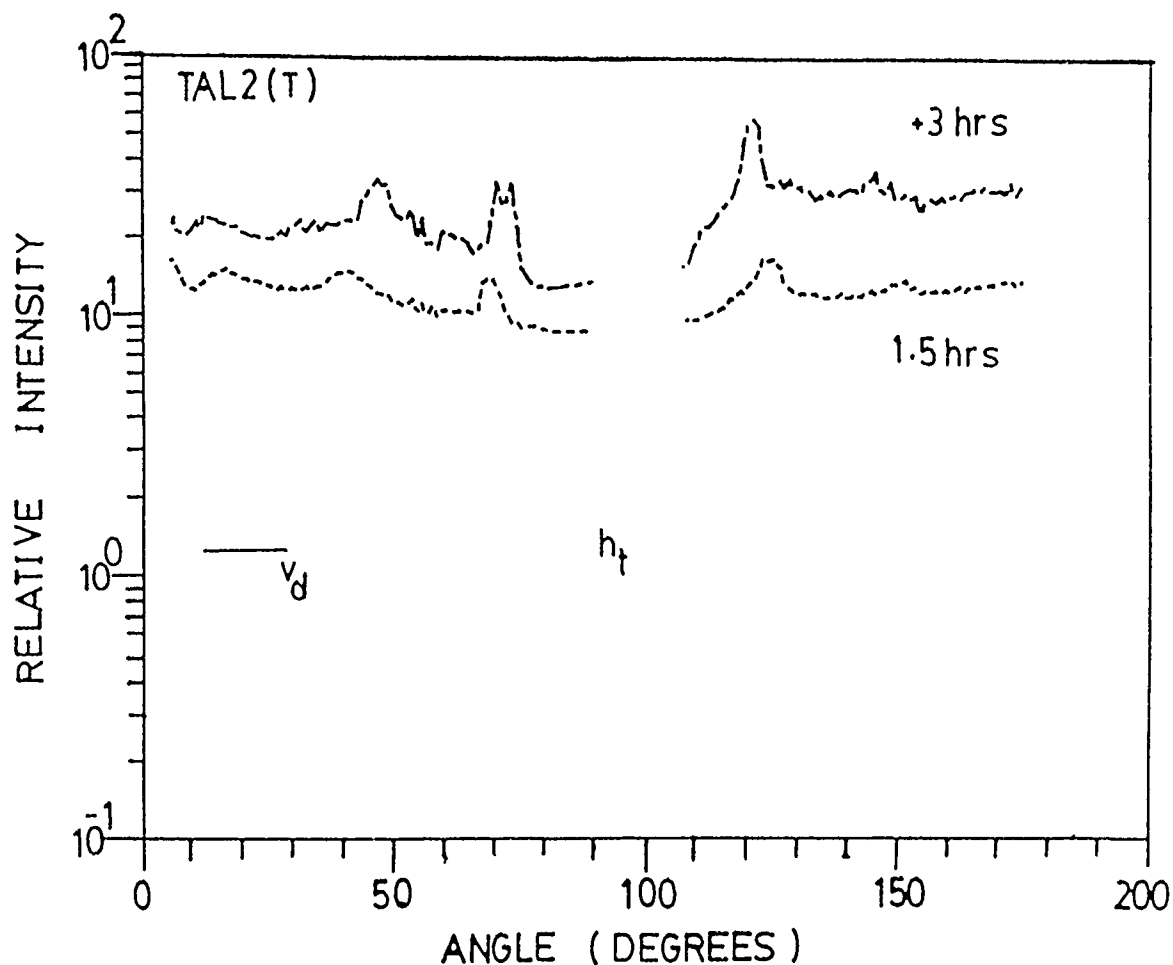
Figure 5.29.   Same as Fig. 5.28 except at base-on incident.

Figure 5.30. Angular distribution of fluorescent scattering from sample TAL3 treated
with Oxazine, for horizontally polarized incident light at tip-on incidence,
when the sample edge (toward 90° scattering angle) is left open.
Below is a typical electronmicrograph of a replica of the sample.

T A L 3

Figure 5.31. Same as Fig. 5.30 except at base-on incident.

Figure 5.32.   Angular distribution of fluorescent scattering from sample TQ2 (blank) treated with Nile Blue, for horizontally polarized incident light at tip-on incidence, when the sample edge (toward 90° scattering angle) is left open, shown in comparison with that from an untreated blank sample (TQ0) also with edge open.
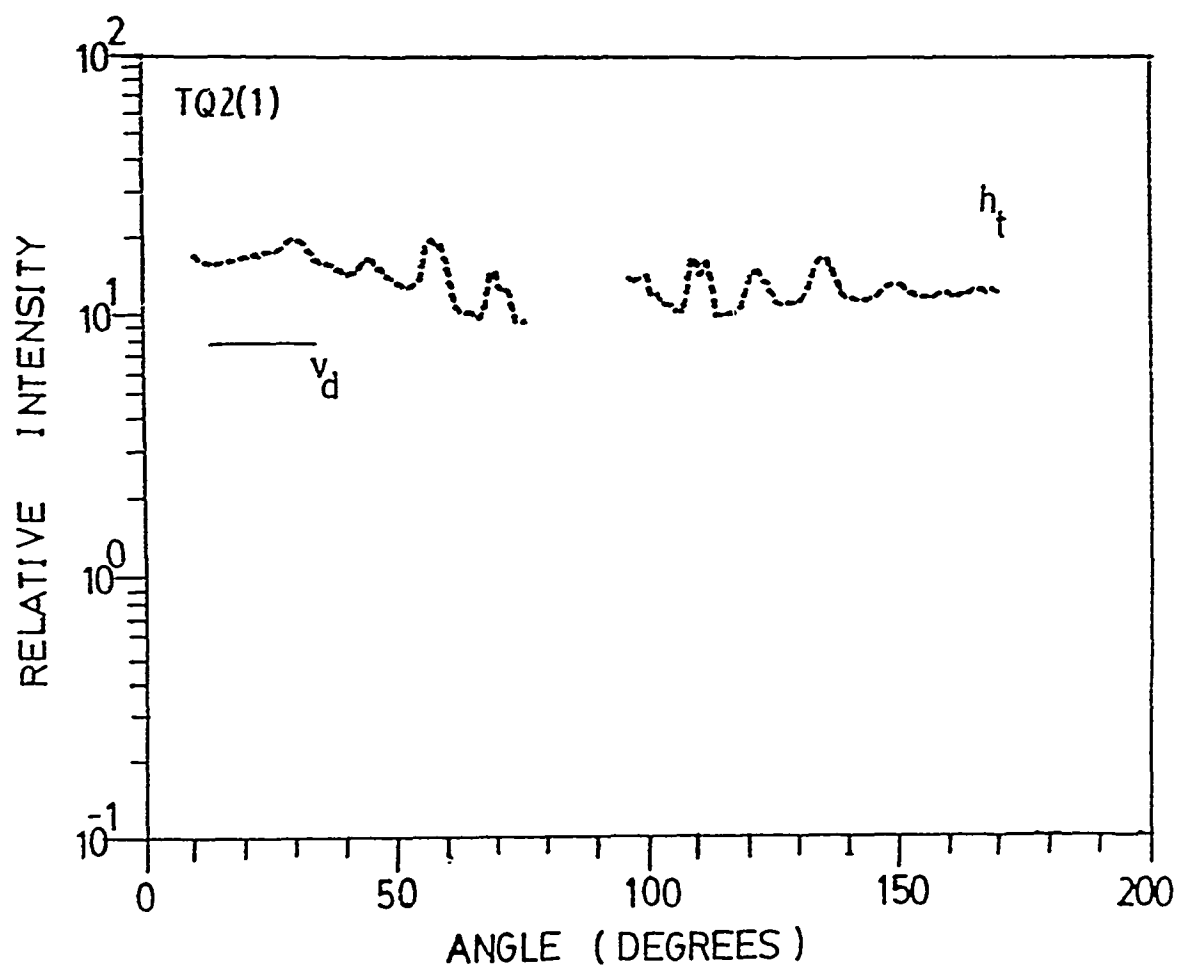
Figure 5.33. Same as Fig. 5.32 for TQ2 except when treated surface is up stream.
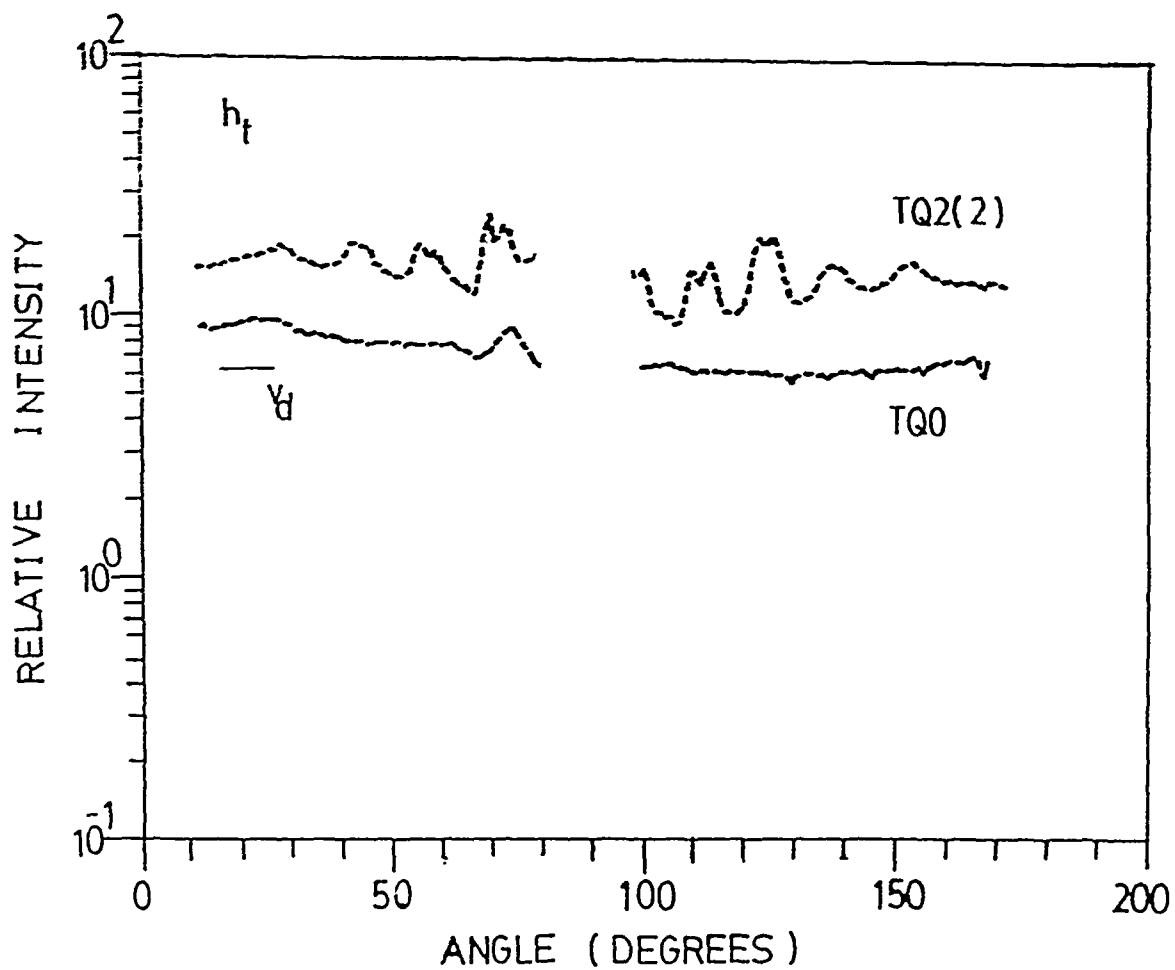
APPENDIX A

Electrical Characteristics and a Spectral Response Curve   of

the Phototransistors GE L14G3 and L14F1
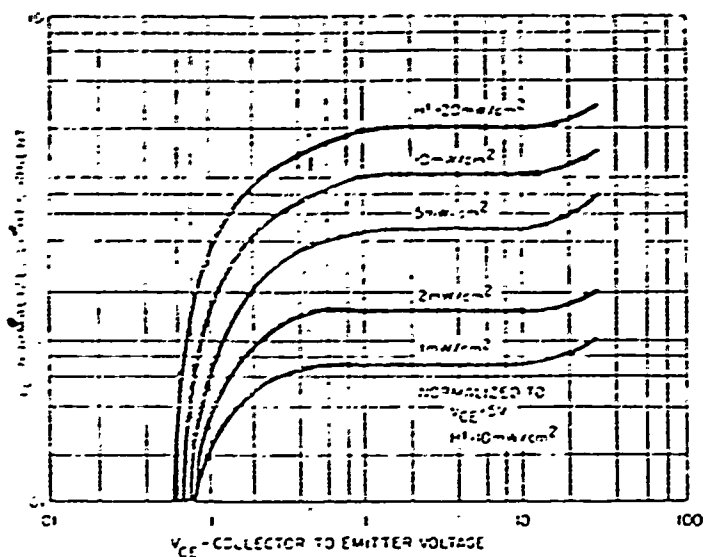
Light Current vs Collector to Emitter Voltage
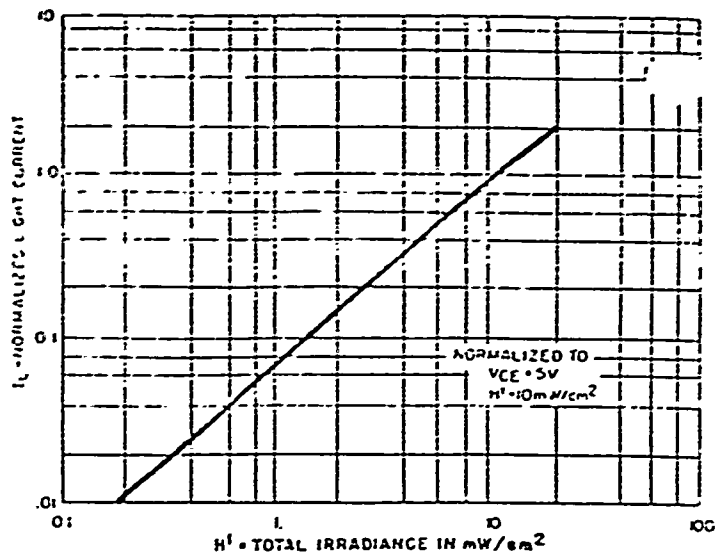
Normalized Light Current vs Radiation
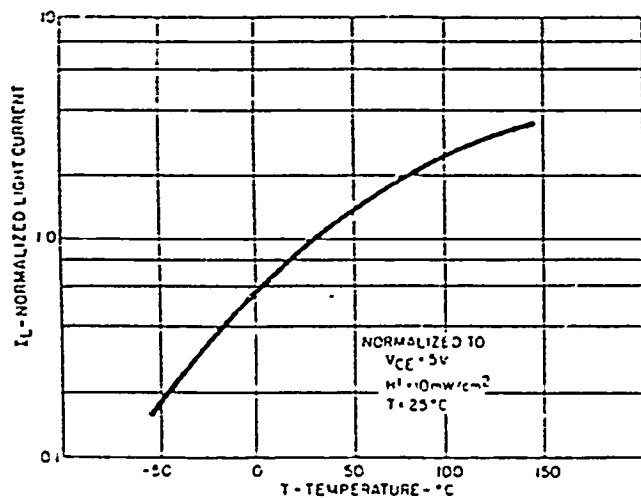
Normalized Light Current vs Temperature
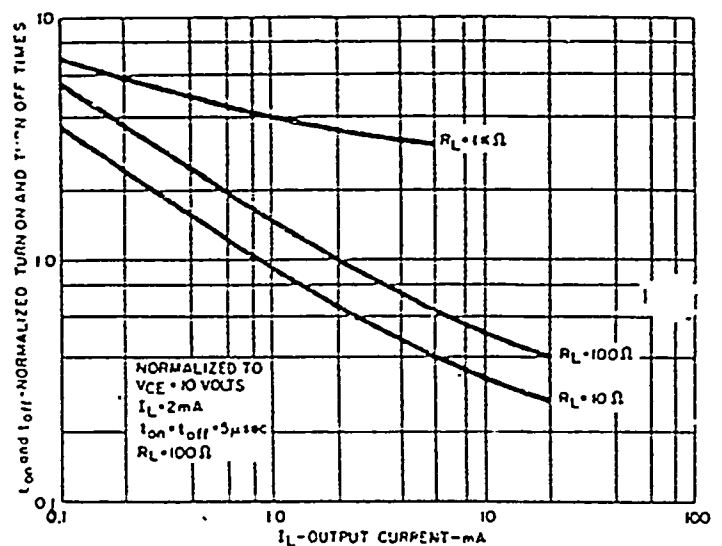
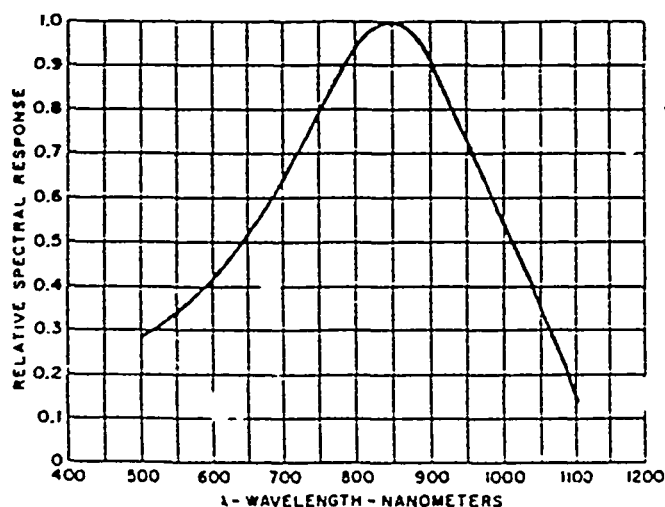Switching Times vs Output Current
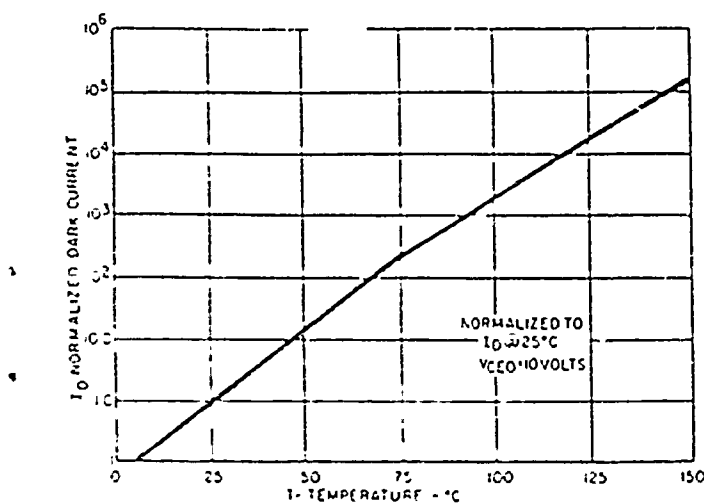
Dark Current vs Temperature
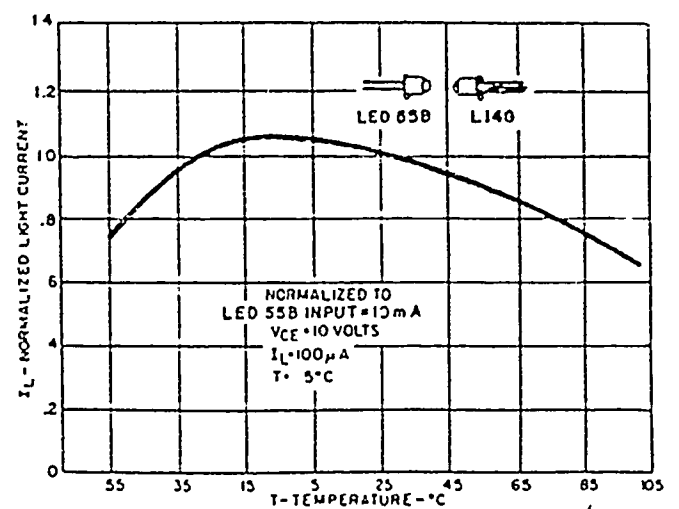
Normalized Light Current vs Temperature
Both Emitter (LED55B) and Detector
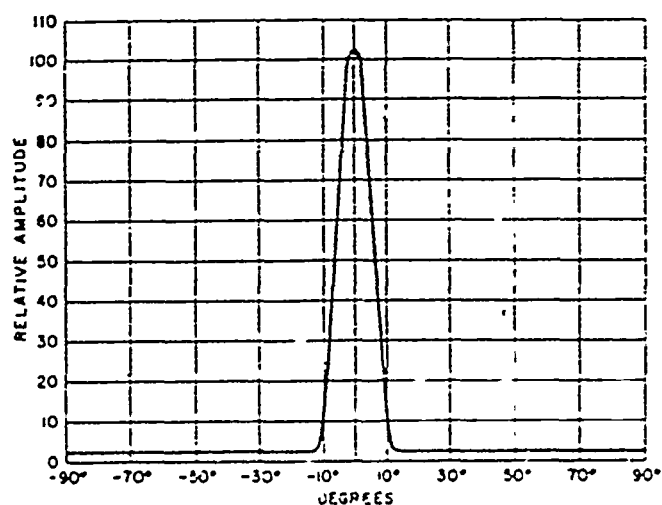*(L14G) at Same Temperature*

161
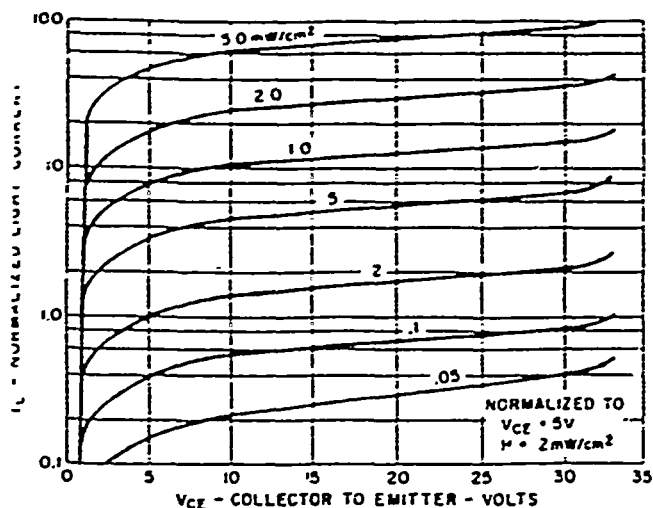
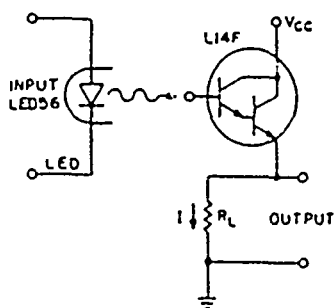1. LIGHT CURRENT VS. COLLECTOR
   TO EMITTER VOLTAGE
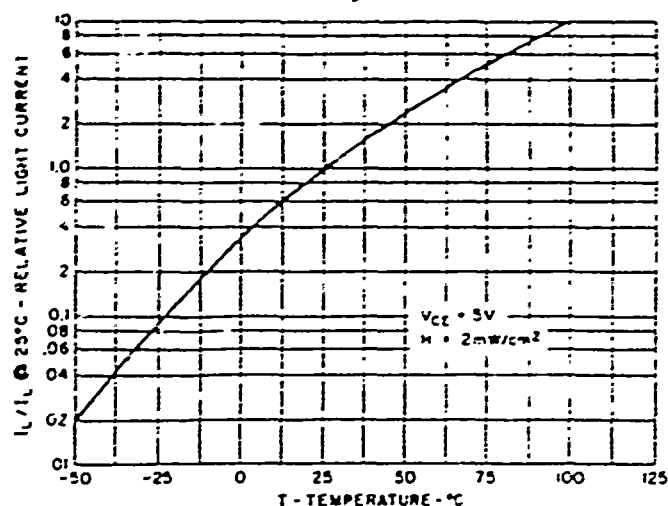
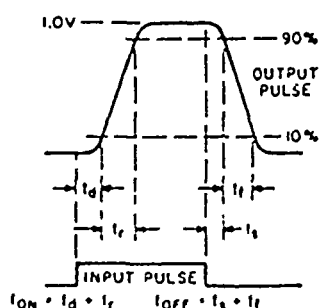2. RELATIVE LIGHT CURRENT VS.
   AMBIENT TEMPERATURE

3. SPECTRAL RESPONSE CURVE

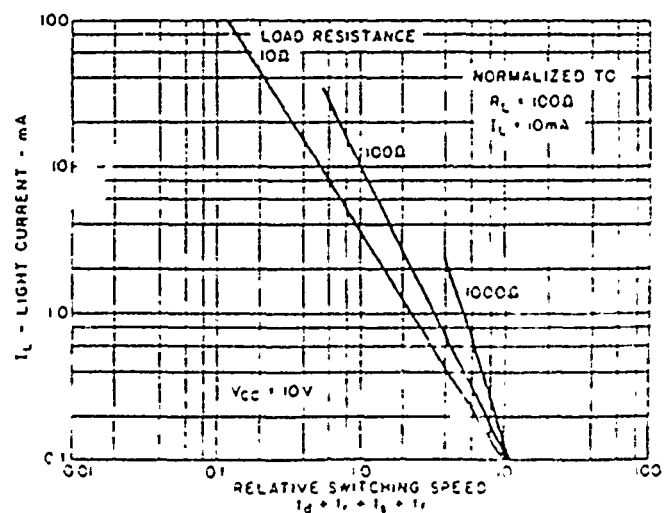4. ANGULAR RESPONSE

5. TEST CIRCUIT

6. WAVE FORMS

162

7. LIGHT CURRENT VS RELATIVE
   SWITCHING SPEED